

# Seismic Waveform Modeling of Natural Hazards and Sharp Structural Boundaries

Thesis by  
Voon Hui Lai

In Partial Fulfillment of the Requirements for the  
Degree of  
Doctor of Philosophy

The logo for the California Institute of Technology (Caltech), featuring the word "Caltech" in a bold, orange, sans-serif font.

CALIFORNIA INSTITUTE OF TECHNOLOGY  
Pasadena, California

2020  
Defended November 18, 2019

© 2020

Voon Hui Lai

ORCID: 0000-0002-0738-0187

All rights reserved except where otherwise noted

*To my parents  
for having faith in my decision to take the road less travelled*

*"The mountains are calling and I must go,  
and I will work on while I can, studying incessantly"*

- John Muir, naturalist

*"For as the rain and the snow come down from heaven  
and do not return there but water the earth,  
making it bring forth and sprout,  
giving seed to the sower and bread to the eater,  
so shall my word be that goes out from my mouth;  
it shall not return to me empty,  
but it shall accomplish that which I purpose,  
and shall succeed in the thing for which I sent it."*

- excerpt from Isaiah 55

## ACKNOWLEDGEMENTS

“It was the best of times.” It could have been the worst of times, but this shall not be my fate because I have been immensely blessed with the wisdom, guidance, and generosity of many people on this PhD journey.

I had the greatest fortune to interact with many professors here at Seismo Lab and Caltech in various capacities: as mentee, as teaching assistant, and as student. First of all, thank you Don for opening my eyes to the secrets the wiggles can hold, and having fun while studying them. I will miss our afternoon discussions trying to make sense of the complicated Earth. Much thanks to Zhongwen for showing me how to have vision for the science that we do and maintain optimism despite setbacks; to Victor for exposing me to so many new areas of geophysics and pushing me and your group members to set our minds on important questions in our field; to Jennifer for the opportunity to think deeper, more than just Earth, and expand seismology to other planets; to Rob Clayton, for being a great academic advisor, helping me with various questions and keeping me on track with my research; and to Mike for serving as my thesis committee member at such late notice, and for the dedication in sustaining a vibrant lab environment, which I think is the key to all the great and innovative science being produced here.

I would also like to thank Rob Graves for his patient guidance on running numerical simulations and getting me started on my own research journey. I am thankful for the opportunity to learn from several professors here, including Mark, Joann, Jean-Phillipe, Hiroo, Egill, and Zach, either from classes or during coffee hour or conversations at the hallway. A special thanks to Joe Kirschvink as well for leading Ge136 and Pahoehoe field trips, which allowed me to connect the sometimes-abstract geophysics to reality and be awed, particularly by how truly dramatic the collapse is at Kilauea.

I am also indebted to several members at the Seismo Lab who have been a tremendous resource throughout my time here. In particular, I want to thank South Mudd 252 (Kim, Donna, Priscilla, Sarah, and Rosemary), for always taking care of the students' needs, even before we knew we need it, and for allowing me to help myself to their office snacks. I also want to thank Ellen for her help on questions related to the seismic network; Ken and Scott for the hardware troubles; and the gentlemen in the basement for helping me to do real geophysics without a computer.

I am surely going to miss South Mudd 362 and its residents. To Jorge and Zhichao, thank you for being such great officemates and friends. Every morning, I look forward to coming into our office and working alongside both of you, knowing I will leave each evening more inspired. I also want to say a very special thanks to Semechah, whose life is parallel to mine in so many ways. Thank you for being a trailblazer and a role model that I look up to. To Yuan-Kai, I am glad that you are in very good hands. To Yiran and Kangchen, thank you for all the guidance and help with my many questions. To Valère and honorary member Jack, thanks for the wonderful conversations inside and outside of the office.

To the current Seismo Fam and former student members of the Seismo Lab, thank you all for the good times together and the collective wisdom. To Chris, Bryan, Steve and Howard, thanks for taking me right under your wings when I first arrived at Caltech, and keeping check on me so that I do not lose perspective. To the postdocs, thank you for the wonderful discussions and helpful advices. To director Nancy Sulaihan and my wonderful choral friends, it has been a great pleasure to make music together. On the days when seismic waves feel like cacophonies, the sound waves we make together bring much joy and wonder. To Jenn and Cassandra at CTLO, thank you for the knowledge and the inspiration to become a good teacher-scientist.

I must also thank Doug Dreger, who first introduced me to seismology and patiently taught me the basics over the summer of 2012; Dr Taka'aki Taira for the guidance during my time at the Berkeley Lab; and the former members of the Dreger group (Avinash, Andrea, Sierra, Seung Hoon, and Aurelie) for their encouragement to pursue a PhD. I still have the Aki & Richards, now more worn.

While at Caltech, I am fortunate to have met many new friends from all over the world and am grateful for all the friendships forged. I particularly want to give a shout out to Bekah for being my biggest cheerleader and for the permanent shotgun. I also thank the Malaysians at Caltech (Cynthia, Marcus, Ying Shi, Linus, Shu-Fay, and Yoke Peng), Leah, Mali, Simon, Heidi, Palma, Ellen, Dan, and Alistair (aka "Musical Buddies") for all the wonderful memories and precious times together. Thank you as well to my friends at GCF and Missio (Jamie, Kim, Jonas, adik Widi, Brandon, Albert, Andy, Robbie, Mark, Len, and many more) for reminding me to fix our eyes on the things that are unseen, and actively think how to love science, people who do science, and the people whom science serves. To friends from Berkeley days (Estrella, Ashley, Soomin, and friends from GP and GAB) and from home

(Caro, Jane, YC, Linda Shareen, Sam, and Zoe), thank you for being my source of encouragements and comfort, and creatively cared for me during the ups and downs of PhD despite the distance.

Thank you as well to Laura and Daniel from ISP, for taking care of all the issues an international student can face; Alice for taking care of me during the sick days; Tony for all the library inquiries; and Trader Joes for the daily bread.

Last but not least, to my family, thank you for believing in me while I am on this journey, with no precedence from anyone that we know of, nor ever thought of while growing up. To Ah Pa, thank you for planting the love for nature and the desire to observe acutely in me at the first place. Finally, your wait is over. To Ah Ma, thank you for the daily support and prayers, and just enjoying the wonders of science as I share during our phone conversations. To brother, thank you for showing me that excellence can be achieved, and making sure that I keep my sense and wits, and my foot on the ground.

“It is a far, far better thing that I do, than I have ever done.” Thank you, from the deepest of my heart, for enriching my PhD experience in ways far beyond what I have ever imagined!

## ABSTRACT

Seismic waveform modeling is a powerful tool for seismologists to learn about the Earth's dynamics, either how a natural hazard evolves with time, or the long-term deformation process governed by fine-scale structures along boundaries inside the Earth. Knowing that the recorded seismograms reflect the cumulative effects of the source, the earth structure, and the instrument response, I carefully study the characters of the seismograms such as the arrival time, amplitude, frequency content, and multipathing, for several settings, with the goal of improving our description of either the source or the structure.

Part 1 focuses on source characterization for non-earthquake natural hazards. I perform moment tensor inversions for the large seismic events at the Kilauea summit to infer the triggering mechanisms for the explosive eruptions and caldera collapse during the 2018 eruption sequence. The addition of infrasound data is crucial to resolve the uncertainties in the moment tensor solutions, particularly the depth and the necessity of the isotropic component. I also present a new mechanistic model to describe the seismic signal from debris flow and apply to the 2018 Montecito debris flow in which key parameters such as boulder size and flow rate and their evolution during the event can be determined using a single seismic station.

Part 2 consists of three studies spanning from the crust to the core, where forward waveform modeling is used to improve our understanding of the sharp structural boundaries and their role in observed ground motion and long-term dynamics. Numerical simulation and dense array analysis are used to model the direct effect of shallow basin structures in Los Angeles on shaking duration and reveal the importance of basin edges and attenuation model for predicting ground motion during large shallow ruptures. I also identify a strong velocity contrast in the lower crust – upper mantle structure across the San Andreas plate boundary system and, given velocity is a proxy to lithospheric strength, the sharp contrast can have a significant role in modulating the long-term plate deformation. Lastly, we observe strong waveform anomalies at the edge of the Pacific Large Low Shear Velocity Province (LLSVP) which have great importance in governing deep mantle convection. To fit the observation, I propose a model of ultra-low velocity zone (ULVZ), plume and slab interacting at the edge of the LLSVP. The configuration and location of this ULVZ-plume-slab interaction is important in inferring the mechanism behind plume generation which gives rise to the Hawaii-Emperor Seamount chain.

## PUBLISHED CONTENT AND CONTRIBUTIONS

Lai, V. H., Graves, R. W., Wei, S. and Helmberger, D. (2017). “Evidence for strong lateral seismic velocity variation in the lower crust and upper mantle beneath the California margin”. In: *Earth and Planetary Science Letters* 463, pp. 202-211 DOI: 10.1016/j.epsl.2017.02.002.

V.H.L. performed all data analysis, and wrote most of the manuscript. The numerical simulation code used in the data analysis is provided by R.W.G.

Lai, V. H., Tsai, V. C, Lamb, M. P., Ulizio, T. P. and Beer, A. R. (2018). “The seismic signature of debris flows: Flow mechanics and early warning at Montecito, California”. In: *Geophysical Research Letters* 45.11, pp. 5523-5535. DOI: 10.1029/2018GL077683.

V.H.L. performed all seismic data analysis except Figure 3.6, and contributed to the manuscript writing, which is spearheaded by V.C.T and M.P.L.. T.P.U. and A.R.B. contributed to the geomorphological analysis presented in the paper.

## TABLE OF CONTENTS

Acknowledgements . . . . .	v
Abstract . . . . .	viii
Published Content and Contributions . . . . .	ix
Table of Contents . . . . .	x
List of Illustrations . . . . .	xii
List of Tables . . . . .	xvii
Chapter I: Introduction . . . . .	1
1.1 Studies on Seismic Sources . . . . .	2
1.2 Studies on Sharp Structural Boundaries . . . . .	3
References . . . . .	4
Chapter II: Insight on the Evolution of Kilauea Caldera during the 2018 Eruption through Seismic Source Characterization . . . . .	5
2.1 Abstract . . . . .	5
2.2 Introduction . . . . .	5
2.3 Background of Kilauea Volcano . . . . .	8
2.4 Observations . . . . .	9
2.5 Source mechanism from Moment Tensor Inversion . . . . .	12
2.6 Mechanisms for Explosion and Collapse Events . . . . .	31
2.7 Reconciling seismic observations with geodetic signals . . . . .	38
2.8 Conclusion . . . . .	40
2.9 Acknowledgments . . . . .	40
References . . . . .	40
Chapter III: The Seismic Signature of Debris Flows: Flow Mechanics and Early Warning at Montecito, California . . . . .	45
3.1 Abstract . . . . .	45
3.2 Introduction . . . . .	45
3.3 Mechanistic Model . . . . .	47
3.4 Data and Results . . . . .	50
3.5 Conclusion . . . . .	62
3.6 Appendix . . . . .	63
3.7 Acknowledgements . . . . .	66
References . . . . .	67
Chapter IV: Shallow Attenuation and Scattering Key to Improved Prediction of Shaking Duration in the Los Angeles Basin . . . . .	71
4.1 Abstract . . . . .	71
4.2 Introduction . . . . .	71
4.3 Observations . . . . .	73
4.4 Results from 3D Simulations . . . . .	81
4.5 Beamforming Analysis on Dense Array . . . . .	92

	xi
4.6 Discussion . . . . .	93
4.7 Conclusion . . . . .	95
4.8 Acknowledgements . . . . .	96
References . . . . .	96
Chapter V: Evidence for Strong Lateral Seismic Velocity Variation in the Lower Crust and Upper Mantle Beneath the California Margin . . . . .	100
5.1 Abstract . . . . .	100
5.2 Introduction . . . . .	100
5.3 Observations . . . . .	104
5.4 Modeling . . . . .	113
5.5 Discussion and Conclusion . . . . .	121
5.6 Acknowledgements . . . . .	124
References . . . . .	124
Chapter VI: Seismic Evidence for the source of the Hawaiian Hotspot . . . . .	128
6.1 Abstract . . . . .	128
6.2 Introduction . . . . .	128
6.3 Data . . . . .	131
6.4 Modeling . . . . .	144
6.5 Discussion . . . . .	154
6.6 Conclusion . . . . .	156
6.7 Acknowledgements . . . . .	156
References . . . . .	156
Chapter VII: Conclusion . . . . .	161

## LIST OF ILLUSTRATIONS

<i>Number</i>	<i>Page</i>
2.1 Distribution of instruments at southeast of Big Island, Hawai'i. . . . .	8
2.2 Infrasonic data and Global Centroid Moment Tensor solutions for all M4.5+ events. . . . .	10
2.3 Backazimuths measured from horizontal particle motions for all the events. . . . .	11
2.4 Waveform fit of regional data using GCMT solution for explosion 05/17b. . . . .	15
2.5 Waveform fit of near-field and regional data using GCMT solution for explosion 05/17b . . . . .	16
2.6 Waveform fit of near field and regional data using best-fitting deviatoric solution for explosion 05/17b. . . . .	17
2.7 Waveform fit of near-field and regional data using best-fitting full moment tensor solution for explosion 05/17b. . . . .	18
2.8 Grid search results of source duration and depth for all explosions using gCAP. . . . .	19
2.9 Correlation between source duration from inversion and measured pulse durations. . . . .	19
2.10 Inversion results for the explosions. . . . .	20
2.11 Bootstrapping results of strike, rake, and dip for the explosions. . . . .	21
2.12 Waveform fit of regional data using best-fitting deviatoric and full moment tensor solution for collapse on 07/15. . . . .	23
2.13 Comparison of raw infrasound and synthetics of deviatoric and isotropic solutions. . . . .	24
2.14 Fit of antipodal PKIKP with different isotropic solutions. . . . .	24
2.15 Comparison of raw infrasound and synthetics generated at different depths and with different velocity models. . . . .	26
2.16 Moment tensor solutions for all collapse events. . . . .	27
2.17 Backazimuths measured from horizontal particle motions recorded by broadband seismometers for rockfalls and explosions . . . . .	32
2.18 Comparison of infrasound synthetics for explosion and collapse. . . . .	33

2.19	Observations of raw infrasound data and the peak delay for rockfalls and explosions. . . . .	34
2.20	Schematic of the evolution at Kilauea Caldera. . . . .	39
3.1	Montecito debris flows (a) Map (b and c) Photographs . . . . .	47
3.2	Detection of the Montecito debris flows from seismic ground motion data . . . . .	52
3.3	Elevation profiles along Montecito Creek, San Ysidro Creek and Romero Creek . . . . .	53
3.4	Across channel profiles of Montecito Creek, San Ysidro Creek and Romero Creek . . . . .	54
3.5	Boulders observed at Montecito Creek and San Ysidro Creek . . . . .	54
3.6	Acceleration PSDs at station TA.544A . . . . .	55
3.7	Evolution of power spectral density (PSD) during the debris flow . . . . .	57
3.8	Seismic velocity time series and their respective spectrogram highlighting signals with various types of sources. . . . .	60
3.9	PSDs measured from deglitched versus raw seismic data. . . . .	61
3.10	Mean PSDs averaged over 5-10 Hz observed at station CI.QAD and station CI.SBC . . . . .	61
3.11	PSD observed at station CI.QAD at 4:13:45AM . . . . .	62
4.1	Map showing the location of M4.4 Fontana event pairs and M3.2 Westwood and M3.5 Beverly Hills events . . . . .	75
4.2	Cut-and-paste inversion result for 2012 Beverly and 2017 Westwood event . . . . .	76
4.3	Record section of velocity in tangential component for 2012 Beverly Hills and 2017 Westwood events. . . . .	77
4.4	Record section of velocity in radial component for 2012 Beverly Hills and 2017 Westwood events. . . . .	78
4.5	Record section of velocity in vertical component for 2012 Beverly Hills and 2017 Westwood events. . . . .	78
4.6	Record section of the tangential velocity for M4 Fontana earthquake pairs and their respective M3 aftershocks. . . . .	79
4.7	Seismograms comparison at soft rock and hard rock stations . . . . .	80
4.8	Record sections showing the comparison between 3-D synthetics (generated at $Q_s = 50V_s$ ) and data for 2012 M3.2 Beverly Hills event. . . . .	82
4.9	Record sections showing the comparison between 3D synthetics and data for the shallow Fontana event. . . . .	83

4.10	Record sections showing the comparison between 3D synthetics and data for the deep Fontana event. . . . .	84
4.11	Record sections showing the comparison between data and 3D synthetics generated from CVM-S4.26.M01 with several modifications for the shallow M4.4 Fontana event, filtered at 2 - 20 seconds. . . . .	87
4.12	Record sections showing the comparison between data and 3D synthetics generated from CVM-S4.26.M01 with several modifications for the shallow M4.4 Fontana event, filtered at 5 - 20 seconds. . . . .	88
4.13	Record sections showing the comparison between 3D synthetics (generated at $Q_s = 200V_s$ ) and data for 2012 M3.2 Beverly Hills event. . . . .	89
4.14	Record sections showing the comparison between tangential velocity data for 2012 M3.2 Beverly Hills event and 3D synthetics generated with three different scaling for $Q_s$ . . . . .	90
4.15	Cross-section showing the shear wave velocity structure from the CVM-S4.26.M01 model and CVM-H model . . . . .	91
4.16	Beamforming analysis of Santa Fe Springs (SFS) array. . . . .	93
4.17	Attenuation scaling in Los Angeles Basin from different models . . . . .	95
5.1	A schematic drawing of California velocity structure. . . . .	101
5.2	Seismic lithospheric thickness beneath California margin (Reproduced from Melbourne and Helmberger, 2001) . . . . .	102
5.3	Location of the earthquakes in Mendocino and Napa regions . . . . .	104
5.4	Sensitivity kernel of SH wave to shear wave speed for different periods across depth. . . . .	107
5.5	Cross-correlation results for station SMI, SBB2 and SLA. . . . .	108
5.6	Time delay between the observed long period SH waves and the 1-D synthetics using focal mechanisms from catalog . . . . .	109
5.7	Time delay between the observed long period SH waves and the 1-D synthetics using focal mechanisms from CAP . . . . .	110
5.8	Record sections display broadband (1-100s) SH waveforms in displacement from the coastal stations and from inland stations . . . . .	111
5.9	Azimuthal record sections of the broadband SH waves from the 2014 Mendocino event . . . . .	112
5.10	Record sections of 1-D synthetics to test the effects due to: (left) different crustal thickness and (right) different lid thickness . . . . .	113
5.11	Map illustrating the configuration used in the 3-D finite difference modeling. . . . .	115

5.12	Cross-section profiles of shear wave ( $V_s$ ) structure along coast and inland. . . . .	116
5.13	Maps showing time delay between the long period SH waves from the 2014 Mendocino event, and (a) the 1-D synthetics from ‘Gil 7’ model, (b) the 3-D synthetics from our proposed model . . . . .	117
5.14	Maps showing the time delay between the recorded long period SH waves from the 2014 Mendocino event, and the synthetics from (a) our preferred model, (b) USGS Bay Area and CVM-S4.26 Southern California model and (c) USGS Bay Area and CVM-Harvard Southern California model. . . . .	118
5.15	Map showing the boundary for each 3D velocity model used in the study . . . . .	119
5.16	Azimuthal record sections show long period (30 – 50 seconds) SH waveforms recorded along Profile A, B and C for the 2014 Mendocino event. . . . .	120
5.17	Interpretation of the GPS velocity fields along three profiles perpendicular to (i) Northern California, (ii) Central California, and (iii) Southern California. . . . .	123
6.1	Map shows the shear wave velocity perturbation at the core-mantle boundary for GyPSuM model, location and ray paths of events used in this study. . . . .	130
6.2	Shear wave seismic velocity perturbation at 2850 km depth for four global models (GyPSuM, SEMUCB-WM1, S40RTS, and S362ANI). . . . .	132
6.3	Multiple ScS modeling of the 2019-05-04 M6.9 earthquake on the Island of Hawai’i, recorded at IU.KIP station. . . . .	133
6.4	Measurements of ScS-S differential travel time residuals for several events in Fiji-Tonga region. . . . .	135
6.5	Record section on the right shows S and ScS along two azimuths for Event A and Event B. . . . .	137
6.6	(a) Cross-sections of GyPSuM model for event A and B (b) Maps showing the arrival time of S and ScS phase, and differential ScS-S time at each station. . . . .	138
6.7	Record sections compare data stacks at three different azimuth bins. . . . .	139
6.8	Record sections comparing stacked tangential displacement data at five different distances for Event A. . . . .	140

6.9	Record sections comparing stacked tangential displacement data at five different distances for Event B. . . . .	141
6.10	Observation of $S^*$ for Event C using multipath detector. . . . .	142
6.11	Record sections comparing stacked tangential displacement data from Event C. . . . .	143
6.12	Record sections comparing stacked tangential displacement data from Event C and synthetics generated using GyPSuM model . . . . .	146
6.13	Record sections comparing ULVZ with uniform velocity and gradient velocity. . . . .	147
6.14	Record sections comparing different locations of ULVZ. . . . .	148
6.15	Record sections comparing ULVZ of different widths. . . . .	149
6.16	Record sections showing the effect of the ULVZ, slab and plume structure on the synthetics for Event B. . . . .	150
6.17	Record sections showing effects of increasing perturbation of GyP-SuM model for Event B. . . . .	151
6.18	Record sections showing synthetics from best model for Event A and Event B. . . . .	152
6.19	Record sections showing synthetics from best model for Event C. . .	153

## LIST OF TABLES

<i>Number</i>	<i>Page</i>
2.1 Table listing the best-fitting focal mechanisms inverted using gCAP for all 62 events in this study. . . . .	28
2.2 Continued from Table 2.1 . . . . .	29
2.3 Continued from Table 2.2 . . . . .	30
5.1 The earthquake source parameters used in this study are provided by the ANSS Comprehensive Earthquake Catalog (ComCat). . . . .	105
5.2 Description of the modified 1-D ‘Gil7’ model . . . . .	106
6.1 Deep events in Fiji-Tonga region used in measuring differential ScS-S time in Figure 6.4. . . . .	134

*Chapter 1*

## INTRODUCTION

A major source of information on the dynamics during natural hazards and long-term dynamics within Earth comes from seismology. The recorded seismic waves provide detailed source processes that excite these waves and reveal the structure of the Earth's interior at various length scales, which govern regional and global deformation. These waveforms can be represented as a sequence of linear filters where the recorded ground displacement,  $U$  is a result of a source function ( $S$ ), operated on a propagation function ( $G$ ) and modulated by the recording instrument response ( $I$ ), such that  $U = S * G * I$ . Seismic waveform modeling studies have built on this concept of linear filter theory by separating the contribution of the source and the structure to study their individual effects on the character of the observed waveforms such as arrival time, amplitude, frequency content, or multipathing effect. The procedure involves modifying either  $S$  or  $G$  to generate synthetic measurements that best match the observation. Through waveform modeling, seismologists have made significant advances in understanding complex earthquake rupture processes and also described new novel seismic sources such as glacial earthquakes [1] and seismic noise generated by sediment transport in rivers [2]. The propagation effect, which involves the medium that the seismic waves are traveling through, are accounted by the accurate description of regional and global Earth models. In recent decades, several developments including the expansion of instrument coverage, new data sets including ambient noise, and advances in computational power have further improved our capability to image the three-dimensional velocity structures in the Earth and provide crucial constraints to the properties of the Earth's interior structures.

Seismic waveform modeling, using both the forward and inverse approaches, has been instrumental in understanding the physics behind the generation of these seismic waves, and helps resolve many outstanding problems in the Earth sciences including, but not limited to, predicting ground motion during catastrophic earthquakes, providing early warning for natural hazards, and describing the nature of mantle convection. However, there remain challenges to accurately describe the source and propagation terms due to several reasons, such as inherent trade-offs in seismic observation and lack of sharp details in the tomography models. In this the-

sis, I will demonstrate how modeling new seismic (and non-seismic) observations through forward numerical simulations and inversion can overcome these challenges and improve the descriptions of the source and structure terms in five different contexts, and therefore refine our overall understanding of dynamics in natural hazards and the role of sharp boundaries in controlling deformation process.

### **1.1 Studies on Seismic Sources**

For seismic sources shorter compared to the observed seismic wavelengths, the sources can be considered as point sources and mathematically represented by a  $3 \times 3$  symmetric tensor called the moment tensor [3]. Tectonic earthquakes, which are modeled as shear fractures, can be represented by a specific moment tensor representation that is a double-couple source where both the trace and determinant of the moment tensors are zero. The description of the moment tensor, however, is fully generalized, and can be used to describe more complicated non-double-couple seismic sources such as volcanic eruptions (e.g. [4]) and nuclear explosions (e.g. [5]). In Chapter 2, moment tensor inversion is used to characterize a series of seismic events marking the eruption and collapse of the Kilauea caldera at Hawaii in 2018. However, characterizing non-double couple sources using only long period waveforms is challenging as there is a strong correlation between the two non-double couple parameters, i.e. isotropic and compensated-linear-vector-dipole (CLVD) components [6]. By incorporating the information from infrasound data, which is sensitive to the upward radiated seismic energy, we can resolve the source ambiguity from seismic data alone, distinguish the contribution of isotropic component to the seismic source, and therefore identify a distinct evolution of the seismic sequence, from explosions to normal faulting collapse events. Particle motion from seismic data further constrains the migration of the seismic source, which helps us to infer how the deformation at depth controls the collapse process.

While moment tensor is an effective tool to understand the seismic energy from sources at depth, there is an increasing need to develop theoretical frameworks to interpret seismic signatures from unconventional sources such as debris flows. In Chapter 3, we present a new mechanistic physical model (published in [7]) to describe the seismic ground motion generated by debris flows and apply the model to the devastating debris flows in Montecito, California on 9 January 2018. By fitting the amplitude and the frequency spectrum of the seismic signal using the model, several key parameters controlling debris flows, such as the debris-flow speed, boulder sizes, and location, can be estimated. Our model provides a

key step towards creating a physics-based early warning system, which is a major improvement from previous empirical approaches that are very site-specific.

## **1.2 Studies on Sharp Structural Boundaries**

Careful identification of the seismic phases has revealed many major discontinuities and structural and compositional boundaries within the Earth's interior including the Moho, the mantle-transition zone, and the core-mantle boundary. While seismic tomography has been extremely useful in revealing 3-D heterogeneities within the earth, the smoothing process during the seismic tomography inversion inherently smears the sharp boundaries. The remainder of this thesis will traverse from the crust to the core, using forward waveform modeling to improve our understanding of sharp boundaries and their role in observed ground motion and long-term dynamics.

Chapter 4 focuses on modeling the direct effect of shallow basin structures in Los Angeles on ground motion intensity and shaking duration, most prominently during shallow earthquakes. From beamforming analysis on dense array data, we can deduce that the role of basin edge in exciting the long duration. Combining observations and results from numerical simulations based on the current 3-D velocity models, we show that to improve our overall capability in predicting ground motions during future earthquakes, a better description of shallow heterogeneities, sharp boundaries, and the shallow attenuation model is necessary.

Chapter 5, published in [8], concerns the challenges in resolving the lower crust – upper mantle velocity structure across the boundary between the Pacific plate and North American plate. While there may be little travel time differences observed in the teleseismic phases with nearly vertical ray paths, regional long period SH waveforms suggest otherwise, and show strong travel time variations across the boundary. From numerical simulations, we can show these travel times are best fit by a model consisting of a fast lid abutting a thick slow crust. Taking velocity as a proxy to lithospheric strength, this sharp contrast has a strong influence in how the plate boundary deforms over time and may explain the observed asymmetric strain rate across the boundary.

Lastly, in Chapter 6, we recognize several observations, that are the rapid variation of differential ScS-S travel time and multipathing of Sdiff phase, at the edge of the Pacific Large Low Shear Wave Province (LLSVP) southeast of Hawaii, cannot be explained by the global tomographic models and require fine-scale strong heterogeneities at the lowermost mantle. Using an iterative forward modeling approach,

we propose a model of ultra-low velocity zone (ULVZ), plume, and slab at the edge of the LLSVP that best fits the observation. The configuration and location of this ULVZ-plume-slab interaction, estimated from the modeling process, is important in inferring the mechanism behind plume generation which gives rise to the Hawaii-Emperor Seamount chain.

## References

- [1] G. Ekström, M. Nettles, and G. A. Abers. Glacial earthquakes. *Science*, 302(5645):622–624, 2003.
- [2] V. C. Tsai, B. Minchew, M. P. Lamb, and J.-P. Ampuero. A physical model for seismic noise generation from sediment transport in rivers. *Geophysical Research Letters*, 39(2), 2012.
- [3] K. Aki and P. G. Richards. *Quantitative Seismology*. 2002.
- [4] B. R. Julian and S. A. Sipkin. Earthquake processes in the Long Valley caldera area, California. *Journal of Geophysical Research: Solid Earth*, 90(B13):11155–11169, 1985.
- [5] D. Dreger and B. Woods. Regional distance seismic moment tensors of nuclear explosions. *Tectonophysics*, 356(1-3):139–156, 2002.
- [6] H. Kawakatsu. Observability of the isotropic component of a moment tensor. *Geophysical Journal International*, 126(2):525–544, 1996.
- [7] V. H. Lai, V. C. Tsai, M. P. Lamb, T. P. Ulizio, and A. R. Beer. The seismic signature of debris flows: Flow mechanics and early warning at Montecito, California. *Geophysical Research Letters*, 45(11):5528–5535, 2018.
- [8] V. H. Lai, R. W. Graves, S. Wei, and D. Helmberger. Evidence for strong lateral seismic velocity variation in the lower crust and upper mantle beneath the California margin. *Earth and Planetary Science Letters*, 463:202–211, 2017.

*Chapter 2***INSIGHT ON THE EVOLUTION OF KILAUEA CALDERA  
DURING THE 2018 ERUPTION THROUGH SEISMIC SOURCE  
CHARACTERIZATION****2.1 Abstract**

The deformation at the Kilauea summit and Lower East Rift Zone during the 2018 eruptive episode shows a tightly-connected magmatic plumbing system from the summit caldera to the lower east rift zone. Using multiple approaches including seismic waveform analysis, moment tensor inversion, and infrasound simulation, we characterized the 62 M4.7+ events at the summit from 2018-05-17 to 2018-08-02 to infer the evolution of the magmatic reservoir and its impact on the caldera-rift system. The inclusion of local seismic and infrasound data is particularly important in ascertaining the role of non-double couple component in these seismic events. We estimated that the first 12 events from 2018-05-17 to 2018-05-26 to be highly explosive and share the same source location as explosive events triggered by past rockfalls. We inferred the source to be the previously-estimated Halema'uma'u reservoir, based on both seismic inversions and travel times of the infrasound signal. Once the reservoir has drained sufficiently and is no longer pressurized, the explosive events ceased, and the caldera subsequently experienced partial collapse through a series of shallow normal events along inward dipping faults, with minimal non double-couple contribution. The migration of the sources suggested by the seismic and infrasound data coincides with the change of surface deformation patterns observed independently by geodetic signals and radar imagery. The characterization of these large seismic events provides important constraints on the triggering mechanisms for the explosions and collapses which is driven by magma withdrawal from the summit due to the rift intrusion. In particular, we infer the collapse events to be represented by a combination of piecemeal-trapdoor-style collapses and differ from the commonly assumed 'piston' model.

**2.2 Introduction**

Caldera collapses at basaltic volcanoes are very dynamic and often coupled with intense eruptions at the caldera and rift intrusions along the flanks, posing major geological hazards to the local communities and the global airline industry. Charac-

terizing the large seismic events associated with the eruptions and caldera collapses is one way to understand the mechanism behind the caldera collapse and monitor the overall evolution of the caldera-rift zone system. The 2018 Kilauea eruption, well-recorded by multiple complementary geophysical instruments, provides an unprecedented opportunity to study the dynamics during caldera collapse. The eruption evolved over the course of several months starting in late April until early August, with the opening of new fissures downstream at the Lower East Rift Zone (LERZ) in early May, intense seismicity including the largest Mw 6.9 earthquake in 43 years along the *décollement*, draining of lava lake at the summit and numerous Mw 4.7 to 5.4 seismic events associated with the volcanic eruptions and subsequent collapse of the caldera [1]. The eruptive behavior at the rift such as effusive surges followed by collapse events at the summit [1] and the almost-linear relationship of volume change between the summit subsidence and LERZ lava flows [2] suggest a very well-connected subsurface magma plumbing system from the summit to the rift zone. Therefore, understanding the seismic events at the summit can provide critical insights into the changes in the subsurface magmatic reservoirs near the summit, and their role behind volcanic explosions and caldera collapses.

Apart from Kilauea, strong seismic activity during caldera collapse has been recorded at a few volcanoes globally (e.g. Bárðarbunga, Iceland [3], Piton de la Fournaise on Réunion Island [4, 5] and Miyake-jima, offshore Japan [6]). Due to difficult accessibility, these processes are monitored with stations at teleseismic distances and few on-site stations. The characterization of the seismic source mechanisms is restricted in using only far-field long-period surface-wave data. However, there are several limitations. First, the long period waves have little depth sensitivity and cannot resolve shallow depths [7]. For instance, at Piton de La Fournaise, Fontaine et al. [4] find similar mechanisms fit waveforms at a large range of depth, between 5 and 15 km. The magma reservoirs beneath volcanoes are complex, multi-layered, and can occupy a wide range of depths, from 1-2 km beneath the surface to a depth of  $\sim 20$  km. Accurate determination of the source depths can help identify which reservoir is deforming and provide high resolution of the subsurface magmatic process.

In addition, caldera collapse often generates seismic sources with significant non double-couple contributions. However, the long-period waveform is unable to distinguish the isotropic and vertical compensated linear vector dipole (CLVD) components for shallow earthquakes such as these volcanic events due to the strong

correlation between the two components [8]. This has strong implications in the interpretation of the collapse mechanisms, demonstrated in the following two examples. Volcanic earthquakes, resolved using centroid moment tensor method (e.g. [9, 10]), consider deviatoric solution (trace of moment tensor equals to zero) and prefer compensated-linear-vector-dipole (CLVD) focal mechanisms, either by vertical compression (vertical-P) or extension, which indicates ring-faulting. Meanwhile, at Miyake-jima, distinct very-long-period (VLP) events at 10 - 50 seconds with dominant volumetric components are observed, which is interpreted as inflationary signals from a piston-like collapse, where magma flow causing the piston to slide and pressurize the magma chamber, causing the chamber to expand [6].

Incorporation of local, near-field data can help discriminate the source process. For example, Duputel and Rivera [5] were able to use stations within 10 km to ascertain the role of vertically closing crack, rather than ring-faulting, in the collapse of Piton de La Fournaise and determine the overall duration of the source time function. Using other types of geophysical data can further complement seismic data by providing a different perspective on the source process. An example of such use is the inclusion of pressure gauge array data in the 2015 volcanic tsunami earthquake at the submarine Smith Caldera [11] as the pressure gauge is sensitive to energy radiating upward from the source. Fukao et al. [11] showed that the recorded tsunami motion required a significant sea-surface uplift which cannot be reproduced by the vertical-CLVD seismic source model published in the catalogs and require a new mechanism with efficient tsunami but weak seismic radiation.

The dense and diverse instrumentation on the Kilauea summit, including broadband seismometers, accelerometers, and infrasound sensors maintained by the USGS Hawai'i Volcano Observatory (Figure 2.1), allows us to use multiple perspectives to describe the possible source mechanisms involved in the complex sequence of explosive eruptions and subsequent collapse at Kilauea. The goal of this study is to use direct observations from seismic and infrasound data, and moment tensor inversion to characterize the large Mw 4.7 to 5.4 seismic events recorded at the Kilauea summit and understand the evolution during the 2018 Kilauea eruption. In the following sections, we will discuss: how the past deformation activity at Kilauea provides our knowledge on the magmatic system at Kilauea; direct observation from seismic and infrasound data on the 2018 eruption showing four distinct episodes; the moment tensor inversion results for the explosions and collapses, identifying the changes in source characteristics; the mechanisms driving the collapse; and

lastly how the quasi-periodic seismic events reconcile with the continuous aseismic deformation throughout the eruption.

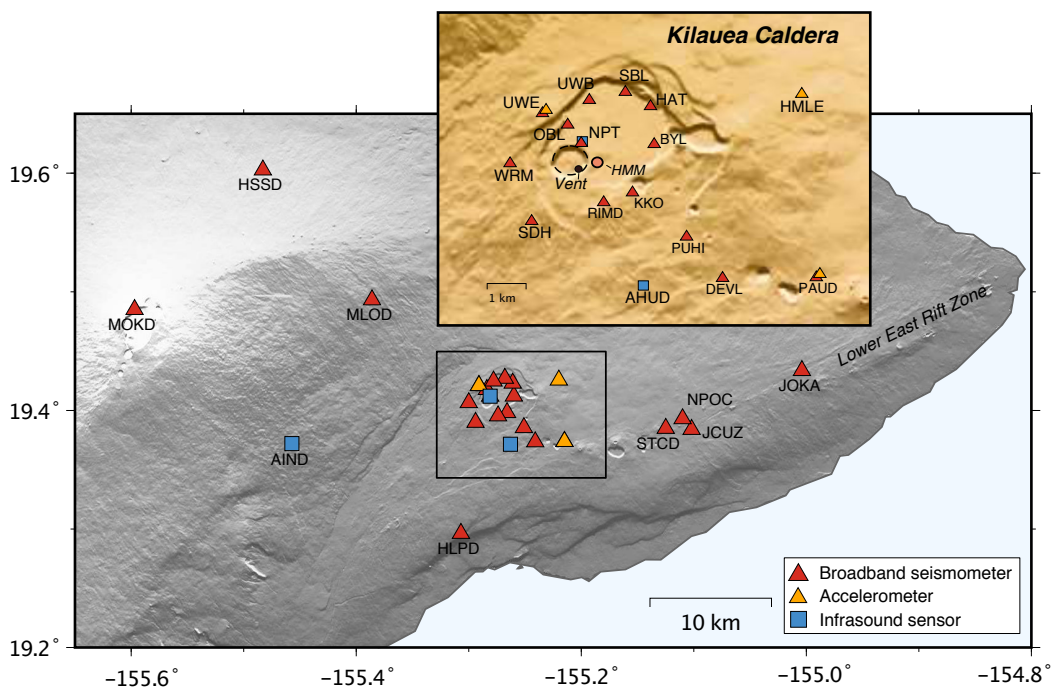


**Figure 2.1:** Distribution of instruments in southeast Hawai'i. Map highlights the main features of the Kilauea Volcano, the summit caldera and the Lower East Rift Zone where the eruptive fissures are located. The inset shows the main features of Kilauea Caldera, including the smaller Halema'uma'u crater (in dashed black line), the vent with an active lava lake. The predicted location of the Halema'uma'u (HMM) magma reservoir is marked by an orange circle in the inset. The red triangles represent broadband seismometers (HH channels), yellow triangles represent accelerometer (HN channels), and blue squares represent infrasound sensor (BDF and HDF channels).

### 2.3 Background of Kilauea Volcano

Kilauea Volcano, one of the youngest shield volcanoes in the Hawaiian hotspot chain, has a long-recorded history of eruptions at the summit caldera and at its flanks along the rift zones. Prior to the eruption and caldera collapse in the summer of 2018, a new vent opened within the Halema'uma'u crater at the Kilauea summit in 2008 (Figure 2.1) and marked a decade of small continuous eruptions simultaneously at the summit and along the east rift zone [12]. This vent is filled with lava and the level of the lava lake fluctuates in the time scales of minutes to months, over several tens of meters due to changes in magma reservoir pressure, and to a smaller degree the outgassing processes [13]. During degassing, a variety of seismic activities, such

as Very-Long-Period (VLP) events [14, 15, 16], Long-Period (LP) seismicity, and tremor [17], is often detected, suggesting a connected pathway between the seismic source and the vent at the summit. Furthermore, observed since at least the 1990s, perturbation in the magma system within the Kilauea Volcano also produces episodic deflation-inflation (DI) events that last hours to days at the summit which induces temporal changes in flow rate down at the rift zone, showing that the magmatic plumbing system from the summit to the rift zone is highly connected [18].

This interesting relation between activities at the summit and the eruption behavior at the rift zone motivates much research to understand the source of the seismic signal and the controlling mechanisms. The results from various independent techniques and observations, including inversion of tilt meter data of the DI events [18], deformation modeling using interferometric synthetic aperture radar (InSAR) data [19], seismic modeling based on radial semblance method [15], grid search of moment tensor results [14], and P-wave tomography [20], point to a common shallow source, namely the Halema'uma'u reservoir (HMM, Figure 2.1). HMM is projected to be slightly east of the Halema'uma'u crater, at a depth of between 1 - 2 km below the surface and thought to be connected through a network of dikes and sills to a deeper magma reservoir beneath the southern part of the Kilauea caldera [21].

## 2.4 Observations

In the 2018 eruption, a total of 62 significant Mw 4.7 to 5.4 seismic events occurred at the Kilauea summit between May 17 and August 2. These events are recorded by a permanent monitoring network maintained by USGS Hawai'i Volcano Observatory (HVO) with a mix of broadband instruments, accelerometers, and infrasound array covering the caldera vicinity and southern part of the island (Figure 2.1). Using long period surface waves, both global centroid moment tensor (GCMT) catalog [<https://www.globalcmt.org>] and W-phase Moment Tensor catalogs [maintained by USGS, accessed through <https://earthquake.usgs.gov>] show that all the 62 events share very similar focal mechanisms, which are vertical CLVDs with a vertical-P axis. However, the infrasound waves, which are measured by the nearby AHUD station (about 4.5 km from crater), indicate otherwise and show a distinction between the events (Figure 2.2). The first 12 events from May 17 to May 26 have fairly weak pressure signals, and for the stronger ones, the main peaks show an upward polarity. The remaining 50 events from May 29 to August 2 have stronger amplitude signals, with clear initial peaks pointing downward. An upward polarity would represent compression, which can be seen as volume expansion due to sources like explosions,

while an initial downward polarity would indicate decompression or rarefaction. In addition, there is a significant delay in arrival times of the main peaks from the crater to the station between the first 12 events and the remaining 50 events, which implies that the two groups of events might be caused by very different source processes.

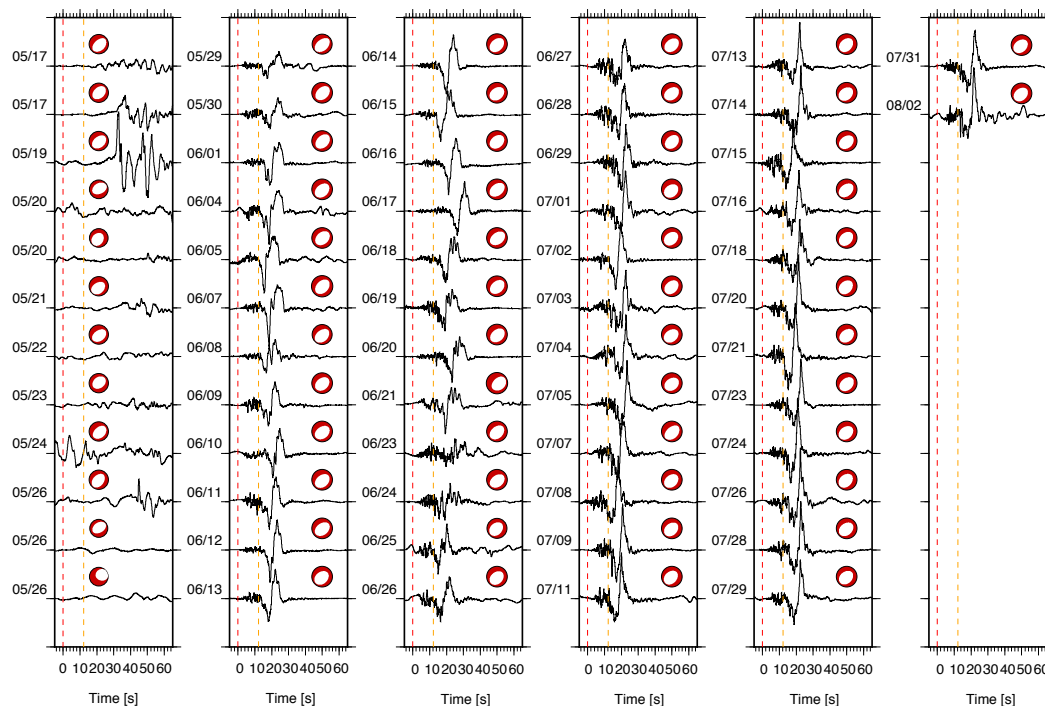


**Figure 2.2:** Figure shows raw infrasound data for AHUD sensor and the Global Centroid Moment Tensor (GCMT) solutions for the 62 M4.5+ seismic events happening at the summit. The red dashed line is a marker for origin time and the orange dashed line marks the expected arrival time of the infrasonic pulse traveling at acoustic speed ( $\sim 340$  m/s) from source to sensor. The GCMT solutions are similar for all events. The infrasound data, on the other hand, have two distinct patterns. Data from 05/17 to 05/26 vary greatly between each event and have no clear arrival at the expected time. Data from 05/29 onwards have a distinct high frequency signal followed by a strong downward pulse which travels at acoustic speed. The data are plotted on the same amplitude scale.

Long period particle motions from the seismic events are useful in determining the source location. We calculated the horizontal particle motion using data from three accelerometers (UWE, HMLE and PAUD, see Figure 2.1 inset) over the course of the eruption. The data are filtered to long period (12.5 - 33 seconds) and the back-azimuth is measured by treating the two horizontal components as a covariance matrix and calculating the angle of rotation of the eigenvector with the largest eigenvalue. In Figure 2.3, the measurements from the accelerometers are

shown, as unlike the broadband seismometers, the amplitude of the accelerometer data remains unclipped throughout all 62 events. In extreme environments such as volcanic caldera, the strong velocity heterogeneities and sharp topographic change can distort the ray path from the direct great-circle path, hence the particle motions from the stations do not project onto a common point at the caldera. Nonetheless, the particle motions, marked by the back-azimuths, show three consistent transitions where the seismic source migrate across the caldera. The accelerometer closest to the caldera, UWE, shows a consistent back-azimuth for the first 12 events from May 17 to May 26 (Figure 2.3). The particle motions from the broadband seismometers show very little variation as well, indicating the seismic source for the first 12 events are very localized.

For the remaining 50 events, we see the back-azimuth changes with time at station UWE and PAUD, with a marked transition around June 23 and 25. For UWE, the

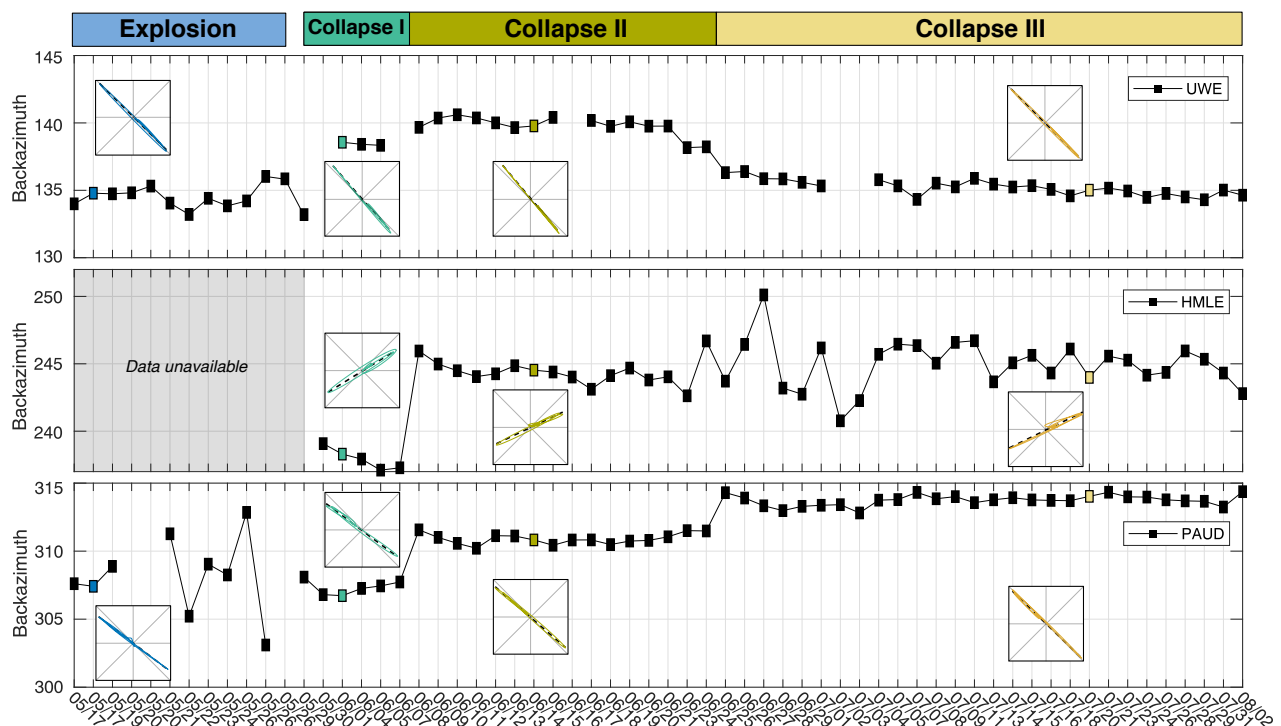


**Figure 2.3:** Backazimuths measured from horizontal particle motions for all the events. Figure shows backazimuths measured from the horizontal particle motions for three accelerometers (UWE, HMLE, PAUD). The changes in backazimuth indicate four possible episodes, namely ‘Explosion’, ‘Collapse I’, ‘Collapse II’, and ‘Collapse III’, which is further discussed in the text. The particle motions from the representative events for each episode are shown and color-coded based on the episode.

decrease in back-azimuth shows an eastward migration of the source. For PAUD, which is located south of caldera, the increase in back-azimuth also shows consistent migration towards the east. The change in back-azimuth for HMLE is minimal. Given HMLE is to the east of caldera, an eastward migration of the source would have little effect on the back-azimuth. The timing of the transition determined by the particle motion corroborates with the changes in displacement behavior observed in several GPS stations and tiltmeters at the caldera [1].

The spatial migration is also remarkably consistent with the findings from the differential topography maps from airborne InSAR reconnaissance surveys [2] and radar amplitude images (acquired by the Agenzia Spaziale Italiana CosmoSkyMed satellite system, accessed through [volcanoes.usgs.gov](http://volcanoes.usgs.gov)). The surveys captured snapshots of the continuous deformation process of the Halema'uma'u crater, at about weekly to biweekly intervals. First, they showed a localized subsidence at the eastern edge of the crater, at the same location as the proposed HMM reservoir from May 17 and 26. From May 29 onwards till mid-June, the caldera began to experience major collapse, first locally at the location of HMM reservoir, then towards the west of the reservoir with steep drops and big topographic change. From late June to early August, the collapse migrated eastward with a less severe drop in elevation. The images further show the collapse is mostly asymmetrical, where the caldera floor dropped significantly more towards the north, and west compared to east.

From the particle motion analysis, we can determine four distinct episodes in the whole eruption sequence. Characterizing the source mechanisms during these episodes will help us to understand how the changes in the subsurface processes beneath the caldera control the observed deformation.

## **2.5 Source mechanism from Moment Tensor Inversion**

In this section, we will determine the seismic source mechanism for all the 62 significant events through an inversion process of the observed ground motion. This source mechanism, represented mathematically by a  $3 \times 3$  symmetric tensor with six independent components, can be decomposed into deviatoric (no volume change) and isotropic (volumetric) terms [22]. In this study, we use the generalized Cut-and-Paste (gCAP) method [23, 24, 25] to perform the source inversion for a few reasons. The Green's functions are computed with the frequency-wavenumber method described in Zhu and Rivera [26] with a 1-D layer average model of a 3-D local seismic tomography of Mauna Loa and Kilauea volcanoes in Hawaii

constructed using regional P-waves [27]. However, we find that the 3-D local seismic tomography has a very heterogeneous velocity structure with phase velocity perturbation close to 10% even at long period centered at 23 seconds. Anisotropic behavior cannot be ruled out as well, for fine-scale layering in dyke or sill complexes can affect shear wave velocities [28]. Given such a complicated velocity structure which cannot be adequately described in 1-D velocity model, the gCAP method cross-correlates the predicted and observed waveforms, allowing independent time-shifts for all three components to maximize the cross-correlation coefficients, and hence minimize the effect of imperfect Green's Functions and event location in the inversion process. The gCAP method includes the decomposition of general seismic potency (deviatoric and isotropic) and moment source tensors to represent the relative strength of the double-couple (DC), isotropic (ISO), and compensated linear vector dipole (CLVD) components within the seismic source. The inversion process searches for strike, dip, rake, moment, and two dimensionless parameters which account for the ISO and CLVD source terms. The source is approximated by a point source, with an isosceles triangular source time function of some duration. Different weighting for data at near field (< 3km) and far field stations is applied to prevent the large amplitude waves, particularly from close-by stations, from dominating the inversion.

The seismic data used in the inversion are recorded by a distribution of seismometers, 14 of those within 3 km of the caldera and 8 within 35 km of the caldera (Figure 2.1). Data from stations further away on the island are not used in the analysis as they show strong multipathing behavior with no clear single elliptical particle motion, indicating surface waves arriving in multiple wave fronts. For stations near the caldera, we only use the vertical component because horizontal components at long period are highly susceptible to tilt from deflation or inflation processes [29].

### **Explosions From May 17 to May 26**

For the first 12 events between May 17 and May 26, based on the particle motion and radar imagery, we set the hypocenter at the location of HMM reservoir (19.4069°, -155.2752° as reported in Baker and Amelung [19]). The input data are filtered between 12.5 to 33 seconds (0.03-0.08 Hz). The role of near-field data is particularly crucial in distinguishing the necessity of a highly isotropic source. The GCMT solution, which is only deviatoric, can only fit the far-field data and not the near-field stations (Figure 2.4 and 2.5). Similarly, when we only consider deviatoric moment tensor solutions (ISO = 0) in the inversion, we found the best fit deviatoric

solution cannot fit the near-field data (Figure 2.6). On the other hand, we are able to find full moment tensor solution that fit the near-field and far-field data well (Figure 2.7). With that, we only invert for full moment tensor solutions and performed grid-search to find the best depth and source duration. The grid search results show that the events do not share the same source duration (Figure 2.8) and the source durations are found to be correlated to the length of the pulse in the raw waveform (Figure 2.9). The source durations of these explosions are much longer than expected for similar-size earthquakes, from 10 to 20 seconds. Event 4 and 5 have exceptionally long source durations, and hence their focal mechanisms are not well-determined. The long source duration also indicates the centroid time differs from the origin by several seconds. However, the use of time-shift in the gCAP inversion does not allow us to determine the centroid time for each event.

Despite the difference in source duration, we found that the events are highly similar, with moment magnitude between  $M_w$  4.37 to 4.95, highly isotropic at an average of 72.4% and has significant double-couple component (average 27.4%) and negligible CLVD component (Figure 2.10). The strike, rake, and dip of the focal mechanisms remain similar (average 66, -72, 49) and stable throughout the events, as shown in the bootstrapping analysis (Figure 2.11). As for the source depth, the grid search results show that most of the explosions fit similarly well at a depth range between 0.5 and 2.5 km, with the best depth at 900 m from surface (Figure 2.8). The depth, with the uncertainty, is similar to the depths estimated for HMM reservoir in other studies (1 km in Chouet et al. [14] to 2 km in Baker and Amelung [19]).

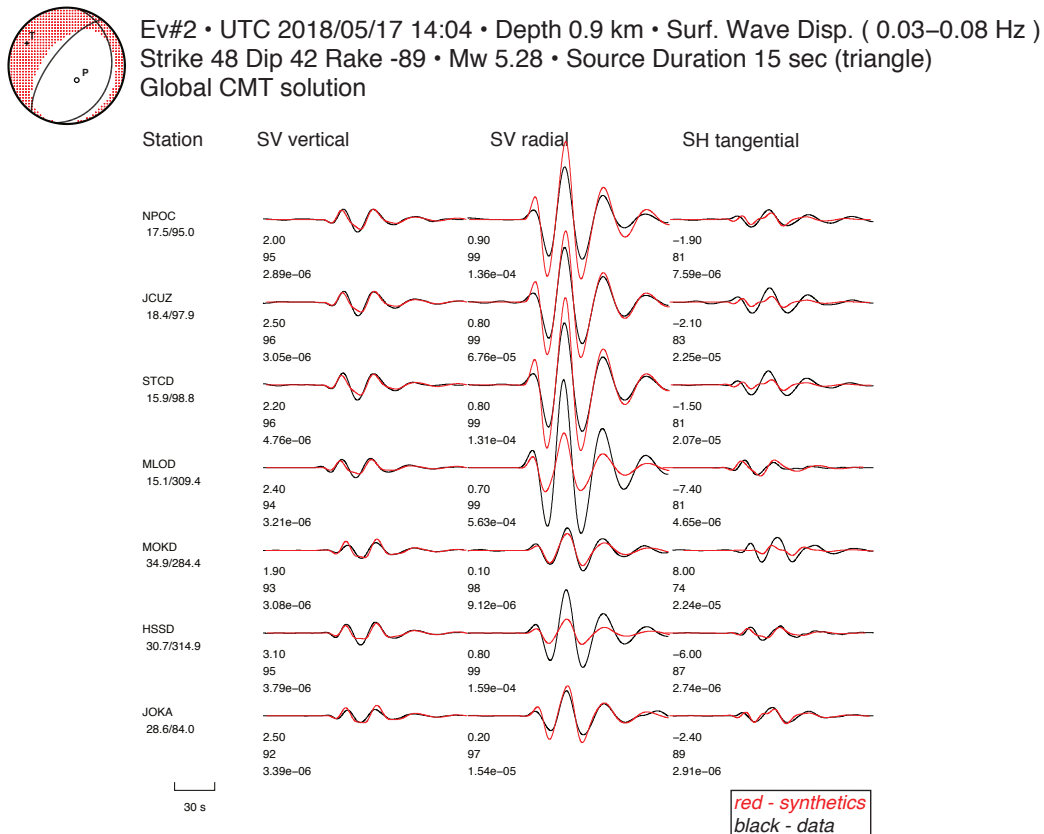
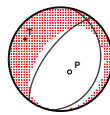


**Figure 2.4:** Waveform fit of regional data using GCMT solution for explosion 05/17b. Plot shows the comparison of synthetics (in red) generated using the GCMT solution for explosion on 05/17b (i.e. event 2) with long period surface wave (in black) recorded by regional stations located 15 to 35 km away from the source. The source location is fixed at HMM reservoir at 0.900 km depth. The synthetics are cross correlated with the data to improve fit. The magnitude of the event is allowed to float as well to minimize the misfit. The fit on regional long period surface wave using GCMT solution is reasonably well.



Ev#2 • UTC 2018/05/17 14:04 • Depth 0.9 km • Surface Wave Displacement ( 0.03–0.08 Hz )  
 Strike 48 Dip 42 Rake -89 • Mw 4.61 • Source Duration 15 sec (triangle)  
 Global CMT solution

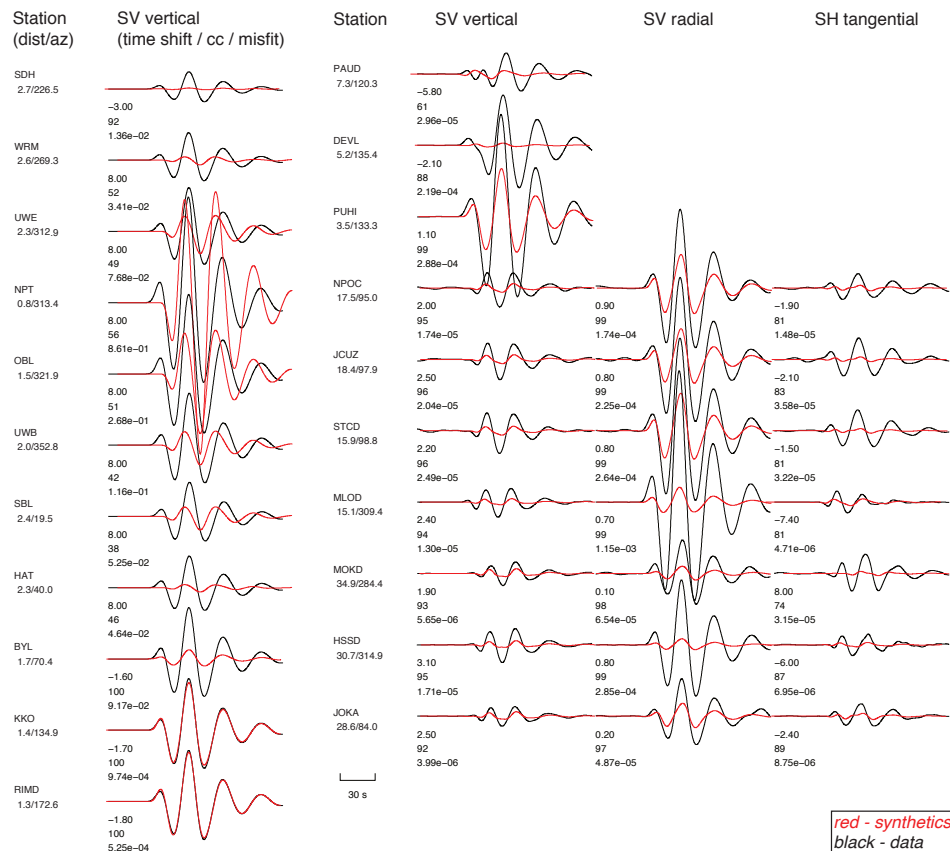


**Figure 2.5:** Waveform fit of near-field and regional data using GCMT solution for explosion 05/17b. Similar to Figure 2.4, the plot shows the comparison of synthetics (in red) generated using the GCMT solution for explosion on 05/17b (i.e. event 2) with long period surface wave (in black) recorded by both near field stations on the summit and regional stations located 15 to 35 km away from the source. The GCMT solution does not fit well for several near-field stations.

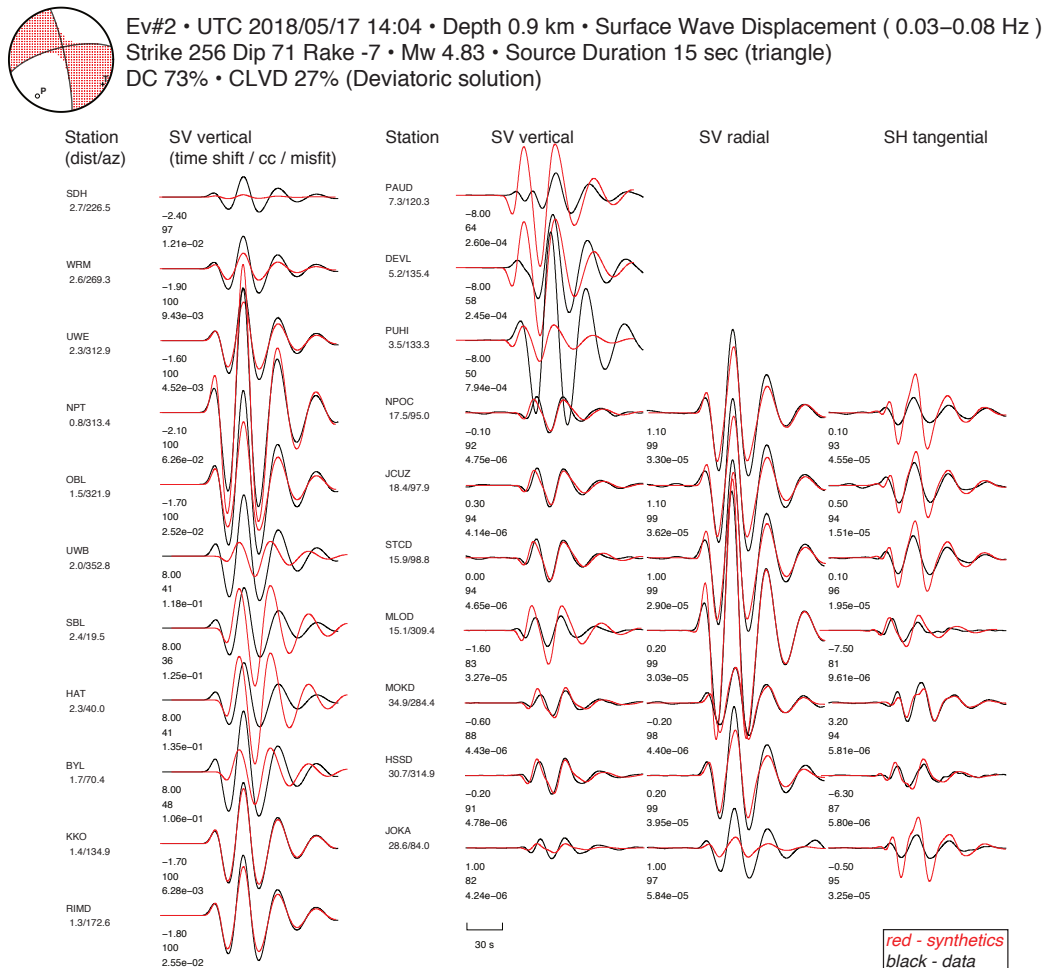


**Figure 2.6:** Waveform fit of near field and regional data using best-fitting deviatoric solution for explosion 05/17b. The plot shows the comparison of synthetics (in red) generated using the best-fitting deviatoric solution inverted using gCAP for explosion on 05/17b (i.e. event 2) with long period surface wave (in black) recorded by both near field stations on the summit and regional stations located 15 to 35 km away from the source. The source location is fixed at HMM reservoir at 0.900 km depth. The solution fits regional data reasonably well but does not fit well for several near-field stations.

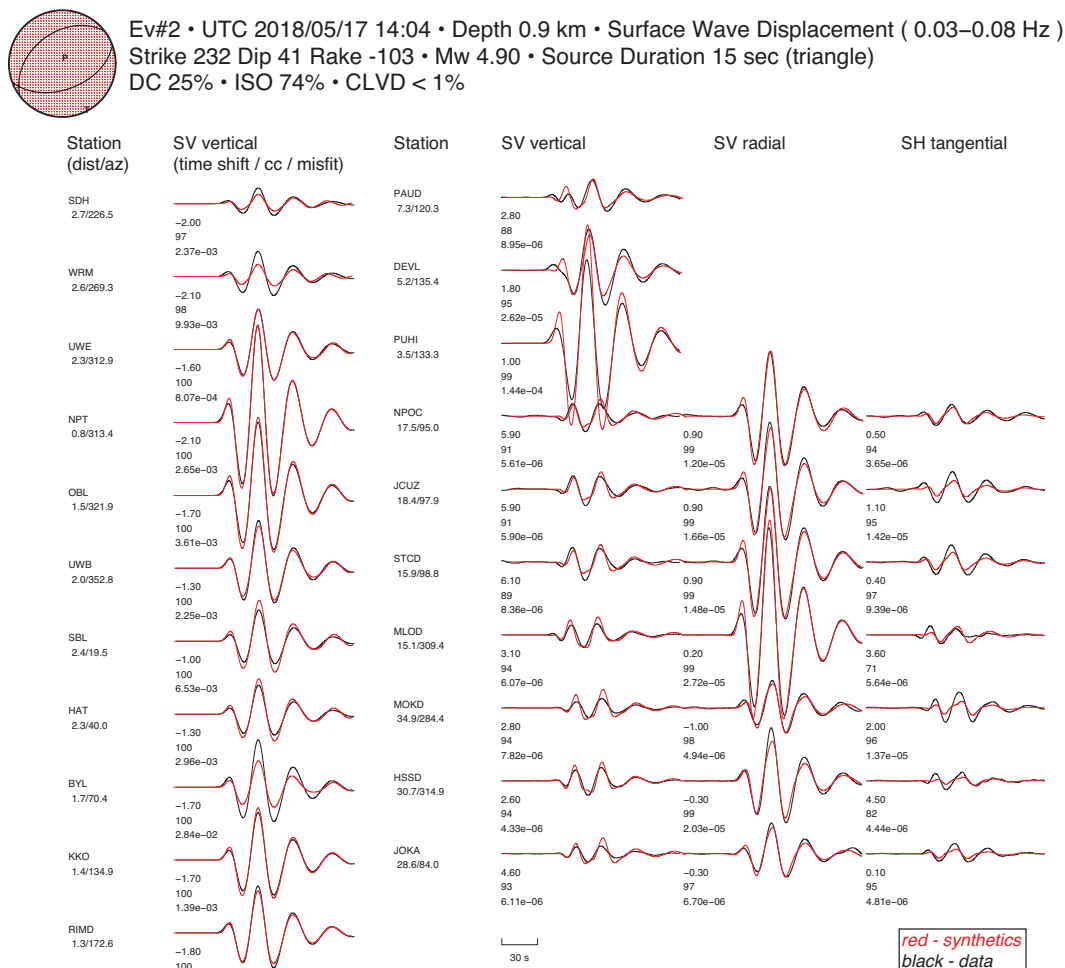


**Figure 2.7:** Waveform fit of near-field and regional data using best-fitting full moment tensor solution for explosion 05/17b. The plot shows the comparison of synthetics (in red) generated using the best-fitting full moment tensor solution inverted using gCAP for explosion on 05/17b (i.e. event 2) with long period surface wave (in black) recorded by both near field stations on the summit and regional stations located 15 to 35 km away from the source. The source location is fixed at HMM reservoir at 0.900 km depth. The solution fits both near-field and regional data very well.

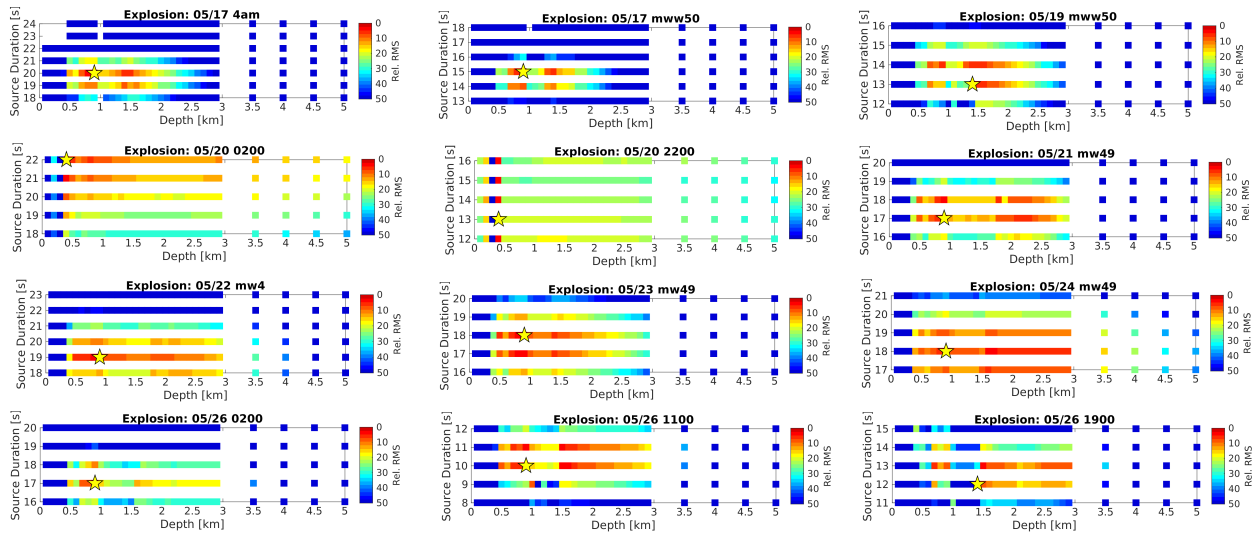


**Figure 2.8:** Grid search results of source duration and depth for all explosions using gCAP. Figure shows the misfits using various source duration and depth combination for the full moment tensor inversions of the twelve explosions between 05/17 to 05/26 using both near-field and regional data. The misfit in root mean square is scaled to the best-fit solution for each event, which is marked by the yellow star. Most events prefer depths at 0.900 km while the preferred source duration is independent for each event. Event 4 and 5 (both on 05/20) have waveforms more complex than other events and have little sensitivity to the grid search results.

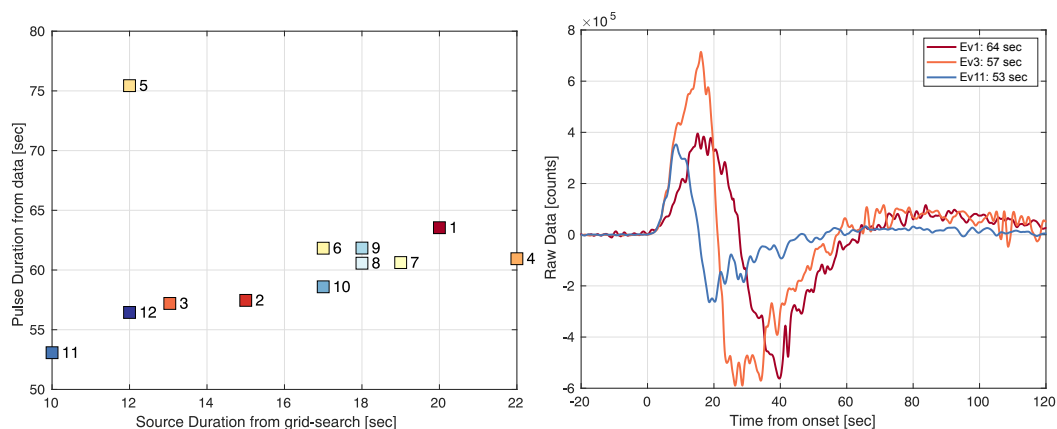


**Figure 2.9:** Correlation between source duration from inversion and measured pulse durations. Plots show a strong correlation between the preferred source duration from inversion and the measured pulse duration for each event, labelled with number. Event 4 and 5 do not fit the trend. Their waveforms are more complicated and their moment tensor solutions are also poorly determined (Figure 2.10). The pulse duration is measured from the first zero crossing before onset to the third zero crossing at the end of the signal. There is no clear correlation between the source duration and other parameters such as event number (i.e. time) or event magnitude.

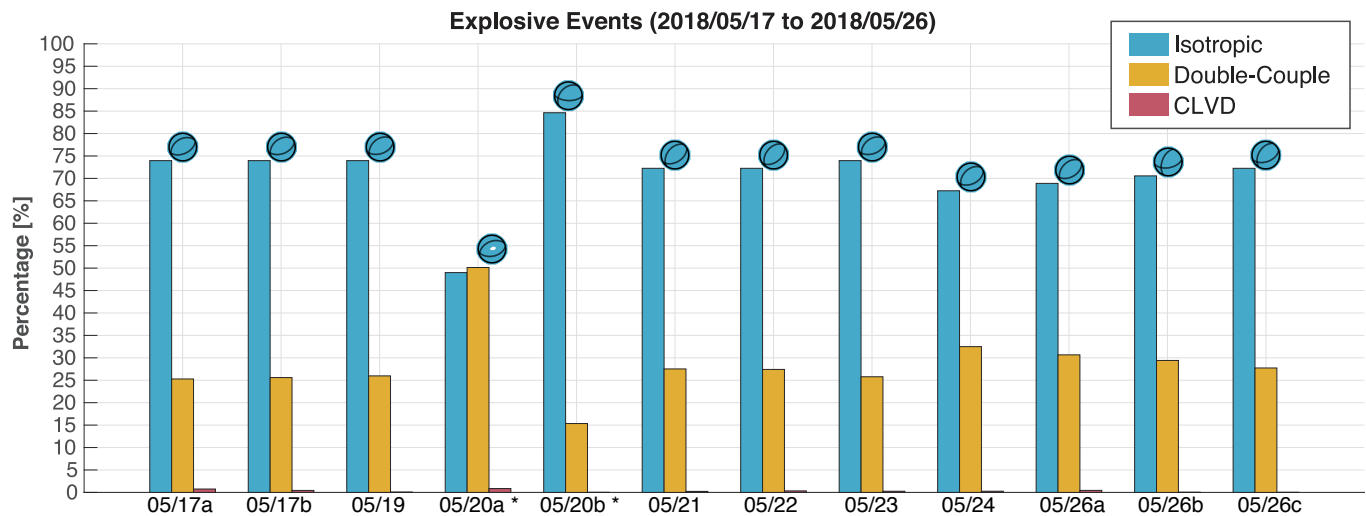


**Figure 2.10:** Inversion results for the explosions. Graph shows the best-fitting full moment tensor solutions for all explosions between 05/17 and 05/26, and the contributions of the isotropic, compensated linear vector dipole (CLVD), and double-couple components to the solution. Events 05/20a and 05/20b, marked with asterisk, are poorly determined. For the other events, they show consistently high isotropic component (72.4%), substantial double couple component (27.4%) with minimal CLVD contribution. The strike, rake, and dip are also very similar for all the events.

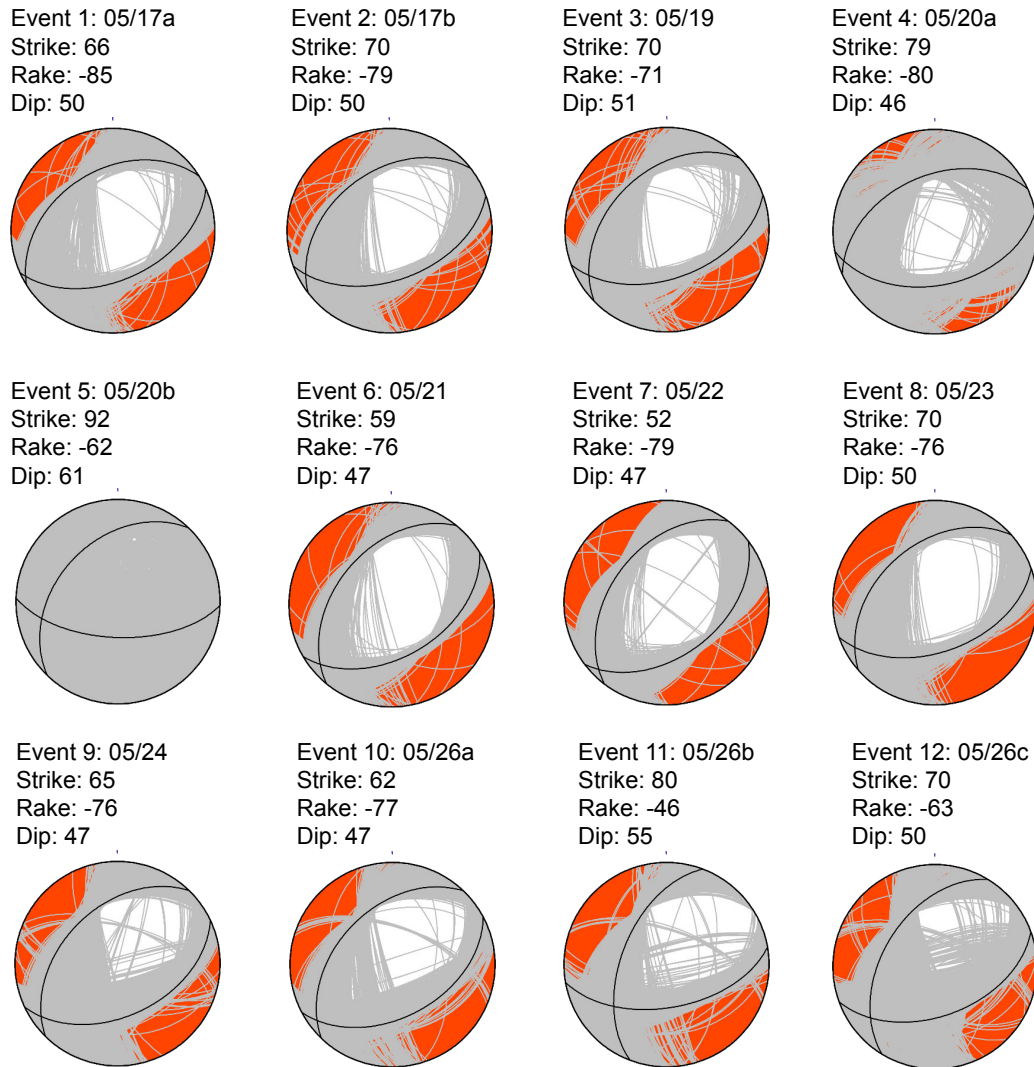


**Figure 2.11:** Figure shows the bootstrapping results for the strike, rake, and dip for all explosions between 05/17 and 05/26. Only the double-couple component is plotted on the focal mechanism. Black lines represent the most preferred nodal planes. Grey lines represent all other nodal planes obtained from bootstrapping. Events 05/20a and 05/20b, as determined from previous discussion, are poorly determined. For the other events, the results show consistent strike, rake, and dip.

### **Collapses From May 29 to August 2**

For events from May 29 and August 2, the waveforms from near-field broadband stations are clipped and not usable, and therefore we only use far-field stations (10 – 35 km) near the caldera. The input data for the inversion are filtered between 12.5 to 50 seconds (0.02-0.08 Hz). The long period waveforms from the far-field stations do not have much sensitivity to different centroid locations we tested around the caldera, so we fixed the location of the hypocenter to be at the same location as the proposed HMM reservoir.

The limitation of only using far-field stations in the inversion is that we cannot distinguish between deviatoric and full moment tensor solution as both solutions fit the waveforms equally well (Figure 2.12). Near-field infrasound signal, on the other hand, is sensitive to the upward radiation pattern and can distinguish between the two solutions. For the raw infrasound, we observed two distinct arrivals: (1) weak broadband wave traveling at the seismic surface wave velocity and (2) strong low frequency pulse with initial downward polarity and traveling at the acoustic speed (about 340 m/s) (see Figure 2.2 and 2.13). To test, we generate infrasound synthetics from the two best-fit solutions using a hybrid Galerkin – 2D spectral element method [30]. The method accounts for the wave propagation from the seismic source and the propagation of acoustic wave due to the coupling between solid Earth and atmosphere. The effects of atmospheric structure and variability can be ignored for synthetics generated at very close distance to source (less than 4 km). The synthetics test show that the infrasound signal prefers the deviatoric solution as it preserves the late upward pulse which is not observed with the mostly isotropic solution (Figure 2.13). On the other hand, stacked antipodal PKIKP polarities compiled by Butler [31] provide the opposite view as the energy propagates vertically downward from the collapse source. These PKIKP have dilatational first motions which is inconsistent with the mostly isotropic solution. We also tested solutions with different isotropic contributions and no CLVD component, and found that the PKIKP polarities can only be fit with solutions with minimal isotropic component at less than 5% (Figure 2.14). Therefore, we only invert for deviatoric solution for the collapse events.

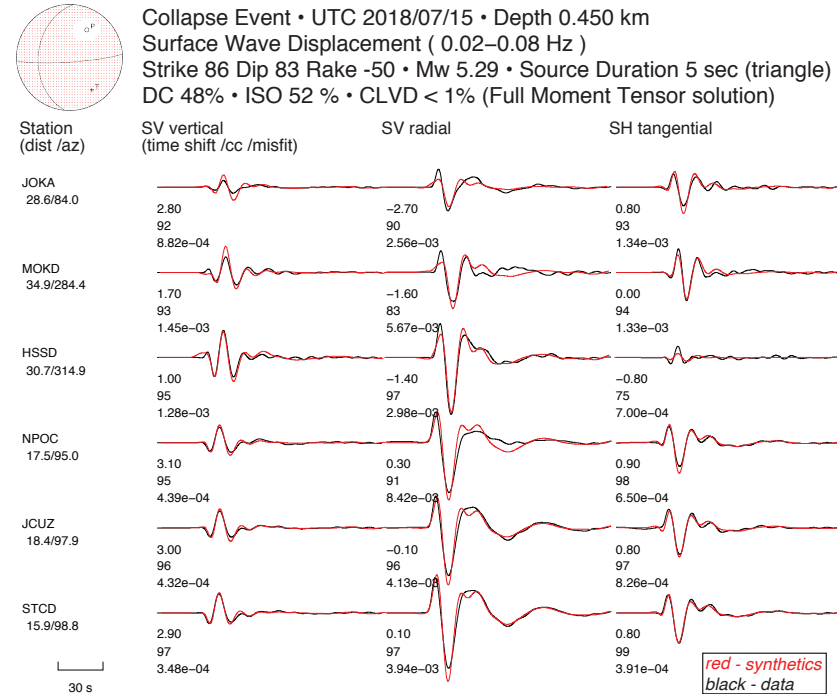
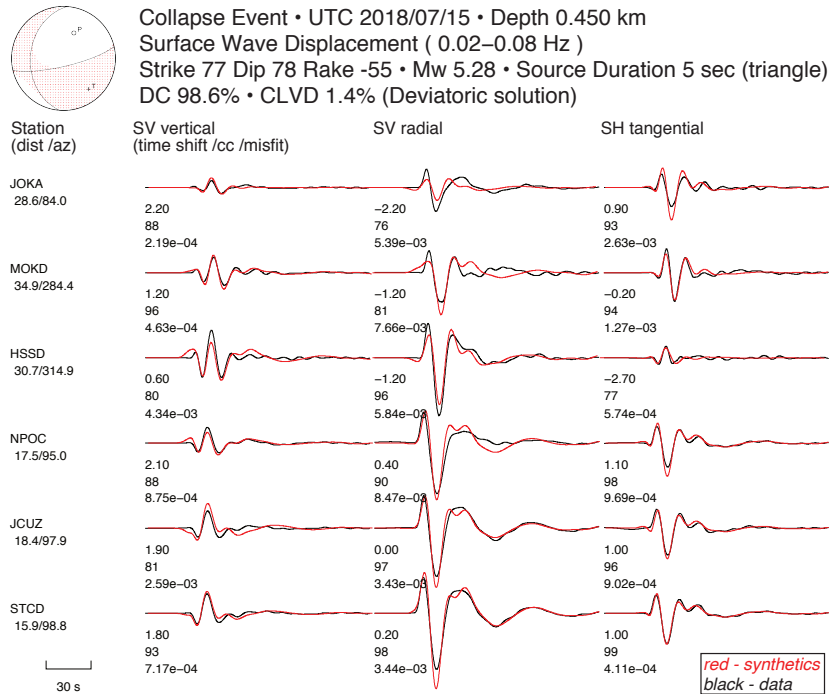


**Figure 2.12:** Waveform fit of regional data using best-fitting deviatoric and full moment tensor solution for collapse on 07/15. The plots show the comparison of synthetics (in red) generated using the best-fitting deviatoric (left) and full moment tensor (right) solutions inverted using gCAP for collapse on 07/15 (i.e. event 51) with long period surface wave (in black) recorded by regional stations located 15 to 35 km away from the source. The source location is fixed at HMM reservoir at 0.450 km depth. The solutions show that the regional data cannot distinguish between deviatoric and isotropic solution.

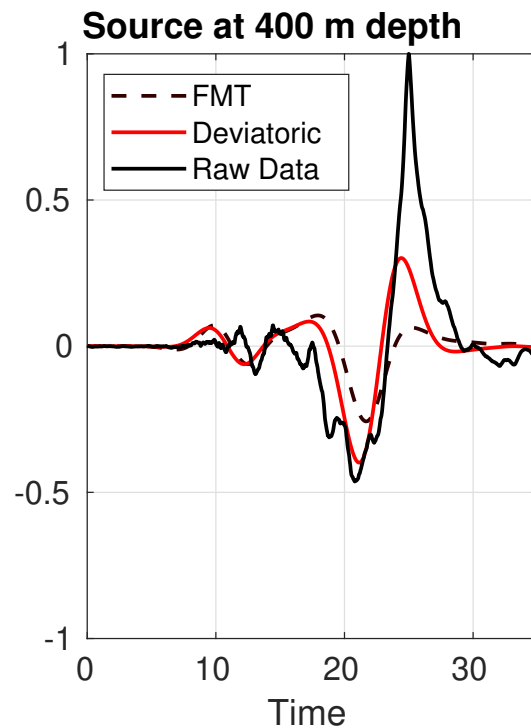


**Figure 2.13:** Comparison of raw infrasound and synthetics of deviatoric and isotropic solutions. Plot shows the comparison of raw infrasound data (stacked from 06/25 to 08/02) in black and two synthetics generated using deviatoric (red line) and full moment tensor (mostly isotropic; dashed black line) solutions at depth of 400 m. There are two signals in the raw data: (1) the higher frequency signal traveling at surface wave speed and (2) strong downward followed by upward pulse arriving at acoustic speed. The deviatoric solution is preferred over the isotropic solution as it captures both the downward and upward pulse.

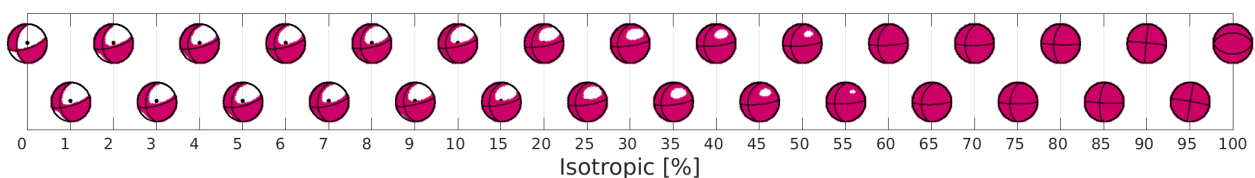


**Figure 2.14:** Fit of antipodal PKIKP with different isotropic solutions. Figure shows the focal mechanisms expected with different contribution of isotropic component for the collapse event. The CLVD contribution is fixed at zero. The stacked antipodal PKIKP from Butler [2019] is plotted over the focal mechanisms as a black dot. The only solutions that match with the dilatational polarity are solutions with very little isotropic component ( $< 5\%$ ).

Furthermore, the amplitude ratio between the acoustic pulse and Rayleigh pulse in the infrasound data is sensitive to the source depth, where the acoustic pulse is significantly stronger than the Rayleigh pulse if the source is shallow. This provides

additional constraint to the lower bound of depth when seismic waveforms alone have little depth sensitivity. We found that the amplitude ratio is large ( $> 2$ ) for source depths shallower than 1 km (Figure 2.15). For source depth at 2.5km, the amplitude for both the acoustic pulse and Rayleigh pulse is similarly weak. Apart from depth, additional slow layer near the surface, which is not properly characterized in the 1-D velocity model, can further increase the amplitude ratio. The effect of slow layer is most pronounced for sources at shallower depths and does not significantly affect the ratio for sources at deeper depths. Based on this qualitative analysis and comparison with the observation, we can infer that the seismic events occur at depths shallower than 1 km and possibly rupture all the way to the surface. The seismic events are estimated to have a magnitude of 5, which indicates a rupture length close to 1 km [32], so we fix the centroid depth of the seismic events to be at 450 m.

To recap, from infrasound simulations and PKIKP polarities, we place constraints on the inversion to only consider deviatoric solution at the source depth of 450 m. The centroid location is fixed at the HMM reservoir. We search a range of source duration, and choose a total duration of 5 seconds, which is the preferred duration for the majority of the events. The inversion results show that the remaining 50 events are predominantly normal-faulting events with minimal CLVD component, and occur along inward-dipping faults (Figure 2.16). These collapse-type events have three distinct transitions in the parameters (strength of CLVD, strike, rake, and dip). The timing of the transitions coincides with changes in particle motion and radar imagery discussed in Section 2.4. In the beginning of the collapse sequence, the events have higher CLVD with average strike, rake, and dip of (73,-50,75). From June 8, the strength of CLVD decreases, along with changes in the strike, rake, and dip with new average of (69,-38,75) until June 25 where the focal mechanism stabilizes and remain fairly constant till the end of the collapse sequence. The later focal mechanisms have very little CLVD component, and have an average strike, rake, and dip of (74,-52,75).

### **Summary of Moment Tensor Results**

The moment tensor inversions show that there are four distinct episodes during the whole eruptive sequence, namely “Explosion” from May 17 to May 26, “Collapse I” from May 29 to June 7, “Collapse II” from June 8 to June 24 and “Collapse III” from June 25 to August 2. For the explosion events, the preferred solution is predominantly isotropic (72.4%) over very long source duration (10 – 20 seconds). On the contrary, the collapse events are non-isotropic, and prefer a mostly double couple solution,

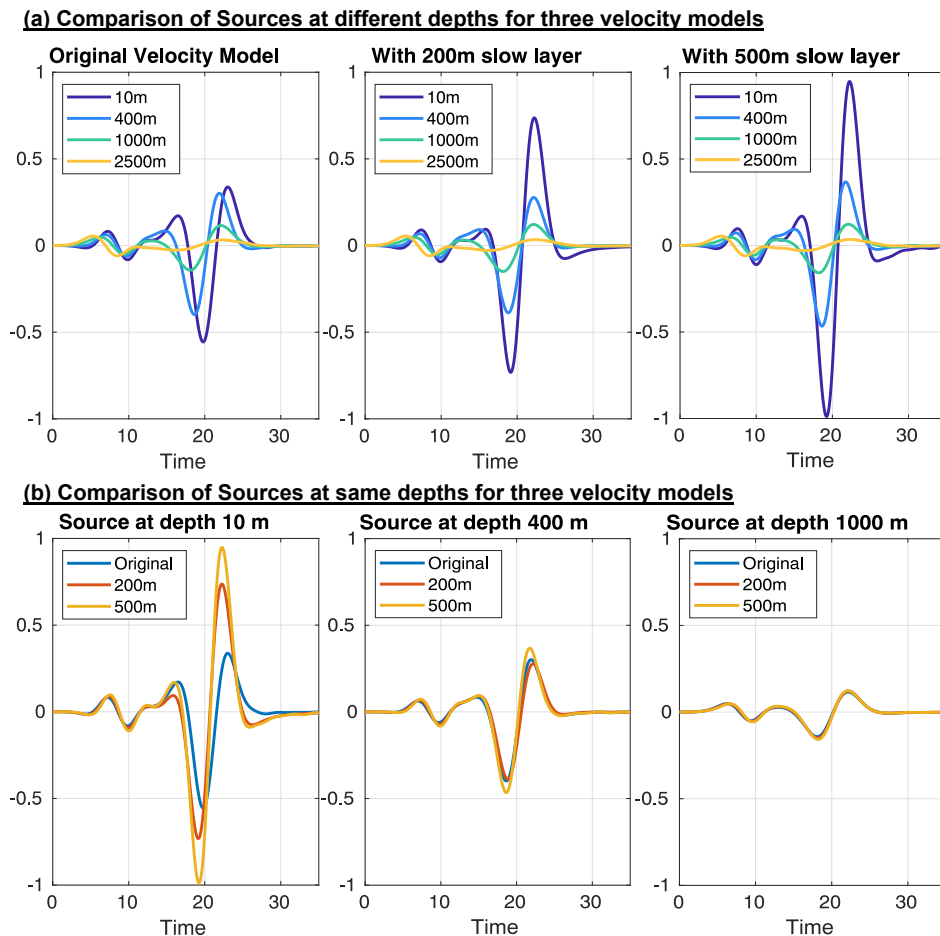


**Figure 2.15:** Comparison of raw infrasound and synthetics generated at different depths and with different velocity models. (a) Plot shows the comparison of synthetics generated using deviatoric solution at various depths using the velocity model used for inversions, and two modified velocity models in which the top 200 and 500 m are replaced with a slow layer. (b) Plot shows similar comparison but for synthetics at fixed source depth for the three velocity models. The synthetics show that the amplitude ratio between the acoustic and Rayleigh pulse is stronger for source at shallower depth. The amplitude ratio increases as well when there are slow surface layer, particularly for sources at shallower depth. We can exclude sources at depth greater than 1 km, as the amplitude ratio is close to 1, which is not observed in data, and the ratio does not change greatly with velocity models.

with much shorter source duration (5 seconds). Despite the difference in the non-double couple contributions, both explosion and collapse events share similar range of strike, rake, and dip, and similar orientation for the pressure and tension axis, which means they are subjected to a similar stress field throughout the eruption sequence. The catalog for the moment tensor solutions can be found in Table 2.1.

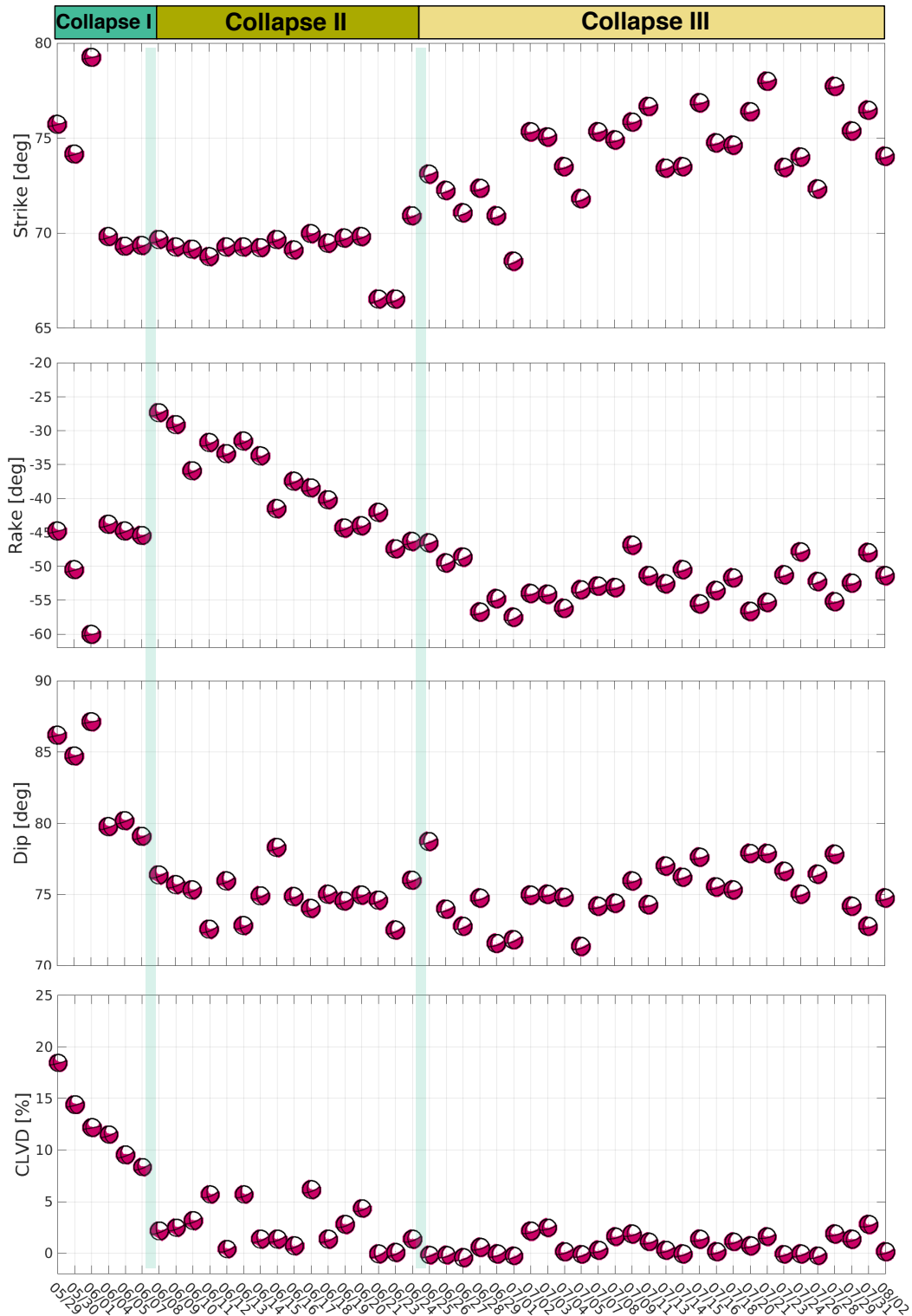


**Figure 2.16:** Moment tensor solutions for all collapse events. Plots show the best-fitting deviatoric moment tensor solution inverted using gCAP for all the collapse events. The changes in strike, rake, dip, and CLVD component during the collapse episode follow the marked transition observed by the particle motion in Figure 2.3, represented by the green lines.

Event	Origin UTC Time	Depth [km]	Mw	Strike	Rake	Dip	Dura.	ISO [%]	DC [%]	CLVD [%]
1	2018-05-17T04:15:30.350Z	0.900	4.94	66	-85	50	20	75.69	24.30	0.01
2	2018-05-17T14:04:10.700Z	0.900	4.90	70	-79	50	15	73.96	25.60	0.44
3	2018-05-19T09:58:33.210Z	0.900	4.90	70	-71	51	13	73.96	26.03	-0.01
4**	2018-05-20T01:58:13.320Z	0.900	4.83	79	-80	46	22	49.00	50.14	0.86
5**	2018-05-20T21:50:07.310Z	0.900	4.38	92	-62	61	12	84.64	15.35	-0.01
6	2018-05-21T10:55:19.180Z	0.900	4.83	59	-76	47	17	72.25	27.53	0.22
7	2018-05-22T03:51:11.860Z	0.900	4.84	52	-79	47	19	70.56	29.20	0.24
8	2018-05-23T07:58:46.290Z	0.900	4.88	70	-76	50	18	73.96	25.83	0.21
9	2018-05-24T04:43:49.890Z	0.900	4.81	65	-76	47	18	70.56	29.25	-0.19
10	2018-05-26T02:15:52.250Z	0.900	4.90	62	-77	47	17	70.56	29.08	0.36
11	2018-05-26T10:44:37.620Z	0.900	4.56	80	-46	55	10	70.56	29.41	-0.03
12	2018-05-26T19:34:41.160Z	0.900	4.37	70	-63	50	12	72.25	27.74	-0.01
13	2018-05-29T11:56:11.570Z	0.450	5.21	76	-45	86	5	0.00	81.51	18.49
14	2018-05-30T20:53:50.830Z	0.450	5.26	74	-50	85	5	0.00	85.56	14.44
15	2018-06-01T23:37:15.150Z	0.450	5.38	79	-60	87	5	0.00	87.75	12.25

**Table 2.1:** Table listing the best-fitting focal mechanisms inverted using gCAP for all 62 events in this study. The information includes strike, rake, dip, magnitude, source duration and contributions of the double-couple and non double-couple components. The explosions (event 1 - 12) consider the full moment tensor solutions, with fixed depth at 0.900 km. The solutions for the collapse events (event 13 - 62) are only deviatoric, with fixed depth at 0.450 km and source duration at 5 seconds. Events that are marked with asterisks are not well-determined.

<b>Event</b>	<b>Origin UTC Time</b>	<b>Depth [km]</b>	<b>Mw</b>	<b>Strike</b>	<b>Rake</b>	<b>Dip</b>	<b>Dura.</b>	<b>ISO [%]</b>	<b>DC [%]</b>	<b>CLVD [%]</b>
16	2018-06-04T01:50:48.690Z	0.450	5.32	70	-44	80	5	0.00	88.44	11.56
17	2018-06-05T14:32:34.450Z	0.450	5.34	69	-45	80	5	0.00	90.39	9.61
18	2018-06-07T02:06:38.640Z	0.450	5.35	69	-45	79	5	0.00	91.59	8.41
19	2018-06-08T12:44:39.650Z	0.450	5.07	70	-27	76	5	0.00	97.75	2.25
20	2018-06-09T14:48:18.050Z	0.450	5.17	69	-29	76	5	0.00	97.44	2.56
21	2018-06-10T10:51:01.890Z	0.450	5.19	69	-36	75	5	0.00	96.76	3.24
22	2018-06-11T14:43:54.340Z	0.450	5.23	69	-32	73	5	0.00	94.24	5.76
23	2018-06-12T11:52:51.230Z	0.450	5.21	69	-33	76	5	0.00	99.51	0.49
24	2018-06-13T13:39:37.610Z	0.450	5.25	69	-32	73	5	0.00	94.24	5.76
25	2018-06-14T13:19:37.120Z	0.450	5.24	69	-34	75	5	0.00	98.56	1.44
26	2018-06-15T21:56:39.920Z	0.450	5.25	70	-41	78	5	0.00	98.56	1.44
27	2018-06-16T20:18:17.660Z	0.450	5.25	69	-37	75	5	0.00	99.19	0.81
28	2018-06-17T16:26:13.090Z	0.450	5.25	70	-38	74	5	0.00	93.75	6.25
29	2018-06-18T16:12:48.500Z	0.450	5.21	69	-40	75	5	0.00	98.56	1.44
30	2018-06-19T15:05:34.000Z	0.450	5.22	70	-44	75	5	0.00	97.11	2.89
31	2018-06-20T14:22:23.430Z	0.450	5.22	70	-44	75	5	0.00	95.59	4.41
32	2018-06-21T23:12:59.370Z	0.450	5.17	67	-42	75	5	0.00	99.99	0.01
33	2018-06-23T04:52:16.210Z	0.450	5.15	67	-47	73	5	0.00	99.84	0.16
34	2018-06-24T02:34:36.270Z	0.450	5.10	71	-46	76	5	0.00	98.56	1.44
35	2018-06-25T02:12:24.200Z	0.450	5.13	73	-46	79	5	0.00	99.91	-0.09
36	2018-06-26T03:02:44.720Z	0.450	5.13	72	-50	74	5	0.00	99.91	-0.09
37	2018-06-27T08:40:40.310Z	0.450	5.17	71	-49	73	5	0.00	99.64	-0.36
38	2018-06-28T14:48:50.400Z	0.450	5.24	72	-57	75	5	0.00	99.36	0.64

**Table 2.2:** Continued from Table 2.1

<b>Event</b>	<b>Origin UTC Time</b>	<b>Depth [km]</b>	<b>Mw</b>	<b>Strike</b>	<b>Rake</b>	<b>Dip</b>	<b>Dura.</b>	<b>ISO [%]</b>	<b>DC [%]</b>	<b>CLVD [%]</b>
39	2018-06-29T17:50:46.270Z	0.450	5.16	71	-55	72	5	0.00	99.96	0.04
40	2018-07-01T00:51:13.010Z	0.450	5.24	69	-57	72	5	0.00	99.84	-0.16
41	2018-07-02T11:24:46.190Z	0.450	5.23	75	-54	75	5	0.00	97.75	2.25
42	2018-07-03T12:17:03.810Z	0.450	5.21	75	-54	75	5	0.00	97.44	2.56
43	2018-07-04T20:19:10.470Z	0.450	5.28	74	-56	75	5	0.00	99.75	0.25
44	2018-07-05T23:20:04.690Z	0.450	5.19	72	-53	71	5	0.00	99.99	-0.01
45	2018-07-07T04:04:37.630Z	0.450	5.27	75	-53	74	5	0.00	99.64	0.36
46	2018-07-08T12:54:50.330Z	0.450	5.25	75	-53	74	5	0.00	98.31	1.69
47	2018-07-09T19:20:46.280Z	0.450	5.25	76	-47	76	5	0.00	98.04	1.96
48	2018-07-11T15:45:53.220Z	0.450	5.26	77	-51	74	5	0.00	98.79	1.21
49	2018-07-13T00:42:27.110Z	0.450	5.22	73	-52	77	5	0.00	99.64	0.36
50	2018-07-14T05:08:03.680Z	0.450	5.24	73	-50	76	5	0.00	99.96	0.04
51	2018-07-15T13:26:05.130Z	0.450	5.28	77	-56	78	5	0.00	98.56	1.44
52	2018-07-16T21:42:35.500Z	0.450	5.25	75	-53	76	5	0.00	99.75	0.25
53	2018-07-18T11:28:04.040Z	0.450	5.26	75	-52	75	5	0.00	98.79	1.21
54	2018-07-20T02:33:01.690Z	0.450	5.31	76	-57	78	5	0.00	99.19	0.81
55	2018-07-21T19:43:28.660Z	0.450	5.32	78	-55	78	5	0.00	98.31	1.69
56	2018-07-23T06:53:38.820Z	0.450	5.24	73	-51	77	5	0.00	99.99	-0.01
57	2018-07-24T16:41:10.140Z	0.450	5.24	74	-48	75	5	0.00	99.99	0.01
58	2018-07-26T22:09:11.280Z	0.450	5.26	72	-52	76	5	0.00	99.84	-0.16
59	2018-07-28T12:37:25.390Z	0.450	5.30	78	-55	78	5	0.00	98.04	1.96
60	2018-07-29T22:10:25.570Z	0.450	5.25	75	-52	74	5	0.00	98.56	1.44
61	2018-07-31T17:59:46.000Z	0.450	5.25	76	-48	73	5	0.00	97.11	2.89
62	2018-08-02T21:55:12.060Z	0.450	5.25	74	-51	75	5	0.00	99.75	0.25

**Table 2.3:** Continued from Table 2.2

## **2.6 Mechanisms for Explosion and Collapse Events**

It is noteworthy to mention that the 2018 sequence shares great similarity with the 1924 sequence, including the draining of lava lake at the summit, earthquake swarms along east rift zones, 2.5 week-long explosions at Halema'uma'u crater, and the enlargement of the crater. There was subsidence at the summit as well during the 1955 and 1960 eruptions in the Lower East Rift Zone. In this section, we will discuss the results from our analysis and present evidence showing how the Kilauea summit evolved from explosions to caldera collapse due to magma withdrawal from the summit. The insights we gain from this sequence will help us to re-evaluate the mechanisms for previous less-instrumented episodes.

### **Mechanism for Explosive Events**

The 1924 explosions are thought to be steam-driven due to groundwater interaction with hot rock. However, this mechanism is found to be incompatible with the 2018 explosions where large increases and peaks in sulfur dioxide emission, which originates from magmatic reservoir [33], is reported in Neal et al. [1]. Sporadic plume emission along with VLP seismic signals have also been observed prior to the 2018 eruption. Several mechanisms have been proposed including (1) gas slug ascending, expanding and eventual bursting, exciting the VLP signal at depth [14], and (2) rockfalls impacting the lava lake, triggering both shallow degassing and VLP signal from the pressure transient transmitted along the conduit [34].

Understanding the relationship of the observed infrasound signal and the seismic signal can provide additional constraints to the nature of the explosive events. The simulation of the infrasonic signal generated directly from the explosion shows a very weak signal, and thus we infer the strongest signal from the infrasound is due to the degassing burst at the vent (Figure 2.18). Apart from the major explosions from May 17 onwards, there were several explosive plumes at the summit on March 15, April 6, and May 9, which generated infrasound and long-period seismic signals. The summit webcam recordings showed that the explosions were caused by the rockfalls. Although the rockfalls occurred near the vent at the surface, the seismic signal from the rockfalls is estimated to be originated from the HMM reservoir (Figure 2.1) based on modeling the long period seismic oscillation [35]. We compared the particle motion from the broadband seismic instruments for the May 17 - 26 explosive events and the rockfall events (Figure 2.17), and found that the direction of the particle motion is highly similar, indicating that the seismic signals of explosive events originate from the same HMM reservoir.

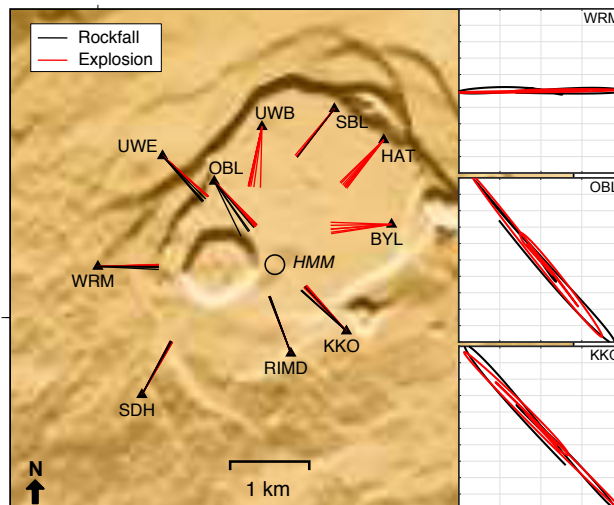


**Figure 2.17:** Backazimuths measured from horizontal particle motions recorded by broadband seismometers for rockfalls and explosions. Figure shows backazimuths measured from the horizontal particle motions recorded by the broadband seismometers at the Kilauea caldera for explosions (05/17 to 05/26 in red) and three rockfall events (03/15, 04/06, 05/09, in black). Three representative particle motions of rockfall and explosions from station WRM, OBL and KKO are shown. The particle motions for the rockfall and explosions generally overlap with each other, with some scatters for stations at the east side of the caldera.

For the infrasonic signals, both the explosion events and rockfalls show compressional peaks, yet the arrival time varies with events. In Figure 2.19a, we plot the infrasonic signals recorded at multiple distance range ( $< 1$  km, 4.5 km and 19 km), corrected for the time an acoustic wave (340 m/s) takes to travel from vent to station. The origin time is assumed to be the arrival time of the first signal of the closest seismic station to the vent (for rockfall events) and catalog origin time (for explosions). For March 15 and April 6, we observed that the strong infrasonic peak arrives at the zero mark, meaning the degassing process happens at the same time as the generation of the seismic signal. From May 9 to the end of the explosions on May 26, the arrivals of the infrasonic peak are delayed with time.

Similar scenario of time lapse of infrasonic is suggested by Kobayashi et al. [36] at Mikayejima where the signal from the degassing process burst through the lava lake surface layer travel at a distinct velocity in the conduit ( $V_c$ ) before reaching the top of the vent and propagate as infrasonic pulse at acoustic speed (340 m/s) to the sensor. In this case at Kilauea, we hypothesize that the source of the degassing and the seismic signal generation is at constant depth as the particle motion from

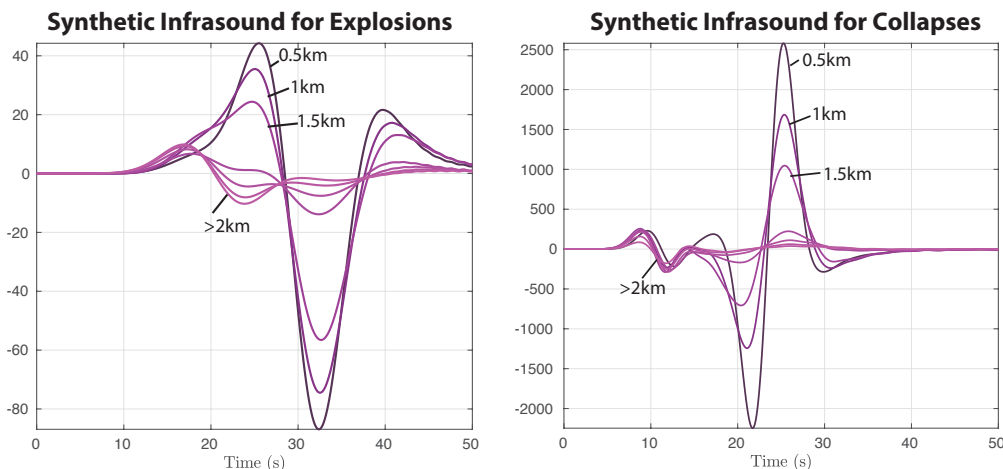


**Figure 2.18:** Comparison of infrasound synthetics for explosion and collapse. Plot shows the comparison of synthetics generated for explosion (left) and collapse (right) for various source depths. Based on the amplitude count, the infrasonic signal for collapse is significantly stronger than that for explosion. Therefore, the infrasonic peak observed during the explosion is not generated by the seismic source but by the ejection of a plume at the vent.

the broadband instruments (for radial and vertical direction) for all events are very similar. Therefore, the time lapse between the degassing and infrasound signal is due to an increase of time taken to travel through the conduit from the source to the surface of the vent. The delay coincides with the behavior of the lava lake at the vent, which was visible at the surface throughout the spring season, overflowed to the floor of the Halema'uma'u crater on April 21, and started to drain on May 2 with an estimated rate of 2.2 meter per hour [USGS HVO Cooperative Report, dated 2018 May 8]. When the elevation of the lava lake is high and close to the crater floor, the signal arrives at the sensor at the expected acoustic time. As the lake begins to drain, the length of drained conduit increases, and in turn delaying the infrasonic signal (see Figure 2.19b).

The relation between the arrival time of the infrasonic signal and the path geometry can be described as total time,  $t_{total} = (1/V_c)d + (1/V_l)(h - d) + (1/V_a)x$ , where  $h$  is the length of conduit from vent to seismic source,  $d$  is the length of the drained portion,  $x$  is the distance from vent to sensor,  $V_c$  is the velocity of the rising plume,  $V_l$  is the speed of degassing signal in the lava medium, and  $V_a$  is the acoustic speed at surface,  $\sim 340$  m/s (Figure 2.19c).  $(1/V_a)x$  is well-determined. Taking the estimated draining rate,  $R$ , remains constant over the course of the eruption, we can calculate  $d$  by taking  $d = R\Delta T$ , where  $\Delta T$  is the time elapsed between each eruption.

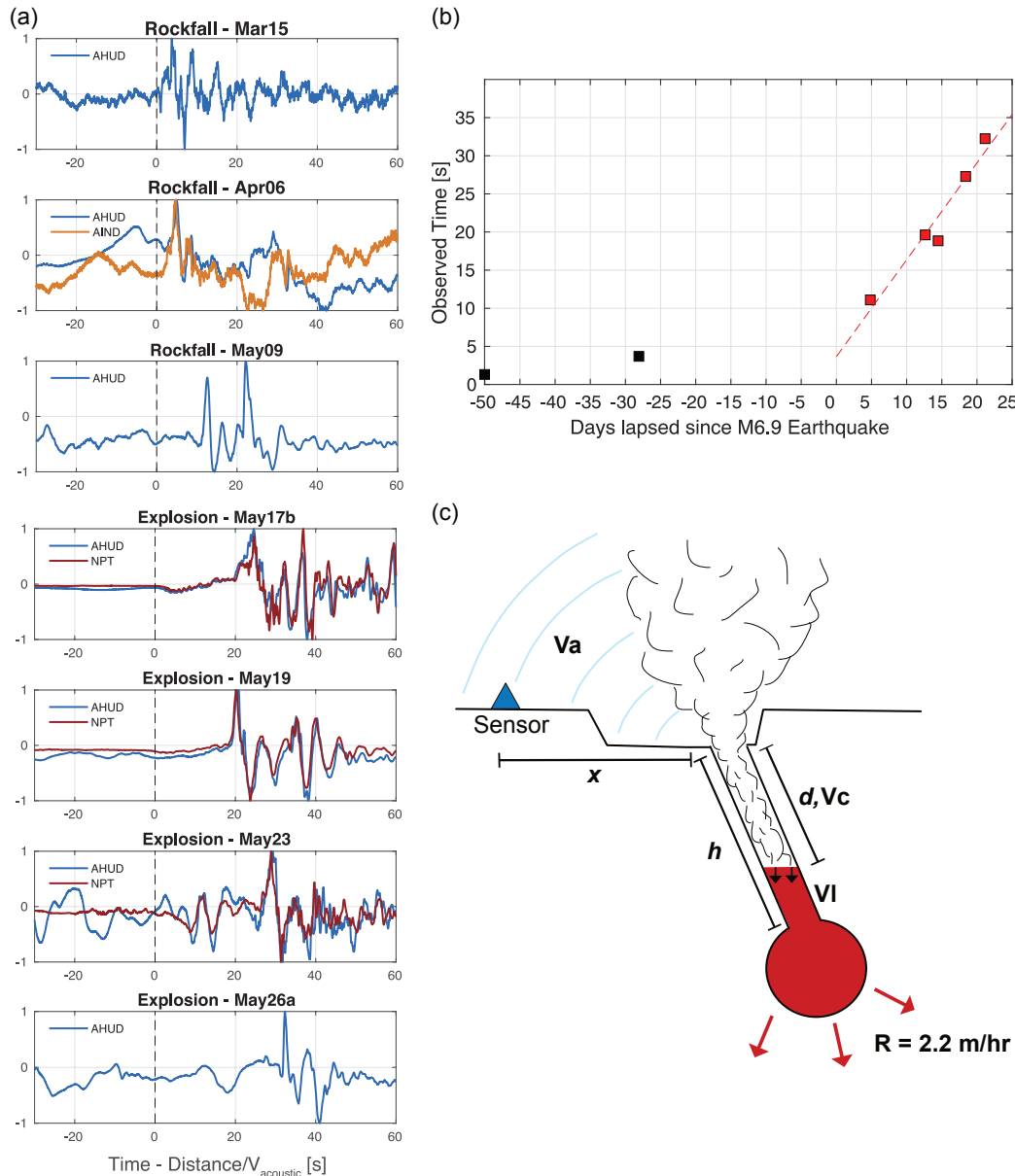


**Figure 2.19:** Observations of raw infrasound data and the peak delay for rockfalls and explosions. (a) Plot shows the raw infrasound data plotted in normalized amplitude for three rockfall events and explosions. The data from all infrasound sensors (AHUD, NPT, AIND) available during the event are plotted at reduced velocity, corrected for the time taken to travel from vent to sensor in acoustic speed of 340 m/s. Data show clear upward peaks which is assumed as the pulse emitted when the plume exits the vent. (b) Graph show observed delay in peak arrival against the amount of days lapsed between each event. We use the M6.9 earthquake as reference as there is an estimation by USGS on the speed of lava lake withdrawing (2.2 m/hr). The red dashed line is the time estimated using the inverted velocities and conduit length. (c) Schematic showing the variables involved in the calculation of various velocities and conduit length using the delay times observed.

To estimate the values for the remaining parameters ( $V_c$ ,  $V_l$  and  $h$ ), we need an additional boundary condition. Based on the proposed process of seismic excitation and degassing, an appropriate constraint we can use is that the entire length of the conduit is completely drained by the last eruptions, that is  $t_{last} = (1/V_c)h$ . The last eruption (i.e. May 26c) has very weak infrasonic signal, so we take a slightly earlier event on the same day (i.e. May 26a) with a clear infrasonic compressional onset as an approximate. With this constraint and measurements from the 5 events, we can estimate the values of  $V_c$ ,  $V_l$  and  $h$  from the simple linear regression of the total time,  $t_{total}$  and time elapsed,  $\Delta T$ . We estimate  $h = 1,188$  m,  $V_c = 37$  m/s, and  $V_l = 326$  m/s. The values of  $V_c$  is in the same order of magnitude as strong Strombolian-type degassing (31 – 34 m/s in Patrick et al. [37]; 38 – 53 m/s in Taddeucci et al. [38]) and comparable to the previously recorded plume velocities at Kilauea (ranging between 5.8 and 16.6 m/s in Fee et al. [39]). The estimated  $h$  is slightly deeper than the depth of the seismic source obtained from the seismic moment tensor inversion at 900 m, but still within the uncertainty from inversion.

The degassing process and the explosion seismic signal are not necessarily mutually inclusive, as degassing activity and small plumes are still observed after the explosion ceases. However, the consistency of reservoir depths obtained through seismic inversion and infrasound analysis does suggest that the condition of the magma reservoir governs the seismic behavior. One way that an isotropic seismic signal is generated is by pressurizing the magma chamber through intrusion of the overburden roof or ‘piston’ resulting in transient expansion, a mechanism suggested for Miyakejima volcano by Kumagai et al. [6]. This expansion can also encourage rapid degassing at depth, with gas bubbles breaking the lava lake surface and ascending as ash-rich plumes along the conduit. The explosion only ceases when the lava lake has drained to the depth of the magma chamber, and the chamber is no longer sufficiently pressurized to generate isotropic signal.

For Kilauea, we speculate the initial intrusion may be slips on fault structures above the chamber. The double-couple component of the focal mechanism for the explosions are significant (27.4%) and there is a common fault plane that slipped during all explosions given the consistency of the strike, rake, and dip. The fault may fail and start to develop as the magma pressure at the summit reduces due to the eruption downstream. This fault probably did not rupture to the surface but created a minor depression (‘downsag’) above the chamber, as seen in the radar imagery. However, we cannot exclude rockfall as a triggering mechanism, which

can generate degassing and explosion signal almost simultaneously, like the slipping of a fault. An emptying conduit is also favorable in creating rockfalls onto the lava lake. However, based on the later collapse events where we observe multiple faults slipping (discussed in the following section), we prefer the fault mechanism where the magma withdrawal from summit is the driver for both explosions and collapses.

### **Mechanism for Collapse Events**

Like volcanic explosions, caldera formation is thought to be due to pressure change within the subsurface magma chamber, and there are five end-member cases of caldera collapse, reviewed by Lipman [40], which are 'piston', 'piecemeal', 'trapdoor', 'downsag' and 'funnel'. Out of the five, 'piston', 'piecemeal', and 'trapdoor' collapse have been used to describe collapses in basaltic volcano systems. In a piston-type collapse, a coherent rock column bounded by a ring-fault above the magma chamber subsides. The subsidence can pressurize the magma chamber which results in the generation of the VLP seismic signal, observed at Miyake-jima volcano [6]. The slip on the ring-fault during the piston-type collapse can also radiate seismic energy with strong isotropic and CLVD component, observed at Piton de La Fournaise (e.g. [4, 41]). Piecemeal collapses describe downward displacement of multiple independent blocks. Trapdoor collapse, as suggested by the name, resembles an asymmetric depression at the caldera, with a hinge. Piecemeal and trapdoor style collapses should result in a predominant double couple failure.

The accurate characterization of the seismic events during the collapse is crucial in inferring the mechanisms. Looking at the example of another basaltic volcano, i.e. 2014 Bardabunga caldera collapse in Iceland, the differences in the resolved focal mechanisms using two distinct methods result in two contrasting mechanisms being proposed. In Gudmundsson et al. [3], the seismicity associated with the collapse are inferred to occur along outward-dipping, reverse faults around the caldera, extending to a depth of 12 km, and therefore supports a piston-type collapse. On the other hand, Agustsdottir et al. [42] used an alternate technique and found that the same set of seismicity focuses on one corner of the caldera and at shallow depths not deeper than 4 km. Their mechanisms are predominantly double-couple, along multiple inward-dipping normal faults. The style of asymmetric failure points towards a combination of piecemeal and trapdoor collapse.

During the collapse episode at Kilauea summit, the focal mechanisms of the large seismic events we obtained share great similarity to the results in Agustsdottir et

al. [42]. They are predominantly double-couple along steep inward-dipping normal faults (Figure 2.16). Based on the change in strike, rake and particle motion, we propose the failure occur sequentially on three main strands. The first strand is near the HMM reservoir, and the fault is significantly curved which explains the relatively high CLVD component ( $\sim 12\%$ ), an apparent effect due to the simultaneous failure of multiple arcuate faults. Later, the fault west of the HMM reservoir starts to subside. The fault is inferred to be fairly linear, as the strike of the focal mechanisms stays constant, and there is little CLVD component. However, the rake becomes increasingly negative, from  $-25^\circ$  to  $-55^\circ$ , suggesting the faulting is evolving and becoming more 'strictly normal'. Lastly, from June 25 onwards, the failure migrates towards the east of the HMM reservoir. The rake remains fairly constant, while the strike of the faulting increases, suggesting the slips happen on a continuous curved fault structure. The dips of the event also are generally becoming less steep (from  $85^\circ$  to  $73^\circ$ ), consistent with the drop of caldera floor where the caldera subside significantly deeper earlier in the collapse sequence than later.

The style of failure across multiple fault strands can represent several potential scenarios such as (1) development of a new ring-fault like structure within the caldera, (2) reactivation of old ring-fault bounding the caldera or (3) failure along pre-existing non-ring fault structures such as dikes. Apart from collapses, Kilauea summit has also experienced multiple fissures opening, most recently in 1974 on the floor of HMM crater [43] with similar strikes to the ones obtained in this analysis. The repeating collapses and fissures can create heterogenous mechanical properties across the caldera, which fails under different stress thresholds, and contribute to the observed asymmetric collapse. Another potential structure is a dual-dike structure hinged at the HMM reservoir, cutting across the crater with similar strikes, that is determined using the oscillation modes of short period waves in previous explosive bursts [44]. Additional observation such as relocation of the seismic events and microseismicities will be able to help distinguishing the different scenarios.

Based on the observations and results from the moment tensor inversion, we propose that the Kilauea caldera experienced a piecemeal and trapdoor style collapse, like Bardabunga described in Agustsdottir et al.[42], rather than a piston-type collapse of a coherent block suggested for several other calderas in similar basaltic volcanic system. Observations of CLVD earthquakes at calderas are often used to justify for piston-type collapse, yet these source characterizations are made primarily using stations at teleseismic distance (greater than 1 degree) which are biased towards

CLVD solutions. The dense station coverage near the summit caldera, combined with other geophysical instruments, makes it possible to quantify the importance of CLVD and double couple components in the seismic signals and in turn infer the collapse mechanism.

### **The evolution at Kilauea summit**

The characterization of seismic events at the Kilauea summit provides a clearer picture of the mechanisms involved in the complex sequence of explosive eruptions and subsequent collapse at Kilauea, represented in Figure 2.20. The eruption began with the dike intrusion at the Lower East Rift Zone with new fissures opening. The highly-connected pathway from caldera to rift zone means that magma pressure within the shallow reservoir at the summit reduces as a result of the fissure activity downstream, indicated by the drop of the lava lake elevation. The inert fault structures at the caldera, which were supported by friction and internal pressure of the magma chamber, begin to slip. Each slip intrudes into the magma chamber and pressurize the chamber at depth, generating long-duration, explosive signals (“Explosion” in Figure 2.10 and 2.20). The slips also trigger the degassing process within the chamber in which a gas and ash mixture exits through a conduit to the open vent as plumes. The lava inside the conduit continues to drain, delaying the arrival time of infrasonic pulse from the plume exiting the vent. When the lava level drops to the depth of the magma chamber, the chamber pressure condition changes and turns unfavorable in producing the explosive signals. As the eruption at the rift zone focuses to a single fissure with very high effusion rate [1], the magma pressure at the summit further decreases which drives a series of normal-faulting collapse events, across multiple inward-dipping fault structures at the caldera. The collapse initially starts above the chamber (“Collapse I”), and later migrates westward (“Collapse II”) and lastly eastward (“Collapse III”), resulting in an asymmetrical deformation across the caldera (Figure 2.16 and 2.20).

### **2.7 Reconciling seismic observations with geodetic signals**

Although the large seismic events capture a significant (and dramatic) portion of the complex deformation process at the Kilauea summit, overall, the deformation process throughout the eruption is mostly aseismic, as evidenced by the continuous geodetic measurements. Over the course of a few months, both Global Positioning System (GPS) and tilt measurements [1, 45] show trends of long-term subsidence at the caldera, punctuated temporarily by inflationary deformations (i.e. radially

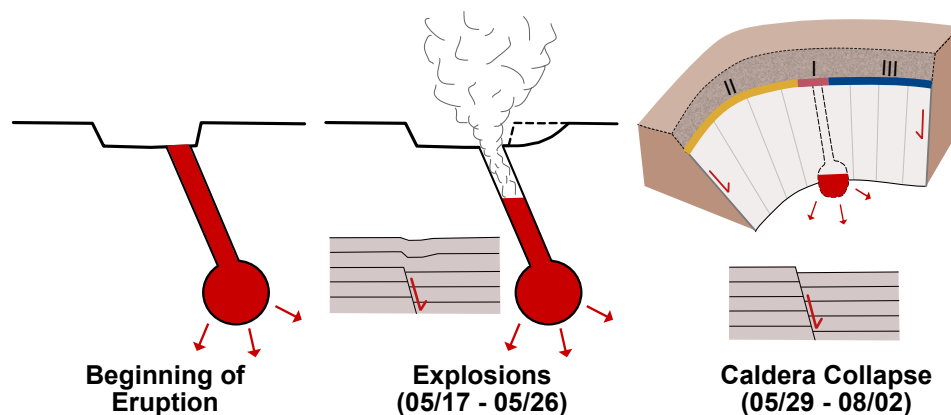


**Figure 2.20:** Schematic of the evolution at Kilauea Caldera. At the beginning of eruption around April 30, magma pressure in the shallow magmatic reservoir began to withdraw, represented by the arrows. During the explosion (05/17-05/26), fault slip above the chamber triggers explosions and generate VLP signal and degassing. There is also localized deformation. From 05/29 to 08/02, as the magma pressure continue to withdraw, the caldera experiences piecemeal collapse where the location of slips migrates westward and late towards the east.

outward tilt and uplift) outside the caldera during the collapse events. It is not immediately obvious how our focal mechanism for the collapse events, which is predominantly double-couple and no volumetric component, can be reconciled with the geodetic observations. Similar inflationary deformation has been observed in other volcanoes such as Piton de La Fournaise, where Michon et al. [41] argue the inflation is due to elastic rebound from the sudden slips along the ring fault. Based on the geodetic measurements from this Kilauea eruption, Segall et al. [45] propose a different mechanism where the transient inflation is due to the magma pressurization when the slips on block-bounding faults cause a pressure increase in the magma chamber. If the fault is dipping, elastic rebound will contribute to a tiny fraction of the total inflation. From this model, they find that in order to fit the tilt direction (upward and outward), the faults have to be vertical or inward-dipping but not outward-dipping, which is in agreement with what we have found.

Inflation models based on elastic-rebound requires a complete slip around the rock column ('piston') to maintain symmetry, and hence the expected seismic signal from the slip would be mostly vertical CLVD. The model from Segall et al. [45], although set up for piston-type collapse, may still apply to asymmetric collapse that we observed, as the inflation is mostly driven by magma pressurization from the slip and not elastic rebound. The model is also consistent with earlier explosion events where inflation is observed both seismically and geodetically, hence providing a

continuity in force-system throughout the entire caldera collapse despite changes in the seismic behavior. Future investigation, with additional constraints on key parameters from the moment tensor solutions, can help to quantify the contribution of the observed explosions and collapses on the inflationary deformation.

## 2.8 Conclusion

Using several approaches including moment tensor inversion, particle motion analysis and infrasound simulation, we characterized the large Mw 4.7 to 5.4 seismic events recorded at the Kilauea summit during the 2018 eruption sequence. We resolve the limitations of only using far-field seismic data, which are prevalent in previous source studies for caldera collapses, by incorporating local near-field seismic stations at the summit and infrasound data which gives a different perspective on the seismic source. Our results reveal a consistent underlying mechanism where magma withdrawal from the summit due to rift intrusion drives the initial explosions and the later caldera collapse. In particular, the collapse events are normal-faulting events along inward-dipping faults, which implies a combination of piecemeal-trapdoor style of collapse and differs from the commonly-assumed ‘piston’ model for caldera collapse.

## 2.9 Acknowledgments

This work is primarily advised by Professor Zhongwen Zhan. Quentin Brissaud assisted in the infrasound simulations for this analysis. We thank Greg Waite for providing the data for NPT infrasound sensor. We also thank Luis Rivera, Mark Simons, Osamu Sandanbata, and Hiroo Kanamori for the insightful discussions. All other data are maintained by USGS HVO and obtained through IRIS webservices.

## References

- [1] C. A. Neal, S. R. Brantley, L. Antolik, J. L. Babb, M. Burgess, K. Calles, M. Cappos, J. C. Chang, S. Conway, L. Desmither, et al. The 2018 rift eruption and summit collapse of Kilauea Volcano. *Science*, 363(6425):367–374, 2019.
- [2] P. R. Lundgren, M. Bagnardi, and H. Dieterich. Topographic changes during the 2018 Kilauea eruption from single-pass airborne InSAR. *Geophysical Research Letters*, 2019.
- [3] M. T. Gudmundsson, K. Jónsdóttir, A. Hooper, E. P. Holohan, S. A. Halldórs-son, B. G. Ófeigsson, S. Cesca, K. S. Vogfjörd, F. Sigmundsson, T. Högnadóttir, et al. Gradual caldera collapse at Bárðarbunga volcano, Iceland, regulated by lateral magma outflow. *Science*, 353(6296):aaf8988, 2016.

- [4] F. R. Fontaine, G. Roult, B. Hejrani, L. Michon, V. Ferrazzini, G. Barruol, H. Tkalčić, A. Di Muro, A. Peltier, D. Reymond, et al. Very-and ultra-long-period seismic signals prior to and during caldera formation on La Réunion Island. *Scientific Reports*, 9(1):8068, 2019.
- [5] Z. Duputel and L. Rivera. The 2007 caldera collapse of Piton de la Fournaise volcano: Source process from very-long-period seismic signals. *Earth and Planetary Science Letters*, 527:115786, 2019.
- [6] H. Kumagai, T. Ohminato, M. Nakano, M. Ooi, A. Kubo, H. Inoue, and J. Oikawa. Very-long-period seismic signals and caldera formation at Miyake Island, Japan. *Science*, 293(5530):687–690, 2001.
- [7] A. M. Dziewonski, T.-A. Chou, and J. H. Woodhouse. Determination of earthquake source parameters from waveform data for studies of global and regional seismicity. *Journal of Geophysical Research: Solid Earth*, 86(B4), 1981.
- [8] H. Kawakatsu. Observability of the isotropic component of a moment tensor. *Geophysical Journal International*, 126(2):525–544, 1996.
- [9] G. Ekström. Anomalous earthquakes on volcano ring-fault structures. *Earth and Planetary Science Letters*, 128(3-4):707–712, 1994.
- [10] A. Shuler, G. Ekström, and M. Nettles. Physical mechanisms for vertical-CLVD earthquakes at active volcanoes. *Journal of Geophysical Research: Solid Earth*, 118(4):1569–1586, 2013.
- [11] Y. Fukao, O. Sandanbata, H. Sugioka, A. Ito, H. Shiobara, S. Watada, and K. Satake. Mechanism of the 2015 volcanic tsunami earthquake near Torishima, Japan. *Science Advances*, 4(4):eaao0219, 2018.
- [12] M. R. Patrick, T. Orr, A. J. Sutton, E. Tamar, and D. Swanson. *The First Five Years of Kīlauea’s Summit Eruption in Halema’uma’u Crater, 2008-2013*. US Department of the Interior, US Geological Survey, 2013.
- [13] M. R. Patrick, T. R. Orr, D. A. Swanson, T. Elias, and B. Shiro. Lava lake activity at the summit of Kīlauea Volcano in 2016. Technical report, US Geological Survey, 2018.
- [14] B. A. Chouet, P. B. Dawson, M. R. James, and S. J. Lane. Seismic source mechanism of degassing bursts at Kilauea volcano, hawaii: Results from waveform inversion in the 10-50 s band. *Journal of Geophysical Research: Solid Earth*, 115(B9), 2010.
- [15] P. B. Dawson, M. C. Benitez, B. A. Chouet, D. Wilson, and P. G. Okubo. Monitoring very-long-period seismicity at Kilauea volcano, Hawaii. *Geophysical Research Letters*, 37(18), 2010.

- [16] M. Patrick, D. Wilson, D. Fee, T. Orr, and D. Swanson. Shallow degassing events as a trigger for very-long-period seismicity at Kīlauea Volcano, Hawai‘i. *Bulletin of Volcanology*, 73(9):1179–1186, 2011.
- [17] J. Almendros, B. Chouet, and P. Dawson. Spatial extent of a hydrothermal system at Kilauea Volcano, Hawaii, determined from array analyses of shallow long-period seismicity: 1. method. *Journal of Geophysical Research: Solid Earth*, 106(B7):13565–13580, 2001.
- [18] K. R. Anderson, M. P. Poland, J. H. Johnson, and A. Miklius. Episodic deflation–inflation events at Kīlauea volcano and implications for the shallow magma system. *Hawaiian Volcanoes: From Source to Surface*, 208:229, 2015.
- [19] S. Baker and F. Amelung. Top-down inflation and deflation at the summit of Kīlauea volcano, Hawai‘i observed with InSAR. *Journal of Geophysical Research: Solid Earth*, 117(B12), 2012.
- [20] P. B. Dawson, B. A. Chouet, P. G. Okubo, A. Villaseñor, and H. M. Benz. Three-dimensional velocity structure of the Kilauea caldera, Hawaii. *Geophysical Research Letters*, 26(18):2805–2808, 1999.
- [21] M. P. Poland, A. Miklius, and E. K. Montgomery-Brown. Magma supply, storage, and transport at shield-stage. *Charact. Hawaii. Volcanoes*, 179(1801): 179–234, 2015.
- [22] K. Aki and P. G. Richards. *Quantitative seismology*. 2002.
- [23] L.-S. Zhao and D. V. Helmberger. Source estimation from broadband regional seismograms. *Bulletin of the Seismological Society of America*, 84(1):91–104, 1994.
- [24] L. Zhu and D. V. Helmberger. Advancement in source estimation techniques using broadband regional seismograms. *Bulletin of the Seismological Society of America*, 86(5):1634–1641, 1996.
- [25] L. Zhu and Y. Ben-Zion. Parametrization of general seismic potency and moment tensors for source inversion of seismic waveform data. *Geophysical Journal International*, 194(2):839–843, 2013.
- [26] L. Zhu and L. A. Rivera. A note on the dynamic and static displacements from a point source in multilayered media. *Geophysical Journal International*, 148(3):619–627, 2002.
- [27] G. Lin, P. M. Shearer, R. S. Matoza, P. G. Okubo, and F. Amelung. Three-dimensional seismic velocity structure of Mauna Loa and Kilauea volcanoes in Hawaii from local seismic tomography. *Journal of Geophysical Research: Solid Earth*, 119(5):4377–4392, 2014.

- [28] K. Jaxybulatov, N. M. Shapiro, I. Koulakov, A. Mordret, M. Landès, and C. Sens-Schönfelder. A large magmatic sill complex beneath the Toba caldera. *Science*, 346(6209):617–619, 2014.
- [29] E. Wielandt and T. Forbriger. Near-field seismic displacement and tilt associated with the explosive activity of Stromboli. *Annals of Geophysics*, 42(3), 1999.
- [30] Q. Brissaud, R. Martin, R. F. Garcia, and D. Komatitsch. Hybrid Galerkin numerical modelling of elastodynamics and compressible Navier–Stokes couplings: applications to seismo-gravito acoustic waves. *Geophysical Journal International*, 210(2):1047–1069, 2017.
- [31] R. Butler. Composite earthquake source mechanism for 2018 m w 5.2-5.4 swarm at Kīlauea caldera: Antipodal source constraint. *Seismological Research Letters*, 90(2A):633–641, 2019.
- [32] H. Kanamori and D. L. Anderson. Theoretical basis of some empirical relations in seismology. *Bulletin of the seismological society of America*, 65(5), 1975.
- [33] K. Kazahaya, H. Shinohara, K. Uto, M. Odai, Y. Nakahori, H. Mori, H. Iino, M. Miyashita, and J. Hirabayashi. Gigantic SO<sub>2</sub> emission from Miyakejima volcano, Japan, caused by caldera collapse. *Geology*, 32(5):425–428, 2004.
- [34] T. R. Orr, W. A. Thelen, M. R. Patrick, D. A. Swanson, and D. C. Wilson. Explosive eruptions triggered by rockfalls at Kīlauea volcano, Hawai ‘i. *Geology*, 41(2):207–210, 2013.
- [35] C. Liang, L. Karlstrom, and E. M. Dunham. Magma oscillations in a conduit-reservoir system, application to very long period (VLP) seismicity at basaltic volcanoes—Part I: Theory. *Journal of Geophysical Research: Solid Earth*, 2020.
- [36] T. Kobayashi, Y. Ida, and T. Ohminato. Small inflation sources producing seismic and infrasonic pulses during the 2000 eruptions of Miyake-jima, japan. *Earth and Planetary Science Letters*, 240(2):291–301, 2005.
- [37] M. R. Patrick, A. J. L. Harris, M. Ripepe, J. Dehn, D. A. Rothery, and S. Calvari. Strombolian explosive styles and source conditions: insights from thermal (FLIR) video. *Bulletin of Volcanology*, 69(7):769–784, 2007.
- [38] J. Taddeucci, P. Scarlato, A. Capponi, E. Del Bello, C. Cimarelli, D. M. Palladino, and U. Kueppers. High-speed imaging of strombolian explosions: The ejection velocity of pyroclasts. *Geophysical research letters*, 39(2), 2012.
- [39] D. Fee, M. Garcés, M. Patrick, B. Chouet, P. Dawson, and D. Swanson. Infrasonic harmonic tremor and degassing bursts from Halema’uma’u Crater, Kilauea Volcano, Hawaii. *Journal of Geophysical Research: Solid Earth*, 115 (B11), 2010.

- [40] P. W. Lipman. Subsidence of ash-flow calderas: Relation to caldera size and magma-chamber geometry. *Bulletin of Volcanology*, 59(3):198–218, 1997.
- [41] L. Michon, N. Villeneuve, T. Catry, and O. Merle. How summit calderas collapse on basaltic volcanoes: New insights from the April 2007 caldera collapse of Piton de la Fournaise volcano. *Journal of Volcanology and Geothermal Research*, 184(1-2):138–151, 2009.
- [42] T. Ágústsdóttir, T. Winder, J. Woods, R. S. White, T. Greenfield, and B. Brandsdóttir. Intense seismicity during the 2014–2015 Bárðarbunga-Holuhraun rifting event, Iceland reveals the nature of dike-induced earthquakes and caldera collapse mechanisms. *Journal of Geophysical Research: Solid Earth*.
- [43] R. T. Holcomb. Eruptive history and long-term behavior of Kilauea Volcano. *US Geol. Surv. Prof. Pap*, 1350(1):261–350, 1987.
- [44] B. Chouet and P. Dawson. Shallow conduit system at Kilauea volcano, Hawaii, revealed by seismic signals associated with degassing bursts. *Journal of Geophysical Research: Solid Earth*, 116(B12), 2011.
- [45] P. Segall, K. R. Anderson, I. Johanson, and A. Miklius. Mechanics of inflationary deformation during caldera collapse: Evidence from the 2018 Kilauea eruption. *Geophysical Research Letters*.

*Chapter 3***THE SEISMIC SIGNATURE OF DEBRIS FLOWS: FLOW MECHANICS AND EARLY WARNING AT MONTECITO, CALIFORNIA**

Lai, V. H., Tsai, V. C, Lamb, M. P., Ulizio, T. P. and Beer, A. R. (2018). “The seismic signature of debris flows: Flow mechanics and early warning at Montecito, California”. In: *Geophysical Research Letters* 45.11, pp. 5523-5535. doi: 10.1029/2018GL077683.

**3.1 Abstract**

Debris flows are concentrated slurries of water and sediment that shape the landscape and pose a major hazard to human life and infrastructure. Seismic ground motion-based observations promise to provide new, remote constraints on debris flow physics, but the lack of data and a theoretical basis for interpreting them hinders progress. Here we present a new mechanistic physical model for the seismic ground motion of debris flows and apply this to the devastating debris flows in Montecito, California on 9 January 2018. The amplitude and frequency characteristics of the seismic data can distinguish debris flows from other seismic sources and enable the estimation of debris-flow speed, width, boulder sizes, and location. Results suggest that present instrumentation could have provided 5 min of early warning over limited areas, whereas a seismic array designed for debris flows would have provided 10 min of warning for most of the city.

**3.2 Introduction**

Debris flows are concentrated slurries of sediment and water that are typically triggered in steep mountain landscapes following intense precipitation [1], and they are especially common following wildfire [2, 3]. Debris flows are capable of rapidly transporting large volumes of sediment and large boulders over long distances, making them destructive and dangerous [4, 5]. Despite the significant danger and importance for landscape change [6], limited work has been done to make direct measurements of natural debris flows because they occur infrequently and are difficult and dangerous to instrument [3, 5]. Ground shaking measured by seismometers provides a potential breakthrough in debris flow measurements

because instruments can be placed outside of the channel, and the seismic signal might be used to invert for both debris flow occurrence and debris flow mechanics [7, 8, 9, 10, 11, 12]. However, in contrast to earthquake studies, only limited work has been done to deploy seismometers to monitor debris flows, and we lack a theoretical framework to interpret the seismic signature of debris flows to constrain flow mechanics, although important theoretical advances are being made for related phenomena in rivers and landslides [8, 13, 14, 15, 16, 17, 18].

Seismic monitoring of debris flows also has the potential to provide advanced warning of imminent debris flows that could significantly mitigate loss of life. One of the most successful advanced warning systems for debris flows in the U.S. is the joint National Oceanic and Atmospheric Administration and U.S. Geological Survey effort, which uses a combination of predicted and measured rainfall rates and past debris-flow occurrence in recently burned areas to make 24 to 48-hr predictions of the likelihood of severe debris flows [19, 20]. While these predictions are useful, by necessity, they have erred on the side of caution, with some false warnings. To complement predictions made hours to days in advance, it would be useful to have an early warning system that accurately and robustly determines debris flow characteristics in real time and hence only triggers an alert when there is a large event detected, and ideally far enough in advance that loss of life can be prevented. Applications of ground-motion based early warning systems have been slow to advance because we often lack a nearby network of permanent real-time seismic stations dedicated to debris flow detection, the seismic signature of debris flows has not been well established, and therefore early warning criteria proposed have been ad hoc and specific to each site [10, 12].

Here we address these concerns by developing a mechanistic physical model for the high-frequency ground shaking produced by debris flows and applying the model to seismic data observed within a few kilometers of the Montecito debris flows that occurred on 9 January 2018 (Figure 3.1a), a large event that destroyed many structures in the city of Montecito, California and caused at least 20 casualties. We demonstrate that important physical quantities can be constrained and describe implications for potential debris flow early warning application.

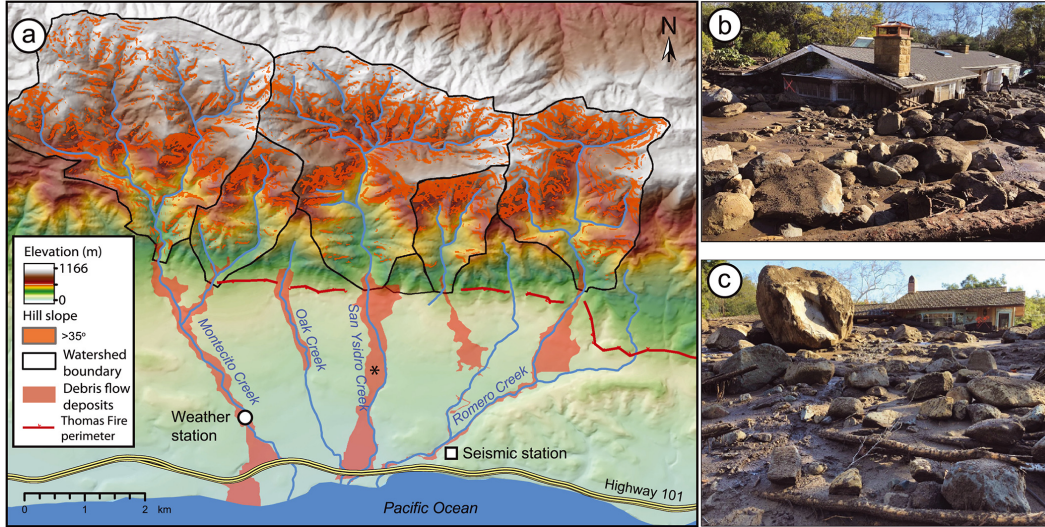


**Figure 3.1:** Montecito debris flows. (a) Map of the Montecito area showing the burned Santa Ynez Mountains to the north and the major creeks that flow through Montecito. Debris flow deposits were mapped based on aerial imagery and house damage maps produced by Santa Barbara County. Major damage was focused along Montecito and San Ysidro creeks. The seismic station is CI.QAD from the Southern California Seismic Network, and the weather station is the Montecito Station from Santa Barbara County. (b and c) Photographs following the debris flows located near the asterisk along San Ysidro Creek in (a). Photo credit: Mike Eliason, Santa Barbara County Fire.

### 3.3 Mechanistic Model

To make a theoretical prediction for the high-frequency ( $>1$  Hz) seismic ground motion produced by a debris flow, we begin with the bed load impact model of Tsai et al. [18]. A series of particles are assumed to stochastically impact a channel bed, producing seismic waves that travel to the seismic station and, to simplify the prediction, the largest amplitude ground motions are assumed to primarily come from surface waves. Additionally accounting for a minor improvement to the accuracy of the impulse response functions [14], and assuming a single average source-station distance,  $r_0$ , the same model can be used to predict the ground motion due to an arbitrary set of stochastic impacts of particles, whether transported fluvially or by debris flows, yielding

$$P = \frac{0.6^2(1 + \xi)^2 \pi^2}{4\rho_g^2 v_c^5} \cdot m^2 \Delta w_i^2 \cdot \frac{f^3 \left(\frac{f}{f_0}\right)^{5\xi}}{r_0} \cdot e^{-2\pi f r_0 (1+\xi) \left(\frac{f}{f_0}\right)^\xi / (v_c Q)} \cdot R_i \quad (3.1)$$

where  $\xi \approx 0.25 - 0.5$  is a parameter related to how strongly seismic velocities increase with depth at the site [18],  $\rho_g$  is the ground density,  $v_c$  is the Rayleigh-wave

phase velocity at 1 Hz,  $m$  is the mass of each particle,  $\Delta w_i$  is the change in impact velocity at each impact,  $f$  is frequency,  $f_0$  is a reference frequency set to 1 Hz,  $r_0$  is the average distance of the station from the debris flow,  $Q$  is the quality factor for Rayleigh waves (assumed independent of frequency within the observed range), and  $R_i$  is the total rate of impacts (number per unit time) integrated over the entire surface, assumed to be phased randomly with respect to each other.  $P$  is the seismic power spectral density (PSD) of velocity as a function of frequency,  $f$ , and has 2 units of  $(m/s)^2/Hz$ , with absolute ground motion velocities over a frequency band  $\Delta f$  then given by  $\sqrt{P\Delta f}$ . We assume that grains are spherical and have a representative grain diameter  $D$ , discussed below, so that  $m \approx \frac{\pi}{6}\rho_D D^3$ , where  $\rho_D$  is the density of each grain. In order to use equation 3.1 for debris flows, we must estimate  $\Delta w_i$  and  $R_i$ . Tsai et al. [18] showed that seismic noise is dominated by the very coarse fraction of the load; for a nearly lognormal distribution typical of river beds, for example,  $D$  represents the 94th percentile of the grain size distribution. The coarse load of debris flows often occurs at the flow front, in a boulder snout, and these boulders are pushed from the flow behind [5]. With this simple conceptualization in mind, we assume that large clasts are pushed and dragged along the riverbed in what we define as a “washboard” model, such that the average impact velocity scales with the average velocity of the flow,  $u$ . We set  $\Delta w_i = 2u$  to account for significant rebound with each impact. To estimate  $R_i$  for the same washboard type model, we assume that each clast impacts the ground every time it encounters a bump in the ground surface; that is, it has an impact rate of  $\frac{u}{L_b}$ , where  $L_b$  is the length scale between significant bumps on the ground surface. While  $L_b$  is not well constrained, if the debris flow traverses a granular bed composed of similar material in the coarse snout, it is reasonable to assume that  $L_b = D$ . For debris flows over a bedrock bed, some granular flow experiments [21] suggest that when the ground is rough at many scales, clasts tend to interact most favorably with roughness elements close to the same scale, that is, that  $L_b = D$  is still a reasonable assumption. Integrating over the area over which clasts are distributed, and assuming the clasts are relatively well packed results in a total  $R_i = \frac{uLW}{D^3}$ , where  $L$  is the length of the boulder-rich snout and  $W$  is the width of the flow. Making these substitutions results in

$$P = \frac{0.6^2(1 + \xi)^2 \pi^4 \rho_D^2}{36\rho_g^2 v_c^5 r_0} \cdot LWD^3 u^3 \cdot f^{3+\xi} \cdot e^{-2\pi f^{1+\xi} r_0(1+\xi)/(v_c Q)} \quad (3.2)$$

where  $f$  is assumed to be in Hz. (If  $L$  were much greater than  $r_0$ , one should use an effective length of  $L = r_0$  in equation 3.2 to account for attenuation of the seismic signal.) Assuming the sediment and ground densities to be equal, substituting  $\xi \approx$

0.4 [18, 22], and numerically evaluating coefficients in equation 3.2 yields

$$P = 1.9 \cdot LWD^3 u^3 \cdot \frac{f^{3+5\xi}}{v_c^5 r_0} \cdot e^{\frac{8.8f^{1+\xi} r_0}{v_c Q}} \quad (3.3)$$

While this formula is only expected to provide an order-of-magnitude estimate of the seismic PSD,  $P$ , its functional form provides significant insight into the PSD signature of debris flows. Importantly, for a known set of seismic ground properties, the frequency dependence only depends on the source-station distance,  $r_0$ , and is independent of debris flow properties, whereas the amplitude of  $P$  depends strongly on both boulder size and flow speed to the third power, while having a weaker linear dependence on flow snout width and length. Interestingly, equation 3.3 has no direct dependence on debris flow thickness, though thickness may correlate with flow speed. The peak frequency  $f_p$  of equation 3.3 can be determined analytically by setting  $dP/df = 0$  and solving for  $f$ . Doing so and solving for  $r_0$  gives

$$r_0 = \frac{(3 + 5\xi)v_c Q}{2\pi(1 + \xi)^2 f_p^{1+\xi}} \quad (3.4)$$

which can be used to estimate  $r_0$  from measurements of  $f_p$ . The debris flow speed toward the seismometer can be calculated from changes in  $r_0$  as a function of time recorded by the seismometer. To estimate the debris flow speed along the channel, these speeds can be corrected by an orientation factor that accounts for the direction of the flow relative to the direction to the seismometer. Our theoretical analysis differs from previous debris flow early warning approaches and inversions for debris flow fluxes from seismic data. In previous early warning approaches (e.g., [12]), multiple seismic stations in a dense array were required since no mechanistic model was used to predict the absolute amplitude of seismic signal expected of a debris flow. In this work, we make a specific prediction for the absolute amplitude of the seismic signal of debris flows, allowing us to create a straightforward threshold based purely on seismic power. While previous inversions for debris flow fluxes [17] have also built upon the Tsai et al. [18] model, this previous work has also refrained from discussing absolute amplitudes and instead has normalized seismic power relative to events with known fluxes. Since events with known fluxes are typically not available, and were not available in Montecito, this type of approach would not be feasible in most locations. Thus, while our approach of using absolute seismic amplitudes has uncertainties in the various parameters of the model, it allows for a more straightforward estimation of important physical parameters of debris flows through equations 3.3 and 3.4.

### 3.4 Data and Results

On 9 January 2018, debris flows were triggered in the Santa Ynez Mountains that border the city of Montecito to the north (Figure 3.1a) following a downpour of approximately 20 mm of rain over a 10-min period in Montecito at ~3:45 a.m. (Figure 3.2d). A month earlier, the mountains burned in one of the largest wildfires in California history, the Thomas Fire, leaving characteristic barren hillslopes and dry river channels loaded with loose sediment [23]. Debris flows are common in southern California following wildfire, especially in steep terrain where hillslope gradients exceed the frictional stability of soil in the absence of plants ( $>35^\circ$ ); under these conditions, annual sediment yields can increase by 10-fold or more [24]. Based on local reports, debris flows began to inundate the northern parts of Montecito around 3:50 a.m. Debris flows moved through the uplands, where ~37% of the terrain exceeds  $35^\circ$  and creek-bed gradients are ~12% (Figures 3.1a and 3.3) and flowed south into a series of creeks, with gradients of ~5%, that drain south through the city of Montecito to the Pacific Ocean. Although the creeks are incised by more than 5 m into the surrounding terrain (Figure 3.4), the debris flows overflowed the valleys, often at bridge crossings, carrying boulders commonly 0.5–2 m, and up to 5 m, in diameter into the neighboring residential areas (Figures 3.1b and 3.1c and 3.5). The debris flow deposits cover ~7 km<sup>2</sup>; damage was concentrated within a few hundred meters of the creeks and was most pronounced along Montecito and San Ysidro Creeks (Figures 3.1b and 3.1c). Hundreds of homes were damaged or destroyed and at least 20 people died.

The primary seismic station (CI.QAD) used in this analysis is located within ~250 m of Romero Creek and ~1.5 km of the zone of major damage near San Ysidro Creek (Figure 3.1a) and had real-time data with latencies of less than 5 s between measurement and analysis output [25]. Ground motions at the station due to the debris flows were very anomalous, with high-frequency filtered (5–10 Hz) ground motion velocities with amplitudes in excess of  $10^{-5}$  m/s lasting more than 10 min (Figure 3.2c). Despite other periods of rain, wind, ocean waves, earthquakes, and cultural noise over the 6-month deployment of the seismometer, no other time period had sustained ground motions of this magnitude when averaged over 60 s or longer (Figure 3.2a). The seismic signature of debris flows may be distinct; for example, shaking from earthquakes is typically shorter, and with energy distributed over a wider frequency band [26, 27], strong rain, wind, water flow, and fluvial sediment transport are significantly weaker seismic sources [28, 29, 30], and ocean waves have lower frequency energy ([31, 32, 33], Figure 3.6). Thus, a simple criterion based

on time-averaged filtered ground motion amplitude exceeding  $6 \times 10^{-12} \text{ (m/s)}^2/\text{Hz}$  accurately discriminates between the Montecito debris flows and any other event (Figure 3.2a). Due to significant attenuation of the seismic signal with distance from the source, this threshold was not met until 4:06:30 a.m. (Figure 3.2b, inset) despite reported debris flows earlier and small but significant debris flow seismic energy starting by 3:48:00 a.m. (see Figures 3.2c and 3.7c), highlighting the importance of station location for early detection as discussed below.

The success of such a simple criterion and constraints on debris flow physics can be understood in the context of equations 3.3 and 3.4. Taking estimates of seismic parameters for the site of  $v_c=953 \pm 200 \text{ m/s}$ ,  $Q=45 \pm 15$ , and  $\xi=0.417 \pm 0.05$  (see Appendix; [34, 35, 36]) allows estimates of source-station distance  $r_0$  from observed peak frequency through equation 3.4. At the time of the largest ground motions at 4:06:45 a.m. in Montecito, peak frequency is observed in the range of 6–7 Hz (Figures 3.7a and 3.7b). Given the significant uncertainties in seismic parameters [17], this frequency band results in an estimated average source-station distance of  $1,220 \pm 600 \text{ m}$  (see Appendix), consistent with the distance to the zones of major damage along San Ysidro and Romero Creeks (Figure 3.1). Because the debris flows were triggered by a brief period of intense rainfall, flows were likely active simultaneously in multiple creeks. Although the lower portion of Romero Creek is within  $\sim 250 \text{ m}$  of the station (see Figure 3.1a), debris flows there appear to have been smaller and confined to the channel, consistent with the seismic data that suggest that the peak amplitude occurred farther upstream (i.e., at a distance of  $1,220 \pm 600 \text{ m}$ ) in Romero Creek or in nearby San Ysidro Creek. For example, with the seismic parameters as above, a source at 250 m would have its peak at 20 Hz, far from the observed 6 to 7-Hz peak.

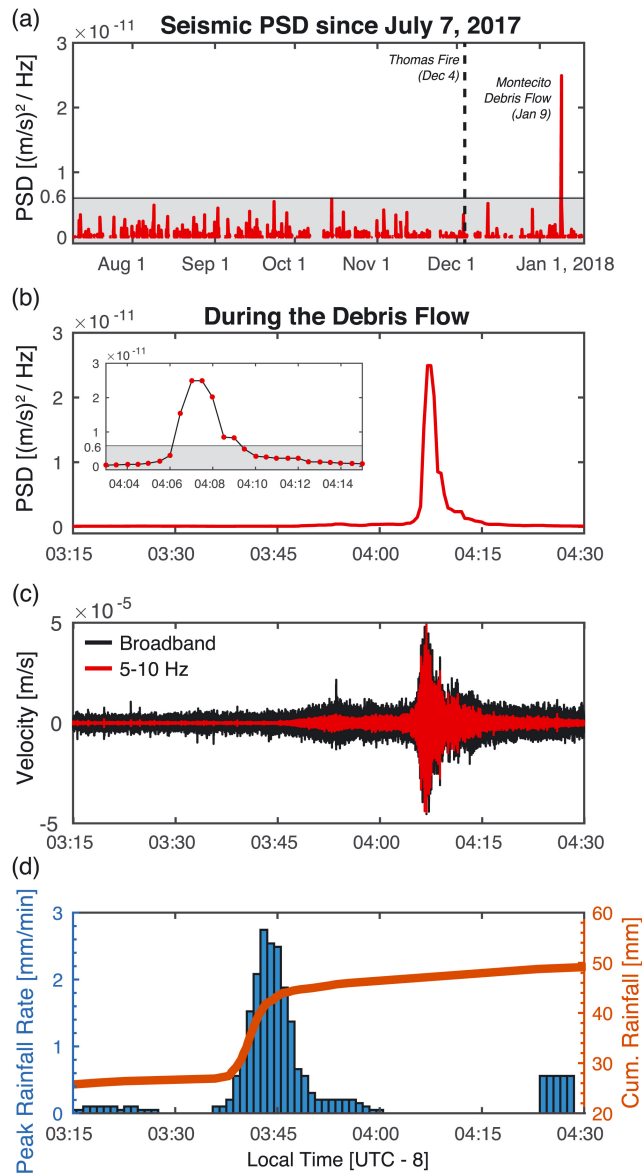


**Figure 3.2:** Detection of the Montecito debris flows from seismic ground motion data. (a) Mean power spectral density (PSD) for velocity data in a 5 to 10-Hz frequency band, averaged over 1-min time intervals, recorded on a vertical component accelerometer at seismic station CI.QAD (Figure 3.1a), from beginning of operation (7 July 2017) until 17 January 2018. Deglitching is necessary to remove spikes due to electrical noise (see Figures 3.8 and 3.9). PSD from the debris flow is significantly above the background noise. For early warning purposes, a threshold of  $6 \times 10^{-12}$  (m/s)<sup>2</sup>/Hz is sufficient to distinguish the debris flow signal from other signals. (b) Mean PSD (5–10 Hz) during the debris flow episode. Inset shows the PSDs at 30-s intervals, where the signal intensifies over a short time period (<2 min.). A threshold of  $6 \times 10^{-12}$  (m/s)<sup>2</sup>/Hz is reached by 4:06:30 a.m. (c) Seismic ground motion time series for the broadband data (in black) and filtered at 5–10 Hz (in red). The debris flow signal is dominated by the 5 to 10-Hz signal; there is also an increase in overall energy, particularly in the 1-Hz frequency range shortly after peak rainfall (see Figure 3.7). (d) Peak rainfall rate and cumulative rainfall recorded at the Montecito site (see Figure 3.1a). Peak rainfall rate is averaged over 5-min windows. Highest peak rainfall is around 3:45 a.m.

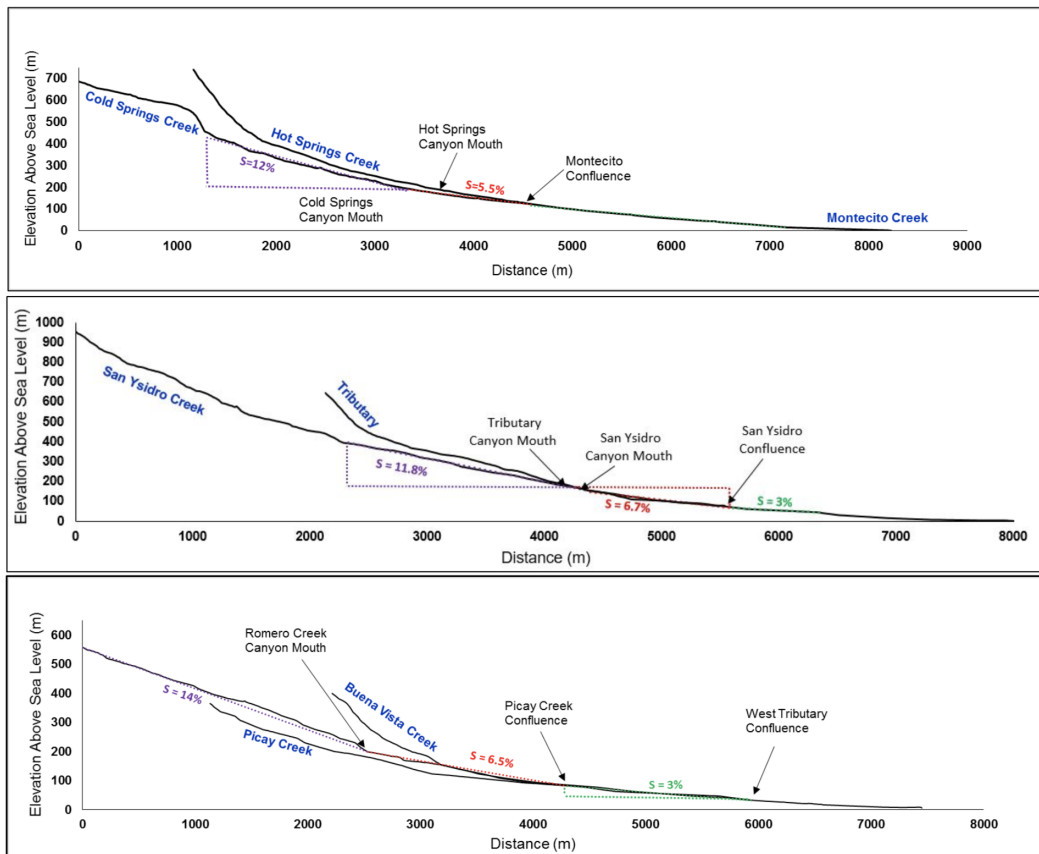


**Figure 3.3:** Elevation profiles along Montecito Creek (top), San Ysidro Creek (middle) and Romero Creek (bottom) from the drainage divide in the Santa Ynez Mountains to the Pacific Ocean. Some of the most severe debris flow damage was at the confluence of the main creeks and their tributaries (Hot Springs Creek and an unnamed creek, respectively). Montecito, San Ysidro and Romero Creeks all have gradients,  $S$ , of 12% near the canyon mouths in the mountains, and their slopes decrease to 3-7% through the Montecito area. 10-m resolution topographic data from the U.S. Geological Survey.

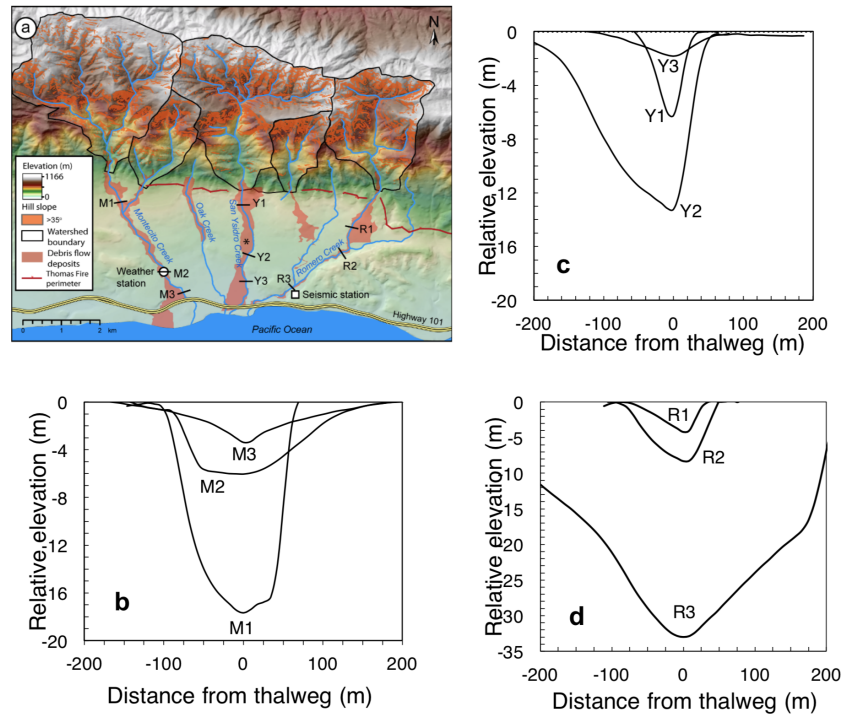


**Figure 3.4:** Across channel profiles. (a) Map of the Montecito area (same as Figure 3.1a) showing channel cross section locations. Cross sections of (b) Montecito Creek, (c) San Ysidro Creek and (d) Romero Creek before the debris flows of 2018. 10-m resolution data from US Geological Survey.

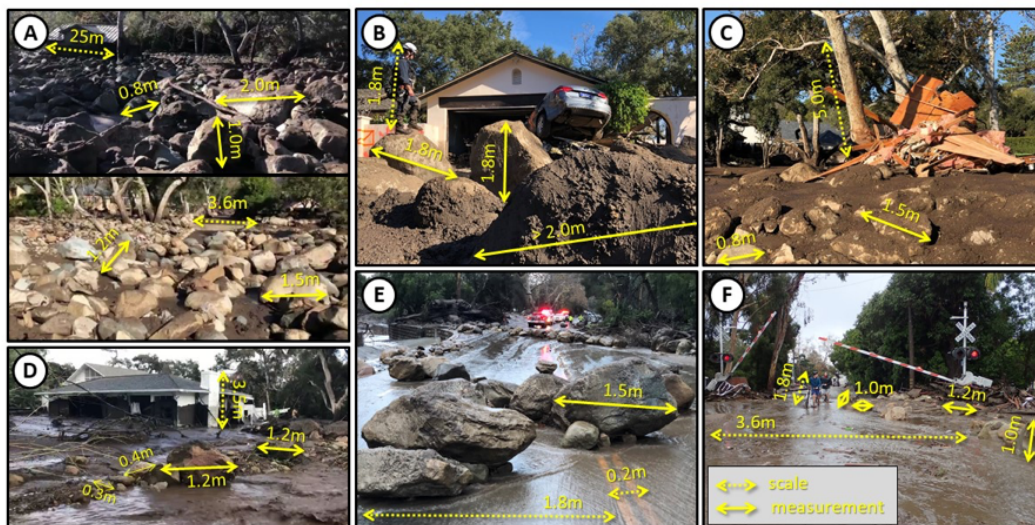


**Figure 3.5:** Boulders observed at San Ysidro Creek (a-c) and Montecito Creek (d-f). Non-emergency responders were not allowed in the area, and size estimations (solid lines) are based on estimated sizes of visible structures (dashed lines). Photo credit: Mike Eliason, Santa Barbara County Fire.

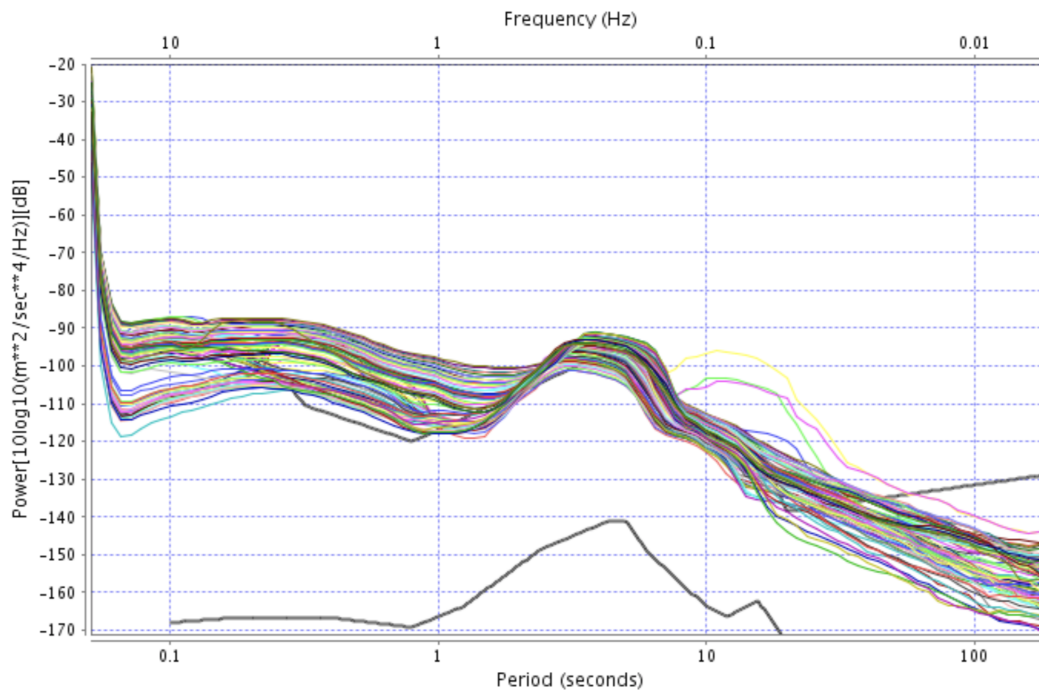


**Figure 3.6:** Acceleration PSDs at station TA.544A (near New Orleans, Louisiana) over 2 days during the peak winds and rains of Hurricane Isaac (August 30-31, 2012). Colors correspond to different hours. The two thick gray lines correspond to the New High Noise Models and New Low Noise Models [27]. Acceleration PSDs of -90 dB in the frequency range 5-10 Hz correspond to velocity PSDs of  $4 \times 10^{-13} \text{ (m/s)}^2/\text{Hz}$ , whereas acceleration PSDs of -85 dB correspond to velocity PSDs of  $1.4 \times 10^{-12} \text{ (m/s)}^2/\text{Hz}$ . Hurricane force winds therefore never cause ground motions above our threshold of  $6 \times 10^{-12} \text{ (m/s)}^2/\text{Hz}$  even for the most intense wind of Hurricane Isaac. (Our threshold corresponds to an acceleration PSD of -76 dB at 10 Hz, -79 dB at 7.5 Hz, and -82 dB at 5 Hz.) Waves are also anomalously large during these times, but primarily cause an increase in longer period (lower frequency) ground motions. Figure courtesy of IRIS MUSTANG metrics.

Due to attenuation with distance and other ambient seismic noise sources at lower frequencies, the method is not as robust for debris flows that occurred farther than ~3 km from the station, such that potential signals from Montecito Creek or the far upstream extents of San Ysidro and Romero Creeks are not reliably measured (see Appendix 3.6). For example, the seismic data also show a low amplitude peak at <3 Hz and continuous for more than 4 hr, which may be due to nearby short-period ocean waves generated by the storm [32] or water flow and standing waves [14, 37] in the lower reach of Romero Creek near the seismic station. This energy overlaps significantly with signals from more distant debris flows and is the main reason that the seismic station in Santa Barbara, located ~10 km west of the Montecito station, cannot reliably be used in the analysis presented here. Nevertheless, despite being too faint to reliably separate from long-term background noise levels and thus be used for early warning purposes, both stations show clear energy above shorter-term background noise levels (e.g., Figure 3.2c) starting around 3:48:00 a.m. and continuing through 3:55:00 a.m. (Figure 3.10). These earlier, lower amplitude records are consistent with eye-witness reports of the timing of debris flows in the upper parts of Montecito and San Ysidro Creeks. Debris flows in Romero Creek, which likely occurred later due to the storm moving from west to east, or flow in the downstream section of San Ysidro Creek, are within 3 km of the Montecito seismic station but were farther away from and appear not to be detected by the Santa Barbara seismic station.

After subtracting off the <3 Hz signal, it is clear that the peak frequency from debris flows detected by the Montecito station shifts over time, from generally lower frequencies earlier (e.g., 5.5 Hz at 4:04:45 a.m. and 6.0 Hz at 4:06:00 a.m.) to higher frequencies later (e.g., 7.0 Hz at 4:08:45 a.m. and 8.0 Hz at 4:10:00 a.m.; Figures 3.7a and 3.7b), but with significant complexity in between (Appendix). Using our preferred parameters, equation 3.4 indicates that the shift in peak frequency corresponds to the average distance between the source and the seismometer changing from 1,540 to 1,360 m, 1,220 m, 1,100 m, and then 910 m in 1.25, 0.75, 2.0, and 1.25 min, respectively (Figure 3.7c). The flow path is unlikely to have been straight, and the bimodal peaks at certain times (e.g., 4:06:00 a.m., Figure 3.7a) suggest that at least two separate debris flow pulses were recorded. By accounting for the likely average angle between the debris flow direction and the direction of the station (~45° for lower San Ysidro Creek or ~0° for Romero Creek), we estimate an average speed over the 5.25 min of strongest signal to be  $u = 2.4 \pm 1.7$  m/s. This estimate of both distance and debris flow speed can be made

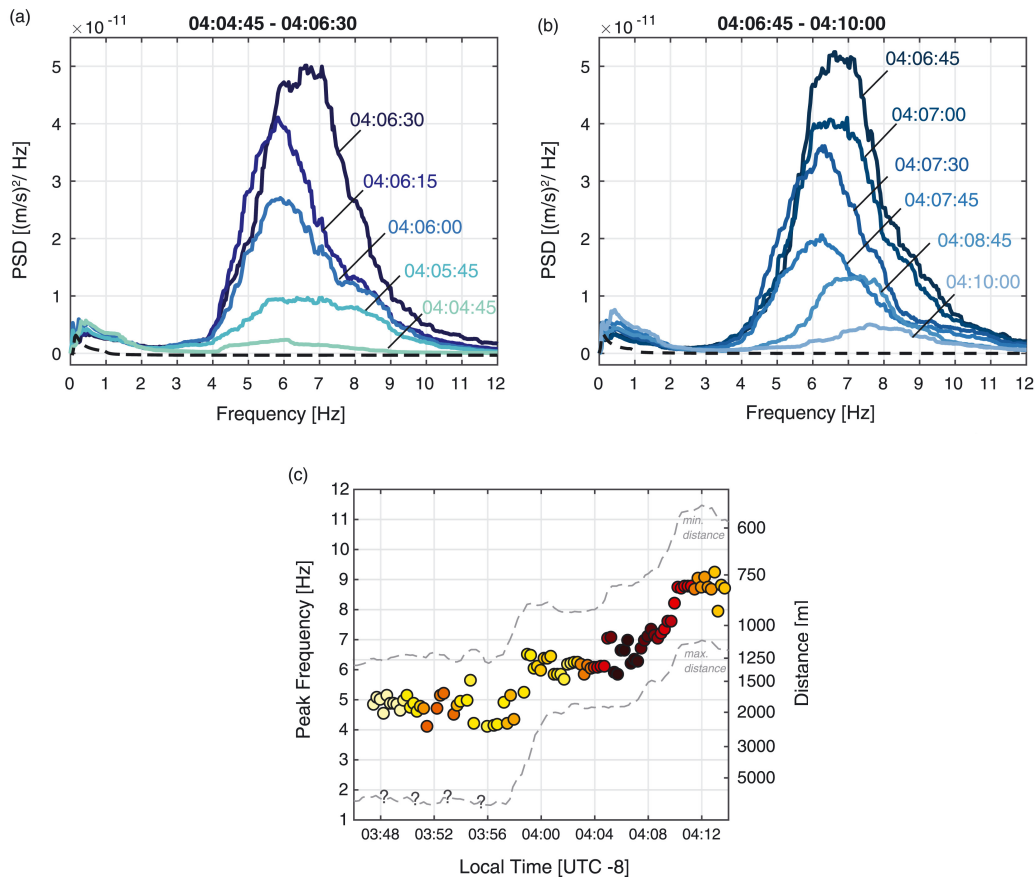


**Figure 3.7:** Evolution of power spectral density (PSD) during the debris flow. (a) PSDs recorded from 4:04:45 a.m. to 4:06:30 a.m. have initial power at 5–6 Hz (4:04:45 a.m.) over the background levels (dashed line), which increases in amplitude through 4:06:30 a.m. and changes peak frequency to 6–7 Hz. (b) PSDs recorded from 4:06:45 a.m. to 4:10:00 a.m. have power that decreases with time, with PSDs after 4:10:00 a.m. nearing background levels (dashed line). (c) Peak frequency generally increases to higher frequencies over the course of the debris flow. The warmer colors denote higher PSDs. The dashed gray lines denote the range of estimated distances after accounting for uncertainties in the seismic parameters. All PSDs are smoothed with a 2-Hz moving window. At early times, significant energy below 3 Hz from sources other than debris flows (see (a) and (b)) makes it challenging to reliably pick peak frequencies below 4 Hz. Thus, we have conservatively picked peaks that are within the more reliable 4 to 10-Hz band, despite significant energy at lower frequencies from 3:47 to 3:56 a.m. We therefore likely underestimate the distance of flows at these early times.

with a single nearby seismic station and is consistent with available information as well as observed debris flow speeds in similar terrains [5]. After the seismic peak, the pattern of decreasing seismic amplitude with decreasing distance to the station suggests that the flows lost significant momentum after they were forced from the channel, spread, and deposited mud and boulders in the zones of major damage. At these late times (particularly at 4:12–4:15 a.m.), there is also a much larger fraction of seismic energy above 10 Hz (including energy at 20 Hz), in a possibly bimodal distribution, consistent with the inference of weaker but closer flows at these times (Figure 3.11).

Constraints on the product  $LWD^3u^3$  can be obtained from the observed seismic amplitudes through equation 3.3, with a factor of  $\sim 20$  uncertainties after accounting for uncertainties in the seismic parameters (see Appendix). With these uncertainties in mind, we estimate peak values of  $LWD^3u^3$  of  $8.0 \times 10^4 \text{ m}^8/\text{s}^3$ , with best estimates of the time history going from  $7.9 \times 10^3 \text{ m}^8/\text{s}^3$  at 4:04:45 a.m. to  $6.8 \times 10^4 \text{ m}^8/\text{s}^3$  at 4:06:00 a.m.,  $1.2 \times 10^4 \text{ m}^8/\text{s}^3$  at 4:08:45 a.m., and  $2.1 \times 10^3 \text{ m}^8/\text{s}^3$  at 4:10:00 a.m. Using our estimate of  $u = 2.4 \text{ m/s}$  and estimating  $W \sim L \sim 50 \text{ m}$  for the width and length of the boulder snout based on channel widths ( $\gtrsim 10 \text{ m}$ ; Appendix) and the lateral extent of postevent boulder fields ( $\lesssim 100 \text{ m}$ ), we estimate  $D = 1.3 \pm 0.6 \text{ m}$  at peak signal and  $D = 0.7 \pm 0.4 \text{ m}$  closer to the station, consistent with visual observations (Figures 3.1b and 3.1c and 3.5). More importantly, our ability to constrain physical parameters of the debris flow provides clear guidelines for a debris flow early warning criterion based on whether  $LWD^3u^3$  exceeds a certain threshold, where a threshold of  $2,000 \text{ m}^8/\text{s}^3$  could correspond to a flow with  $L = W = 45 \text{ m}$ ,  $D = 0.5 \text{ m}$ , and  $u = 2 \text{ m/s}$ . At a nominal source-station early warning distance of 1,000 m and the seismic parameters as chosen above, a threshold of  $2,000 \text{ m}^8/\text{s}^3$  corresponds with a maximum PSD amplitude of  $6 \times 10^{-12} \text{ (m/s)}^2/\text{Hz}$  (Figure 3.2a) or an average (5–10 Hz) filtered ground motion velocity threshold of  $5 \times 10^{-6} \text{ m/s}$ . If ambient noise levels at a station were higher than the proposed corresponding threshold, our analysis implies that the straightforward early warning methodology proposed here would fail. Finally, our model suggests that the onset and decay of seismic energy over several minutes (Figure 3.2b) may be characteristic of debris flows on depositional fans, with the onset being mostly due to decreasing average distance of the flow to the station, and the decay being mostly related to decreasing flow speed and grain size as the flow traverses the distal, lower gradient fan and deposits the largest boulders.

Our analysis of the ground-motion data suggests that debris flow early warning could have been accomplished for Montecito, even with a single accelerometer with moderate sensitivity in the 5 to 10-Hz frequency band providing real-time data. With the nominal threshold and estimates discussed above, the early warning time would have been approximately 5 min for locations within about 600 m of the station (Appendix). While such an early warning would not have helped for locations farther upstream, including the most heavily affected areas, a seismic network designed specifically for debris flow early warning could clearly improve upon the warning area and time. Locating multiple stations upstream of the potentially affected communities, near the border of Montecito with the Santa Ynez Mountains at each creek, could provide up to 10 min of early warning for all residents affected by the Montecito debris flows, depending on the debris flow initiation locations (Appendix). There is a trade-off between the robustness of the detection, size of the event targeted, and the amount of warning time desired, but the simple theoretical prediction of equation 3.3 provides a pragmatic and justifiable criterion upon which to base a warning threshold, with site-specific modifications based on the parameters discussed being clear ways in which different sites could have different ground-motion thresholds for the same targeted early warning level. While there are many practical issues that still need to be addressed before the ground-motion based debris flow early warning system proposed here would be robust and useful (e.g., [38, 39, 40]), the physics-based approach should help with better understanding the uncertainties that underlie the measurement.

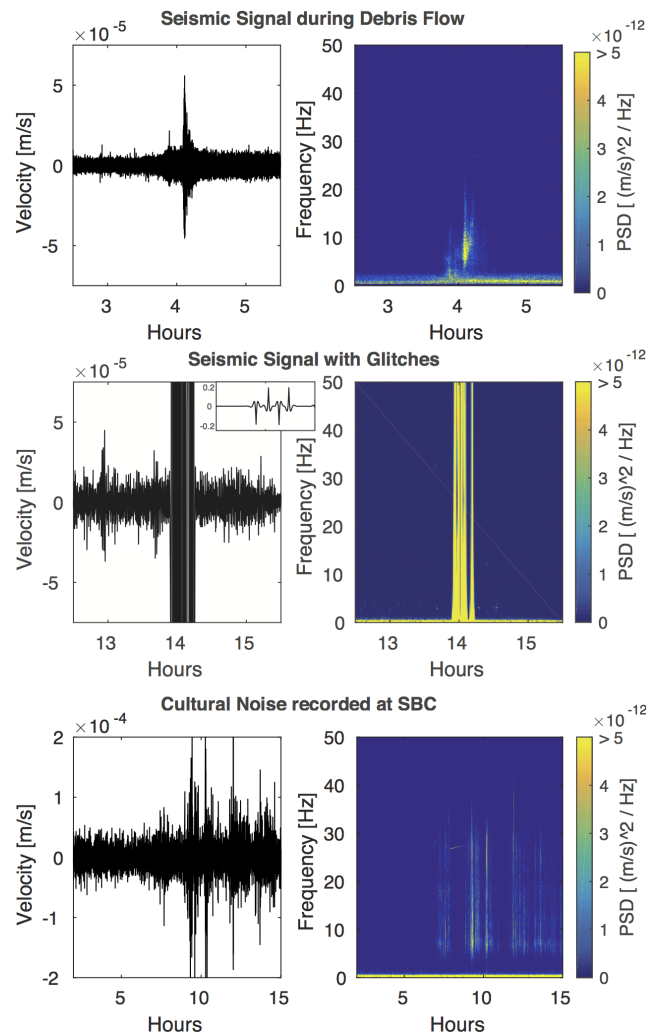


**Figure 3.8:** Seismic velocity time series and their respective spectrogram highlighting signals with various types of sources. (Top panel) Seismic signal from Montecito debris flow recorded at the Montecito Station (CI.QAD) has a distinctive waveform characteristic, and its frequency content is bounded within a small bandwidth between 3 – 15 Hz, peaking around 7 Hz in this particular scenario. (Mid panel) Seismic signal recorded at CI.QAD on November 15, 2017 showing glitches which behave as white noise and occupy the whole frequency bandwidth up to Nyquist frequency at 50 Hz. The inset shows the waveform for glitches which has sharp discontinuities and an amplitude increase by 4 orders of magnitude. (Bottom panel) Seismic signal recorded at CI.SBC near Old Santa Barbara Mission, 10 km west of Montecito, on one of the work days with strong anthropogenic signals starting around 8AM local time. In this particular case, the signal occupies the frequency bandwidth around 3 - 30 Hz and can be higher in amplitude depending on the nature of the activity. The signal does not always resemble white noise and hence, the simple detection algorithm we used at Montecito would be insufficient to completely remove the high anthropogenic noise observed in Santa Barbara. The threshold of detection can be adjusted (for instance find anomalous signals in frequency band lower than 25 Hz) but it will trade off with the performance of robustly detecting a debris flow signal.

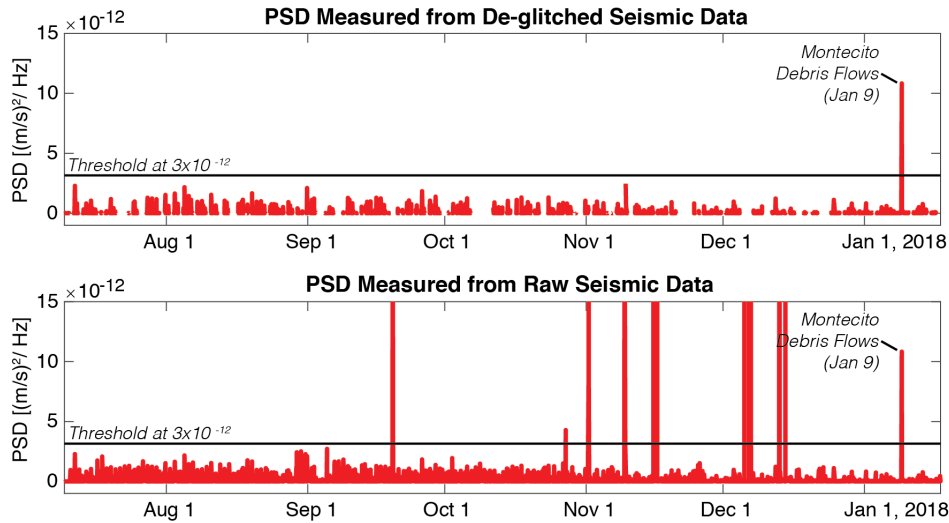


**Figure 3.9:** PSDs measured from deglitched versus raw seismic data. (Top panel) Average PSD over 1-minute intervals using seismic data deglitched with the routine discussed in the supplementary methods section. (Bottom panel) Average PSD over 1-minute intervals using raw seismic data.

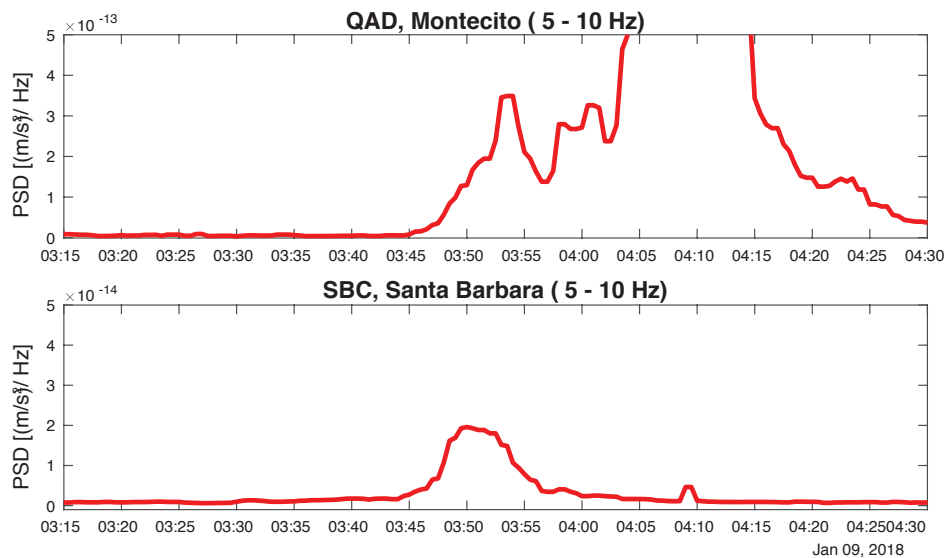


**Figure 3.10:** Mean PSDs averaged over 5-10 Hz observed at station CI.QAD in Montecito and station CI.SBC (located at  $34.44076^{\circ}\text{N}$ ,  $119.71492^{\circ}\text{W}$ ) in Santa Barbara over the 1.25 hours surrounding the Montecito debris flows. The time series for QAD is clipped (see Fig. 3.2b) to highlight the lower amplitude signals before and after the peak signal. Despite the peak PSD for SBC occurring below 5 Hz, signal leaks into the higher 5-10 Hz frequency band, giving a robust signal from 3:48-3:55AM, significantly higher than the short-term background over this time range. Primarily due to the farther distance of SBC to the debris flows, the amplitudes are an order of magnitude smaller than those for QAD (note difference in y-axis scales).

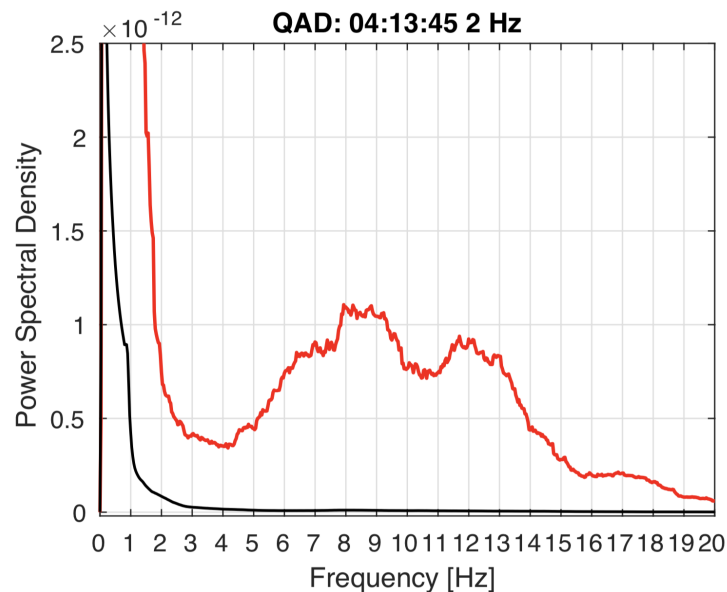


**Figure 3.11:** PSD observed at station CI.QAD at 4:13:45AM, showing that the signal includes significant power above 10 Hz during the later (4:12-4:15AM) time period. The bimodality of the signal may be related to multiple debris flows at different distances relative to the station (e.g. in San Ysidro and Romero Creeks).

### 3.5 Conclusion

We developed a mechanistic model for the high-frequency seismic signature of debris flows. The model suggests that seismic ground motion amplitudes are most sensitive to the product of four physical parameters related to the debris flow: length ( $L$ ) and width ( $W$ ) of the boulder snout, grain size cubed ( $D^3$ ), and average speed cubed ( $u^3$ ). The model also implies that peak frequency of the seismic signal depends on average distance of the debris flow from the instrument. These results have implications for what can be measured robustly with the seismic technique. For example, they suggest that the seismic observables are most sensitive to the largest clasts within the flow and are not directly sensitive to flow thickness except through the expected dependence of average speed on thickness. The results also demonstrate the need for accurate seismic parameter estimates when using the seismic technique. Applying the modeling framework to the Montecito debris flows of 9 January 2018, we find that the average distance to the nearest debris flows can be determined and that estimated grain sizes and flow speeds are consistent with observations. Our work further suggests that seismic networks designed to target debris flow early warning could provide early warning times of up to 10 min for debris flows similar to the ones that produced catastrophic results in Montecito.

### 3.6 Appendix

#### Evaluation of Other Sources of Seismic Energy and Deglitching of Seismic Data

In order to have a robust ground-motion based debris flow early warning system, it is important to be able to discriminate strong debris flows from other environmental sources of ground motion, including strong rain, wind, ocean waves, earthquakes, and anthropogenic cultural noise. In the main text, we demonstrate that early warning for a strong debris flow like what occurred in Montecito could have been declared based on a ground motion threshold of  $6 \times 10^{-12} \text{ (m/s)}^2/\text{Hz}$  averaged over a 5-10 Hz frequency band and averaged over 60 seconds, or equivalently a ground velocity threshold of  $5 \times 10^{-6} \text{ m/s}$  filtered over the same frequency band and with the same averaging time. Here, we demonstrate that other sources of ground motion are not expected to meet this threshold, except possibly under extreme conditions that would be easily identifiable.

Strong rain and wind preceded the debris flows in Montecito, with local precipitation exceeding 2 mm/min and wind speeds exceeding 8 m/s. Despite these anomalously large values, the ground motion during this pre-debris flow time never exceeded an average of  $10^{-13} \text{ (m/s)}^2/\text{Hz}$ . These sources of ground motion can therefore be ruled out. Even during hurricane-force rain and wind, although low-frequency (0.01-0.25 Hz) ground motions can exceed ground motions of over  $10^{-7} \text{ m/s}$  (with peak values of  $3 \times 10^{-7} \text{ m/s}$  during Hurricane Isaac) [29, 30], 5-10 Hz ground motions never exceed  $6 \times 10^{-12} \text{ (m/s)}^2/\text{Hz}$  even during the most intense hours of the hurricane (Figure 3.6), due to the wide area over which this energy is distributed. Ocean waves cause significant ground motions [31, 33], especially during strong storm events, but again the frequency content is typically much lower ( $<1 \text{ Hz}$ ), primarily due to the large distances from the locations where waves are significant [31]. Even for very near coastal stations like the Montecito Station (CI.QAD), which is only a few hundred meters from the coast, the strongest ocean waves cause ground motions of less than -120 dB at 1 Hz, and these ground motions typically decay below anthropogenic levels at higher frequencies [32]. Ground motions often exceed  $10^{-13} \text{ (m/s)}^2/\text{Hz}$  during earthquakes. However, such ground motions are confined to limited times and are usually broadband in frequency. In order for large ground motions to last more than 60 s, the earthquake must be a magnitude 8.0 or greater [26], except under special resonant site conditions, such as in the Valley of the City of Mexico [41]. Earthquakes are also easily distinguished from debris flows by their characteristic sudden onsets, with clear P- and S- waves arriving prior to the main surface waves, as opposed to debris flows which have a characteristic gradual

onset. Frequencies of earthquake ground motions also include lower frequency energy [13]. It should thus be possible to discriminate between earthquakes and debris flows, even in locations where Earth structure is complex.

Perhaps the most challenging hurdle for early warning is large anthropogenic ambient noise sources. Heavy construction and industrial equipment located within a few km of a seismic station are well known to be able to cause 5-10 Hz ambient noise in excess of  $10^{-13}$  (m/s)<sup>2</sup>/Hz [27]. For example, a seismic station in Santa Barbara, CI.SBC, has background noise of this amplitude on weekday work hours between September and November 2017, and could not have been used for debris flow early warning during such times (Figure 3.8). Criteria could be used to reject times with large daily noise fluctuations that are likely to be anthropogenic or, alternatively, such times could be flagged as unsuitable for early warning by local people who would likely be informed of such seismically loud activity. We note that the station CI.QAD in Montecito suffers none of these anthropogenic noise issues over the 188 days of data that are available.

One final problem that affects all seismic data is the occasional presence of glitches, which can be caused by intermittent power failures, network connectivity, and sensor malfunction [27]. Such glitches can look like a strong signal to the casual observer, but are not true signals and must be removed prior to analysis (Figure 3.8). Indeed, station CI.QAD had a series of glitches for which discontinuities in the time series exist, which would have led to false detections had they not been removed (Figure 3.9). Figure 3.2a shows the deglitched data, for which the debris flow detection is robust. Deglitching of the seismic data with a robust automatic algorithm would therefore be important to implementing a debris flow early warning system. In this work, we use a deglitching procedure that takes advantage of the fact that electronic glitches behave like white noise, amplifying all frequencies, not just the 5-10 Hz frequencies that are characteristic of a nearby (<3 km) debris flow event. This deglitching step can be done in real-time as part of the early warning detection, and involves (1) calculating the power spectra at 1-minute intervals, with an overlap of 50%, (2) rejection of data with amplified power above 20 Hz to its Nyquist frequency, and (3) further filtering with a 3-point median filter to remove other glitches less than 30 seconds in duration. Selection of the time window in step 1 is crucial since shorter time windows allow for longer warning times but longer windows result in more robust signal-to-noise criteria. The choice made here may not be optimal for all applications, and we suggest that further analyses should be carried out, based

on criteria such as sampling rate, background noise spectral levels and telemetry consistency to select the most suitable time window. In step 2, power exceeding 3 standard deviations from the average power over the previous 3-5 hours is used as a threshold and glitch times are suppressed from having any detections. Figure 3.9a shows the result of the deglitching routine as compared with the data with glitches (Figure 3.9b).

### **Estimates of Distance, Debris Flow Amplitude and Early Warning Timing, Given Uncertainties in Model Parameters**

Many of the parameters of Equations 3.3 and 3.4 are not well constrained, leading to uncertainties in the final estimates of both source-station distance and debris flow amplitude ( $LWD^3u^3$ ). To constrain the seismic velocity parameters  $\xi$  and  $v_c$  in the Montecito region, we use the P wave scaling relation proposed by Brankman [34] that is generally appropriate for the Ventura Basin area of southern California. This relation has been used in the Southern California Earthquake Center (SCEC) community velocity model (CVM-H 15.1.0) [36] and states that  $v_p = 361z^{0.2944}$ , where  $v_p$  is S wave velocity and  $z$  has been converted to depth in km. This power-law form of  $v_s$  is precisely the form that produces an exact power law for phase velocity as a function of frequency so that applying the formalism in Tsai and Atiganyanun [22] yields  $c = 953f^{0.417}$ , where  $c$  is phase velocity in m/s and  $f$  is frequency in Hz. Thus,  $\xi = 0.417$  and  $v_c = 953$  m/s are our best estimates of the two velocity parameters. Given the uncertainties shown in Figures 3.3 and 3.6 in Brankman [34], we estimate plausible ranges of  $0.35 < \xi < 0.45$ ,  $800 < v < 1200$ . Estimates of  $Q$  are more challenging, but we bound  $Q$  by measurements of  $Q$  in southern California at a range of relevant depths. On the low end, Hauksson et al. [42] found that  $Q$  can be as low as  $25 \pm 10$  at depths down to 1500 m in the Newport-Inglewood Fault Zone in the middle of the Los Angeles Basin. On the high end, Hauksson and Shearer [35] found that  $Q$  in the Santa Barbara-Montecito-Carpinteria area at depths of 1 km have values as low as 53, 98 and 104 interspersed among under-constrained (higher) values. Since Montecito is at the edge of the Ventura Basin, it is unlikely to have shallow  $Q$ 's as low as in the Newport Inglewood Fault Zone nor as high as the 1-km values from Hauksson and Shearer [35]. We therefore assume that  $30 < Q < 60$ , with  $Q=45$  being our preferred value. Assuming uncertainties on  $\xi$ ,  $v_c$  and  $Q$  are independent, uncertainties on  $Q$  dominate and lead to a factor of 2 uncertainty in source-station distance and approximately a factor of 20 uncertainty in the product  $LWD^3u^3$ . It is clear that estimates of source-station distance and

of other debris flow parameters could be significantly improved if estimates of the seismic parameters were better. Finally, we note that given estimated parameters, station CI.SBC's distance of 5.5-11 km from the Montecito debris flows implies peak frequencies of 1-3 Hz, significantly overlapping with other ambient seismic noise sources as described in subsection above, and peak amplitudes that are an order of magnitude lower than those for station CI.QAD in Montecito. Observed power at CI.SBC is consistent with these predictions, with clear signal peaking below 5 Hz but leaking into the 5-10 Hz frequency band during the earliest times (see Figure 3.10). Conversely, at late times (4:12-4:15AM) on station CI.QAD, there is significant energy above 10 Hz, suggesting very nearby sources of debris flow energy (see Figure. 3.11).

Early warning time is estimated for the observed data based on a detection distance of 1540 m. For a location 600 m upstream of the station, and an assumed flow speed of 2.4 m/s, this would provide 390 seconds, or 6.5 minutes, of early warning time. For the same detection distance, but with a station located at the edge of the city, then this 1540 m would provide 640 seconds, or 10.7 minutes, of early warning time for the entire city and an extra minute of warning for every 144 m farther upstream the station is placed. For a location 1 km downstream of this point, there would be 17 minutes of early warning time. Site-specific calibration of the parameters of Equation 3.1 would reduce uncertainties in both estimated distances and estimates of the product  $LWD^3u^3$ , and we suggest that such calibration be done for any future debris flow early warning site. We also note that the Montecito seismometer was not located with debris flow early warning in mind, and so was not optimally located. Including data transmission and processing time (5 s) and an averaging time of 60 s reduces the early warning times described above by 65 s. Accounting for this 65 s of reduced early warning time, a station would need to be placed 60 m upstream of the city border to provide the entire city with 10 minutes of early warning.

### 3.7 Acknowledgements

The authors thank three anonymous reviewers for comments. Funding was provided by the U.S. National Science Foundation EAR-1558479 to V.C.T. and M.P.L. and EAR-1346115 to M.P.L. A.R.B. acknowledges support from the Swiss National Science Foundation. V.H.L. processed the seismic data, V.C.T. designed the model, M.P.L. analyzed the geomorphic data, T.P.U. measured the geographical data, and A.R.B. measured boulder data. V.C.T. and M.P.L. wrote the paper, with editorial contributions from all authors. All authors contributed to the interpretation of re-

sults. All waveform data were accessed through the Southern California Earthquake Data Center (SCEDC) at Caltech, <https://doi.org/10.7909/C3WD3xH1>.

## References

- [1] R. M. Iverson. The physics of debris flows. *Reviews of geophysics*, 35(3): 245–296, 1997.
- [2] S. H. Cannon. Debris-flow generation from recently burned watersheds. *Environmental & Engineering Geoscience*, 7(4):321–341, 2001.
- [3] J. W. Kean, D. M. Staley, and S. H. Cannon. In situ measurements of post-fire debris flows in southern California: Comparisons of the timing and magnitude of 24 debris-flow events with rainfall and soil moisture conditions. *Journal of Geophysical Research: Earth Surface*, 116(F4), 2011.
- [4] J. A. Coe, J. W. Kean, J. W. Godt, R. L. Baum, E. S. Jones, D. J. Gochis, and G. S. Anderson. New insights into debris-flow hazards from an extraordinary event in the Colorado Front Range. *GSA Today*, 24(10):4–10, 2014.
- [5] T. Takahashi. Debris flow: Mechanics. *Prediction and*, 2007.
- [6] J. Stock and W. E. Dietrich. Valley incision by debris flows: Evidence of a topographic signature. *Water Resources Research*, 39(4), 2003.
- [7] M. Arattano. On the use of seismic detectors as monitoring and warning systems for debris flows. *Natural Hazards*, 20(2-3):197–213, 1999.
- [8] A. Burtin, N. Hovius, B. W. McArdell, J. M. Turowski, and J. Vergne. Seismic constraints on dynamic links between geomorphic processes and routing of sediment in a steep mountain catchment. *Earth Surface Dynamics*, 2(1):21–33, 2014.
- [9] A. Schimmel and J. Hübl. Approach for an early warning system for debris flow based on acoustic signals. In *Engineering Geology for Society and Territory-Volume 3*, pages 55–58. Springer, 2015.
- [10] A. Schimmel and J. Hübl. Automatic detection of debris flows and debris floods based on a combination of infrasound and seismic signals. *Landslides*, 13(5):1181–1196, 2016.
- [11] L. Turconi, V. Coviello, M. Arattano, G. Savio, and D. Tropeano. Monitoring mud-flows for investigative and warning purposes: The instrumented catchment of Rio Marderello (north-western Italy). In *Engineering Geology for Society and Territory-Volume 3*, pages 85–90. Springer, 2015.
- [12] F. Walter, A. Burtin, B. W. McArdell, N. Hovius, B. Weder, and J. M. Turowski. Testing seismic amplitude source location for fast debris-flow detection at

- Illgraben, Switzerland. *Natural Hazards and Earth System Sciences*, 17(6): 939–955, 2017.
- [13] A. Burtin, N. Hovius, D. T. Milodowski, Y.-G. Chen, Y.-M. Wu, C.-W. Lin, H. Chen, R. Emberson, and P.-L. Leu. Continuous catchment-scale monitoring of geomorphic processes with a 2-D seismological array. *Journal of Geophysical Research: Earth Surface*, 118(3):1956–1974, 2013.
- [14] F. Gimbert, V. C. Tsai, and M. P. Lamb. A physical model for seismic noise generation by turbulent flow in rivers. *Journal of Geophysical Research: Earth Surface*, 119(10):2209–2238, 2014.
- [15] H. Kanamori and J. W. Given. Analysis of long-period seismic waves excited by the May 18, 1980, eruption of Mount St. Helens—A terrestrial monopole? *Journal of Geophysical Research: Solid Earth*, 87(B7):5422–5432, 1982.
- [16] H. Kawakatsu. Centroid single force inversion of seismic waves generated by landslides. *Journal of Geophysical Research: Solid Earth*, 94(B9):12363–12374, 1989.
- [17] J. W. Kean, J. A. Coe, V. Coviello, J. B. Smith, S. W. McCoy, and M. Aratano. Estimating rates of debris flow entrainment from ground vibrations. *Geophysical Research Letters*, 42(15):6365–6372, 2015.
- [18] V. C. Tsai, B. Minchew, M. P. Lamb, and J.-P. Ampuero. A physical model for seismic noise generation from sediment transport in rivers. *Geophysical Research Letters*, 39(2), 2012.
- [19] S. H. Cannon, E. M. Boldt, J. L. Laber, J. W. Kean, and D. M. Staley. Rainfall intensity-duration thresholds for postfire debris-flow emergency-response planning. *Natural Hazards*, 59(1):209–236, 2011.
- [20] NOAA-USGS Debris Flow Task Force. NOAA-USGS debris-flow warning system. *Final report: US Geological Survey Circular*, 1283, 2005.
- [21] M. Farin, A. Mangeney, R. Toussaint, J. de Rosny, N. Shapiro, T. Dewez, C. Hibert, C. Mathon, O. Sedan, and F. Berger. Characterization of rockfalls from seismic signal: Insights from laboratory experiments. *Journal of Geophysical Research: Solid Earth*, 120(10):7102–7137, 2015.
- [22] V. C. Tsai and S. Atigyanun. Green’s functions for surface waves in a generic velocity structure. *Bulletin of the Seismological Society of America*, 104(5): 2573–2578, 2014.
- [23] R. A. DiBiase, M. P. Lamb, V. Ganti, and A. M. Booth. Slope, grain size, and roughness controls on dry sediment transport and storage on steep hill slopes. *Journal of Geophysical Research: Earth Surface*, 122(4):941–960, 2017.

- [24] M. P. Lamb, J. S. Scheingross, W. H. Amidon, E. Swanson, and A. Limaye. A model for fire-induced sediment yield by dry ravel in steep landscapes. *Journal of Geophysical Research: Earth Surface*, 116(F3), 2011.
- [25] I. Stubailo, M. Watkins, A. Devora, R. J. Bhadha, E. Hauksson, and V. I. Thomas. Data delivery latency improvements and first steps towards the distributed computing of the Caltech/USGS Southern California seismic network earthquake early warning system. In *AGU Fall Meeting Abstracts*, 2016.
- [26] Z. Duputel, V. C. Tsai, L. Rivera, and H. Kanamori. Using centroid time-delays to characterize source durations and identify earthquakes with unique characteristics. *Earth and Planetary Science Letters*, 374:92–100, 2013.
- [27] D. E. McNamara and R. P. Buland. Ambient noise levels in the continental United States. *Bulletin of the seismological society of America*, 94(4):1517–1527, 2004.
- [28] A. Burtin, L. Bollinger, J. Vergne, R. Cattin, and J. L. Nábělek. Spectral analysis of seismic noise induced by rivers: A new tool to monitor spatiotemporal changes in stream hydrodynamics. *Journal of Geophysical Research: Solid Earth*, 113(B5), 2008.
- [29] T. Tanimoto and A. Lamontagne. Temporal and spatial evolution of an on-land hurricane observed by seismic data. *Geophysical Research Letters*, 41(21): 7532–7538, 2014.
- [30] T. Tanimoto and A. Valovcin. Stochastic excitation of seismic waves by a hurricane. *Journal of Geophysical Research: Solid Earth*, 120(11):7713–7728, 2015.
- [31] F. Ardhuin, L. Gualtieri, and E. Stutzmann. How ocean waves rock the Earth: Two mechanisms explain microseisms with periods 3 to 300 s. *Geophysical Research Letters*, 42(3):765–772, 2015.
- [32] F. Gimbert and V. C. Tsai. Predicting short-period, wind-wave-generated seismic noise in coastal regions. *Earth and Planetary Science Letters*, 426: 280–292, 2015.
- [33] M. S. Longuet-Higgins. A theory of the origin of microseisms. *Philosophical Transactions of the Royal Society of London. Series A, Mathematical and Physical Sciences*, 243(857):1–35, 1950.
- [34] C. M. Brankman. *Three-dimensional structure of the western Los Angeles and Ventura basins, and implications for regional earthquake hazards*. Harvard University, 2009.
- [35] E. Hauksson and P. M. Shearer. Attenuation models ( $Q_p$  and  $Q_s$ ) in three dimensions of the southern California crust: Inferred fluid saturation at seismogenic depths. *Journal of Geophysical Research: Solid Earth*, 111(B5), 2006.

- [36] J. H. Shaw, A. Plesch, C. Tape, M. P. Suess, T. H. Jordan, G. Ely, E. Hauksson, J. Tromp, T. Tanimoto, R. Graves, et al. Unified structural representation of the southern California crust and upper mantle. *Earth and Planetary Science Letters*, 415:1–15, 2015.
- [37] B. Schmandt, R. C. Aster, D. Scherler, V. C. Tsai, and K. Karlstrom. Multiple fluvial processes detected by riverside seismic and infrasound monitoring of a controlled flood in the Grand Canyon. *Geophysical Research Letters*, 40(18): 4858–4863, 2013.
- [38] P. Gasparini, G. Manfredi, and J. Zschau. *Earthquake early warning systems*. Springer, 2007.
- [39] D. D. Given, E. S. Cochran, T. Heaton, E. Hauksson, R. Allen, P. Hellweg, J. Vidale, and P. Bodin. Technical implementation plan for the ShakeAlert production system: An earthquake early warning system for the west coast of the United States. Technical report, US Geological Survey, 2014.
- [40] J. D. Goltz. Introducing earthquake early warning in California: A summary of social science and public policy issues. *Caltech Seismological Laboratory, Disaster Assistance Division, A report to OES and the Operational Areas*, 2002.
- [41] V. M. Cruz-Atienza, J. Tago, J. D. Sanabria-Gómez, E. Chaljub, V. Etienne, J. Virieux, and L. Quintanar. Long duration of ground motion in the paradigmatic valley of Mexico. *Scientific Reports*, 6:38807, 2016.
- [42] E. Hauksson, T.-L. Teng, and T. L. Henyey. Results from a 1500 m deep, three-level downhole seismometer array: site response, low Q values, and f max. *Bulletin of the Seismological Society of America*, 77(6):1883–1904, 1987.

*Chapter 4***SHALLOW ATTENUATION AND SCATTERING KEY TO  
IMPROVED PREDICTION OF SHAKING DURATION IN THE  
LOS ANGELES BASIN****4.1 Abstract**

Ground motions in the Los Angeles Basin during large earthquakes are modulated by earthquake ruptures, path effects into the basin, basin effect and local site response. In this study, we analyze the direct effect of shallow basin structures on ground motion intensity and shaking duration at a period of 2 - 20 seconds in the Los Angeles region through modeling and dense array analysis of small magnitude, shallow and deep earthquake pairs. We observe that the source depth modulates the basin response, in particular the shaking duration, and the basin response is a function of path effect and not site condition. Three-dimensional simulations using the CVM-S4.26.M01 velocity model show good waveform fitting to the direct arrivals at periods of 5 seconds and longer, but fail to predict the long shaking duration from strong surface waves and late coda waves that occurs for shallow events. We find that a higher quality factor than traditionally assumed produces synthetics with longer durations; however, they are still unable to accurately match the amplitude and phasing of the shorter period surface waves. Beam-forming analysis using dense array data reveals that the long duration surface waves have the same back-azimuth as the direct arrivals and are generated at the basin edges, while later coda waves are scattered from off-azimuth directions, with potential scatterers such as sharp boundaries offshore. Improving the description of these shallow basin structures and edges, and the shallow attenuation model will enhance our overall capability to predict ground motions in future earthquakes.

**4.2 Introduction**

Understanding the effects of sedimentary basins on ground motion is important in reducing earthquake hazard risks for many metropolitan areas such as Los Angeles. Poorly-consolidated sediments within the basin amplifies ground motion, which can be particularly severe and localized near basin edges due strong constructive interference of seismic waves such as observed during the 1994 Northridge and 1996 Kobe Earthquakes [1, 2]. In addition, basin structures can prolong the duration of

strong shaking. Notably, the M8.1 1985 Michoacán earthquake, despite occurring more than 450 km away, caused an unusually long duration of long-period shaking and resulted in considerable damage and casualties in Mexico City which is situated on top of a lake-bed basin. Kawase and Aki [3] first suggested the distinction in the mechanisms on how basins cause ground motion amplification and long duration by showing that the prolonged shaking in Mexico City is caused by the interaction of soft-surface layer within a deeper basin (type-II basin) beneath the city and not by surface wave reverberation within the basin. Similarly, within the Los Angeles Basin, Saikia et al. [4] proposed that the presence of multiple low-velocity pockets within the basin can trap and delay the surface seismic waves propagating through them, allowing the seismic energy to appear at a later time and cause extensive significant shaking. In recent years, other ideas have also been proposed to explain these prolonged shaking durations including a combination of basin reflections and mountain refractions [5] and surface wave overtones excited at the basin edge [6, 7]. The high density of stations in Kanto Basin, Japan allowed Boué et al. [6] to use ambient seismic field measurements to reconstruct the wavefield propagating across the basin, further highlighting the role of basin edges in exciting higher mode surface waves. However, the mechanisms behind prolonged duration observed in Los Angeles Basin remains difficult to investigate without a highly instrumented basin that can adequately capture the seismic wavefield.

Nonetheless, the development of high resolution 3D velocity models with details on the sedimentary basin structures, combined with numerical modelling techniques that are capable of simulating waveforms accurately down to 1 second period, allows us to simulate and predict the effects of the basin structure on ground motion, particularly on the amplification factor. For Southern California, two Southern California Earthquake Center (SCEC) Community Velocity Models (CVM), which are CVM-S4.26.M01 [8] and CVM-H 15.1.0 [9], are commonly used in ground motion studies. In CVM-S4.26, the initial basin structure is constrained using a rule-based seismic velocity model, derived primarily from well log data [10], where  $V_p$  is a function of sediment age and depth. In CVM-H, basin structures are determined from sonic logs and seismic reflection profiles collected by the petroleum industry [11], with an added high-resolution geotechnical layer (GTL) based on  $V_s30$  measurements [12] to better describe the top 1 km. The models are further refined using tomographic inversions with a variety of data sets including earthquakes, ambient noise correlation, seismic reflection profiles and receiver functions. Based on these high resolution models, ground motion simulations based on scenario

earthquakes, such as TeraShake and recent CyberShake runs, are able to capture the significant influence of the basin structure in amplification and waveguide channeling [13, 14]. In particular, shallow surface rupture from hypothetical M7+ events along the San Andreas Fault can cause strong ground motion within the greater Los Angeles area and unusually high amplifications near the Whittier Narrows region, highlighting the importance of understanding the effects of shallow structures on ground motion. To validate the accuracy of the CVMs, forward simulations of recorded earthquake events have been performed [15, 16], and the models are assessed based on the prediction capability of the observed ground motions with the emphasis on the amplification of ground motion.

Accurate prediction of ground motion, particularly a potential large earthquake such as a San Andreas-type rupture, depends on several important factors including earthquake source magnitude and rupture length, path effects into the Los Angeles Basin, and the local basin effects. There have been several studies focusing on the effect of basin depth (e.g., [17, 18] and surface wave direction [19] on ground motion site amplification, yet the direct effect of earthquake depths on basin response, both amplitude and duration, remains unclear. In this study, we show that shallow earthquakes preferentially amplify ground motion intensity and duration at longer period (2 - 20 seconds) in the Los Angeles region. Through studying local, small magnitude earthquakes using numerical simulations and dense array techniques, we show the importance of better imaging shallow basin structures and sharp boundaries in 3D velocity models to accurately predict the long shaking duration.

### **4.3 Observations**

To study the direct response of earthquake depth on ground motion in basins, we chose two pairs of local earthquakes close to the basin edge that have similar magnitudes but at different depths (Figure 4.1). The first pair is the shallow 2014 Mw4.40 (3.5 km) and deep 2009 Mw4.32 (15 km) Fontana event pair, which sample both the Los Angeles and San Gabriel basin. The second pair is the 2012 Mw3.21 Beverly Hills (1.5 km) and 2017 Mw3.54 Westwood (9.0 km) event pair which is located at the northern end of the Los Angeles basin. The focal mechanisms and depths of the earthquakes are constrained using Cut-and-Paste (CAP) moment tensor inversion method [20, 21], and we utilize a grid search approach that minimizes the waveform misfit to find the best focal depth. For the Fontana event pair, we use the moment tensor solutions and depths determined by Lui et al. [22] which are used extensively in their study on rapid assessment of earthquake source properties. For

the Beverly Hills and Westwood event pair, due to the smaller magnitude, 3D Green's functions from the CVMs are used in the moment tensor inversion to improve the fitting of waveforms at 5.5 – 12.5 seconds particularly for stations within the basin [23, 24]. The depths for the Beverly Hills and Westwood event pair determined from our grid-search, 1.5 km and 9.0 km respectively (Figure 4.2), are similar to those relocated using waveform cross-correlation, 3.5 km and 9.8 km respectively [25].

Direct comparison of the waveforms reveals that earthquake depth has a significant influence on shaking duration. Despite a smaller magnitude, the shallow 2012 M3.2 Beverly Hills event shows stronger and longer shaking for stations within the LA Basin compared to the similarly located, but deeper M3.5 Westwood event at periods of 2 - 20 seconds. This major contrast in shaking duration is observed in all components (Figure 4.3 - tangential; Figure 4.4 - radial; Figure 4.5 - vertical). A similar phenomenon is observed for the Fontana event pair, which share the same magnitude and focal mechanism (4.6). Additionally, the similarity in waveform between the aftershocks and associated mainshocks for the Fontana events further confirm that the elongated shaking seen more prominently in shallow earthquakes is not due to source complexity, but is rather the effect of shallow velocity structure (Figure 4.6). Site conditions can affect the amplitude of the ground motion observed, where soft site shakes more strongly than hard rock site. However, we observe stations with different site classifications recording similarly long shaking durations for the shallow earthquakes and not for the deep earthquakes (Figure 4.7). This points to the role of common path, and not individual site effect in the generation of long shaking. Response from local shallow earthquakes is a proxy to shallow rupture from large, faraway earthquakes and here we show that the earthquake depth strongly modulates the waveform amplitude and shaking duration in the Los Angeles basin.

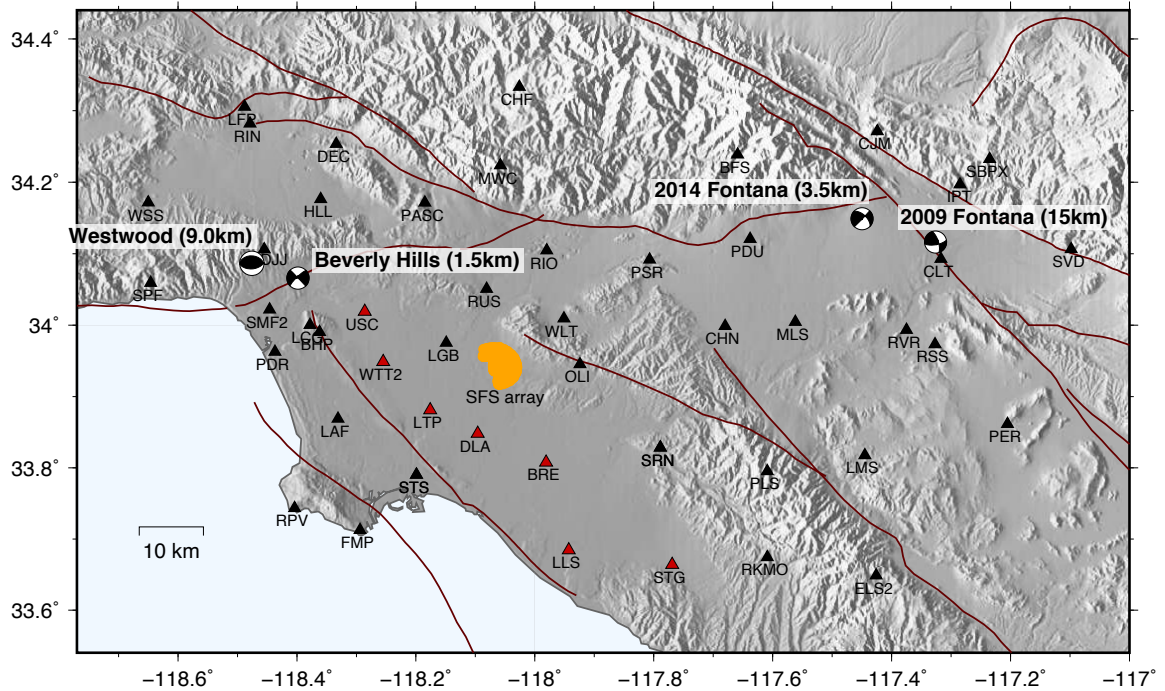


**Figure 4.1:** Map showing the location of two event pairs, i.e. 2017 Mw3.54 Westwood and 2012 Mw3.21 Beverly Hills events directly sampling the Los Angeles Basin and M4.4 Fontana event pair, at the depth of 3.5 km and 15 km, covering the San Bernardino - Los Angeles corridor. Broadband stations from Southern California Seismic Network (SCSN) are shown in black triangles. The extent of the temporary deployment of Santa Fe Springs (SFS) dense array is shown in orange. Red lines delineate known regional faults.

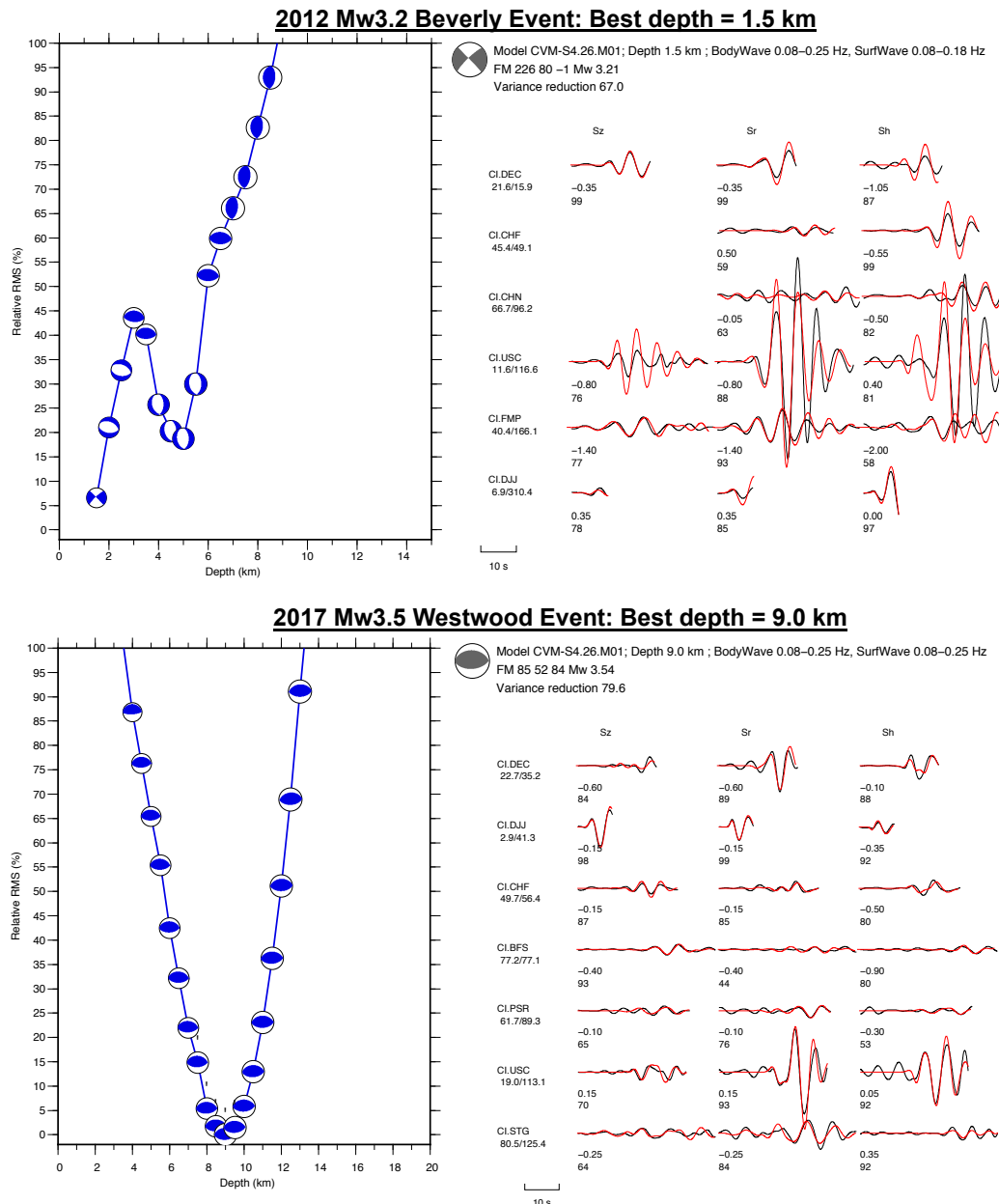


**Figure 4.2:** Cut-and-paste (CAP) method using green functions generated from 3D velocity models allows the characterization of moment tensors for events typically deemed too weak in magnitude. Top panel shows the inversion result for different depths for 2012 Beverly event and the waveform fitting for the best depth of 1.5 km, indicated by the smallest RMS value, is shown on the right. The waveform used are long period surface wave at 0.08 - 0.18 Hz. Bottom panel shows the inversion result for the 2017 Westwood event, where the best-fitting depth is 9.0 km. The waveforms used are long period surface waves at 0.08 - 0.25 Hz.

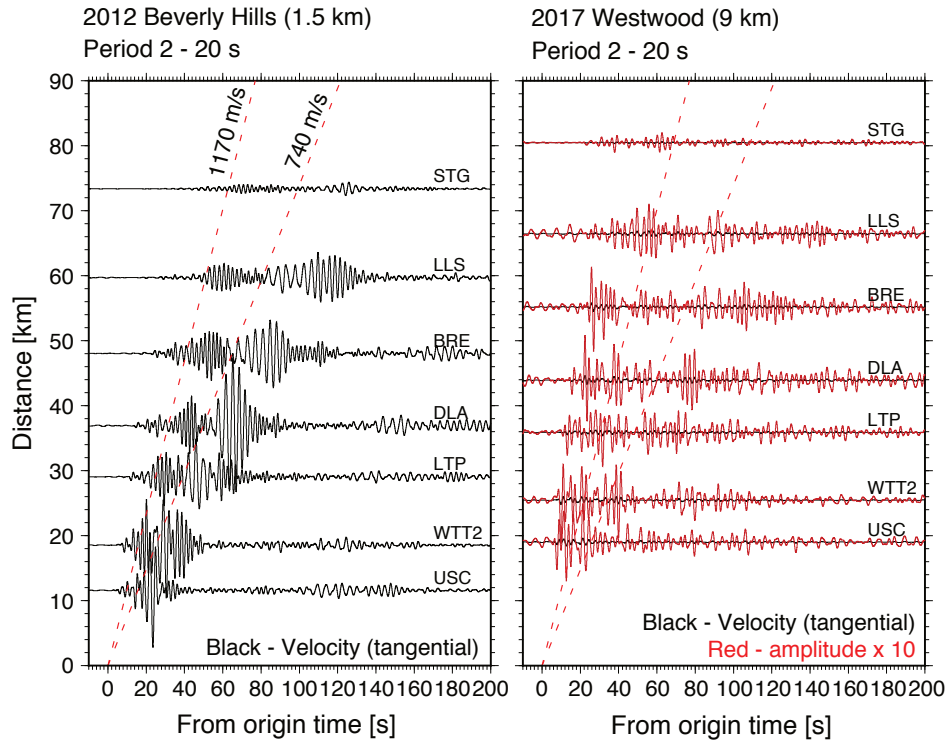


**Figure 4.3:** Record section of velocity in tangential component plotted at absolute amplitude for period 2-20 seconds for 2012 Beverly Hills and 2017 Westwood events. To emphasize that the amplitude for waveforms recorded in 2017 Westwood event is significantly weaker, the waveforms are plotted in black for absolute amplitude and in red for amplitude multiplied by ten. The arrival of initial surface waves and later strong prolonged shaking, traveling at 1170 m/s and 740 m/s, are indicated by the dashed red lines. The stations are located within the main Los Angeles basin, marked in red in Figure 4.1.

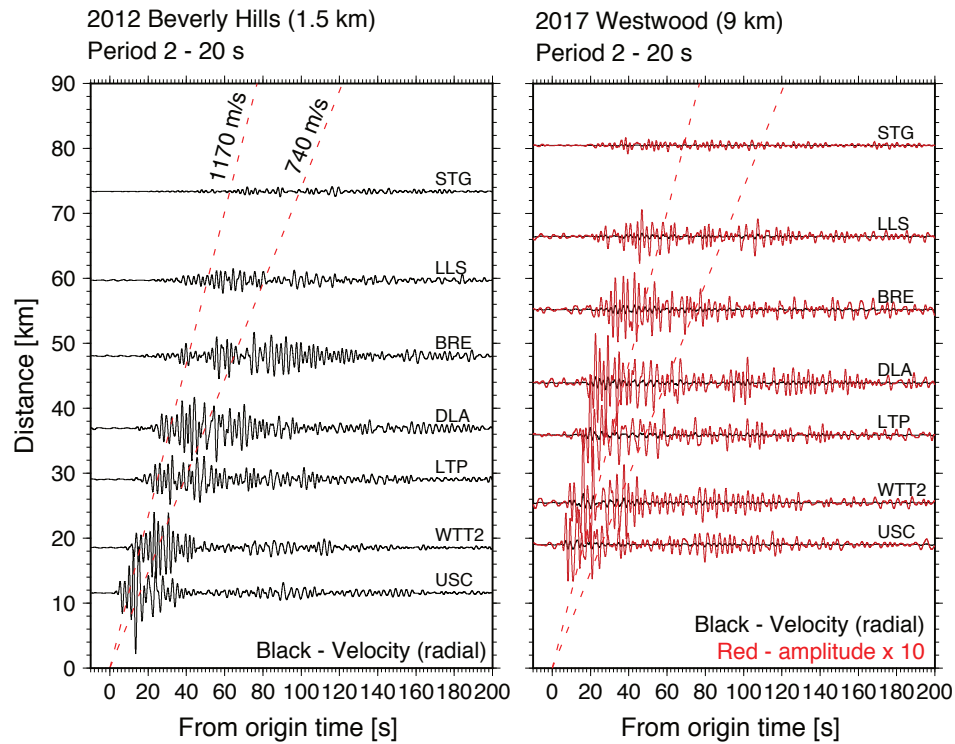


**Figure 4.4:** Similar to 4.3, but for velocity in radial component.

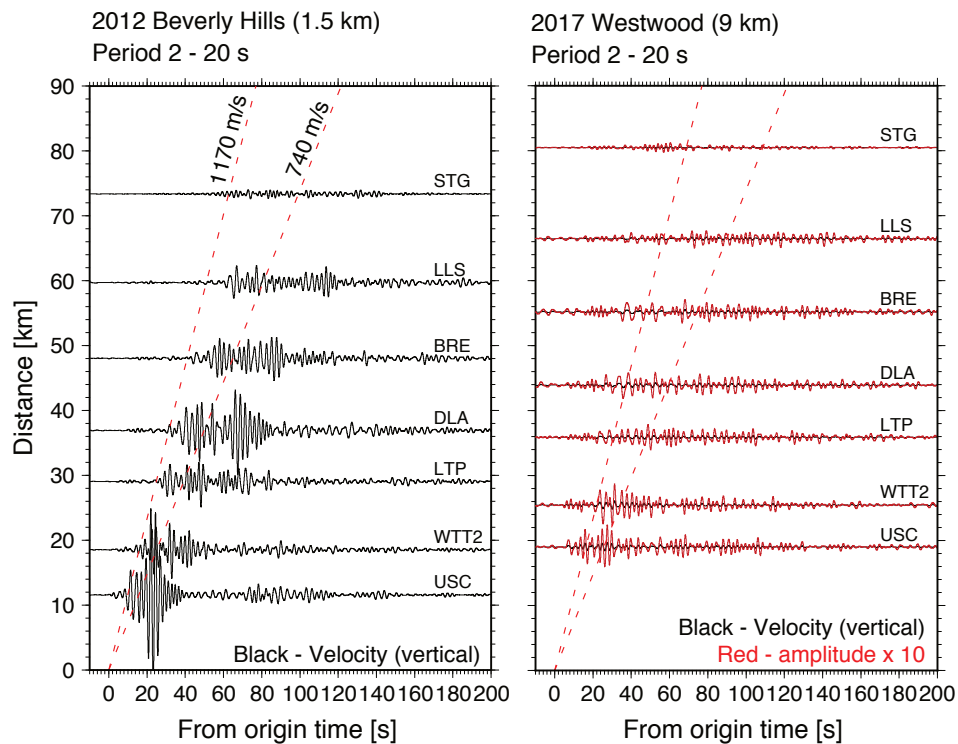


**Figure 4.5:** Similar to 4.3, but for velocity in vertical component.

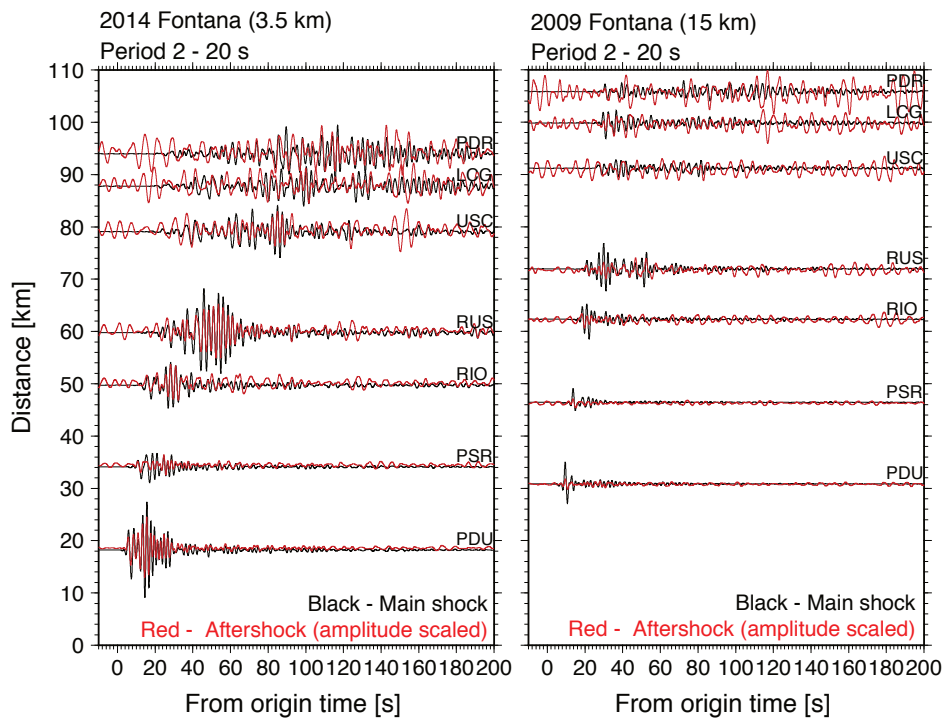


**Figure 4.6:** Record section of the tangential velocity for M4 Fontana earthquake pairs (in black) and their respective M3 aftershocks (in red and scaled with a constant). The station profile starts from northern edge of San Gabriel basin into Los Angeles basin across Whittier Narrows and ends at the coast.

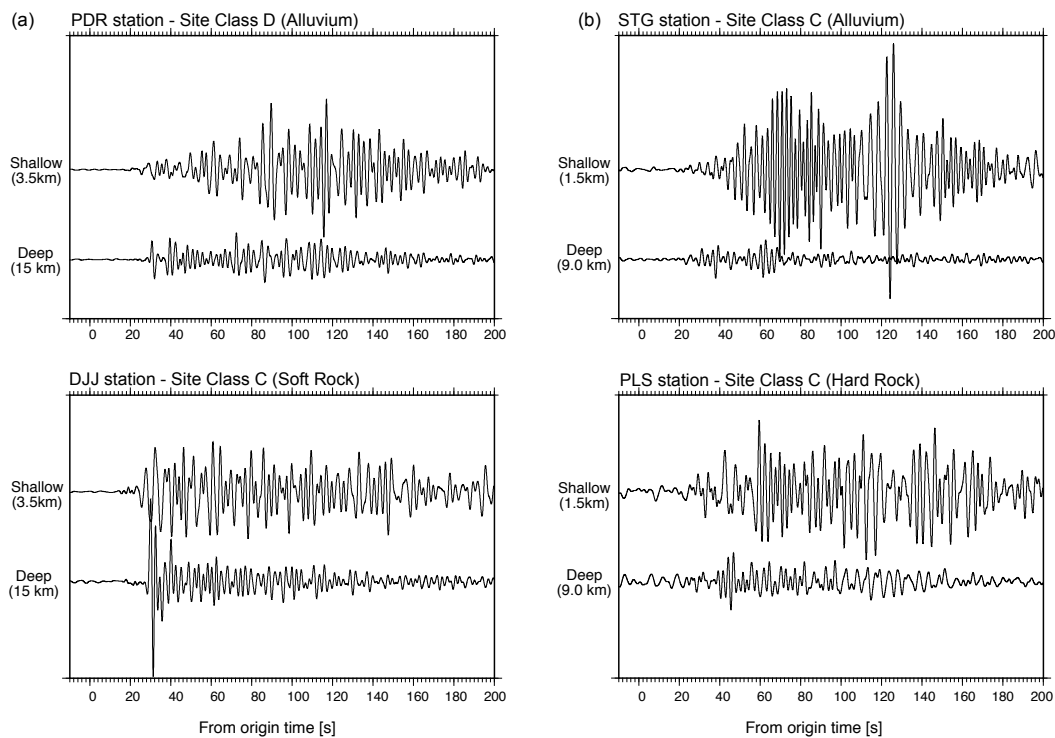


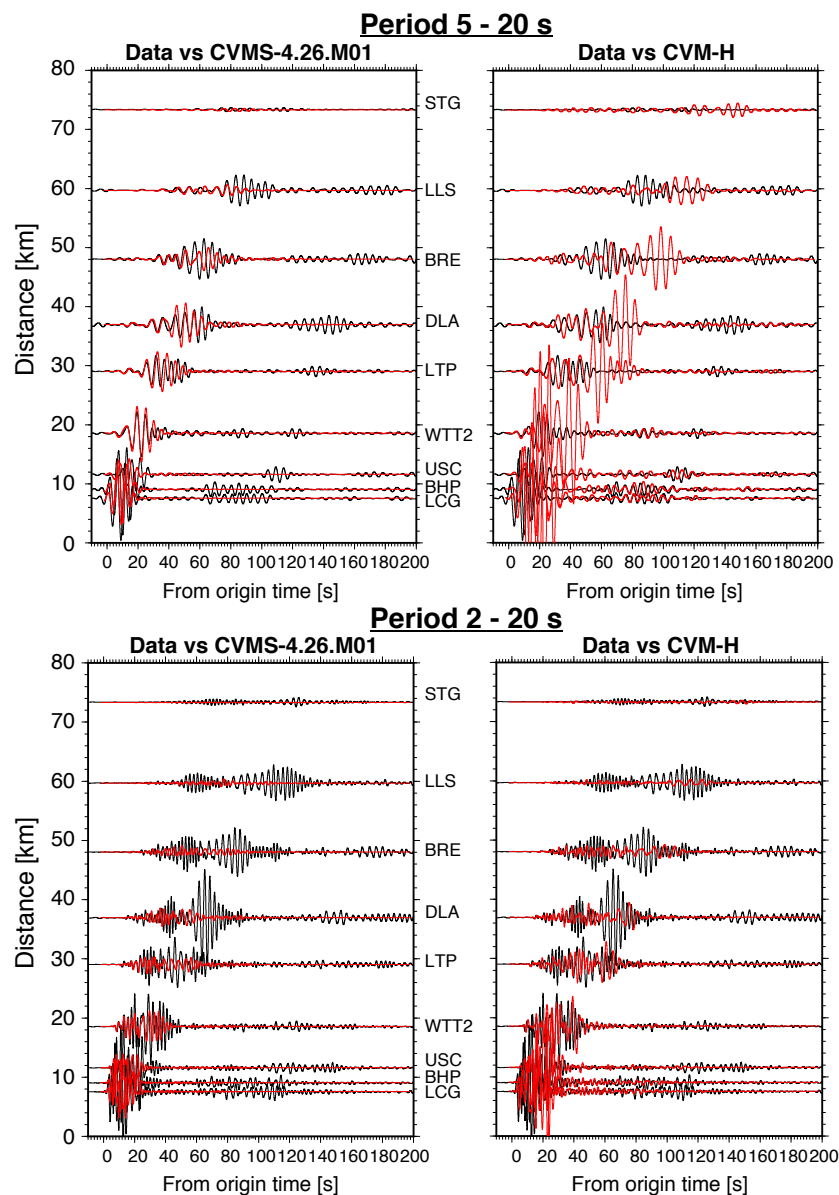
**Figure 4.7:** (a) Seismograms from the Fontana event pair at PDR station (top) and DJJ station (bottom) which are about 100 km away from the epicenter. Seismograms within each panel (i.e. for individual station) are plotted with the same scaling. Although DJJ station is located on soft rock and has a lower amplitude overall, the seismogram from the shallow event exhibits longer significant shaking compared to PDR, a station in the Los Angeles Basin, showing the importance of the path, not site condition, in generating long duration. (b) The same long significant shaking is observed in the Beverly Hills and Westwood event pair at both STG station (top) and PLS station (bottom), located 80 – 85 km away, despite different site conditions.

#### 4.4 Results from 3D Simulations

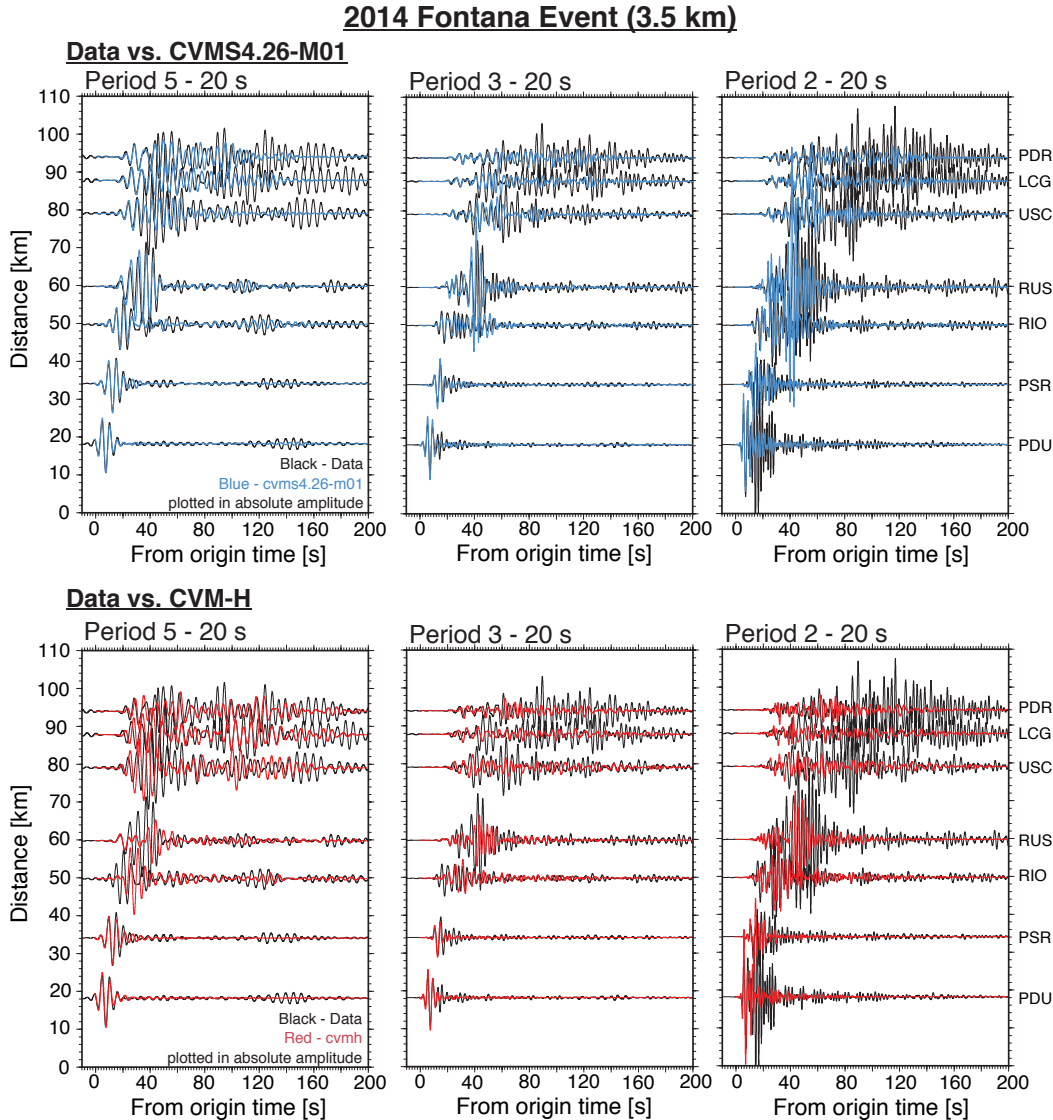
The prolonged shaking at period of 2 – 5 seconds can adversely affect tall buildings, bridges, and large-capacity storage tanks in Los Angeles area as it is within their dominant response [26]. As physics-based ground motion simulations are used more routinely in ground motion hazard analysis, it is vital to validate the performance of widely used 3-D velocity models CVM-H 15.1.0 and CVM-S4.26.M01 velocity models in terms of predicting the shaking duration. These models are considered to be sufficiently good representation of the subsurface structure for at least period longer than 5 seconds [16]. We focus on modeling the shallow Beverly Hills earthquake as its travel path only samples the Los Angeles Basin whose edges and shape are better described due to extensive borehole, seismic reflection and geologic investigations [9, 10, 27]. The small magnitude of the earthquake means it can be treated as point source for the period bandwidth we are investigating. Using the 3-D finite difference method [28], synthetics accurate up to 1 second are generated for the 3-D models with a minimum shear wave velocity ( $V_s$ ) set at 500 m/s with a 100 m spacing. Anelastic attenuation was modeled using the relations  $Q_s = 50V_s$  ( $V_s$  in km/s) and  $Q_p = 2Q_s$ , which are used in several previous simulations (e.g. [2, 13]). Taking the quality factor as a function of shear velocity accounts for the different attenuation behavior between basin and bedrock where basins generally have lower  $V_s$  and hence lower  $Q_s$  due to the presence of unconsolidated material [29].

Figure 4.8 compares synthetics for both CVMs with the observations in two bandwidths: 5 - 20 seconds and 2 - 20 seconds. At a period of 5 seconds, the CVM-S4.26 model fits the initial portion of the waveform shape better than CVM-H 15.1.0, in terms of absolute amplitude and period. The synthetics for CVM-H15.1.0 do produce a large amplitude late arriving wave packet that shares some similarities with the observations; however, the synthetics are larger in amplitude and arrive later than the observed waveforms. This suggests that CVM-H 15.1.0 has the appropriate structural configuration to produce these late arrivals (e.g. sharp basin edge), although the average near surface velocities are likely too low. At period of 2 seconds, both models are not able to reproduce the later arriving phases, although CVM-S4.26.M01 fits the first several tens of seconds better (Figure 4.8). CVM-S4.26.M01 also performs better for the Fontana event including fitting the first several tens of seconds at period up to 2 seconds for both shallow and deep events and also reproducing the unusually large ground motions at station RUS, which is located at Whittier Narrows region (Figure 4.9 and 4.10). Our results are consistent with Taborda et al. [16], who performed simulations for 30 moderate local events

and found that CVM-S4.26.M01 produces a consistently higher goodness-of-fit compared to CVM-H15.1.0 at longer periods.



**Figure 4.8:** Record sections showing the comparison between 3-D synthetics (in red) generated from CVM-S4.26.M01 (left column) and CVM-H (Right column) and data (in black) for 2012 M3.2 Beverly Hills event filtered at two different period ranges, 5 - 20 seconds and 2 - 20 seconds. Both data and synthetics are tangential velocity waveforms, plotted in absolute amplitude. The stations are located within the Los Angeles Basin, trending northwest-southeast. The attenuation scaling used to generate the synthetics is  $Q_s = 50V_s$ .



**Figure 4.9:** Record sections showing the comparison between 3D synthetics generated from CVM-S4.26.M01 (top panel in blue) and CVM-H (bottom panel in red), and data (in black) for the shallow M4.4 Fontana event, filtered at three different period ranges, which are 5 - 20 seconds, 3 - 20 seconds and 2 - 20 seconds. The data and synthetics are tangential velocity waveforms, plotted in absolute amplitude. The station profile starts from northern edge of San Gabriel basin into Los Angeles basin across Whittier Narrows and ends at the coast (station PDR). CVM-S.4.26.M01 fits the waveform data better than CVM-H, particularly at the first several tens of seconds at period up to 2 seconds and also reproduces well the unusually large ground motions at anomalous stations like RUS which is located at Whittier Narrows region. A similar comparison for the deep Fontana event is in Figure 4.10.

### 2009 Fontana Event (15 km)

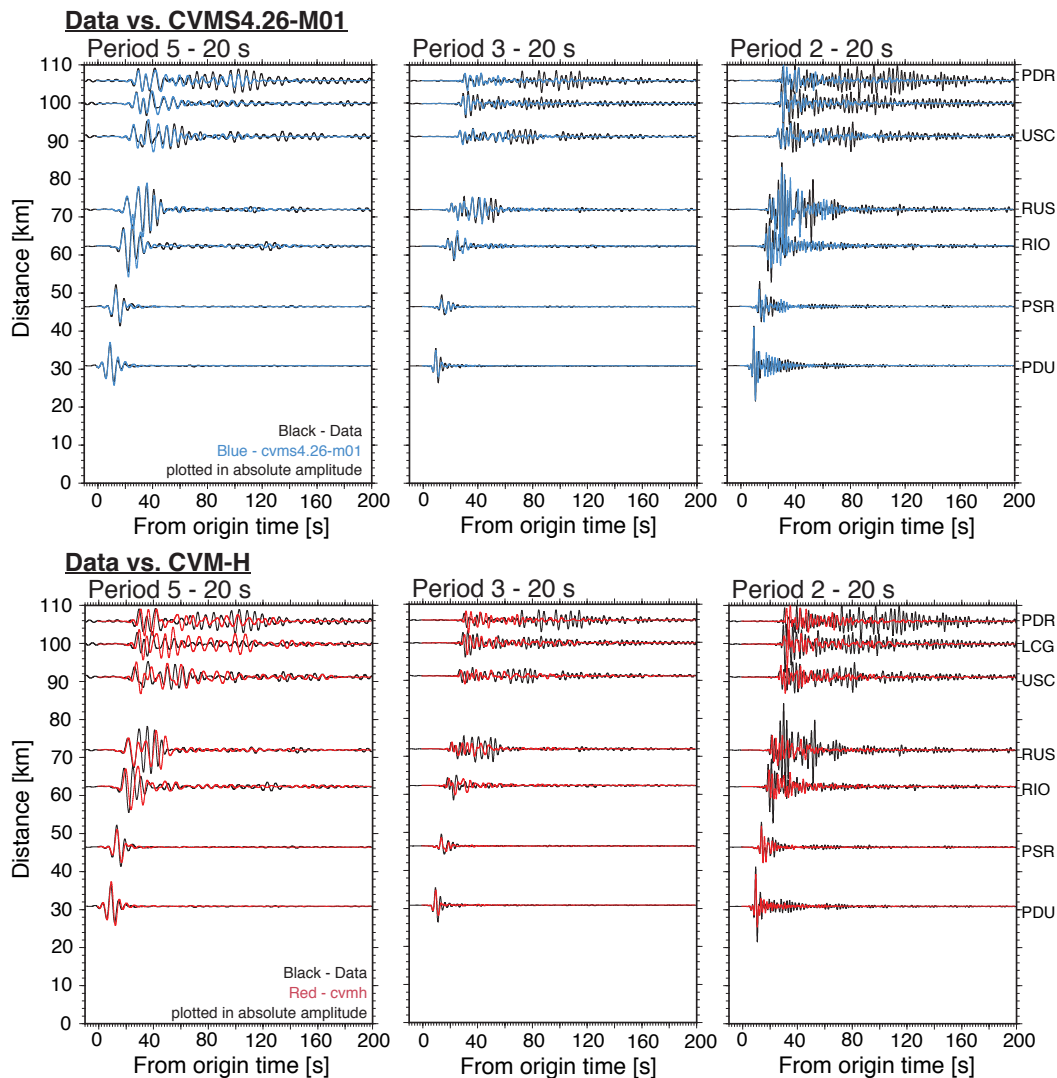


**Figure 4.10:** Similar to Figure 4.9, record sections show the comparison between 3D synthetics generated from CVM-S4.26.M01 (top panel in blue) and CVM-H (bottom panel in red), and data (in black) for the deep Fontana event, filtered at three different period ranges, which are 5 - 20 seconds, 3 - 20 seconds and 2 - 20 seconds. The data and synthetics are tangential velocity waveforms, plotted in absolute amplitude. The station profile starts from northern edge of San Gabriel basin into Los Angeles basin across Whittier Narrows and ends at the coast (station PDR). As a whole, CVM-S.4.26.M01 performs better than CVM-H and can fit waveforms well at period of 5 seconds. At period of 2 seconds, both models do not completely reproduce the waveforms.

Several factors may contribute to the underprediction of the long duration shaking in our simulations, including the minimum shear wave velocity in the velocity model, implementation of near-surface geotechnical layer (GTL) at the top 350 m, inclusion of stochastic, correlated velocity perturbations, and incorrect estimation of event depth. However, our test results in Figure 4.11 show that these factors do not significantly impact the waveforms or the duration in the period range 2 – 20 seconds (Figure 4.11 for period range 5 - 20 seconds) The lower minimum velocity in the velocity model, which affects the shallowmost layers and can further amplify the waveform amplitude, does not have a significant impact at this period range, and the synthetics do not reproduce the strong shaking. Without the near-surface low velocity GTL at the top 350 m, the waveform fits for certain stations like PSR and RUS worsen, but the fits for stations like USC and LCG are mildly improved. Therefore, we conclude that the effect of GTL is insignificant at this period range. Similarly, adding the stochastic perturbations, which can promote scattering and may increase the shaking duration, does not change the fitting significantly in this period band. Finally, the shallower source generates synthetics with stronger amplitude, which overpredicts the amplitude of the initial arrivals but improve the waveform fitting for RUS in particular. However, the long shaking duration is not predicted by the synthetics.

On the other hand, the choice of anelastic attenuation factors can have a strong impact on the modeled duration at shorter period, as with stronger attenuation, energy at shorter periods decays more rapidly with time. Lin and Jordan [30] suggested that the attenuation scaling ( $Q_s = 50V_s$ ) used in earthquake simulations are 4 times weaker than predicted from  $t^*$  measurements by Hauksson and Shearer [29] for 2 - 30 Hz. When a weaker attenuation scaling is used ( $Q_s = 200V_s$ ), we observed that more energy is preserved hence the duration of shaking in both the 5- 20 second and 2 - 20 second bandwidths are increased (Figure 4.13). At 5 seconds period, the fit to the later arrivals produced by CVM-S4.26.M01 is improved, while for CVM-H 15.1.0, the amplitude of the later arrivals is now significantly over-estimated. At 2 seconds period, both models produce later arriving waves; however, neither model is able to adequately match the amplitude or phasing of the observed later arriving motions. A comparison of  $Q_s$  with different scaling factors ( $50 V_s$ ,  $100 V_s$  and  $200 V_s$ ) for CVMS4.26-M01 can be found in Figure 4.14. In this study, we do not attempt to prescribe the right attenuation model but to point out that the choice of attenuation model has strong effect in reproducing accurate shaking duration.

In short, the synthetics from 3D velocity model CVM-S4.26 can reproduce most of the initial phases better than the synthetics from CVM-H15.1.0. CVMH.15.1.0 does produce later arriving waves at 5 seconds period, although they are larger in amplitude and delayed relative to the observations. With weaker attenuation, both models produce longer durations, although neither model fits the phasing of the observed motions very well. The differences seen in the synthetics from the two CVMs stems from differences in the architecture of the shallow structures in the models (Figure 4.15). In CVM-S4.26, the entire model has been updated using waveform tomography, which has a lower period bound of about 5 seconds [8]. The result is that the velocity structure of CVM-S4.26 is smoothly varying and any sharp velocity contrasts from the original CVM-S4 have been blurred out. Without sharp, shallow basin edges, this model does not produce strong basin surface waves for shallow events, particularly for periods below 5 seconds. On the other hand, while CVM-H15.1.0 has also undergone tomographic updates, the basin structures have been reinserted so that the shallow, detailed heterogeneities from the original CVM-H model are preserved. This allows the generation of coherent basin surface waves for shallow events such as those seen at 5 seconds period in Figure 4.8; however, the presence of lateral heterogeneities within the shallow basin sediments breaks up the coherence of the prolonged shaking across the basin at shorter periods. The following section explores the role of shallow heterogeneities in the wave propagation by tracking the wavefront using dense array.

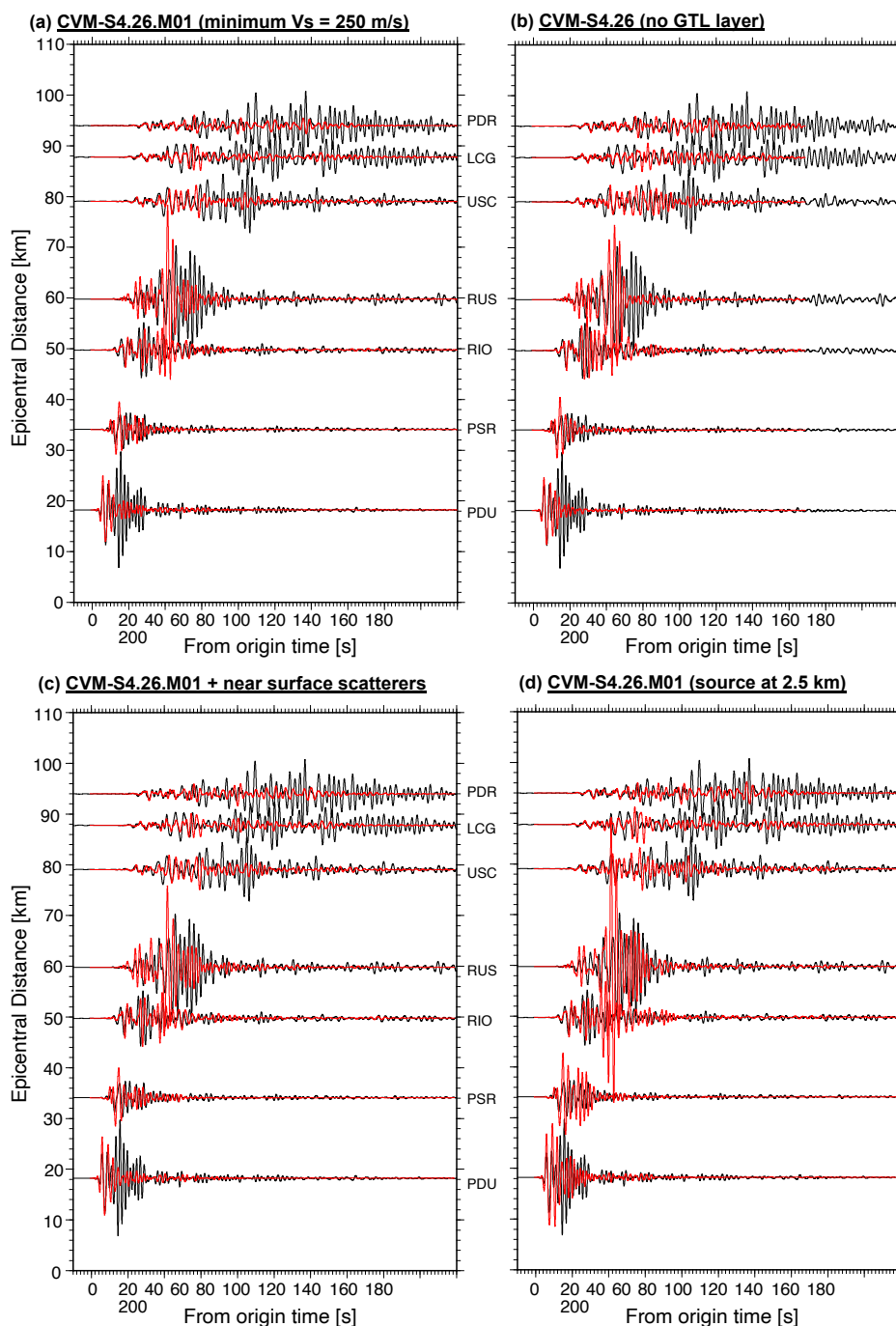


**Figure 4.11:** Record sections showing the comparison between velocity data in tangential component (black) and 3D synthetics generated from CVM-S4.26.M01 (red) for the shallow Fontana event. The 3D synthetics are generated using an attenuation scaling of  $Q_s = 50V_s$ . Both data and synthetics are filtered at 2 – 20 seconds and plotted in absolute amplitude. Results for waveforms at a period of 5 – 20 seconds can be found in Figure S8 (a) 3D synthetics generated from CVM-S4.26.M01 with minimum velocity set at 250 m/s instead of 500 m/s (refer to Figure S5). (b) 3D synthetics are generated from CVM-S4.26, which is CVM-S4.26.M01 without the slow geotechnical layer (GTL) at top 350 m. (c) 3D synthetics generated from CVM-S4.26.M01 with strong perturbations added stochastically in the top 1.2 km (following Graves and Pitarka [31]). (d) 3D synthetics generated from CVM-S4.26.M01 with the earthquake source at 2.5 km instead of 3.5 km.

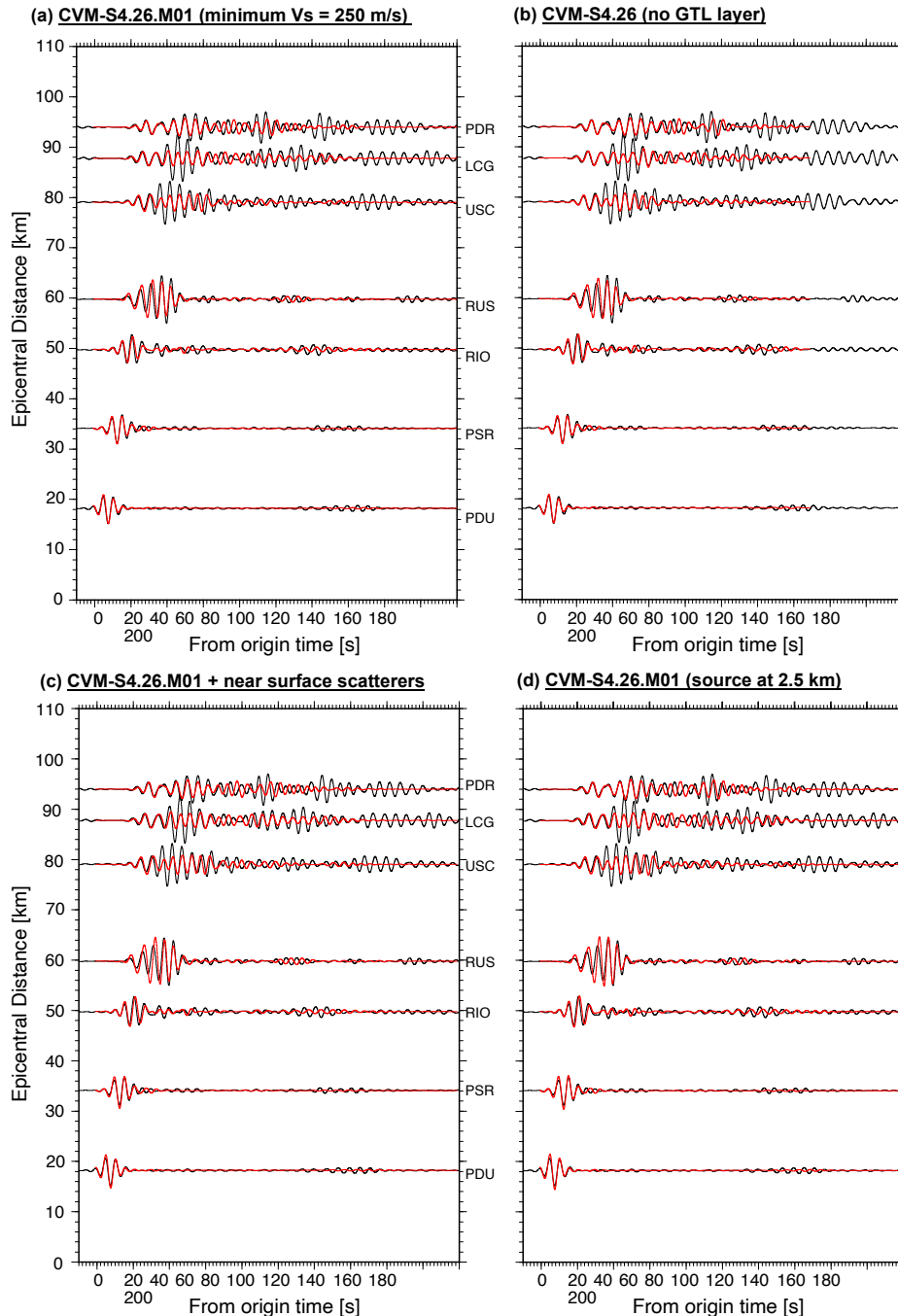


**Figure 4.12:** Similar to Figure 4.11 but for waveforms filtered at 5 – 20 seconds. Record sections show data for shallow M4.4 Fontana event (in black) compared to 3D synthetics (in red) generated from (a) CVM-S4.26.M01 with minimum velocity set at 250 m/s (b) CVM-S4.26, which is CVM-S4.26.M01 without the slow geotechnical layer (GTL) near the surface (c) CVM-S4.26.M01 with strong perturbations added stochastically at the top 1.2 km. (d) Record section comparing data with 3D synthetics generated from CVM-S4.26.M01 with the earthquake source at 2.5 km instead of 3.5 km. At a period of 5 seconds and longer, the various modifications to the model or source depth do not significantly improve the waveform fitting.

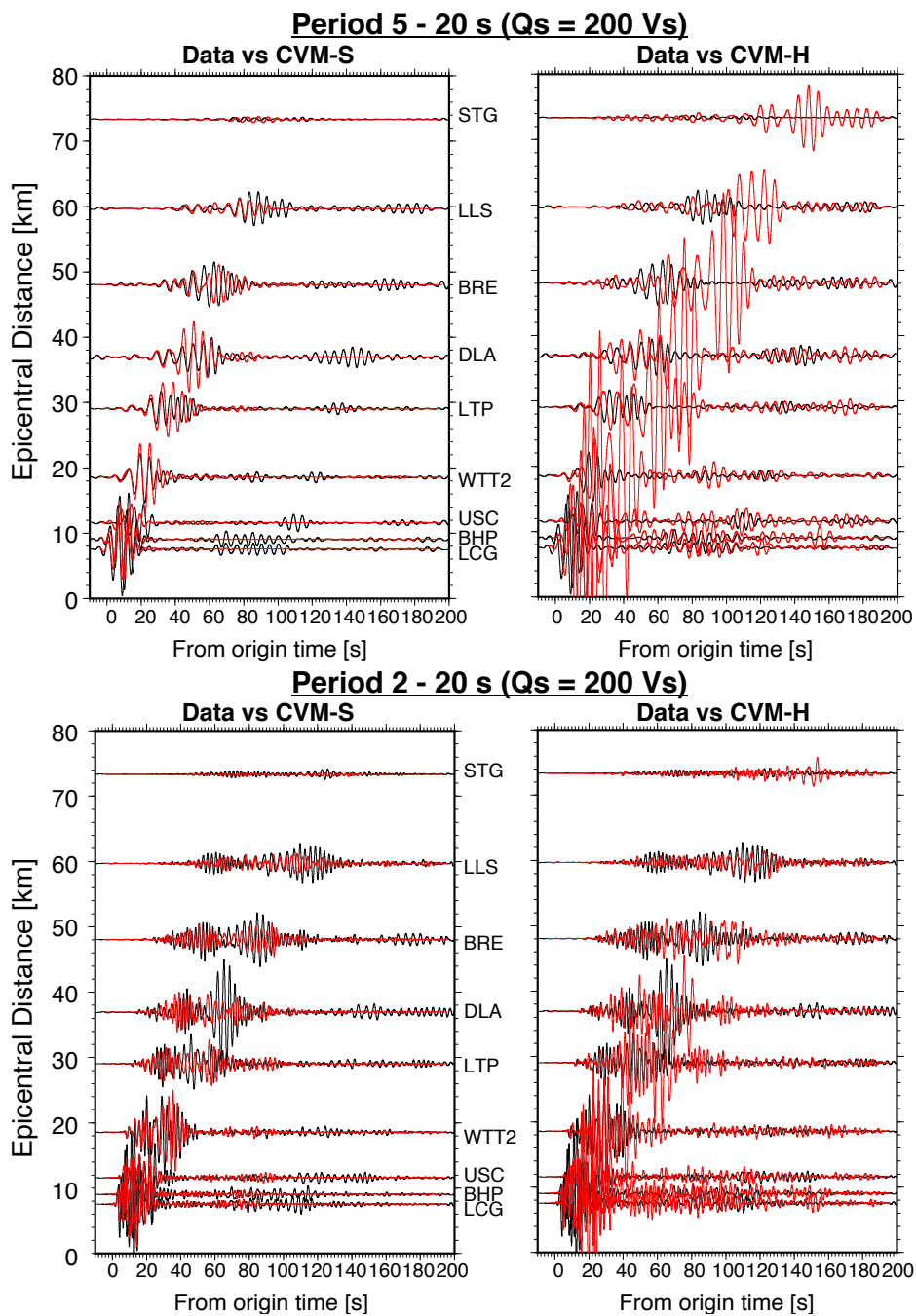


**Figure 4.13:** Record sections similar to Figure 4.8, showing the comparison between 3D synthetics (in red) generated from CVM-S4.26.M01 (left column) and CVM-H 15.1.0 (Right column) and data (in black) for 2012 M3.2 Beverly Hills event. The 3D synthetics are generated using a weaker attenuation scaling of  $Q_s = 200 \times V_s$ .

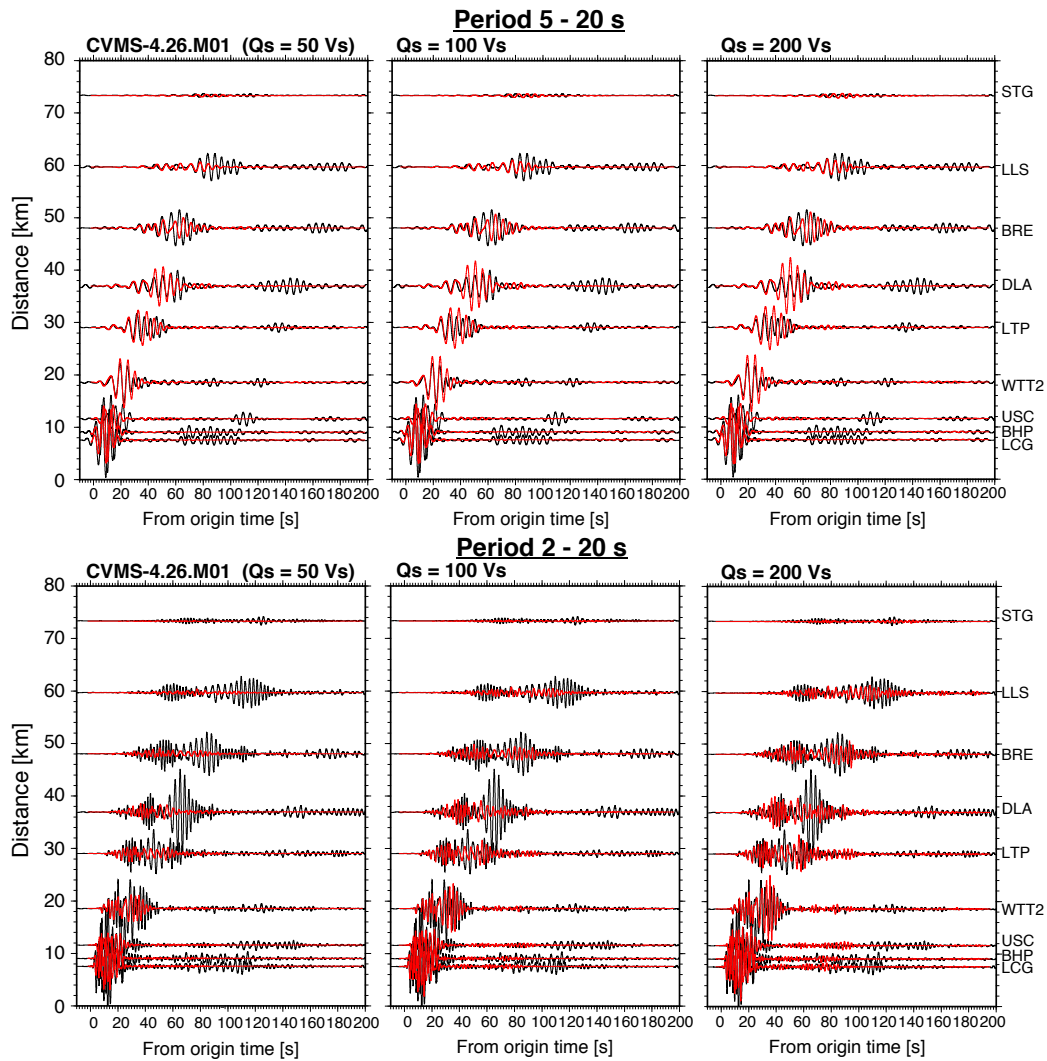


**Figure 4.14:** Record sections showing the comparison between tangential velocity data for 2012 M3.2 Beverly Hills event (in black) and 3D synthetics (in red) generated from CVM-S4.26.M01 with three different scaling factors for  $Q_s$  (i.e.  $Q_s = (50$  or  $100$  or  $200) V_s$ ). The shaking duration is more preserved with weaker attenuation (higher  $Q$ ).

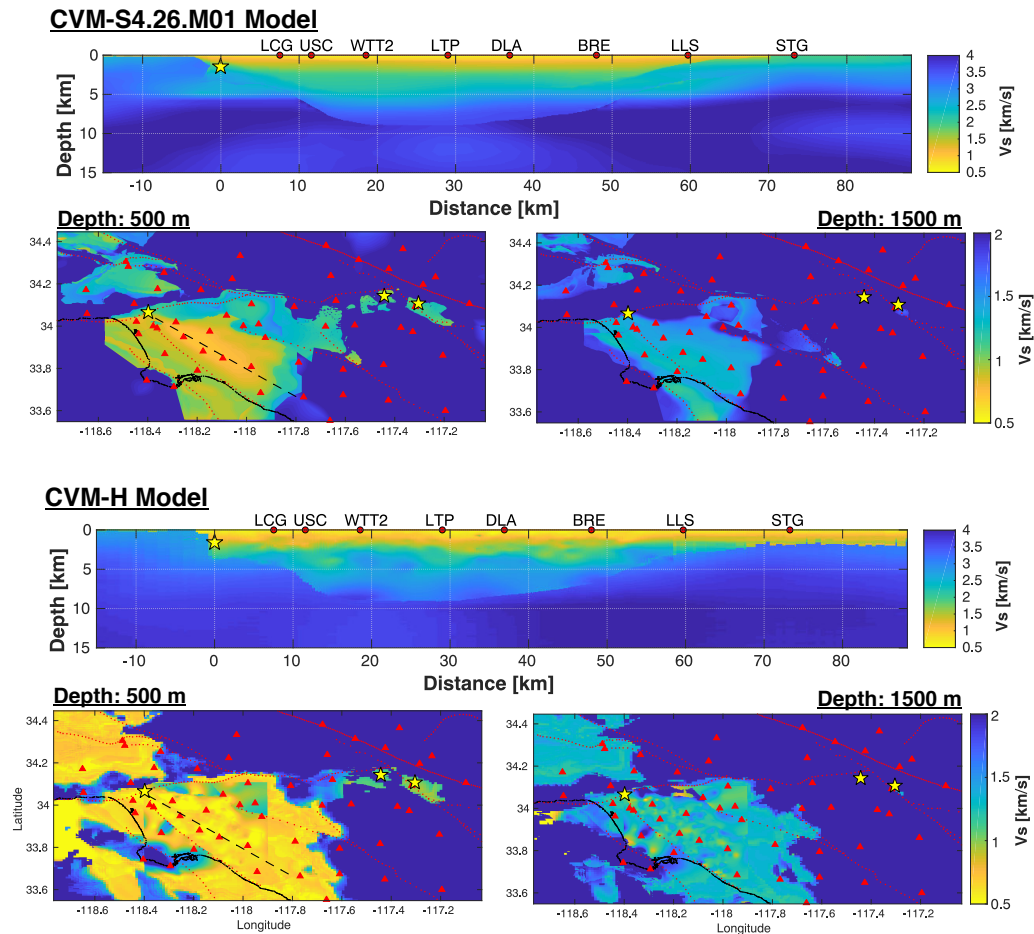


**Figure 4.15:** (top) Cross-section showing the shear wave velocity structure from the CVM-S4.26.M01 model across the Los Angeles Basin, stations (in red) along the profile and the depth of the 2012 Beverly Hills shallow event in yellow stars. The two maps below are horizontal depth profile of the CVM-S4.26.M01 model at depth 500 and 1500 m. The black dashed line shows the location of the cross-section profile. Locations of earthquakes (in yellow stars) and seismometers (in red) are shown as well. Red lines delineate the known regional faults. (bottom) Same, but for the CVM-H model.

#### 4.5 Beamforming Analysis on Dense Array

Array processing techniques, when applied to dense array deployments, can be used to estimate propagation direction, slowness and arrival time of each coherent wavefront passing across the sensors. While array processing techniques have been used extensively to study the fine-scale structure of the Earth's interior [32], recently, they have been used to identify prominent scatterers within the upper crust such as the bathymetric relief in the Southern California Continental Borderland [33]. The particularly dense array deployments of single vertical component sensors from the FairField Node system at the Santa Fe Springs (SFS) array (Figure ??) recorded the shallow 2012 Beverly Hills event, which provides an opportunity to investigate how the path across the Los Angeles basin enables long duration. The SFS array consists of 1464 sensors at the time of earthquake, with a sensor spacing averaging 100 m. Data with bad signal-to-noise ratio and no visible earthquake signals are removed, retaining 97% of SFS array data.

To detect how a seismic wavefield travels across an array, we use the phase stack (or phase coherence) method described in Schimmel and Paulssen [34] and implemented in Yu et al. [33]. In the phase stack method, the seismic traces are first converted into analytic traces using Hilbert transform, and the amplitudes of the traces are normalized to unity sample by sample. The phase coherence is then measured by averaging these analytic traces in the complex plane. Using phase coherence measurements allows us to detect weak but coherent signals recorded at the arrays due to seismic scattering. The phase coherence is scaled with the amplitude to emphasize coherent arrivals that are strong in amplitude; in this case, significant shaking.

At period range 2 - 20 seconds, SFS array show several arrivals of coherent energy with increasing slowness corresponding to P wave, S wave and surface wave (Figure 4.16). When scaled with amplitude, the significant shaking across SFS array lasts up to 80 sec. The prolonged shaking travels with slowness up to 150 s/deg (= apparent velocity of 740 m/s) and arrives from the same azimuth as the earthquake direction, i.e. the energy is traveling on the great circle path. The difference in slowness of the later arrivals (150 s/deg) compared to the first packet of surface waves (100 s/deg) indicates that the later waves are sampling very slow structures not sampled by the initial surface wave packet. .

Additionally, there is a stream of coherent energy recorded at the SFS array that arrived from off-great circle azimuth of 240 degree at later time window of 80 - 120

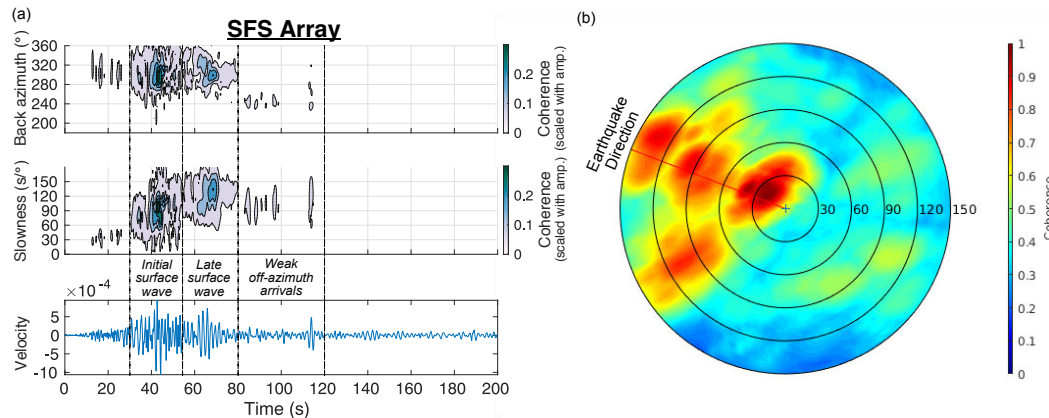


**Figure 4.16:** (a) The back azimuth and slowness of P, S and Surface wave arrivals for data recorded by the Santa Fe Springs (SFS) array located 35.5 km away from the hypocenter. Earthquake epicenter is at a back azimuth of  $291^\circ$ . Shown as well is a vertical-component velocity seismogram recorded by the SFS array. Seismograms are bandpass filtered between 2 - 20 seconds with a two-pass Butterworth filter. (b) Polar plots showing coherence measured from data and are stacked over the entire duration (200 seconds). Warmer color indicates higher coherence. Most coherent energy are confined to the great circle path. There is some coherent energy observed arriving from off-great circle azimuths at time 80 to 120 seconds.

seconds, traveling at the same slowness of 100 s/deg. Assuming constant slowness, we can estimate that the energy from the earthquake is scattered offshore near the edge of the Santa Cruz Basin along the Inner Borderland and recorded by the array as a coherent late arrival. The location where energy is scattered has a pronounced topographic relief and is a prominent scatterer imaged using teleseismic SH waves [33]. This weak late arrival is also observed at other stations, arriving about 40 seconds after the surface wave train (Figure 4.3). Our simulation results further emphasize the role of regional heterogeneities. In comparison to CVM-S4.26.M01, the CVM-H model contains offshore structures and sharp boundaries which can reflect the late arrivals, and hence is able to produce these very late arrivals (Figure 4.13 and 4.15).

#### 4.6 Discussion

The beamforming results suggest that the prolonged shaking is not caused by off-azimuth basin reverberations, as the later arrivals are along the same back azimuth as the earthquake. The prolonged levels of shaking, traveling at increasing slowness, indicates the role of slow velocity structures in the near-surface, which is consistent with many previously proposed hypotheses on exciting long durations [3, 4]. In

addition, the strong shaking develops coherently across the basin, starting from the station closest to the basin edge, suggesting that the reason behind the excitation of the long duration is due to generation of basin surface waves at the basin edges, which are also proposed for the Kanto basin [6] in Japan and Mexico Valley [7]. Due to the shallower incidence angles, the strength of these basin waves is much greater for shallow sources than for deep sources, exhibiting an earthquake depth-dependent behavior on basin response. This phenomenon is frequency-dependent, particularly strong for 2 - 10 seconds wave, posing an increased risk to tall buildings, bridges and large-capacity storage tanks in Los Angeles area.

To improve the performance of the physics-based forward simulation and better constrain the velocity models, it is important to resolve the attenuation model in the shallow crust. In most numerical implementations of waveform forward simulation, intrinsic attenuation is applied using a scaling law with a function of  $V_s$  [16, 35]. Such application would imply strongest attenuation near the surface within basin structure as the velocity values are typically lowest, and reflects the attenuation properties of sedimentary basin. Therefore, surface waves are most affected as they are trapped in the shallow layers of the velocity model. Our initial simulation applies a relation of  $Q_s = 50V_s$ , which means the top 1 km has an average  $Q_s$  of 50 - 100. This relation is consistent with the  $Q_s$  values proposed in Hauksson and Shearer [29] and is higher than prescribed in Olsen et al. [35] where  $Q_s = 20V_s$  for  $V_s < 2$  km/s (Figure 4.17). Our simulation result shows that implementing a weaker attenuation relation (i.e. larger  $Q_s$ ) can reproduce some of the prolonged shaking at 2 seconds.

However, weak attenuation alone is insufficient in predicting the waveform. The synthetics from CVM-H model, despite not fitting the observed waveforms, contain a strong late wave train, which are generated due to presence of thicker slower layer at the surface than CVM-S4.26 (Figure 4.15). The presence of slow heterogeneities within the basin further modulates the amplification of ground motion at individual sites, on top of weak attenuation and slow subsurface layer. The regional heterogeneities, such as offshore structures included in CVM-H, are also important in predicting off-azimuth arrivals. Future improvements to simulating using the 3D velocity models should consider (1) better representation of shallow heterogeneities within the basin and sharp boundaries regionally while preserving the basin edge information and (2) an appropriate shallow velocity and attenuation scaling model. The improvements in station coverage, either seismic instruments or other novel sensors such as distributed acoustic sensing (DAS) system, will be able to improve

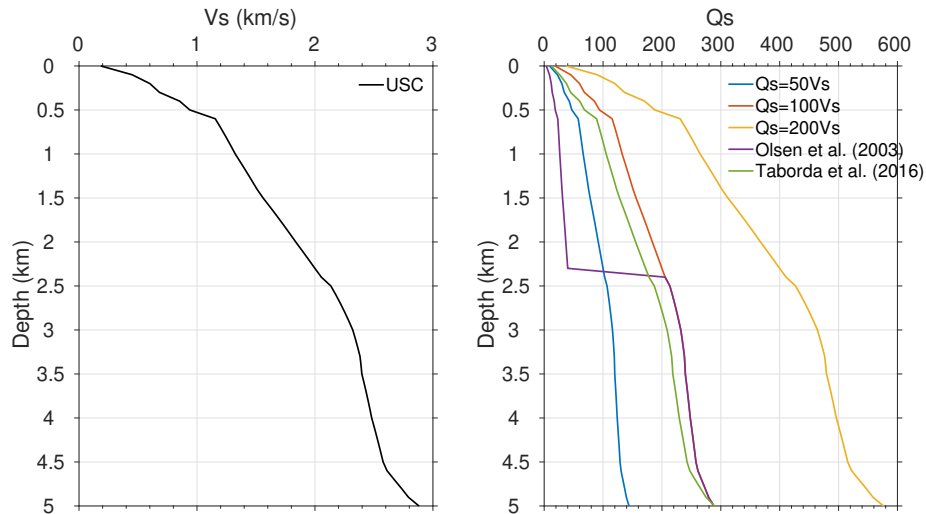


**Figure 4.17:** (Left) 1D Shear wave velocity model queried from CVM-S4.26.M01 below USC station which is within the Los Angeles Basin. (Right) Quality factor for shear wave velocity ( $Q_s$ ), a parameter to account of anelastic attenuation, for each depth below USC station using four types of scaling law based on  $V_s$  value. Olsen et al. [35] uses  $Q_s = 20V_s$  (for  $V_s < 2$  km/s) and  $Q_s = 100V_s$  (for  $V_s \geq 2$  km/s). Taborda et al. [16] uses a regression fitted scaling based on Brocher [36], which is  $Q_s = 10.5 - 16V_s + 153V_s^2 - 103V_s^3 + 34.7V_s^4 - 5.29V_s^5 + 0.31V_s^6$ . Apart from Olsen et al. [35], most scaling laws use rules that avoid abrupt transitions in  $Q_s$ .

our ability to image the shallow heterogeneities and velocity structure in the basin.

#### 4.7 Conclusion

In this study, we analyzed small-magnitude, shallow and deep earthquake pairs recorded across the LA basin and showed that shallow events can generate much longer shaking durations in the bandwidth 2 - 20 seconds compared to deeper events. The observed coherent wave train, combined with beamforming analysis, suggests that the basin edges are responsible in exciting the long duration. Additional late, but weaker shaking is also observed to be arriving off-azimuth, potentially scattered by regional structures. Current 3-D community velocity models do not accurately predict the long shaking in their present form. Possible modifications to these models, including more accurate imaging of basin edges, better imaging of shallow heterogeneities within the basins, and better constraints on the shallow velocity and attenuation structure will likely lead to improved modeling of these basin generated phases.

#### 4.8 Acknowledgements

This work is supported by Southern California Earthquake Center grant (#18128). The computations presented here were conducted on the Caltech High Performance Cluster, partially supported by a grant from the Gordon and Betty Moore Foundation. Waveform data are downloaded from Southern California Earthquake Data Center (SCEDC) doi:10.7909/C3WD3xH1. Several plots were made using the Generic Mapping Tools version 4.2.1 ([www.soest.hawaii.edu/gmt](http://www.soest.hawaii.edu/gmt); [37]). We thank Rob Clayton (Caltech) for his assistance in acquiring the dense array dataset, Breitburn Energy Partners for the usage of the Santa Fe Springs dense array dataset, and Xin Wang for the discussion on CAP code.

#### References

- [1] H. Kawase. The cause of the damage belt in Kobe:“The basin-edge effect,” constructive interference of the direct S-wave with the basin-induced diffracted/Rayleigh waves. *Seismological Research Letters*, 67(5):25–34, 1996.
- [2] R. W. Graves, A. Pitarka, and P. G. Somerville. Ground-motion amplification in the Santa Monica area: Effects of shallow basin-edge structure. *Bulletin of the Seismological Society of America*, 88(5):1224–1242, 1998.
- [3] H. Kawase and K. Aki. A study on the response of a soft basin for incident S, P, and Rayleigh waves with special reference to the long duration observed in Mexico City. *Bulletin of the Seismological Society of America*, 79(5): 1361–1382, 1989.
- [4] C. K. Saikia, D. S. Dreger, and D. V. Helmberger. Modeling of energy amplification recorded within greater Los Angeles using irregular structure. *Bulletin of the Seismological Society of America*, 84(1):47–61, 1994.
- [5] S.-J. Lee, H.-W. Chen, Q. Liu, D. Komatitsch, B.-S. Huang, and J. Tromp. Three-dimensional simulations of seismic-wave propagation in the Taipei basin with realistic topography based upon the spectral-element method. *Bulletin of the Seismological Society of America*, 98(1):253–264, 2008.
- [6] P. Boué, M. Denolle, N.i Hirata, S. Nakagawa, and G. C. Beroza. Beyond basin resonance: characterizing wave propagation using a dense array and the ambient seismic field. *Geophysical Journal International*, 206(2):1261–1272, 2016.
- [7] V. M. Cruz-Atienza, J. Tago, J. D. Sanabria-Gómez, E. Chaljub, V. Etienne, J. Virieux, and L. Quintanar. Long duration of ground motion in the paradigmatic valley of Mexico. *Scientific Reports*, 6:38807, 2016.

- [8] E.-J. Lee, P. Chen, T. H. Jordan, P. B. Maechling, M. A. M. Denolle, and G. C. Beroza. Full 3-D tomography for crustal structure in southern California based on the scattering-integral and the adjoint-wavefield methods. *Journal of Geophysical Research: Solid Earth*, 119(8):6421–6451, 2014.
- [9] J. H. Shaw, A. Plesch, C. Tape, M. P. Suess, T. H. Jordan, G. Ely, E. Hauksson, J. Tromp, T. Tanimoto, R. Graves, et al. Unified structural representation of the southern California crust and upper mantle. *Earth and Planetary Science Letters*, 415:1–15, 2015.
- [10] H. Magistrale, K. McLaughlin, and S. Day. A geology-based 3D velocity model of the Los Angeles basin sediments. *Bulletin of the Seismological Society of America*, 86(4):1161–1166, 1996.
- [11] M. P. Süß and J. H. Shaw. P wave seismic velocity structure derived from sonic logs and industry reflection data in the Los Angeles basin, California. *Journal of Geophysical Research: Solid Earth*, 108(B3), 2003.
- [12] G. P. Ely, T. H. Jordan, P. Small, and P. J. Maechling. A Vs30-derived near surface seismic velocity model. In *Abstract S51A-1907, Fall Meeting*. AGU San Francisco, CA, 2010.
- [13] K. B. Olsen, S. M. Day, J. B. Minster, Y. Cui, A. Chourasia, M. Faerman, R. Moore, P. Maechling, and T. Jordan. Strong shaking in Los Angeles expected from southern San Andreas earthquake. *Geophysical Research Letters*, 33(7), 2006.
- [14] R. W. Graves, B. T. Aagaard, and K. W. Hudnut. The ShakeOut earthquake source and ground motion simulations. *Earthquake Spectra*, 27(2):273–291, 2011.
- [15] D. Komatitsch, Q. Liu, J. Tromp, P. Suss, C. Stidham, and J. H. Shaw. Simulations of ground motion in the Los Angeles basin based upon the spectral-element method. *Bulletin of the Seismological Society of America*, 94(1): 187–206, 2004.
- [16] R. Taborda, S. Azizzadeh-Roodpish, N. Khoshnevis, and K. Cheng. Evaluation of the southern California seismic velocity models through simulation of recorded events. *Geophysical Journal International*, 205(3):1342–1364, 2016.
- [17] C. E. Hruby and I. A. Beresnev. Empirical corrections for basin effects in stochastic ground-motion prediction, based on the Los Angeles basin analysis. *Bulletin of the Seismological Society of America*, 93(4):1679–1690, 2003.
- [18] S. M. Day, R. Graves, J. Bielak, D. Dreger, S. Larsen, K. B. Olsen, A. Pitarka, and L. Ramirez-Guzman. Model for basin effects on long-period response spectra in southern California. *Earthquake Spectra*, 24(1):257–277, 2008.

- [19] D. C. Bowden and V. C. Tsai. Earthquake ground motion amplification for surface waves. *Geophysical Research Letters*, 44(1):121–127, 2017.
- [20] L.-S. Zhao and D. V. Helmberger. Source estimation from broadband regional seismograms. *Bulletin of the Seismological Society of America*, 84(1):91–104, 1994.
- [21] L. Zhu and D. V. Helmberger. Advancement in source estimation techniques using broadband regional seismograms. *Bulletin of the Seismological Society of America*, 86(5):1634–1641, 1996.
- [22] S. K. Y. Lui, D. Helmberger, J. Yu, and S. Wei. Rapid assessment of earthquake source characteristics. *Bulletin of the Seismological Society of America*, 106(6):2490–2499, 2016.
- [23] L. Zhu and X. Zhou. Seismic moment tensor inversion using 3D velocity model and its application to the 2013 Lushan earthquake sequence. *Physics and Chemistry of the Earth, Parts A/B/C*, 95:10–18, 2016.
- [24] X. Wang and Z. Zhan. Moving from 1D to 3D velocity model: automated waveform-based earthquake moment tensor inversion in the Los Angeles region. *Geophysical Journal International*, 2019.
- [25] E. Hauksson, W. Yang, and P. M. Shearer. Waveform relocated earthquake catalog for southern California (1981 to June 2011). *Bulletin of the Seismological Society of America*, 102(5):2239–2244, 2012.
- [26] D. J. Wald and R. W. Graves. The seismic response of the Los Angeles basin, California. *Bulletin of the Seismological Society of America*, 88(2):337–356, 1998.
- [27] T. L. Wright. Structural geology and tectonic evolution of the Los Angeles basin, California: Chapter 3: Part 1. 1991.
- [28] R. W. Graves. Simulating seismic wave propagation in 3D elastic media using staggered-grid finite differences. *Bulletin of the Seismological Society of America*, 86(4):1091–1106, 1996.
- [29] E. Hauksson and P. M. Shearer. Attenuation models ( $Q_p$  and  $Q_s$ ) in three dimensions of the southern California crust: Inferred fluid saturation at seismogenic depths. *Journal of Geophysical Research: Solid Earth*, 111(B5), 2006.
- [30] Y.-P. Lin and T. H. Jordan. Frequency-dependent attenuation of P and S waves in southern California. *Journal of Geophysical Research: Solid Earth*, 123(7):5814–5830, 2018.
- [31] R. Graves and A. Pitarka. Kinematic ground-motion simulations on rough faults including effects of 3D stochastic velocity perturbations. *Bulletin of the Seismological Society of America*, 106(5):2136–2153, 2016.

- [32] S. Rost and C. Thomas. Array seismology: Methods and applications. *Reviews of geophysics*, 40(3):2–1, 2002.
- [33] C. Yu, Z. Zhan, E. Hauksson, and E. S. Cochran. Strong SH-to-Love wave scattering off the southern California Continental Borderland. *Geophysical Research Letters*, 44(20):10–208, 2017.
- [34] M. Schimmel and H. Paulssen. Noise reduction and detection of weak, coherent signals through phase-weighted stacks. *Geophysical Journal International*, 130(2):497–505, 1997.
- [35] K. B. Olsen, S. M. Day, and C. R. Bradley. Estimation of Q for long-period (> 2 sec) waves in the Los Angeles basin. *Bulletin of the Seismological Society of America*, 93(2):627–638, 2003.
- [36] T. M. Brocher. Compressional and shear-wave velocity versus depth relations for common rock types in northern California. *Bulletin of the Seismological Society of America*, 98(2):950–968, 2008.
- [37] P. Wessel and W. H. F. Smith. New, improved version of Generic Mapping Tools released. *Eos, Transactions American Geophysical Union*, 79(47):579–579, 1998.

*Chapter 5***EVIDENCE FOR STRONG LATERAL SEISMIC VELOCITY  
VARIATION IN THE LOWER CRUST AND UPPER MANTLE  
BENEATH THE CALIFORNIA MARGIN**

Lai, V. H., Graves, R. W., Wei, S. and Helmberger, D. (2017). “Evidence for strong lateral seismic velocity variation in the lower crust and upper mantle beneath the California margin”. In: *Earth and Planetary Science Letters* 463, pp. 202-211 DOI: 10.1016/j.epsl.2017.02.002.

**5.1 Abstract**

Regional seismograms from earthquakes in Northern California show a systematic difference in arrival times across Southern California where long period (30 – 50 seconds) SH waves arrive up to 15 seconds earlier at stations near the coast compared with sites towards the east at similar epicentral distances. We attribute this time difference to heterogeneity of the velocity structure at the crust-mantle interface beneath the California margin. To model these observations, we propose a fast seismic layer, with thickness growing westward from the San Andreas along with a thicker and slower continental crust to the east. Synthetics generated from such a model are able to match the observed timing of SH waveforms better than existing 3D models. The presence of a strong upper mantle buttressed against a weaker crust has a major influence in how the boundary between the Pacific plate and North American plate deforms and may explain the observed asymmetric strain rate across the boundary.

**5.2 Introduction**

The lithospheric structure beneath the California margin plays an important role in controlling how the plate boundary between Pacific plate and North American plate deforms. Geodetic studies [1, 2, 3] have shown an asymmetry in strain accumulation across the San Andreas Fault (SAF). The asymmetry is attributed to factors including laterally heterogeneous elastic properties in the upper crust (0 – 20 km) and varying elastic lithospheric thickness across the fault in the lower crust. Here, we present seismic observations that are consistent with the lateral transition in elastic properties across the SAF boundary, involving the lower crust and upper

mantle structure beneath the California margin, as shown schematically in Figure 5.1.

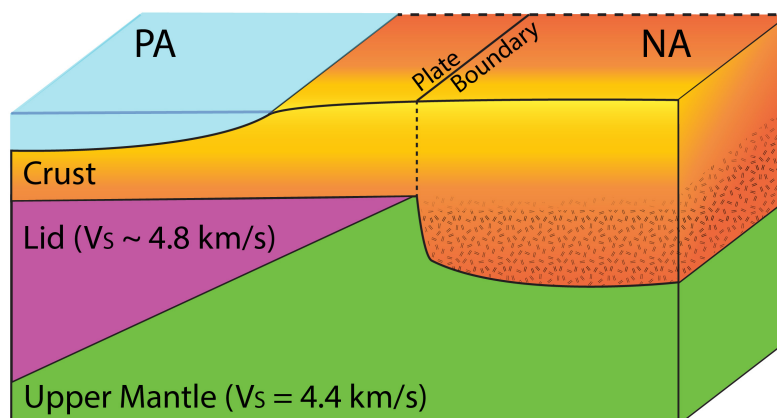


**Figure 5.1:** A schematic drawing of our proposed model. The lid (defined in text), which is faster than its surrounding medium, grows in thickness from the plate boundary towards Pacific plate (PA). In order to better fit the arrival times for inland stations (details in Section 5.4), the crust below the North American plate (NA) is modeled with a thick, relatively low-velocity crust.

The seismic lithosphere or lid, as defined by Anderson [4], is a zone of relatively high seismic velocity in the uppermost mantle, generally overlying a low velocity zone (LVZ) under oceans and cratons. The lid and underlying LVZ are different from the mechanically-defined lithosphere-asthenosphere boundary, although both are closely related, and the seismological layers are often used to outline mechanical structure [5]. Pure path (1D) models indicate that the Pacific plate has a thick (60 km) lid overlaying a strong LVZ extending to below a depth of 300 km [6, 7]. In contrast, the continental Western United States (WUS) structure is characterized by a relatively slower, thinner lid (10 - 20 km) along with a weaker mantle LVZ [8]. Despite these large lateral differences, the vertical travel times through these two structures are quite similar. Thus, studies utilizing teleseismic phases with nearly vertical ray paths (e.g. most global tomographic models) have difficulty resolving the lateral variation in shear wave velocity structure across the plate boundary.

Using regional S-SS differential travel times, Melbourne and Helmberger [9] showed that there is lateral variation within the sub-crustal mantle characterized by the presence of a seismic lid beneath California with thickness increasing from 0 km in Eastern California to 55 km along the Pacific plate (see Figure 5.2). As the Pacific plate with a thick lid has lower dextral strain compared to the North American plate

with a thin lid, they propose that the lid structure may modulate the deformation across the plate boundary. However, the sampling sites of the lid thickness, denoted by the SS reflection points, are located along the coast of Baja California and therefore cannot precisely resolve the lid thickness beneath the main California coastal region.

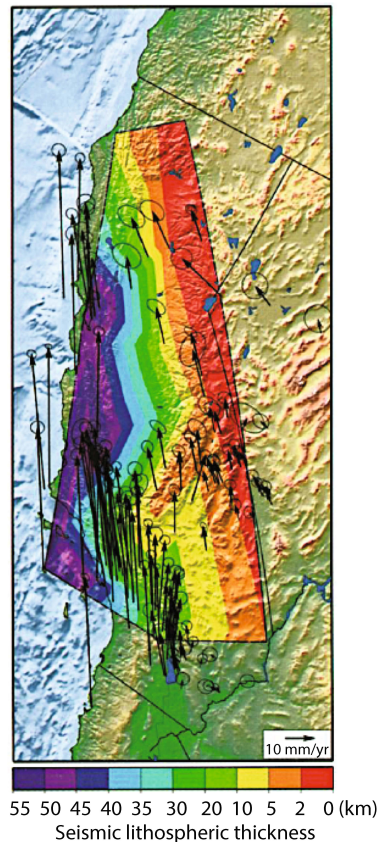


**Figure 5.2:** From S-SS differential time studies for events off Baja California, Melbourne and Helmberger [9] estimate the seismic lithospheric thickness beneath California margin by fitting observed waveforms from a library of 1D synthetics with variable lid thickness. Western California has a thick lid while Eastern California has a thin lid with high thickness gradient. There is a positive correlation with lid thickness gradient with dextral strain across the region, as indicated by the GPS velocities measurements. They propose that the correlation is due to Pacific plate, with the presence of thick lid, plays a key role in modulating the regional crustal deformation. (Reproduced from Melbourne and Helmberger [9])

Understanding how the plate boundary between Pacific plate and North American plate deforms requires an accurate image of the deep structure along the plate boundary. Seismic studies since the 1970s indicate large variability in velocity structure along this boundary. For example, Zandt and Furlong [10] combined

teleseismic travel-time data and thermal models to infer lithospheric-thinning along the San Andreas fault system in northern California. More recently, Wang et al. [11] used surface wave tomography to map out lateral velocity variations to a depth of 300 km throughout the southwestern United States, finding similar lithospheric thinning to the east of the San Andreas fault in the Mendocino region as well as high velocity regions within the upper mantle at depths up to 200 km that they correlate with fossil slab structures. Other recent studies took advantage of the improved station density coverage to retrieve regional velocity structure of the crust and uppermost mantle using seismic tomography (e.g. [12, 13]), adjoint waveform tomography [14] or receiver function techniques (e.g. [15, 16, 17, 18, 19]). Many of these regional velocity features are incorporated in the development of 3D velocity models by the Southern California Earthquake Center (SCEC), which are discussed later.

Multiple earthquakes, namely the 2014-03-10 Mw 6.8, 2005-06-15 Mw 7.2, and 2010-01-10 M6.5 events in Mendocino region and the 2014-08-25 Mw 6.0 Napa earthquake, present a unique opportunity to directly study the lateral variation in the lower crust - upper mantle structure beneath the California margin using regional waveforms. The earthquakes occurred in Northern California and the waveforms were recorded by the BK network operated by the Northern California Seismic Network (NCSN) and the CI network operated by the Southern California Seismic Network (SCSN) at regional distances 3 - 11° (Figure 5.3a inset). The recorded waveforms exhibit significant travel time differences (discussed in Section 5.3), suggesting possible lateral heterogeneity of the lithospheric structure beneath the California margin.

3D waveform-modeling is useful to investigate anomalous behaviors in the seismic wave field, but can be prohibitive when modeling at large continental scales due to high computational cost. One previous known effort in continental-scale modeling [21] is able to explain large scale Rayleigh-wave multipathing phenomenon across western North America, but lacks resolution for detailed study on ocean-continent transition. Specifically modeling the crustal-sensitive waves that sample the whole continental margin on a reduced regional scale allows us to refine current velocity models and constrain key features across the plate boundary.

In this study, we show that the travel times of the regional SH waveforms from these events cannot be well explained by existing 1D and 3D velocity models, which are poorly constrained in lower crust - upper mantle structure. We propose that a fast

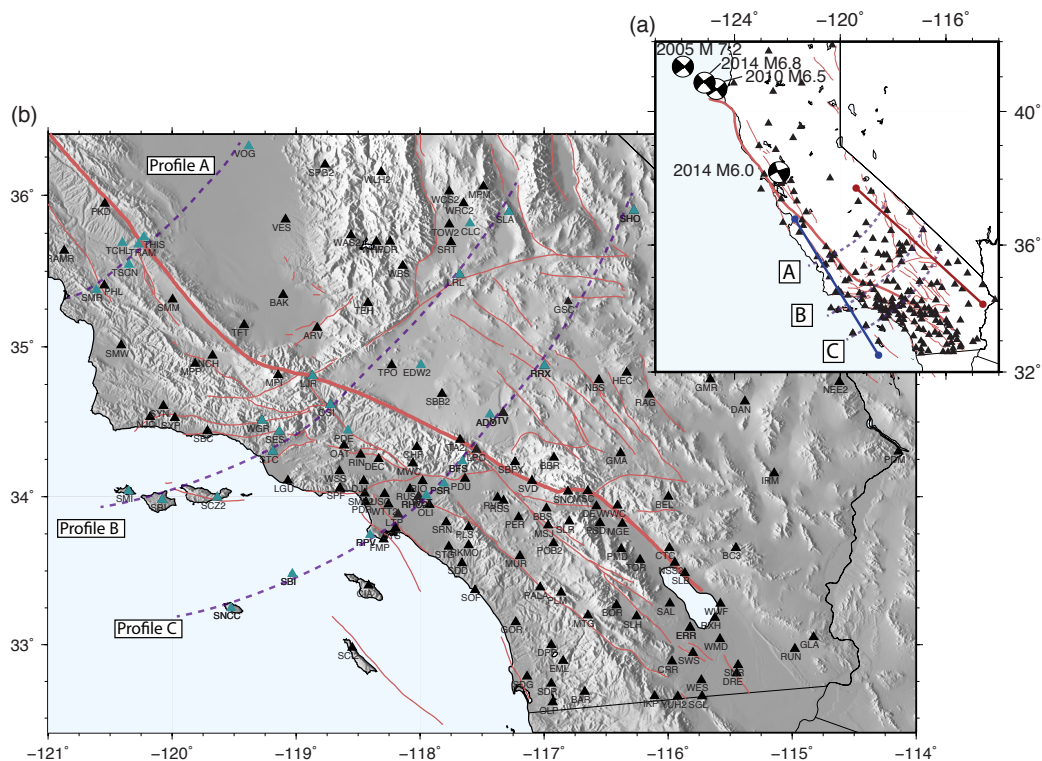


**Figure 5.3:** (a) The inset shows the location of the earthquakes in Mendocino and Napa regions (see Table 5.1, along with the distribution of broadband stations from NCSN and SCSN used in this study. The blue line displays the location of coastal stations and the red line shows the location of inland stations along radial profiles discussed later. The three azimuthal profiles (Profile A, B and C) marked in purple dashed lines are used to examine the timing and waveform variations as a function of back azimuth to the events. (b) Topographic map zoomed in on the location of SCSN stations and azimuthal profiles featured in this study. The fault map is provided by Jennings [20] where the San Andreas Fault is highlighted in bold red line.

seismic layer beneath the California coast coupled with a thick, relative slow crust beneath eastern California is necessary to explain the discrepancies in travel times. The lateral variation of velocity in the lower crust - upper mantle region in our proposed model suggests a similar lateral variation in lithospheric strength which may play a strong role in modulating long term plate deformation and explain the strain rate asymmetry across the SAF.

### 5.3 Observations

The challenge in studying the ocean-continent plate boundary using regional waveforms in California is that it is difficult to model the different types of waveforms (P,

Event Name	Mw	Latitude	Longitude	Depth (km)	Strike	Rake	Dip
2014-08-24 Napa	6.0	38.215	-122.312	11.1	155	172	82
2014-03-10 Mendocino	6.8	40.829	-125.134	16.6	318	-169	88
2005-06-15 Mendocino	7.2	41.292	-125.953	16.0	317	172	83
2010-01-10 Mendocino	6.5	40.652	-124.692	29.3	233	0	85

**Table 5.1:** The earthquake source parameters used in this study are provided by the ANSS Comprehensive Earthquake Catalog (ComCat).

SH and SV) simultaneously because of the limited aperture of the station distribution and the nodes in the radiation patterns for strike-slip events. In this study, we concentrate on the tangential component in displacement, because the stations are located close to the maxima of SH wave radiation pattern for the earthquakes we analyze.

We perform cross-correlation to see how the travel times of the observed SH waveforms compare with that computed from a 1-D velocity model (see Table 5.2) modified from the layered ‘Gil7’ velocity model [22]. The 1-D synthetics are computed using frequency-wavenumber method [23]. The ‘Gil7’ velocity model is derived from broadband waveform modeling and routinely used in moment tensor inversions in Northern California. The ‘Gil7’ model is a relatively fast model, which has a shallow Moho boundary at 25 km and includes a fast, mafic lower crust with a P-wave velocity ( $V_p$ ) of 6.89 km/s and shear wave velocity ( $V_s$ ) of 3.98 km/s, as revealed from the San Francisco Bay area seismic imaging experiment (BASIX) in 1991 [24]. The time differences between the data and synthetics will show how much the 1-D velocity model deviates from the true velocity structure. In this study, we use published moment tensor solutions provided by the ANSS Comprehensive Earthquake Catalog (listed in Table 5.1). We concentrate our analysis in the period range of 30 to 50 seconds. The waveforms sample up to a depth of 100 km and are sensitive to both the lower crust and upper mantle structure (see Figure 5.4).

For both Mendocino and Napa earthquakes, the observed long period SH waves show a systematic pattern of later arrival times (positive time delay) for sites in eastern California and early arrival times (negative time delay) for sites along the coast, demonstrating that the velocity structure varies laterally across California

(Figure 5.5). The range of time shifts for the 2014 Mendocino event is stronger than that seen for the 2014 Napa earthquake, suggesting that the waveforms from the Mendocino event are able to better sample this considerable structural variation, which extends from Mendocino region to the south of Napa region along the coast. Additionally, the pattern and strength of the time shifts seen for the 2014 Mendocino event are consistent with that found for other events of similar magnitudes in the Mendocino Triple Junction region (Figure 5.6). As a check, we also compute our own moment tensor solutions using the cut-and-paste (CAP) inversion method [25, 26] and find that the time shift patterns are stable even with small variations in focal mechanisms (see Figure 5.7). This emphasizes the role of lateral velocity variations in controlling the arrival times as opposed to effects related to source location or mechanism.

Layer	Thickness (km)	Vs (km/s)	Vp (km/s)	Density (g/cc)
Upper Crust	5	2.60	4.50	2.40
	12	3.40	6.21	2.68
Lower Crust (Lid)	8 (18) (varies)	3.98 (3.70) (4.80)	6.89 (6.70) (8.30)	3.00 (2.80) (3.20)
Upper mantle	-	4.40	7.80	3.00

**Table 5.2:** A description of the modified 1-D ‘Gil7’ model. The main modification is a simplification of the crustal layer where the number of layers is reduced from 7 to 3. The Moho depth in this model is 25 km. The parameters of the fast lid and the thicker, slower crust used in western and eastern parts, respectively, of this study’s preferred model, are listed in parentheses.

Aligned waveforms from stations along the coast (blue profile line in Figure 5.3) show Sn-phase moveout of approximately the apparent shear wave velocity, 4.7 km/s (Figure 5.8, top panels). However, waveforms from inland stations, along the red profile line in Figure 5.3, show slower Sn-phase moveout velocities less than ~4.7 km/s (Figure 5.8, bottom panels). As discussed earlier, this feature is much stronger for the Mendocino event than for the Napa event, and it suggests the presence of a shear wave velocity region along coastal California that is faster than any of the structures depicted in the ‘Gil7’ model (see Table 5.2). Note that slight mislocation of the epicenter and origin times only shifts the record sections, leaving the apparent velocity unchanged.

Similarly, we observe in the azimuthal record sections (Figure 5.9), which span across a few hundred kilometers, that the Sn waves arrive systematically earlier

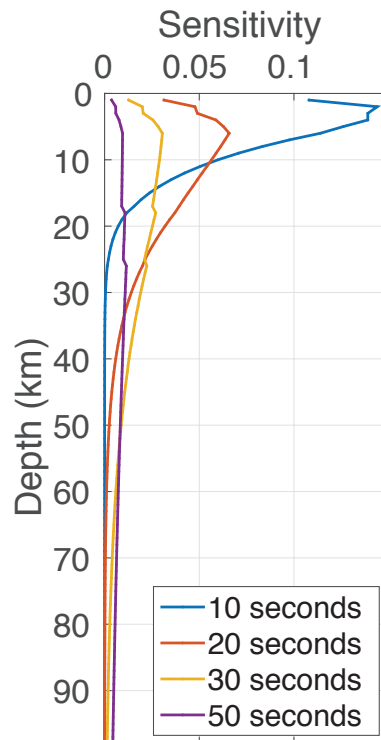


**Figure 5.4:** Sensitivity kernel of SH wave to shear wave speed for different periods across depth. The period chosen for this study is 30 – 50 seconds, which has similar sensitivity across all depths to 70 km and less sensitive to known heterogeneity in the upper crust. The figure is produced using tools from "Computer Programs in Seismology" [27].

for coastal and offshore stations relative to the inland sites. In addition, while the arrivals following the direct  $S_n$  at the inland stations show large amplitude coherent wave trains, the later arrivals at the coastal stations become less coherent and their amplitudes are significantly decreased. The transition in waveform character described above occurs near the SAF on the northernmost profile (Profile A, see Figure 5.3 for location), and then shifts to west of the SAF further south (Profiles B and C).

The difference in travel times suggest that there is a strong east – west lateral variation in the lower crust – upper mantle velocity structure beneath California, where the structure beneath the coastal and offshore stations has a substantially faster shear wave velocity compared to that beneath the inland stations. The variation in velocity structure appears independent of distance, since all three profiles display similar patterns in travel time shift. The heterogeneity in structure may also contribute to the distortion of later arriving waves as seen in the coastal stations.

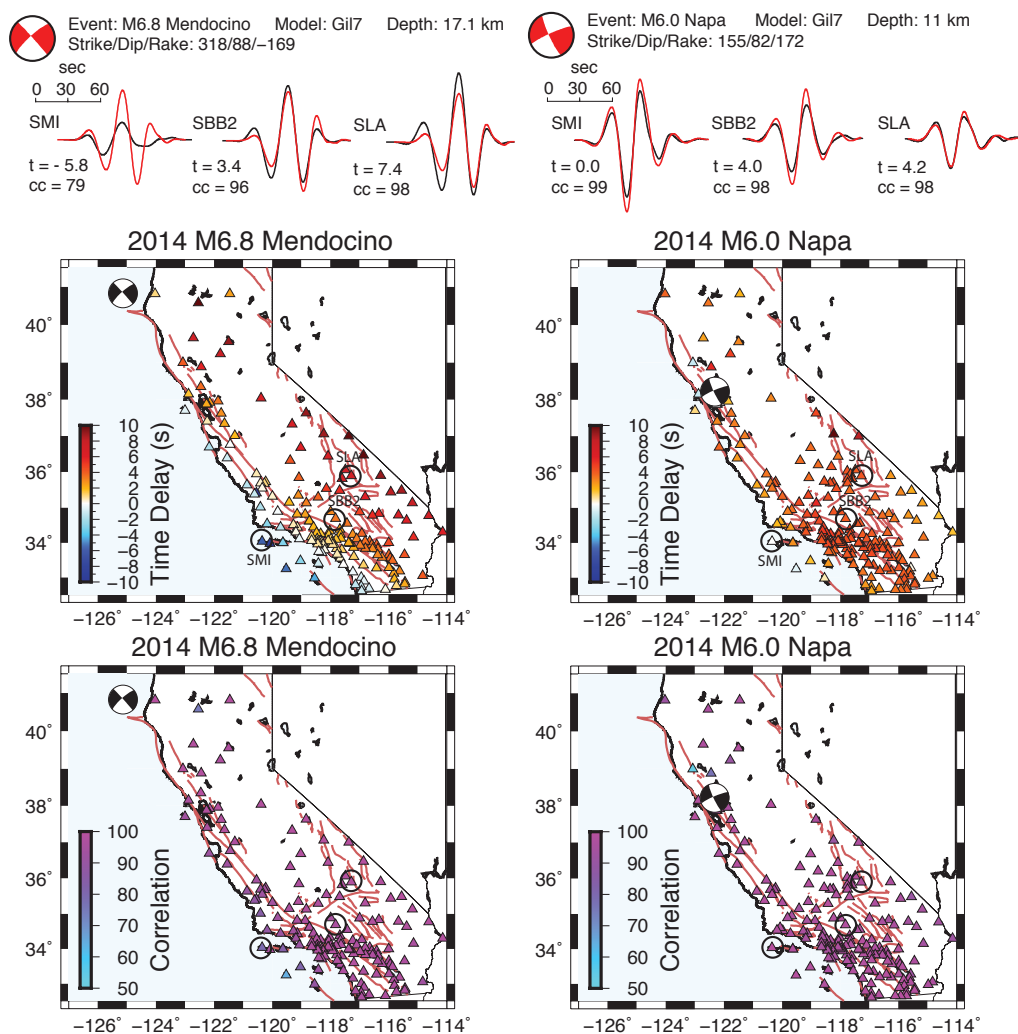


**Figure 5.5:** An example of cross-correlation results shown for three stations, SMI (coastal), SBB2 (near SAF) and SLA (Eastern California), where the time delays and correlation values are stated. Maps show the computed time shifts between the observed long period (30-50s) SH waves and the 1-D synthetics for both earthquake events. Cooler color indicates the observed waves arrive earlier than predicted by the synthetics and warmer colors indicate later wave arrivals. The average time differences (calculated from the eastern border of California to the coast) are about 7 s (Napa) and 14 s (Mendocino) respectively. The correlation of the observations with synthetics is high, with average coefficient above 0.90. The fit decreases for some coastal stations for the Mendocino event due to waveform interference at later arrival times but does not affect the arrival time of the first peak of the wave train.

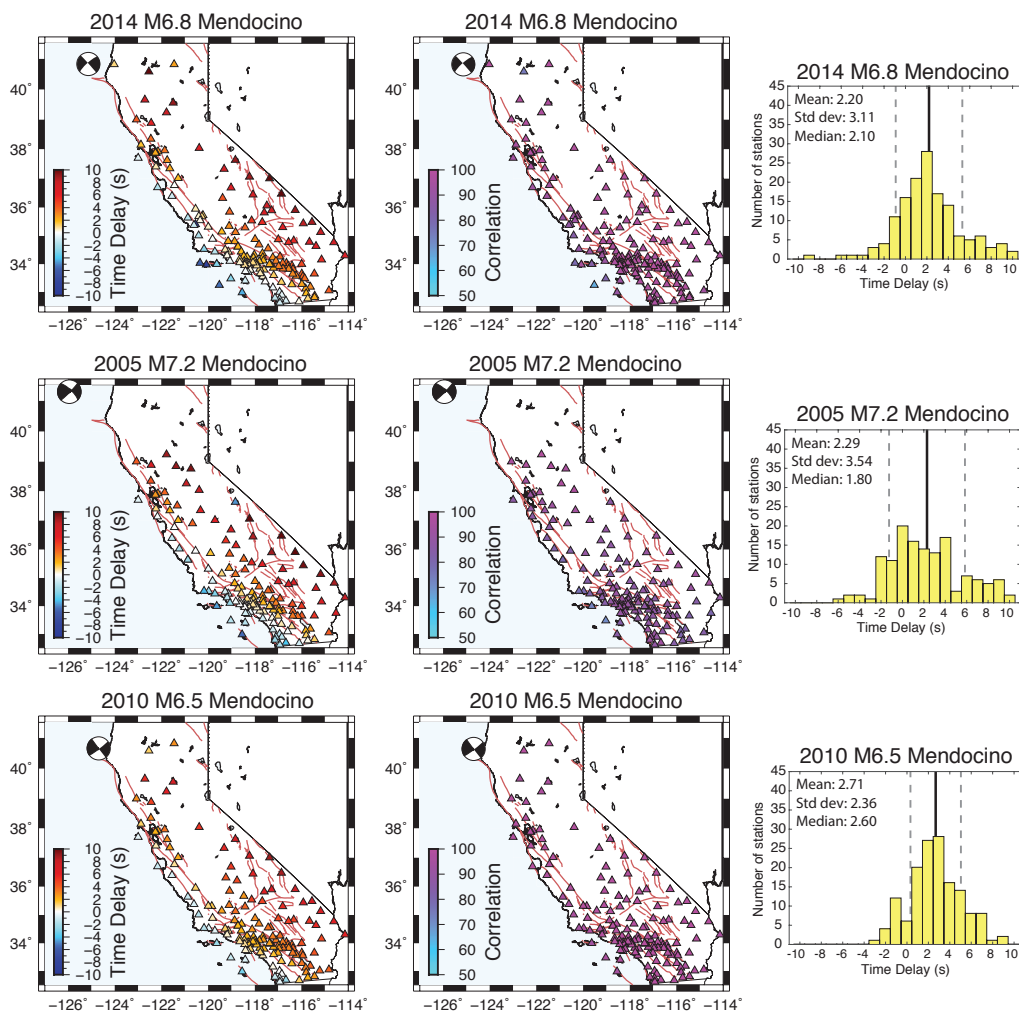


**Figure 5.6:** Similar to Figure 5.5, where maps show the time delay between the observed long period SH waves and the 1-D synthetics for three events of similar magnitudes in the Mendocino region. The correlation of the observations with synthetics is high, with average coefficient above 0.90. For stations towards the coast, the observed waves arrive earlier than predicted by the 1-D synthetics, indicated by cooler colors. For stations in eastern California, the observed waves arrive later than predicted by the 1-D synthetics, indicated by warmer colors. Histograms to the right of the maps show the distribution of the time delays for each event.

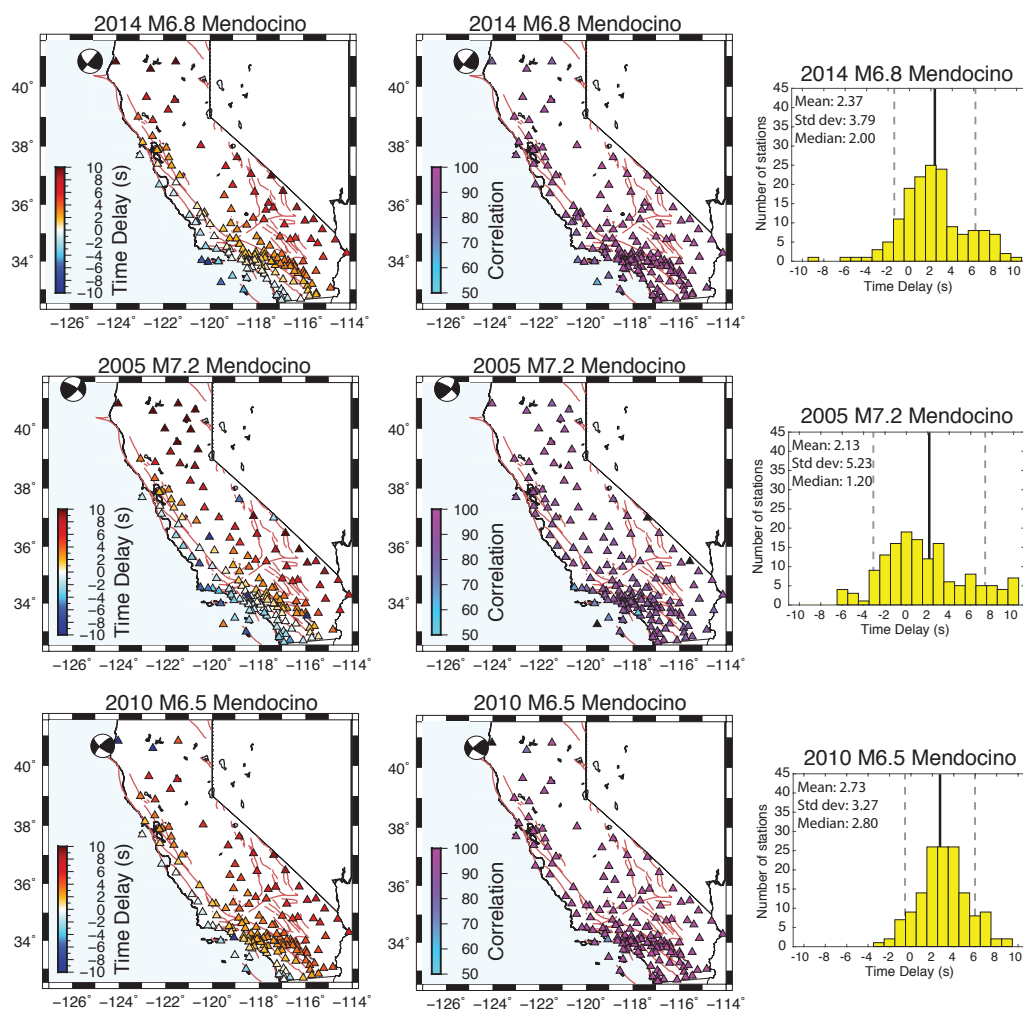


**Figure 5.7:** The maps show the time delay between the observed long period SH waves and the 1-D synthetics for three events of similar magnitudes in the Mendocino region. Instead of using moment tensor solutions published in catalog (shown in Figure 5.6), the focal mechanisms used for each event are determined using cut-and-paste moment tensor inversion [25, 26]. Histograms to the right of the maps show the distribution of the time delays for each event. The general time shift pattern of observed waves arriving earlier than predicted towards the coast (indicated by cooler colors) and those arriving later than predicted towards the east (indicated by warmer colors) remains stable, despite small variation shift in the moment tensor solution, hence emphasizing the role of lateral velocity variations in controlling the arrival times as opposed to effects related to source location or mechanism.

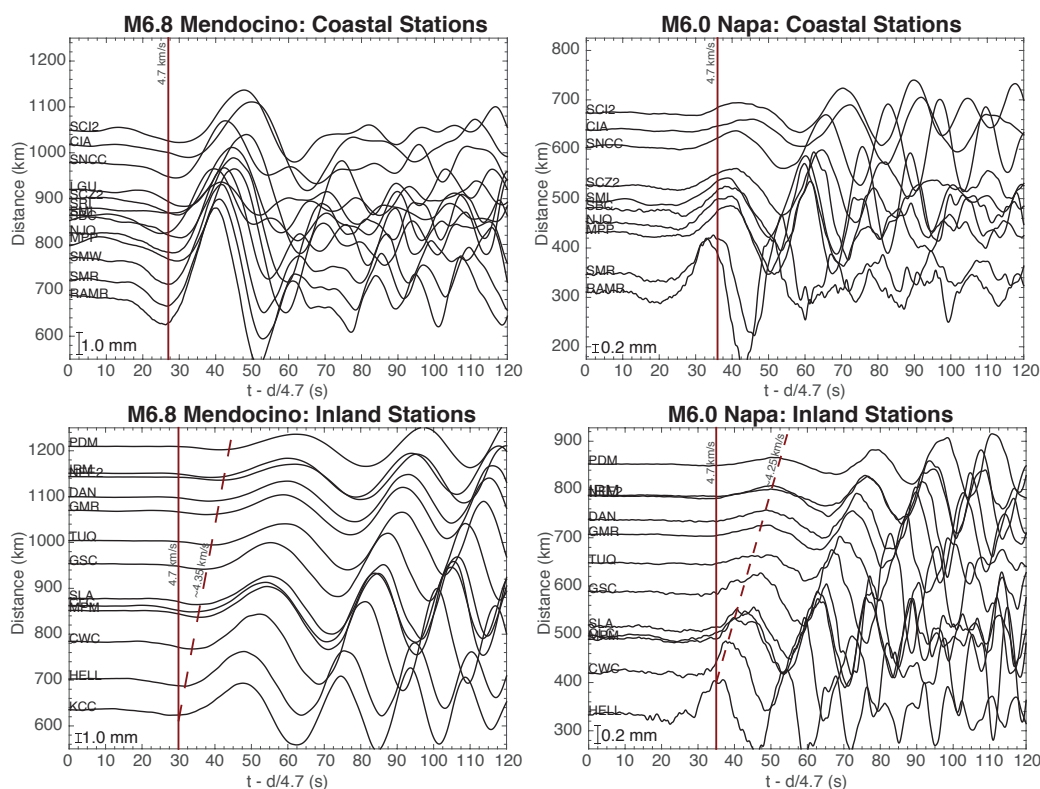


**Figure 5.8:** The record sections display broadband (1-100s) SH waveforms in displacement from the coastal stations in the top row (west of SAF; blue line in Figure 5.3a) and from inland stations in the bottom row (located in Eastern California; indicated by red line in Figure 5.3a) for both earthquake events. The arrivals of the first peak, which are the long period Sn waves, are aligned for coastal stations, showing that the waves are traveling at about the apparent shear wave velocity of  $\sim 4.7$  km/s. For inland stations, there is a strong move-out of the peaks across distances indicated by the dashed lines, showing the peaks are traveling slower than the reduction velocity (4.7 km/s). The move-out velocities are  $\sim 4.35$  km/s and  $\sim 4.25$  km/s for the Mendocino and Napa events, respectively.

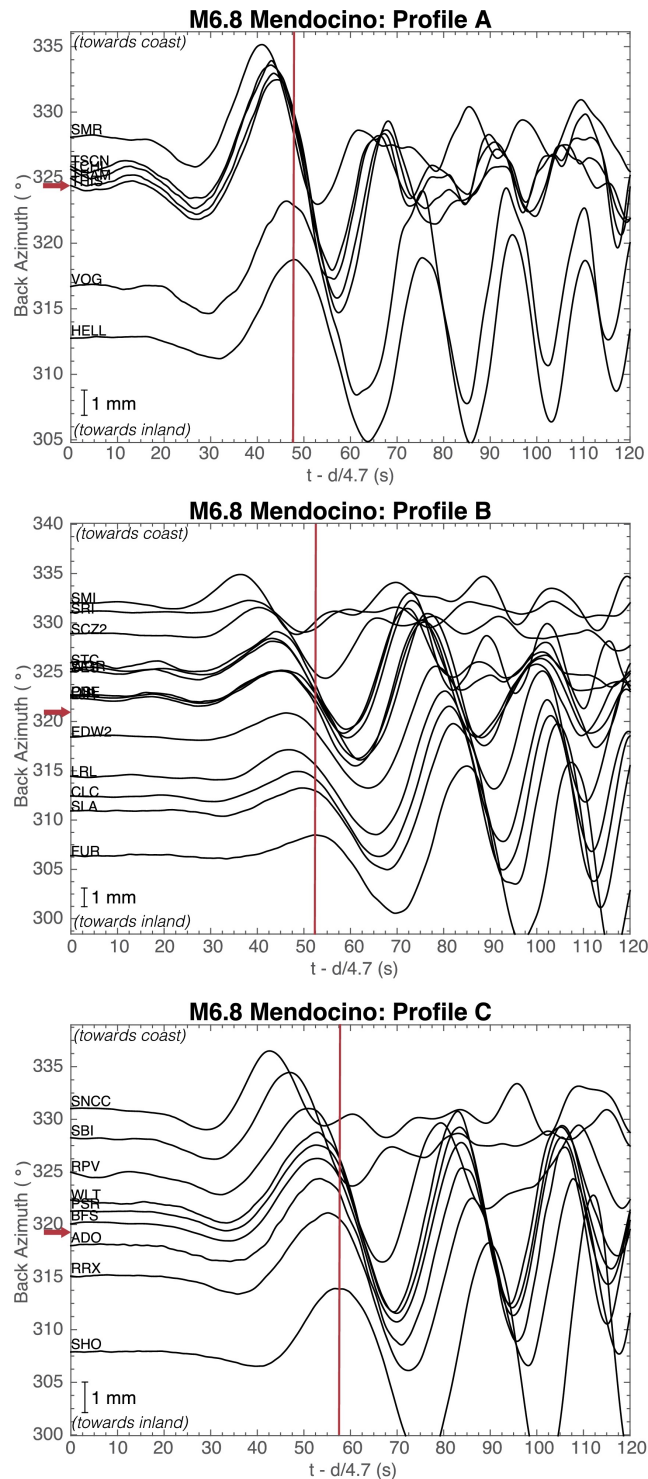


**Figure 5.9:** Figure shows azimuthal record sections of the broadband SH waves from the 2014 Mendocino event, with time plotted using a reduction velocity of 4.7 km/s. The station locations and profile lines are shown in Figure 5.3. The back azimuth increases as the station location shifts from inland towards the coast. The red line acts as a guide to show the SH waves arrive earlier for stations towards the coast. The location of SAF with respect to the stations is indicated by the red arrow in each record section.

## 5.4 Modeling

We propose that the systematic, east-west variation in arrival times of the SH waves is due to the variation in the velocity structure in the lower crust - upper mantle along the plate boundary. There are several scenarios that can contribute to the variation, such as different crustal thicknesses, presence of fast seismic lid, and/or different velocity in the lower crust - upper mantle structure. Tape et al. [14] shows that the Moho depth varies from 20 km offshore to 35 km inland across Southern California (along profile C in Figure 5.3). However, the difference in arrival times cannot be solely from variation in crustal thickness. A quick calculation from synthetics generated from 1-D velocity models shows that for every increase in crustal thickness of 10 km, the arrival times are delayed by  $\sim 2.5$  seconds (see Figure 5.10). A 14 second time difference (calculated from the east California to the coast) would suggest a 56 km difference in crustal thickness across California, which far exceeds the expected crustal thickness in this region.

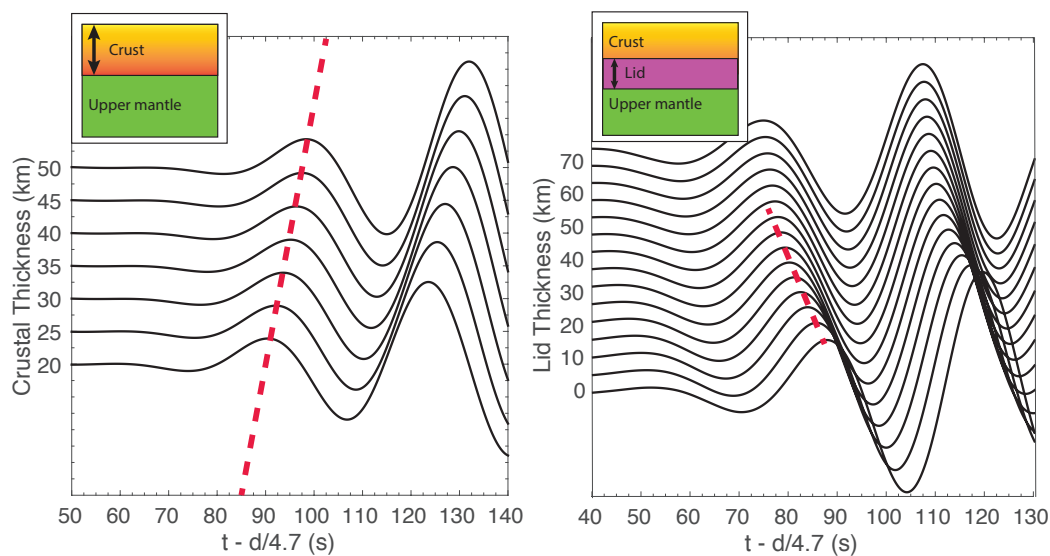


**Figure 5.10:** Record sections of 1-D synthetics to test the effects due to: (left) different crustal thickness and (right) different lid thickness. The velocity structure is the same as shown in Table 5.2, but with varying thickness indicated by the schematic drawings in the insets. The station modeled is RPV in Southern California, right by the coast, with the Mendocino event as the source.

Thus, we propose that the early arrival times at the coastal stations are predominantly due to the presence of a seismic lid west of the SAF and parallel to the coast, as presented schematically in Figure 5.1. In short, this seismic lid shares the same properties as the one observed within the Pacific plate, with a preferred SH velocity

of 4.78 km/s [7]. The presence of the lid is consistent with the observed apparent velocities of the long period Sn waveforms recorded by stations along the coast. As the seismic lid is much faster than the upper mantle ( $V_s$  of 4.8 km/s compared to 4.4 km/s), it has significant impact in shortening the travel times. The velocity contrast across California was previously observed in a 3-D tomographic study [12], where he determined a high  $V_p$  (8.2 km/s) structure at a depth around 20 km beneath the Southern California coastline. The structure is inferred to have a  $V_p/V_s$  ratio of 1.77, which translates to a  $V_s$  of 4.6 km/s, slightly lower than our estimated SH velocity of the lid. This difference can possibly be explained by seismic anisotropy in the oceanic plate where SH velocity is found to be about 5% faster than SV velocity [7]. The gradual decrease in travel times with back azimuth suggests that the lid may grow in thickness from inland towards the coast. The lid thickness is less well constrained compared to the crustal thickness, and can be as thick as 60 km [7].

To explain the delayed arrival times for inland stations, we propose the velocity structure beneath stations east of the SAF is significantly slower than to the west. This is consistent with previous studies that have found eastern California is characterized by a relatively thick crust [15] composed of relative low seismic velocities especially within the lower crust beneath the Mojave block [28, 29].

Our proposed model, shown in Figure 5.11, is a combination of the modified 1-D ‘Gil7’ velocity model with thicker and slower crust on the east, and a fast lid with a shear wave speed of 4.8 km/s, increasing in thickness from 0 km to 70 km offshore. The velocity structure remains uniform trending northwest-to-southeast as indicated in Figure 5.11. The boundary, where the lid grows in thickness, tracks the stations with zero time shifts (from Figure 5.5 and Figure 5.6) and runs mostly parallel with SAF in Northern California, and shifts to the west by 100 km after the ‘Big Bend’ in Southern California. The lower crustal velocity at 3.7 km/s in Eastern California is compatible with regional modeling of Basin and Range events [30].

To test our hypothesis, we use the 3-D finite difference method [31] to generate synthetics from our proposed model. The model is discretized with a uniform spacing of 0.5 km. We consider a 2-step approach to test the effects of the main features in our proposed structure, which are the fast lid on the west, and the low velocity thicker crust on the east. We first model the synthetics using a velocity model that only includes the fast lid, which improves the fit of the SH arrival times between the synthetics and data for the coastal and offshore stations, but does not affect the inland stations (Figure 5.13b). We then use the model that includes both the fast

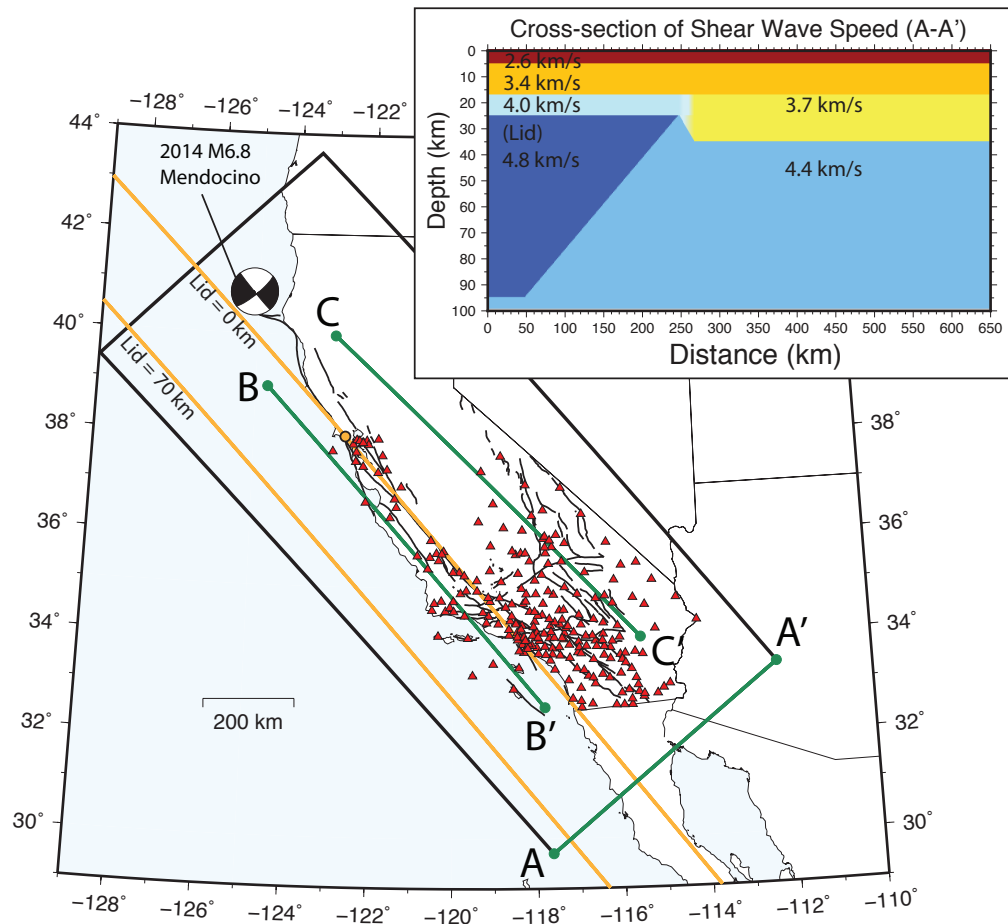


**Figure 5.11:** Map illustrates the configuration used in the 3-D finite difference modeling. Black box marks the surface boundary of the 3-D grid. The cross section profile (A - A') shows the 2-D shear wave velocity structure, which is a modification of the 1-D 'Gil7' model (see Table 5.2) with the lid structure, the thicker crust on the east and an additional low velocity zone. Yellow parallel lines delineate the zone where the lid thickness increases from 0 to 70 km. The event modeled is the 2014 M 6.8 Mendocino earthquake. Profile B-B' and Profile C-C' are shown in Figure 5.12.

lid and the low velocity thicker crust, and this significantly improves the fit for most inland stations (Figure 5.13c). However, this model also decreases the fit for stations in the southernmost portion of California, particularly those in the Salton Trough and Imperial Valley region. It is widely known that this region has a relatively thin crust (e.g. [12, 14]), which is clearly inconsistent with our proposed “thick crust” model. This indicates that additional 3D complexities beyond that currently included in our simplified representation are required to more fully explain all of the observations. The structural complexities in this southernmost portion of the model

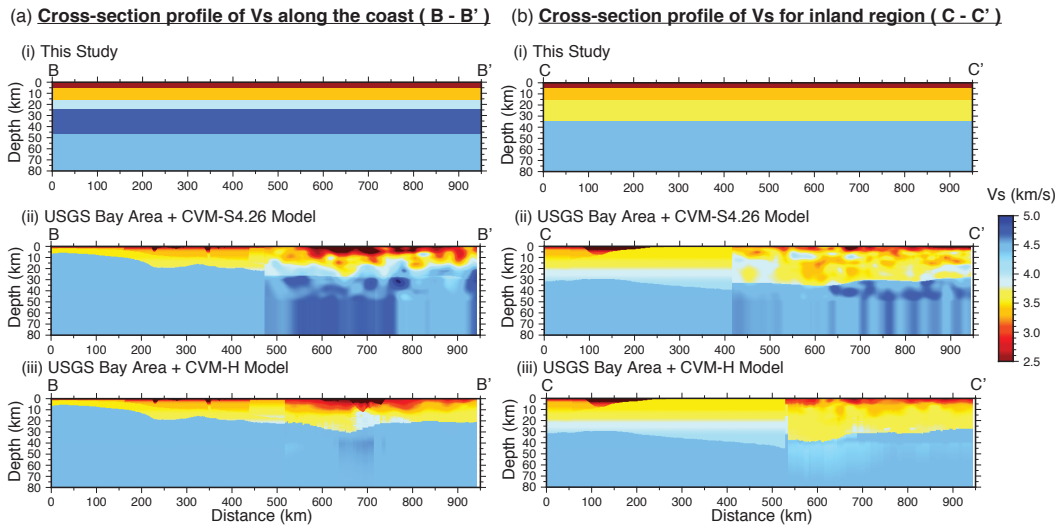


**Figure 5.12:** Cross-section profiles of shear wave ( $V_s$ ) structure along Profile B – B' (coast) and Profile C – C' (inland) for three 3D velocity models. The profile locations are indicated in Figure 5.11.

should also be considered when performing similar analysis of the reverse profile (south to north) using earthquakes occurring in the Baja California region such as the 2010 M7.2 El Mayor-Cucapah event. Incorporating these modifications is the subject of future work.

We further compare our model with the present 3D velocity models available through the SCEC community (Figure 5.14). There are three regional velocity models in total: the USGS Bay Area model v08.3.0 for Northern California [32] and two southern California Community Velocity Models (CVM), which are CVM-S4.26 [33] and CVM-Harvard 15.1.0 [34]. The main advantage of the existing 3D velocity models is that they have high resolution on basin and upper crust structure and those structures are well-resolved. The lower crust – upper mantle structure in the 3D models are derived from seismic tomography and teleseismic surface wave data, and they generally have a poorer resolution, compared to the upper crust. To construct a state-wide velocity model for comparison, we utilize the SCEC Unified Community Velocity Model (UCVM 15.10.0) software framework (<http://scec.usc.edu/scecpedia/UCVM>). This software package allows the combination of the USGS Bay Area model with either of the southern California CVMs. The UCVM package also prescribes a generic 1D velocity model [35] for regions not described by the 3D velocity models. The boundary for each of the 3D velocity models is shown in Figure 5.15. The slight discontinuities at the boundaries

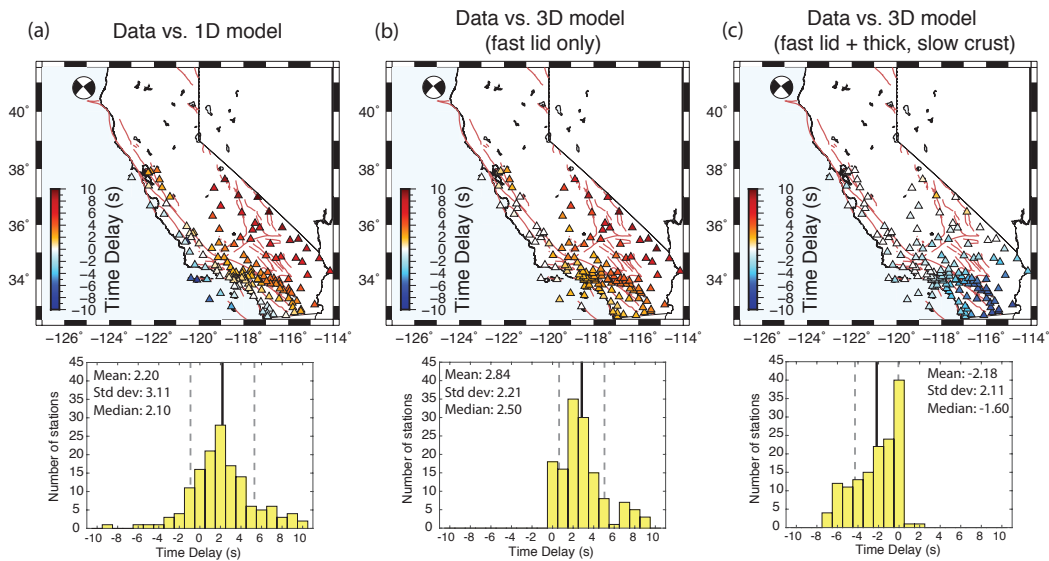


**Figure 5.13:** Maps show the time delay between the long period SH waves from the 2014 Mendocino event, and (a) the 1-D synthetics from ‘Gil 7’ model (same as Figure 5.5 and 5.6), (b) the 3-D synthetics from our proposed model with the lid only (no thick crust on the east), and (c) model with inclusion of both the lid and thicker, slower crust on the east. The histogram of the time shifts for each model comparison are shown below the map. Cooler color indicates the recorded seismograms arrive earlier than the synthetics.

where the different velocity models are combined have no significant impact as the waveforms used in subsequent analysis are filtered at long period (30 – 50 seconds).

For the coastal region, our model generally compares well with the UCVM 3D models. Our model shares some key characteristics with these 3D models as illustrated in the shear wave velocity cross-sections shown in Figure 5.12. These include: (1) the relatively thin crust (average 15 km) under the coastal region, which is evident in the northern region covered by the USGS Bay Area model, and (2) the presence of fast seismic velocities (up to  $V_s = 5.0$  km/s) below the Moho in the southern region, particularly for CVM-S4.26, and to a lesser extent for CVM-H.

For the inland region, both sets of UCVM 3D model synthetics are too fast compared to the data, which is primarily due to the fast (4.0 km/s) structure in the USGS Bay Area model in the lower crust. Hence, our model emphasizes the need for a slower structure beneath Eastern California compared with these models. On the other hand, the UCVM 3D model including CVM-H does well at matching the time delays near Imperial Valley, suggesting this model is adequately capturing the thinning of the crust in this region. The azimuthal record sections for all the models are shown

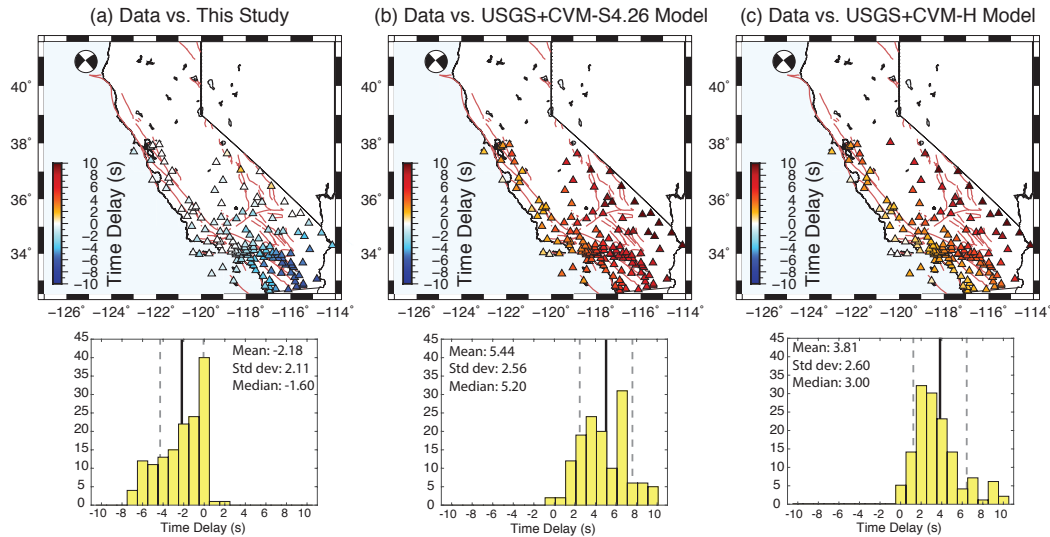


**Figure 5.14:** Maps show the time delay between the recorded long period SH waves from the 2014 Mendocino event, and the synthetics from (a) our preferred model, (b) USGS Bay Area and CVM-S4.26 Southern California model and (c) USGS Bay Area and CVM-Harvard Southern California model. Cooler color indicates the recorded seismograms arrive earlier than the synthetics. Histograms below the map show the distribution of the time delays for each model comparison.

in Figure 5.16. These profiles further highlight the timing differences among the models, and in particular demonstrate that the UCV 3D models predict arrivals at the inland sites that are up to 15 seconds earlier than the observations. We also note that the UCV 3D models have better fits for the amplitude of the later arrivals in the Love wave train, indicating these models have a better-resolved shallow crustal structure than our simplified model.

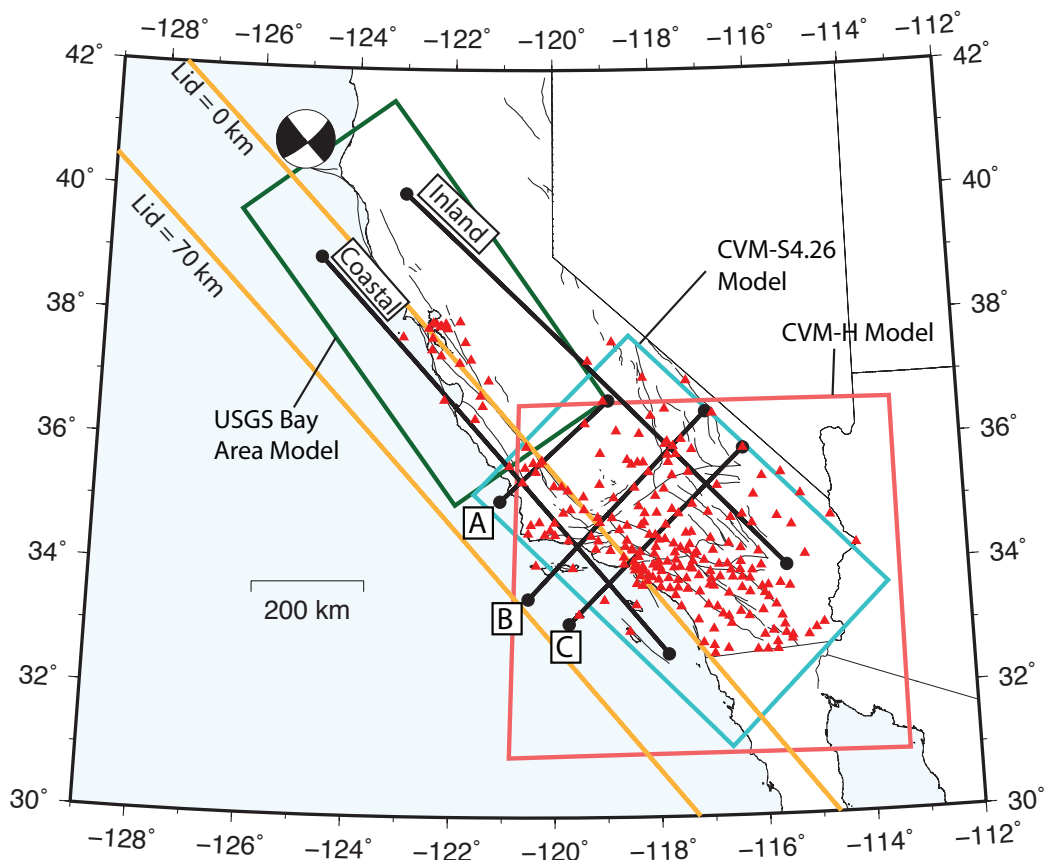


**Figure 5.15:** Map shows the boundary for each 3D velocity model used in this study. The parallel yellow lines delineate the growth of the lid structure in our preferred model. Green, blue and red boxes represent USGS Bay Area, CVM-S4.26 and CVM-H model respectively. The black solid lines show the location of cross-section profiles used in Figure 5.12 and Figure 5.16.

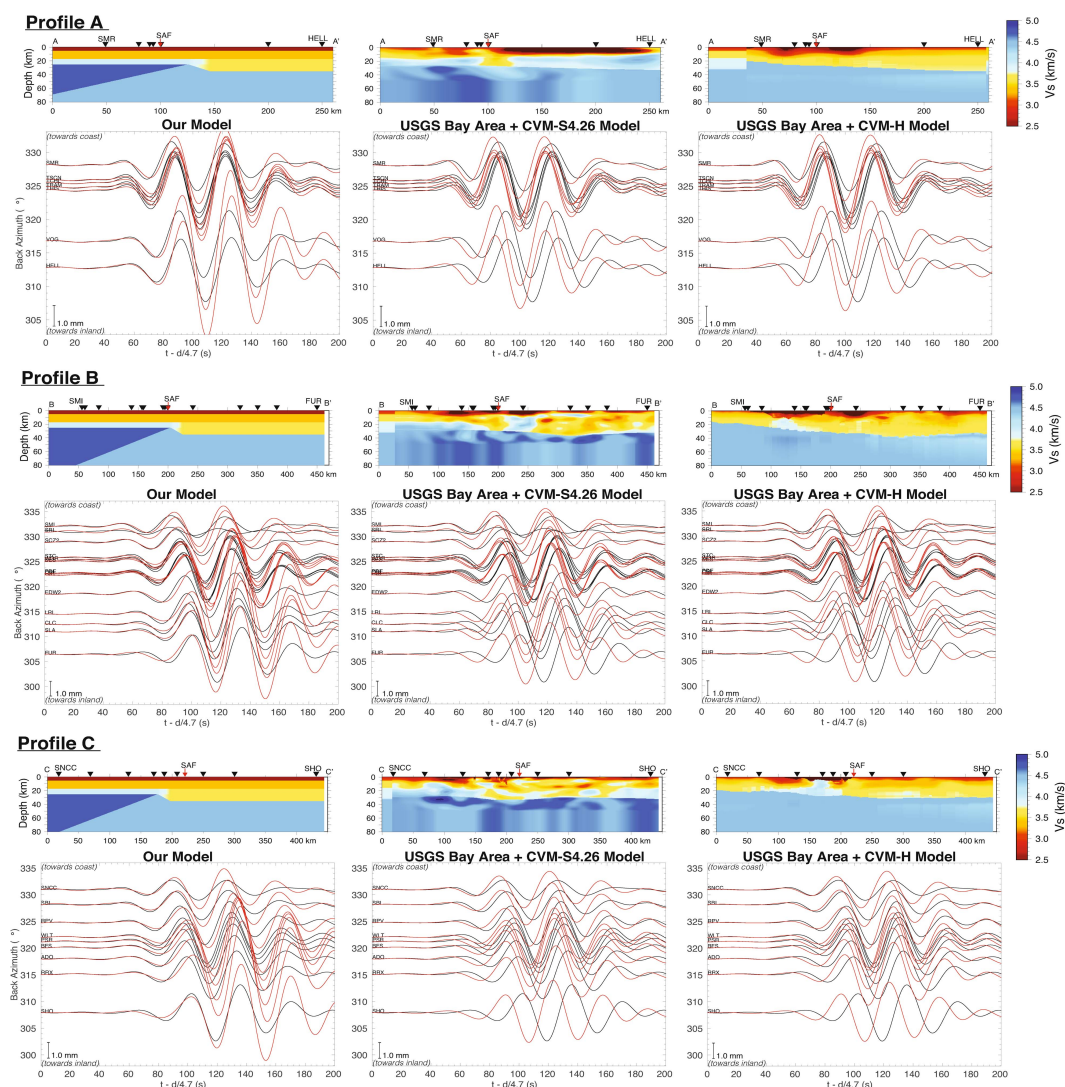


**Figure 5.16:** The azimuthal record sections show long period (30 – 50 seconds) SH waveforms recorded along Profile A, B and C (see Figure 5.3) for the 2014 Mendocino event. Black seismograms are data and red seismograms are synthetics. Synthetics are generated using three different velocity models: (a) our model shown in Figure 5.13, and two 3D velocity models with USGS Bay Area model for Northern California and for Southern California, (b) Community Velocity Model – SCEC (CVM-S4.26) version and (c) Community Velocity Model – Harvard (CVM-H) model. The cross-section profile of the shear wave velocity for each model is shown above the record section.

## 5.5 Discussion and Conclusion

The simple seismic velocity model we have developed in the present work only includes lateral variations in one horizontal dimension, and is thus insufficient to capture the full 3D complexity of the velocity structure in California, as illustrated in Figure 5.13c. In any case, even though our model is simple, it does provide direct evidence for a key characteristic of the lower crust – upper mantle structure beneath, which is the strong west-east lateral seismic velocity contrast across the plate boundary.

Our work suggests that the fast seismic lid feature extends beyond Baja California as initially proposed in Melbourne and Helmberger [9] and is, in fact, a continuous feature parallel to the SAF along the California coastline. The waveforms recorded from the Mendocino events propagate south and sample the lower crust – upper mantle structure along the entire region. In addition, the travel time move-out in the observed waveforms is significantly more pronounced for the Mendocino event compared to the Napa event. The Mendocino event originated 80 km offshore, and hence the waveforms sample more of the oceanic lid along the coast. The propagation path of the waveforms from the Napa event, which originated inland, are mostly restricted to inland paths, away from the coastline and therefore the move-out effect due to the lid is less evident.

The absolute thickness of the lid is not well constrained, as the thickness trades off with the lid velocity. However, the general behavior of the lid growing in thickness holds as we see in Figure 5.5 and Figure 5.6, there is a gradual increase in travel time difference for the waveforms as the ray paths shift westward. In order to fit the observations, the lid has to be significantly faster (i.e.  $V_s = 4.8$  km/s) than the velocity of upper mantle ( $V_s = 4.4 - 4.5$  km/s) in reference models. The high shear wave velocity of the lid suggests a highly mafic composition, consistent with the composition for Pacific oceanic lithosphere [7]. The currently available 3D velocity models for California do not adequately capture the travel-time variations seen in these regional waveform data. This suggests that these data could be used as constraints in future updates of these 3D models.

The observed strong lateral variation in the upper mantle structure beneath California likely contributes to the strain rate asymmetry and should play a significant role in modulating plate deformation. Assuming the seismic velocity as a proxy for lithospheric strength, the lid beneath the Pacific plate, with higher velocity, is thus much stronger than its surroundings and lends strength to the Pacific plate. The shear

wave velocity of the lid ( $V_s = 4.8$  km/s) is significantly higher than its surrounding medium: the lower crust has a maximum  $V_s$  of about 4.0 km/s and the upper mantle averages  $V_s$  of about 4.4 km/s. On the other hand, the relatively lower velocity of the deep crust and absence of a strong lid beneath the North American plate suggests weaker lithospheric strength. Thus, the upper mantle of the Pacific Plate should deform more rigidly and differs from the North American Plate, which is in the plastic flow regime [36].

Schmalzle et al. [3] showed a scenario on how variation in effective elastic thickness (EET) can explain the strain rate asymmetry across the San Andreas fault in the Carrizo Plain region in central California. Their best fitting result requires a 38 km EET west of SAF and an average of 12 km EET east of SAF. Taking the interseismic strain rate to be inversely proportional to the effective elastic thickness (EET) of the lithospheric plate, Chery [1] further showed that the interseismic strain rate profiles across northern, central and southernmost California are best modeled with a thin EET along the plate boundary and thick EET on the Pacific plate and Sierra Nevada province. The change in EET across the plate boundary follows closely along the SAF trace in northern and central California, and moves ~75 km westward towards Elsinore Fault in southernmost California (see Figure 5.17). Similarly, from geodetic data inversion for slip rates on faults in California, Platt and Becker [37] proposed that (1) the present velocity field reflects long-term plate motion and (2) the real lithospheric transform boundary does not necessarily follow the surface trace of SAF, but rather it is a zone up to 80 km wide, notably centered west of the SAF in southern California, and has a trend straighter and closer to the plate motion vector than the SAF.

Likewise, our model supports such a significant lateral variation in lithospheric strength or EET with a strong lid west of the plate boundary and a relatively thick, low velocity crust east of the plate boundary. A similar idea of lateral contrast in lithospheric properties is proposed in Ford et al. [19] through a  $S_p$  receiver function study as they observe a change in character of lithosphere-asthenosphere boundary across the plate boundary. In addition, the transform boundary in our simple model, marked by the growth of the lid structure, roughly follows along the local strike of SAF except in Southern California when it moves westward by ~100 km, which is in agreement with the position of the transform boundary proposed in Platt and Becker [37]. The transform boundary may be characterized as the juxtaposition of the strong Pacific plate due to the seismic lid, with the

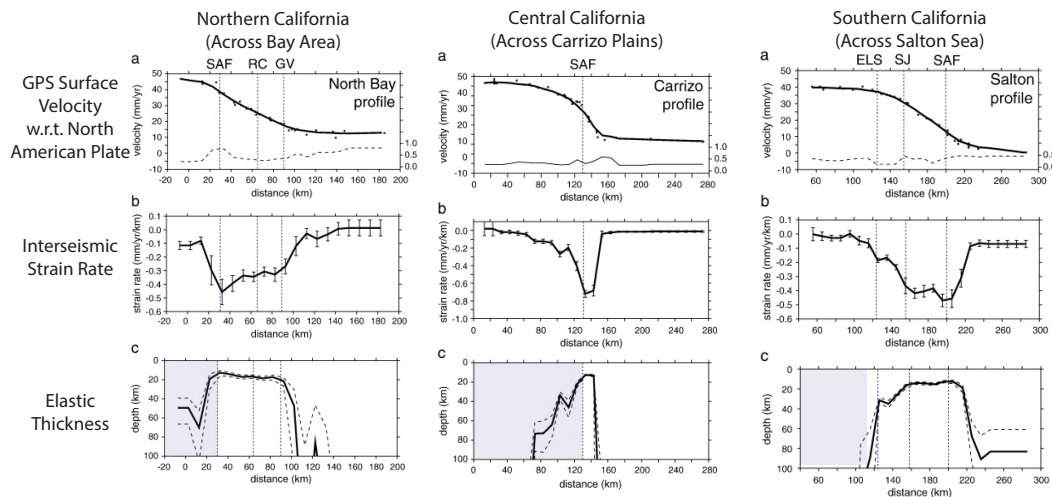


**Figure 5.17:** Interpretation of the GPS velocity fields along three profiles perpendicular to (i) Northern California, (ii) Central California, and (iii) Southern California as shown in Chery ([1], Figure 6,7 and 8). The exact location of each profile is found in Chery ([1], Figure 2). (A) GPS velocity measurement profiles crossing the San Andreas Fault System (SAF – San Andreas fault; RC – Rodgers Creek fault; GV – Green Valley fault; SJ – San Jacinto fault; ELS – Elsinore fault). The velocity measurements are assumed in [1] to be representative of interseismic strain with minimal postseismic signal as there have been no major earthquakes affecting San Andreas Fault since the 1906 San Francisco earthquake and the 1857 Fort Tejon earthquake. The dashed line shows the RMS of the curve and the discrete data points. (B) Fault-parallel horizontal strain rate is given by the slope of the least square adjustment of the interseismic velocity. (C) Assuming interseismic strain is due to deformation of a plate having effective thickness, the strain rate is inversely proportional to the elastic strength of the plate (i.e. the product of average shear modulus of the layer and the effective elastic thickness). The shaded region shows the location of lid suggested by the seismic observation in this paper, which corresponds well to the elastic thickness predicted from the GPS velocity field.

weak, ductile North American plate, where the lower crust - upper mantle structure beneath the Californian margin controls the strain rate observed in California. This plate boundary structure becomes even more complex in the southernmost portion of southern California (Imperial Valley) where the crust is quite thin due to the northward impingement of the East Pacific Rise into the North American plate. To more fully explore the consistency of our model with the strain-rate asymmetry and long-term plate deformation in California, additional quantitative analyses are needed which is beyond the scope of the current work.

The velocity contrast in our model bears resemblance to the slab window formed due to the migration of Mendocino Triple Junction during the evolution of the plate

boundary [38]. Based on our model, the lithospheric thinning [10, 11] may have been a prominent state-wide phenomenon along the east side of the plate boundary at the lower crust – upper mantle depth range. Our model focuses at much shallower depth compared to models from seismic tomography (up to 300 km in Wang et al. [11]), and hence it is less meaningful in terms of understanding past subduction processes or imaging fossil slabs. Nonetheless, our model, constructed from direct seismic observation, can provide useful constraints in the development of the next generation state-wide velocity models and informing the regional plate tectonic history.

This study illustrates the potential of using regional waveforms to investigate the laterally varying seismic velocity structure of the lower crust – upper mantle beneath California. Our simplified model, i.e. a fast seismic lid underlying the Pacific plate abutting against a thick crust with relatively low seismic velocities comprising the continental North American plate, does well at reproducing the systematic travel time variations of long period Sn waves observed across central and southern California for events in the Mendocino region. The strong heterogeneity in velocity suggests similar heterogeneity in lithospheric strength, which may modulate the plate deformation in this region.

## 5.6 Acknowledgements

This work is supported by USGS Earthquake Hazards Program award G15AP00029 along with partial support from NSF-Earthscope program, EAR-1358646 and USGS Cooperative Agreement G14AC00109. Constructive reviews provided by Brad Aagaard, Annemarie Baltay, Carl Tape and an anonymous reviewer were very helpful in improving the manuscript. Waveform data for this study were accessed through the Northern California Earthquake Data Center (NCEDC), doi: 10.7932/NCEDC, and Southern California Earthquake Data Center (SCEDC) at Caltech, doi: 10.7909/C3WD3xH1. Maps were created using General Mapping Tools (GMT) software [39].

## References

- [1] J. Chéry. Geodetic strain across the san andreas fault reflects elastic plate thickness variations (rather than fault slip rate). *Earth and Planetary Science Letters*, 269(3-4):352–365, 2008.
- [2] S. Wdowinski, B. Smith-Konter, Y. Bock, and D. Sandwell. Diffuse interseis-

- mic deformation across the Pacific-North America plate boundary. *Geology*, 35(4):311–314, 2007.
- [3] G. Schmalzle, T. Dixon, R. Malservisi, and R. Govers. Strain accumulation across the Carrizo segment of the San Andreas Fault, California: Impact of laterally varying crustal properties. *Journal of Geophysical Research: Solid Earth*, 111(B5), 2006.
- [4] D. L. Anderson. Lithosphere, asthenosphere, and perisphere. *Reviews of Geophysics*, 33(1):125–149, 1995.
- [5] S. Stein and M. Wysession. *An introduction to seismology, earthquakes, and earth structure*. John Wiley & Sons, 2009.
- [6] J. B. Gaherty, M. Kato, and T. H. Jordan. Seismological structure of the upper mantle: a regional comparison of seismic layering. *Physics of the Earth and Planetary Interiors*, 110(1-2):21–41, 1999.
- [7] Y. Tan and D. V. Helmberger. Trans-Pacific upper mantle shear velocity structure. *Journal of Geophysical Research: Solid Earth*, 112(B8), 2007.
- [8] S. P. Grand and D. V. Helmberger. Upper mantle shear structure of North America. *Geophysical Journal International*, 76(2):399–438, 1984.
- [9] T. Melbourne and D. Helmberger. Mantle control of plate boundary deformation. *Geophysical research letters*, 28(20):4003–4006, 2001.
- [10] G. Zandt and K. P. Furlong. Evolution and thickness of the lithosphere beneath coastal California. *Geology*, 10(7):376–381, 1982.
- [11] Y. Wang, D. W. Forsyth, C. J. Rau, N. Carriero, B. Schmandt, J. B. Gaherty, and B. Savage. Fossil slabs attached to unsubducted fragments of the Farallon plate. *Proceedings of the National Academy of Sciences*, 110(14):5342–5346, 2013.
- [12] E. Hauksson. Crustal structure and seismicity distribution adjacent to the Pacific and North America plate boundary in southern California. *Journal of Geophysical Research: Solid Earth*, 105(B6):13875–13903, 2000.
- [13] K. Prindle and T. Tanimoto. Teleseismic surface wave study for S-wave velocity structure under an array: Southern California. *Geophysical Journal International*, 166(2):601–621, 2006.
- [14] C. Tape, A. Plesch, J. H. Shaw, and H. Gilbert. Estimating a continuous Moho surface for the California unified velocity model. *Seismological Research Letters*, 83(4):728–735, 2012.
- [15] L. Zhu and H. Kanamori. Moho depth variation in southern California from teleseismic receiver functions. *Journal of Geophysical Research: Solid Earth*, 105(B2):2969–2980, 2000.

- [16] Z. Yan and R. W. Clayton. Regional mapping of the crustal structure in southern California from receiver functions. *Journal of Geophysical Research: Solid Earth*, 112(B5), 2007.
- [17] V. Lekic, S. W. French, and K. M. Fischer. Lithospheric thinning beneath rifted regions of Southern California. *Science*, 334(6057):783–787, 2011.
- [18] A. Levander and M. S. Miller. Evolutionary aspects of lithosphere discontinuity structure in the western US. *Geochemistry, Geophysics, Geosystems*, 13(7), 2012.
- [19] H. A. Ford, K. M. Fischer, and V. Lekic. Localized shear in the deep lithosphere beneath the San Andreas fault system. *Geology*, 42(4):295–298, 2014.
- [20] C. W. Jennings et al. *Fault activity map of California and adjacent areas*. California. Division of Mines and Geology, 1995.
- [21] C. Ji, S. Tsuboi, D. Komatitsch, and J. Tromp. Rayleigh-wave multipathing along the west coast of North America. *Bulletin of the Seismological Society of America*, 95(6):2115–2124, 2005.
- [22] D. S. Dreger and B. A. Romanowicz. *Source characteristics of events in the San Francisco Bay region*. University of California, 1995.
- [23] L. Zhu and L. A. Rivera. A note on the dynamic and static displacements from a point source in multilayered media. *Geophysical Journal International*, 148(3):619–627, 2002.
- [24] T. M. Brocher, J. McCarthy, P. E. Hart, W. S. Holbrook, K. P. Furlong, T. V. McEvelly, J. A. Hole, and S. L. Klemperer. Seismic evidence for a lower-crustal detachment beneath San Francisco Bay, California. *Science*, 265(5177):1436–1439, 1994.
- [25] L.-S. Zhao and D. V. Helmberger. Source estimation from broadband regional seismograms. *Bulletin of the Seismological Society of America*, 84(1):91–104, 1994.
- [26] Lupei Zhu and Donald V Helmberger. Advancement in source estimation techniques using broadband regional seismograms. *Bulletin of the Seismological Society of America*, 86(5):1634–1641, 1996.
- [27] R. B. Herrmann. Computer programs in seismology: An evolving tool for instruction and research. *Seismological Research Letters*, 84(6):1081–1088, 2013.
- [28] C. J. Ammon and G. Zandt. Receiver structure beneath the southern Mojave block, California. *Bulletin of the Seismological Society of America*, 83(3):737–755, 1993.

- [29] D. V. Helmberger, X. J. Song, and L. Zhu. Crustal complexity from regional waveform tomography: Aftershocks of the 1992 Landers earthquake, California. *Journal of Geophysical Research: Solid Earth*, 106(B1):609–620, 2001.
- [30] X. J. Song, D. V. Helmberger, and L. Zhao. Broad-band modelling of regional seismograms: The basin and range crustal structure. *Geophysical Journal International*, 125(1):15–29, 1996.
- [31] R. W. Graves. Simulating seismic wave propagation in 3D elastic media using staggered-grid finite differences. *Bulletin of the Seismological Society of America*, 86(4):1091–1106, 1996.
- [32] B. T. Aagaard, R. W. Graves, A. Rodgers, T. M. Brocher, R. W. Simpson, D. Dreger, N. A. Petersson, S. C. Larsen, S. Ma, and R. C. Jachens. Ground-motion modeling of Hayward fault scenario earthquakes, part ii: Simulation of long-period and broadband ground motions. *Bulletin of the Seismological Society of America*, 100(6):2945–2977, 2010.
- [33] E.-J. Lee, P. Chen, T. H. Jordan, P. B. Maechling, M. A. M. Denolle, and G. C. Beroza. Full 3-D tomography for crustal structure in southern California based on the scattering-integral and the adjoint-wavefield methods. *Journal of Geophysical Research: Solid Earth*, 119(8):6421–6451, 2014.
- [34] J. H. Shaw, A. Plesch, C. Tape, M. P. Suess, T. H. Jordan, G. Ely, E. Hauksson, J. Tromp, T. Tanimoto, R. Graves, et al. Unified structural representation of the southern California crust and upper mantle. *Earth and Planetary Science Letters*, 415:1–15, 2015.
- [35] D. Hadley and H. Kanamori. Seismic structure of the Transverse Ranges, California. *Geological Society of America Bulletin*, 88(10):1469–1478, 1977.
- [36] D. L. Kohlstedt, B. Evans, and S. J. Mackwell. Strength of the lithosphere: Constraints imposed by laboratory experiments. *Journal of Geophysical Research: Solid Earth*, 100(B9):17587–17602, 1995.
- [37] J. P. Platt and T. W. Becker. Where is the real transform boundary in California? *Geochemistry, Geophysics, Geosystems*, 11(6), 2010.
- [38] K. P. Furlong and S. Y. Schwartz. Influence of the Mendocino triple junction on the tectonics of coastal California. *Annu. Rev. Earth Planet. Sci.*, 32:403–433, 2004.
- [39] P. Wessel, W. H. F. Smith, R. Scharroo, J. Luis, and F. Wobbe. Generic mapping tools: improved version released. *Eos, Transactions American Geophysical Union*, 94(45):409–410, 2013.

*Chapter 6***SEISMIC EVIDENCE FOR THE SOURCE OF THE HAWAIIAN HOTSPOT****6.1 Abstract**

Strong waveform complexity from Fiji-Tonga earthquakes recorded at particular azimuths and distances by USArray stations suggests a plume structure, located roughly 120 southeast of Hawaii. This location is defined by observations of (1) rapid changes in differential (ScS-S) times and (2) multi-pathing of ScS and diffracted S waveforms. Seismic waveform modelling result shows anomalous seismic features occurring at the edge of the Pacific Large Low Shear Velocity Province (LLSVP), where a slow structure with shear wave velocity ( $V_S$ ) reduction up to 15% and a fast structure ( $V_S$  at +2.5%) intersect. These seismic features are proposed to be a subducting slab impinging on the edge of the LLSVP where a dense ultra-low velocity zone structure is also present. The configuration of the ULVZ and slab at the edge of the LLSVP is ideal for plume initiation which is presented in our model as a slow structure extending upward for at least 600 km with a  $V_S$  reduction of 5%. This slow structure is necessary in order to explain the rapid time variation in S which is not observed in ScS. Recent mantle flow models based on paleo-reconstruction of the north Pacific plate also suggest strong interactions between subducted slabs and the Pacific LLSVP over geological time and places the present-day plume in the same vicinity as our model, which explains the migration pattern and sharp bend of the Hawaiian-Emperor seamount chain.

**6.2 Introduction**

Volcanic hotspot tracks, such as the Hawaii-Emperor seamount chain, with progressive change in volcanism age, were first hypothesized by Wilson [1] to be formed due to Pacific plate moving over a fixed, focused spot of melting in the mantle. Morgan [2] later proposed the melt to originate from plumes in the deep mantle and the changes in the hotspot migration pattern are due to changes in plate motion over a fixed plume. However, the hypothesis of a fixed plume does not explain several key features observed in the Hawaii-Emperor seamount chain and not in other hotspot tracks in the Pacific (e.g. Louisville), which include a relatively sharp bend at 47 Ma, rapid change in migration rate of volcanic islands between 87 Ma and 47 Ma

and the formation of individual volcanoes at different paleolatitudes [3]. While Steinberger et al. [4] focus on the role of global mantle flow model in distorting the plume upwelling and hence the manifestation of several hotspot tracks on surface, Hassan et al. [5] argue that the sharp bend and migration rate in Hawaii hotspot can be explained by the migration of the source of the hotspot plume rooted near the edge of a large thermochemical structure at the core-mantle boundary, known as the Pacific Large Low Shear Velocity Province (LLSVP). With a mantle flow model, Hassan et al. show the influence of strong and persistent subduction activity in the north Pacific in deforming the Pacific LLSVP, controlling deep mantle flow and causing the southward migration of the Hawaiian plume to its current location at the northeastern boundary of the LLSVP (Figure 6.1, Box B).

There have been several observations suggesting the presence of multiple structural anomalies along the northeastern margin of the Pacific LLSVP [7, 8, 9, 10, 11, 12]. A recent study by Sun et al. [7] use teleseismic data from Fiji-Tonga earthquakes recorded by USArray and observe strong multipathing of ScS. These secondary arrivals that follow the main ScS pulse can be modelled by an Ultra-Low Velocity Zone (ULVZ) structure with a preferred thickness of 80 km and shear velocity reduction of -15% at a location southeast of Hawaii at the far edge of the LLSVP (Figure 6.1, Box A). In addition, Scd phases are also observed and these may be indicative of a phase change from bridgmanite to post-perovskite at the top of D'' layer. The phase change can be interpreted either by changes in temperature gradient and iron enrichment towards the edge of the LLSVP [9] or interaction with slabs from past subduction which favors the appearance of D'' [13]. Other seismic observations such as relative travel time from shear wave splitting in S and Sdiff show strong variation in the strength of anisotropy in the same region, with  $V_{SH} > V_{SV}$ , which is interpreted as evidence for strong regional mantle flow [14] although it can be also be described by the presence of past subducted slab material along the core-mantle boundary or a combination of both. However, additional short period diffracted phases from Sun et al. [7], which sample the same region, show  $V_{SV} > V_{SH}$  instead, highlighting the challenges in measuring shear wave anisotropy [15]. The anisotropy measured may also arise from presence of other small-scale structures potentially made of a strongly anisotropic mineral such as magnesiowüstite [16] and complex mantle flow pattern [17] near the edge of the LLSVP.

Global tomographic models (Figure 6.2), inverted from a wide variety of data sets including surface waves, body waves, and normal modes, are useful in broadly

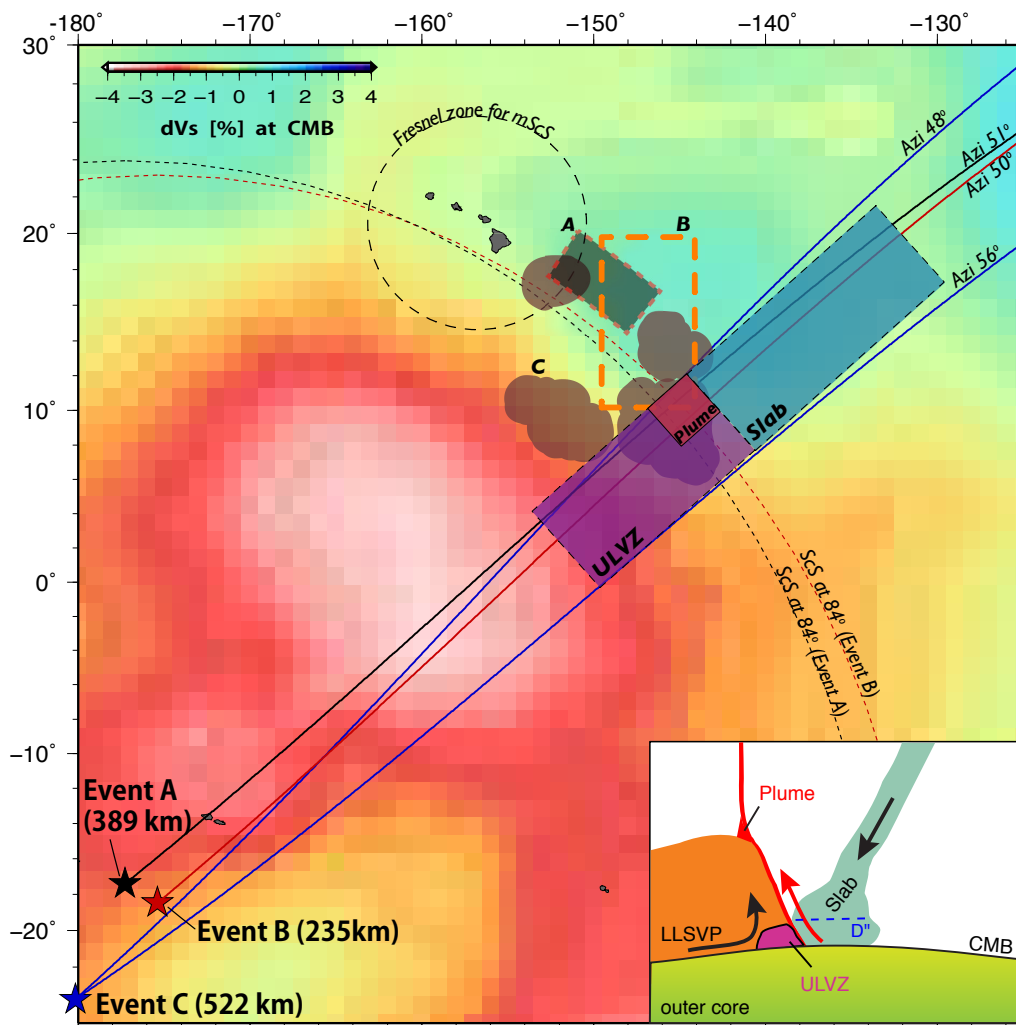


**Figure 6.1:** Colored background shows the shear wave velocity perturbation at the core-mantle boundary from GyPSuM [6]. The map shows the location and ray paths of events used in this study, bounce point of ScS for Event A and B at a distance of  $84^\circ$ , and the location of ULVZ, plume and slab, as suggested by the modeling process in this study. Box A marks the location of ULVZ proposed by Sun et al. [7]; Box B is the estimated current plume location by Hassan et al. [5]. Box C (grey patches) shows the location of various ULVZ structures observed in Zhao et al. [8]. Fresnel zone of 1,000 km diameter for multiple ScS sampling beneath Hawaii is also shown. Inset shows the schematic of the interaction of subducted slab as it encounters the edge of the LLSVP, that encourages the development of an iron-enriched region represented by ULVZ and a feeder to a possible plume.

defining the boundaries of LLSVP and interpreting mantle structures such as possible broad plumes beneath hotspots [18, 19]. ScS and its multiples at near vertical path are sensitive to structure within a diameter of about 1000 km extending down to the core-mantle boundary [20], providing a unique opportunity to test the presence of possible large plume structures directly beneath the hotspots. Kanamori and Rivera [21] show that the Q structure and shear wave speed beneath Hawaii is similar to the average mantle, consistent with the findings from Best et al. [22]. Meanwhile the Q structure and shear wave model is highly anomalous for other island stations, particularly station AFI beneath Samoa Islands. The global models can be tested by predicting the ScS multiple travel times, we generate 3D synthetics from two representative global models, S40RTS [23] and S362ANI [24] using the 3D spectral-element method [25], for the 4 May 2018 M6.9 Hawaii Island earthquake. We observe that the synthetics are significantly delayed compared to the data, which suggest the large vertical plume imaged in the tomographic models directly beneath Hawaii is not compatible with observation (Figure 6.3).

The proximity of subducted slabs and the Pacific LLSVP, as suggested by seismic observation, can give rise to a strong horizontal thermal gradient, causing a sharper and steeper LLSVP edge [28]. Furthermore, internal convection within the LLSVP may concentrate the warmer and compositionally distinct structures like ULVZs to the edges of LLSVP [9], where potential plume upwelling may develop locally near the thermochemical pile margin, summarized by the schematics in Figure 6.1. In this study, we will show seismic evidence for complex interaction between subducted slab and ULVZ at the edge of the Pacific LLSVP, which could provide evidence for the source of the Hawaiian plume.

### 6.3 Data

Waveforms from deep earthquakes in Fiji-Tonga region recorded by the dense USArray provide a unique opportunity to image the rapid lateral variation of the fine-scale structures along the northeastern edge of the Pacific LLSVP. Strong multipathing of ScS have been observed at two distinct patches along this boundary for several earthquakes (Figure 6.4). The northern structure (Figure 6.1, Box A) is modeled extensively in Sun et al. [7]. The southern structure and its implication of the multipathing of Sdiff and ScS-S travel time will be the focus of this study. We use three selected events from the United States Geological Survey (USGS) earthquake catalog, namely Event A (2008-07-19 M6.4 at 389 km), Event B (2008-10-22 M6.4 at 235 km) and Event C (2011-07-29 M6.7 at 522 km) to study the boundary cen-

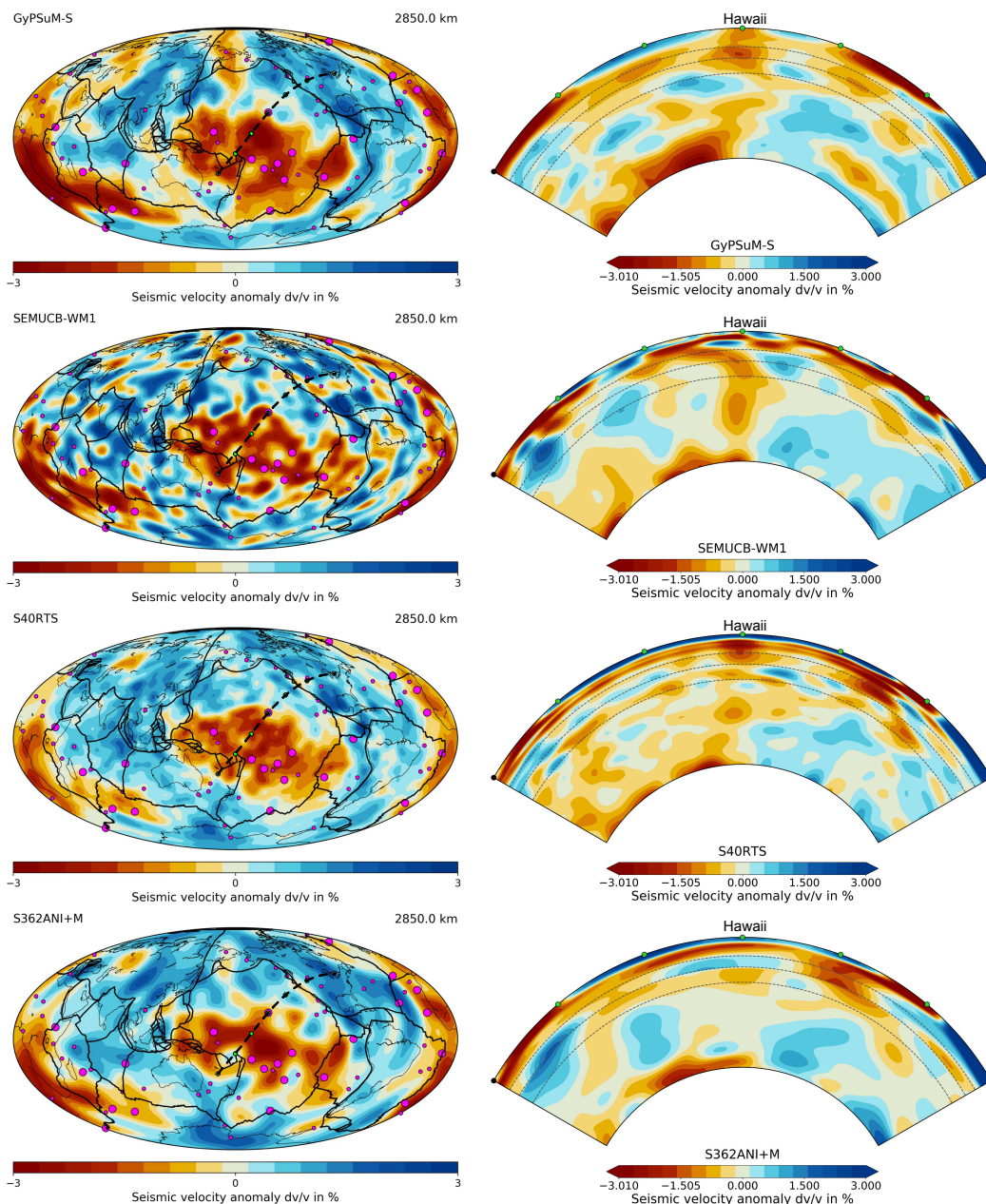


**Figure 6.2:** Left column shows shear wave seismic velocity anomaly at 2850 km depth for four global models (GyPSuM [6], SEMUCB-WM1 [26], S40RTS [23], and S362ANI [24]). Purple dots denote hotspots on surface. Right column shows the cross-section profiles from Fiji-Tonga region, through Hawaii towards North America for the four models. GyPSuM model shows the strongest velocity reduction for the Pacific LLSVP, while models like SEMUCB-WM1 and S40RTS show continuous slow structure from core mantle boundary towards the surface. Figure is made using SubMachine web-based tool [27].

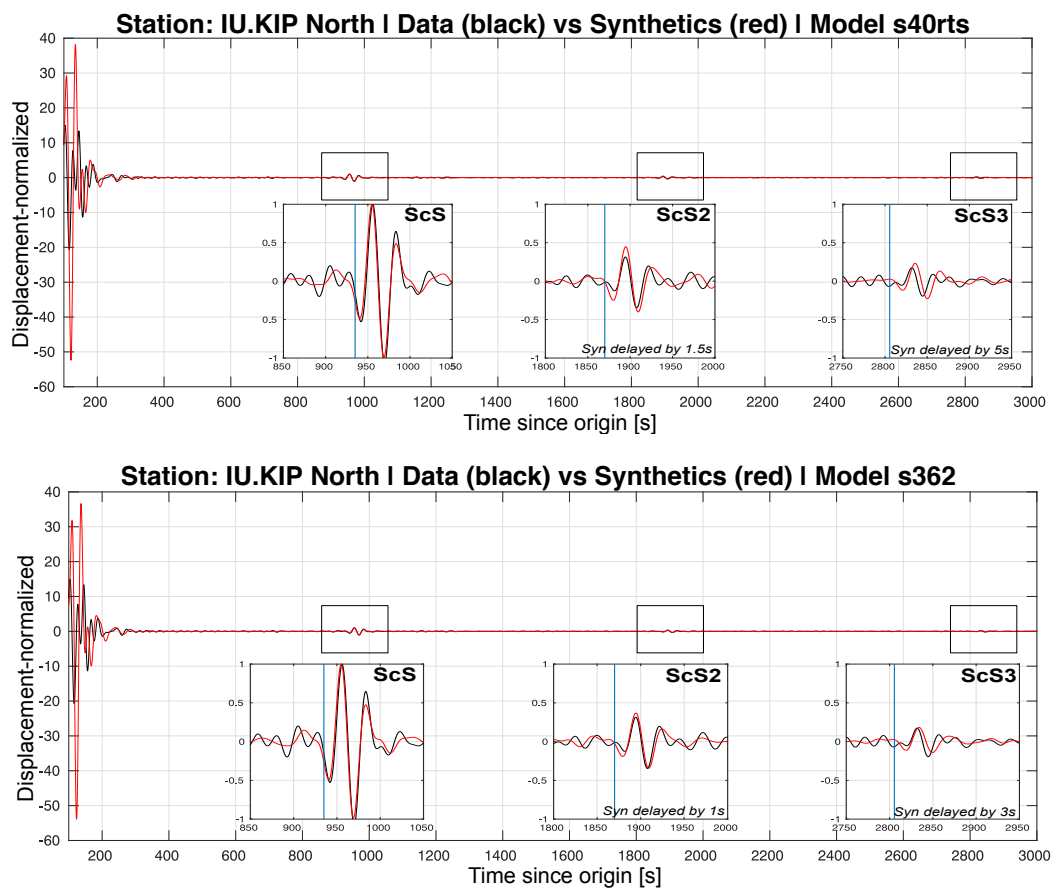


**Figure 6.3:** Multiple ScS with vertical incident angle is particularly sensitive to the structural anomalies across the whole mantle. If there were structural anomalies not predicted by model, the differential time between the multiple ScS will increase as the travel time error accumulates with each pass across the anomalies. We generate synthetics using 3D-SPECFEM for model S40RTS [23] and S362ANI [24] for the 2019-05-04 M6.9 earthquake on Big Island, Hawaii, recorded at IU.KIP station, which is 3 degrees away. The waveforms are normalized based on the first ScS arrival. We show the data (in black), predicted arrivals by PREM (blue line), and the 3D synthetics which are delayed compared to data, particularly for ScS3 (6 passes across the mantle). The 3D models suggest a possible large vertical plume directly beneath Hawaii. However, the mismatch between data and 3D synthetics suggests that the velocity structure directly beneath Hawaii with a Fresnel zone of 1000 km [20] is relatively simple and excludes the model with large vertical plume.

tered at N 10° W 145° (Figure 6.1). Based on the location of the transportable array during the time of earthquake, both Event A and Event B recorded S and ScS phases at distance of 75° to 90°, while Event C recorded S and Sdiff phases at distance of 95° to 105°. To avoid complexities due to anisotropy, we focus only on the tangential component in this study, filtered at 5 - 80 seconds. To increase the signal-to-noise ratio, the data from stations within 83 km are stacked by aligning the waveform at expected arrival time of S in the 1-D IASP reference model. Note that the average distance between stations within USArray is about 70 km.

Event Data	Latitude	Longitude	Depth (km)
2007-10-16	-25.70	179.72	512
2006-08-15	-21.18	-175.70	162
2007-08-26	-17.34	-173.84	130
2008-10-22 (Event B)	-18.40	-174.98	235
2010-08-16	-20.74	-178.67	604
2005-03-19	-21.88	-179.27	609
2005-08-06	-19.60	-175.35	218
2006-06-02	-20.77	-178.54	585
2008-07-19 (Event A)	-17.22	-177.05	389
2010-09-16	-16.00	-173.49	93
2012-04-28	-18.79	-174.26	141

**Table 6.1:** Deep events in Fiji-Tonga region used in measuring differential ScS-S time in Figure 6.4.

At large teleseismic distances, S and ScS share similar ray paths at the source and receiver ends and thus, its differential time (ScS-S) is sensitive to the structural anomalies in the deep mantle. Both Event A and Event B show strong azimuthal variation in differential ScS-S travel time between azimuth 40 - 43° and azimuth 50 - 52° towards the south, where at azimuth 50 - 52°, the differential time at closer distances is larger than that at azimuth 40 - 43° and rapidly becomes smaller at larger distances (Figure 6.5). A different method of stacking leads to a similar observation (Figure 6.7). Record section for Event A and Event B are also plotting in Figure 6.8 and 6.9 respectively. For Event B (Figure 6.9), rapid variation of ScS waveform is observed at azimuth 50 - 55° at distance of 84 - 86°, hinting at the role of complicated structural anomalies affecting ScS at the core-mantle boundary. The azimuthal variation becomes more obvious when the arrival time of S and ScS at each individual station with respect to 1-D IASP model is shown on the map, where S and ScS are significantly late at larger azimuths (Figure 6.6). However, the locations, where the delay in S and ScS are observed, are different, resulting in a

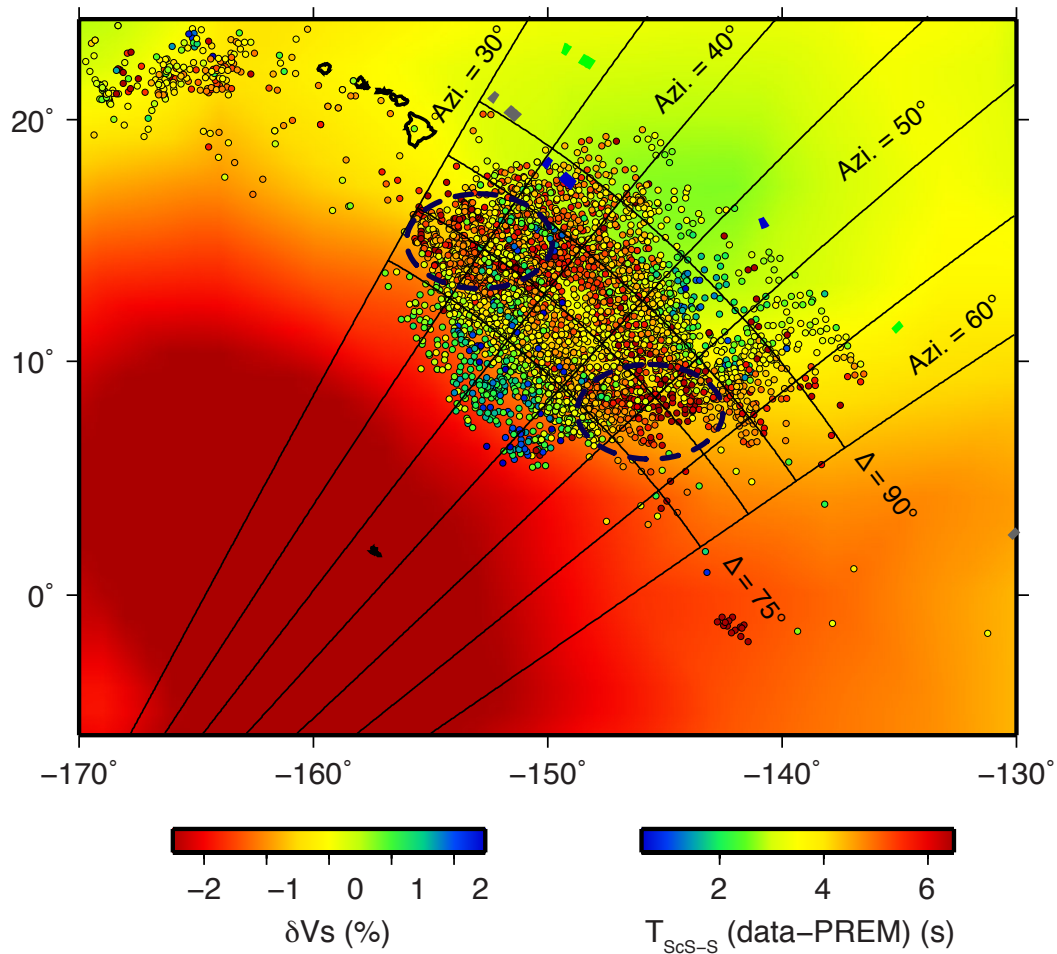


**Figure 6.4:** Measurements of ScS-S differential travel time residuals for several events (in Table 6.1 mapped to ScS core-mantle boundary reflection points. The differential ScS-S travel time are corrected with that expected by the Preliminary Reference Earth Model (PREM). The ray paths are plotted for Event B. The region shows significant variations in the travel time, with two particular regions with dashed black ellipse have differential ScS-S time delayed up to 6 seconds, suggesting possible ultra low velocity zones. The northern structure is modeled extensively in Sun et al. [7]. The southern structure and its implication of the multipathing of Sdiff and ScS-S travel time will be the focus of this study.

steeper gradient in the differential ScS-S travel time observed at the larger azimuths. The different locations also indicate that the structural anomalies causing the travel time differences are not in upper mantle structure at the receiver side, but confined in the lowermost mantle as S turns at a shallower depth and ScS samples the core-mantle boundary. There are some strong anomalies in differential ScS-S time at smaller azimuths due to strong delay in ScS travel time, caused by the previously imaged ULVZ structure in Sun et al. [7].

In addition, S diffracted ‘Sdiff’ phases from Event C recorded at distances greater than  $100^\circ$  show strong azimuthal variation in multipathing, where an additional pulse, namely  $S^*$ , is observed arriving after the main Sdiff pulse. Using a multipath detector developed by Sun et al. [29], we measure the time lapse between  $S^*$  and S for Event C in which a larger time lapse is a proxy to stronger multipathing. At azimuth near  $50^\circ$ , we observe large time lapse, i.e. strong multipathing, with a sharp boundary at azimuth  $48^\circ$  (Figure 6.10). The azimuthal variation of the multipathing effect is stronger at shorter period (less than 8 seconds) and is not seen at period of 15 seconds and longer, highlighting the need of going to shorter period to map lateral variation (Figure 6.11). The strong multipathing in Sdiff at larger azimuths is also observed by To et al. [10], namely phase A in their paper. Although the multipathing is not modeled in their study, their observation and other models suggest that the multipathing of Sdiff is caused by the presence of localized ULVZ existing inside or at the edge of the larger slow anomaly region like the LLSVP.

Both observations of (1) rapid variation of differential ScS-S travel time and (2) multipathing of Sdiff, occurring in the same locality along the Pacific LLSVP, are strong indicators of complex interaction between several distinct structures at the edge of the LLSVP as suggested by several previous studies [7, 8, 9, 10, 11]. In the next few sections, we will show models that can sufficiently explain both independent observations, and the importance of these structures in constraining mantle flow in the lowermost mantle.

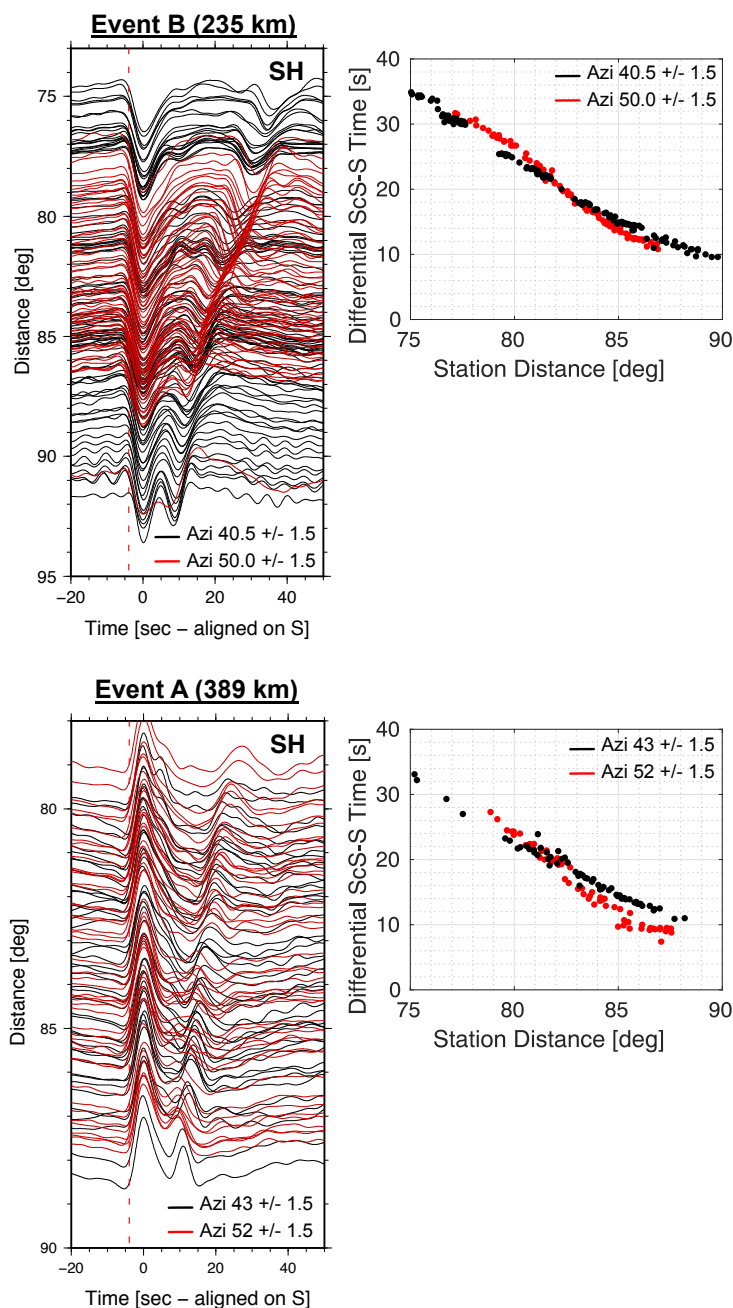


**Figure 6.5:** The record section on the left shows S and ScS (aligned at the peaks of S) along two azimuths for Event A and Event B. The waveforms are tangential displacements filtered at 5 – 80 seconds, black for azimuth  $\sim 40^\circ$  are in black, and red for azimuth  $\sim 50^\circ$ . The graph shows the differential ScS-S travel time with station distance for the two azimuths, highlighting the delay and later speed-up of differential ScS-S time for azimuth  $50^\circ$  compared to azimuth  $40.5^\circ$ . The stations used are shown in the map in Figure 6.6.

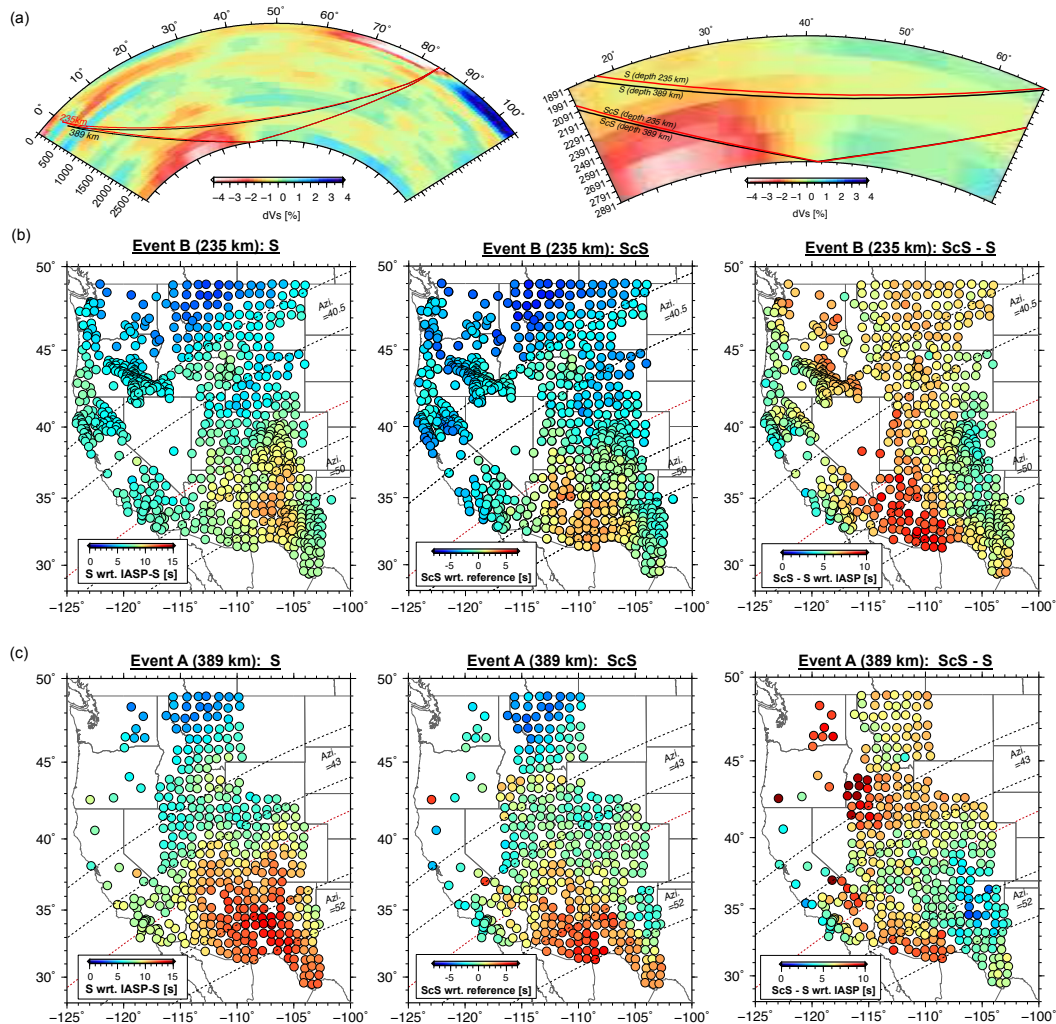


**Figure 6.6:** (a) Cross-sections of GyPSuM model for event A and B, showing the similar ray paths for ScS and S at the receiver ends, but sampling different depths and different structures along the core-mantle boundary. (b) Maps showing the arrival time of S and ScS phase, and differential ScS-S time at each station, with respect to the expected arrival time based on 1-D IASP velocity model for Event B at 235 km. For ScS time, the mean is removed as well. Strong anomalous delays are observed for both S and ScS at stations in Southwest USA and the delays are not co-located, resulting in steeper gradient in differential ScS-S time seen in Figure 6.5.

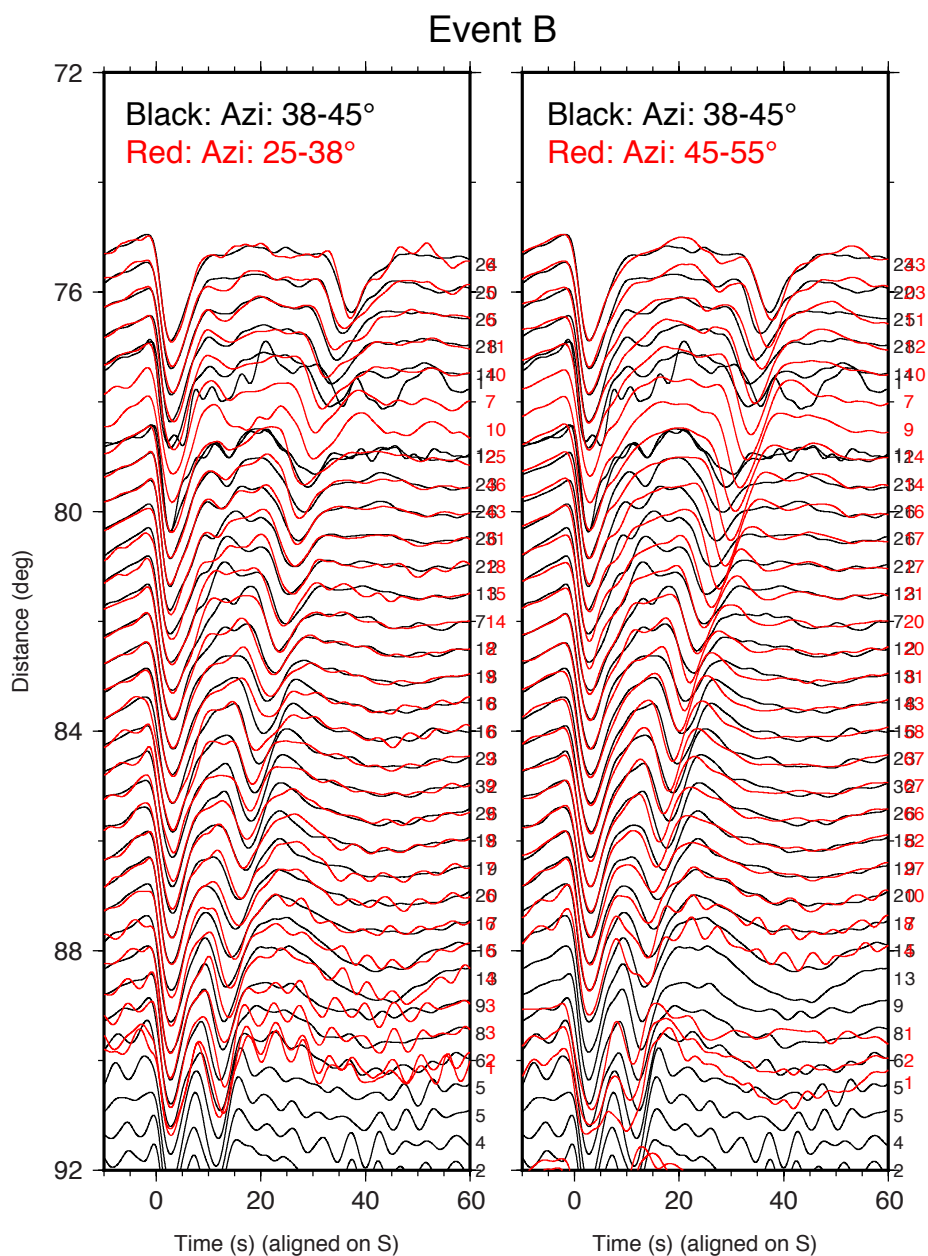


**Figure 6.7:** The record sections compare data stacks at three different azimuth bins ( $25 - 38^\circ$ ,  $38 - 45^\circ$ ,  $45 - 55^\circ$ ) use a different stacking method (also used in Sun et al., 2019) for Event B. The traces are aligned along the peaks of the S phase. Number after each trace indicates the number of stacked records. Left panel shows that there is no difference in the differential ScS-S travel time between the smaller azimuths  $25 - 38^\circ$  (in red) and  $38 - 45^\circ$  (in black). Right panel shows that at the larger azimuth  $45 - 55^\circ$  (in red), ScS arrives late at shorter distances, and speeds up at later distances, compared to that of azimuth  $38 - 45^\circ$  (in black).

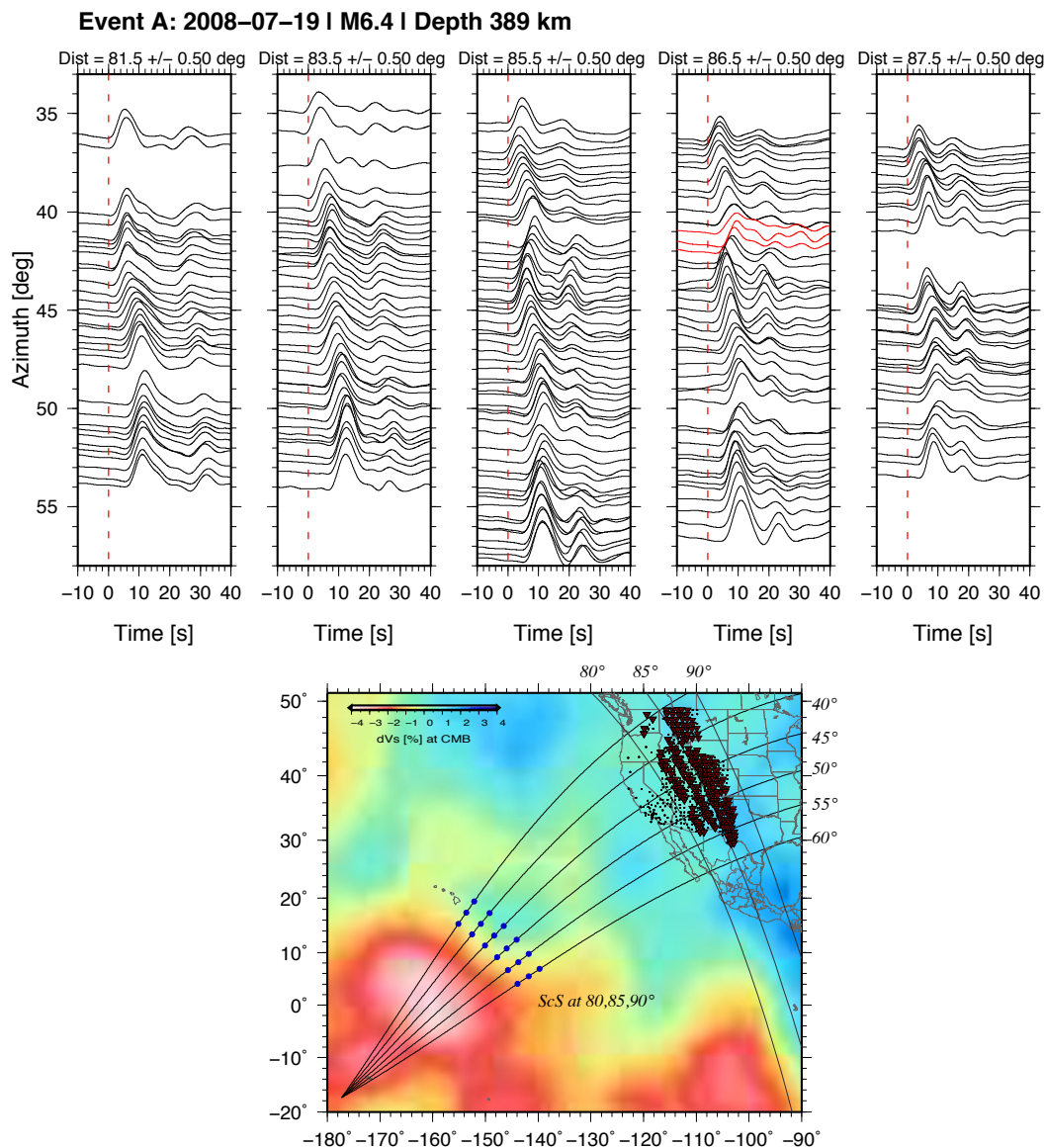


**Figure 6.8:** The record sections compare stacked tangential displacement data at five different distances for Event A (2008-07-19 M6.4 at the depth of 389 km). The data is bandpass filtered at 5 - 80 seconds, and aligned according to IASP S arrival time. Note the weaker amplitude of ScS and S at distance 85.5°, at azimuth 50 - 53°. Red traces mark stations at Yellowstone, which have very complicated waveforms and hence excluded from the ScS-S analysis. Map below shows the location of the stations plotted, ray paths for different azimuths, and the bounce point for ScS at distance 80, 85, and 90°.



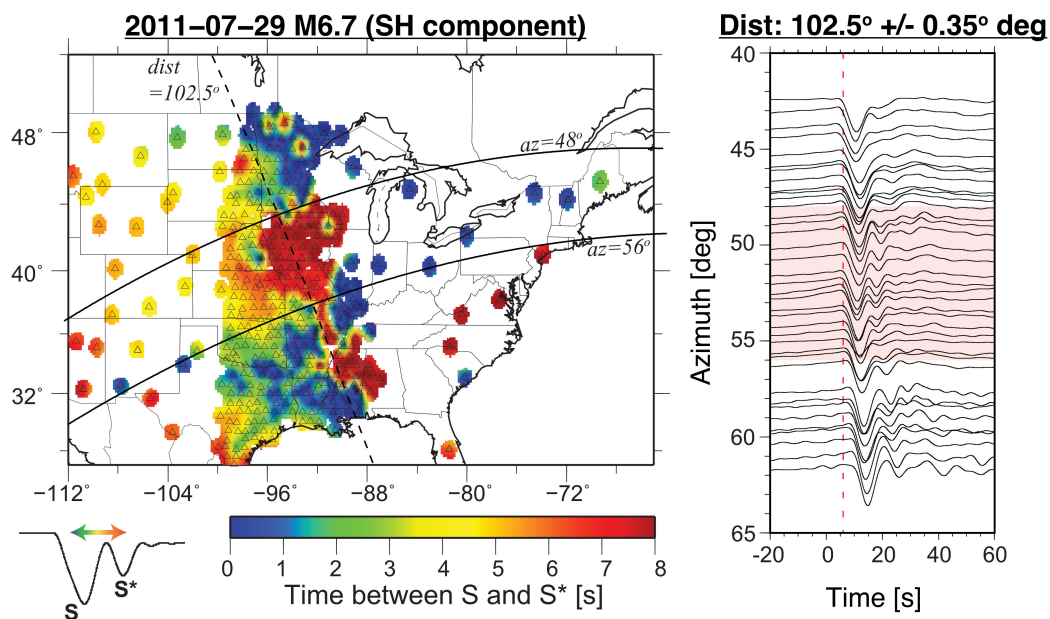


**Figure 6.10:** Left diagram shows the measured time lapse between SH diffracted phase and the observed S\* phase, using the multipath detector [29] for Event C. The phenomenon of S\* is most prominent between azimuth 48° and 56°. Right diagram shows the arrival of SH diffracted phase at distance 102.5° across azimuth, with S\* observed at selective azimuths (48° to 56°) and after 60°. The waveforms are tangential displacement, bandpass filtered at 5 – 80 seconds.

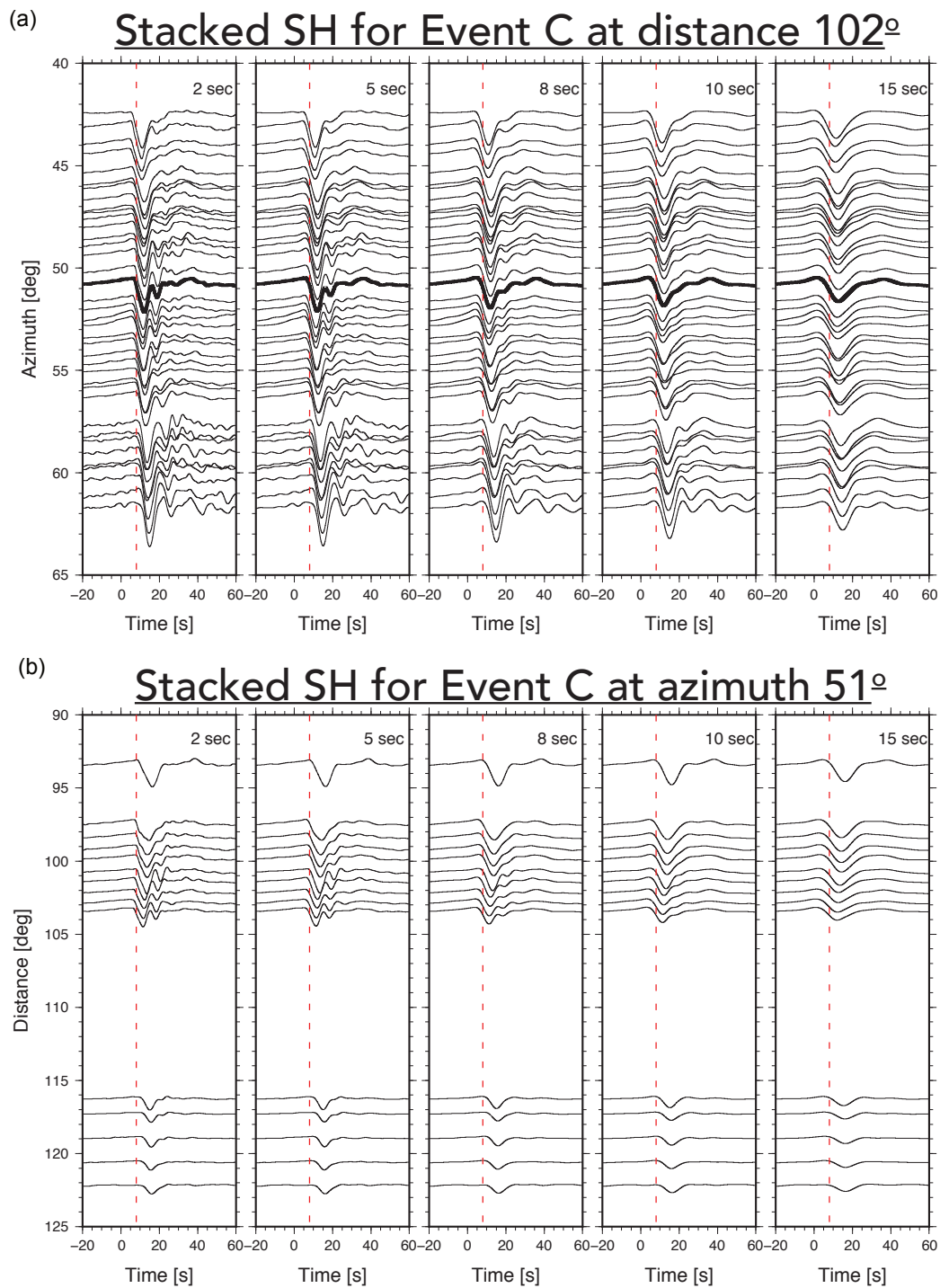


**Figure 6.11:** (a) The record sections compare stacked tangential displacement data from Event C at distance of  $102^\circ$  across a range of azimuth, for five different band pass filter from 80 seconds up to 2, 5, 8, 10, and 15 seconds. The multipathing of Sdiff is only observed at shorter period. (b) Similar to above, the record section is plotted for azimuth  $51^\circ$  across a range of distance.

## 6.4 Modeling

Most global tomography models show a consistent feature of LLSVP in the lowermost mantle, but the fine-scale structures of the LLSVPs are very different across models (Figure 6.2) and remain to be constrained (e.g. Hosseini et al. [30]). Lu and Grand [31] further illustrate the effects such as incorrectly imaging subducted slab structure and errors in source location and origin time, on introducing artifacts in deep mantle tomography even at regions far away from active subduction zones. In this paper, we choose to build our models on the GyPSuM Model [6] which is also the preferred model in He and Wen [11] as they determine that GyPSuM model best corrects the travel time for S and ScS, and their multiples, and therefore produce the best correlation between the corrected ScS travel time residuals and ScS-S differential travel time residuals. The GyPSuM model has the strongest velocity perturbation in the lowermost mantle compared to other models. The strong perturbation is found to be necessary by Liu et al. [32] as well. In order to fit the mantle reverberations associated with the ScS multiples in a similar profile across the Pacific plate from Fiji-Tonga deep events to stations in Southern California, Liu et al. [32] inflates the lowermost 600km of the tomography model S20RTS by a factor of 2, which becomes comparable to the GyPSuM model. The ScS bounce point near surface is accounted by the PAC06 upper mantle model [33], which is similar to the PA5 model developed by Gaherty et al. [34] by inverting S multiples, R1 and G1 surface waves data, and has shown to have excellent fit to the S multiples up to S5 [33] and S triplications data [32].

The waveform synthetics are generated using a graphics processing unit (GPU) based 2-D finite difference (FD) scheme [35] with source focal mechanisms from the USGS W-phase earthquake catalog. The 2-D FD method is highly efficient and flexible for modeling global seismograms and has been used to model core phases up to 3 Hz [36]. We set the FD grid size to 1.5 km and time step to 0.023s to ensure that the simulated wavefield is accurate up to 2 seconds. Considering the complex lateral variation of fine-scale structures along the edge of LLSVP which can be highly 3-D, our 2-D modeling process will not attempt to quantitatively constrain the geometry and velocity of these fine-scale structures but to use as few parameters as possible to demonstrate the necessity of complicated interactions of various structures at the edge of the LLSVP (Figure 6.1 inset).

The observed multipathing of Sdiff, as pointed out by To et al. [10], is not easily explained without strong localized slow ULVZ-like anomalies. The GyPSuM model

alone does not produce multipathing, neither are other alterations such as inflating the velocity perturbation of the GyPSuM model by a factor of 1.5 and 2 (Figure 6.12). Previous forward modeling results show a variety of velocity reductions and geometries of ULVZ in the region, ranging from a gradient ULVZ model of -3 to -5%  $V_s$  reduction with a large thickness of 60 km [11] to a uniform ULVZ model of 30% reduction with varying thickness between 10 and 20 km [8]. In our study, we model with a gradient ULVZ model of -3 to -15% with thickness of 80 km, which is similar to He and Wen [11], and show that it can reproduce the multipathing observation with the right timing and amplitude ratio between the initial and secondary pulse, compared to a model with uniform velocity reduction (Figure 6.13). The ULVZ models, however, are not uniquely constrained as there are notable trade-off between ULVZ thickness and its velocity reduction (e.g. [37]). There is also a strong lateral variation of ULVZ geometries across a narrow range of azimuth [8], and the waveform effect of these 3-D structures is not completely captured by the 2-D modeling process. On the other hand, the multipathing behavior is sensitive to the location of the ULVZ model (Figure 6.14), in which the ray enters the ULVZ from the top and generates a secondary delayed and weaker pulse. With the location constrained, we test a range of widths for the ULVZ models and find that widths of  $5 - 10^\circ$  (about 600 to 1200 km at the core-mantle boundary) can fit the waveform shaper of the multipathing pattern sufficiently well, with two simple pulses (Figure 6.15). A ULVZ model wider than  $10^\circ$  causes severe distortions to the waveform shape and produces multiple late arriving pulses.

Focusing on Event A and B, a pure GyPSuM model does not predict the delay and rapid speed up of differential ScS-S travel time (Figure 6.16a). Although a strong artificial inflation of the perturbation by a factor of 2 may explain the differential ScS-S travel time (Figure 6.17), Event C shows that a strong ULVZ structure of a velocity reduction up to 15% is necessary in the same location and this ULVZ structure can increase the differential ScS-S travel time by delaying the travel time of ScS (Figure 6.16b). However, a single ULVZ structure would not explain the rapid speed up of differential ScS-S travel time at larger distances. There are two ways to reduce the differential travel time at larger distances. One is to include a fast slab-like structure ( $V_s = +2.5\%$ ) which is sampled by ScS at larger distances, thus speeding up ScS (Figure 6.16c). Moreover, for both events, the arrival time of S also shows strong delays for a localized region independent of ScS (Figure 6.6), which is more severe for the deeper event. A possible plume structure in which S at larger distances are more sensitive to may explain the extra slow down of the S

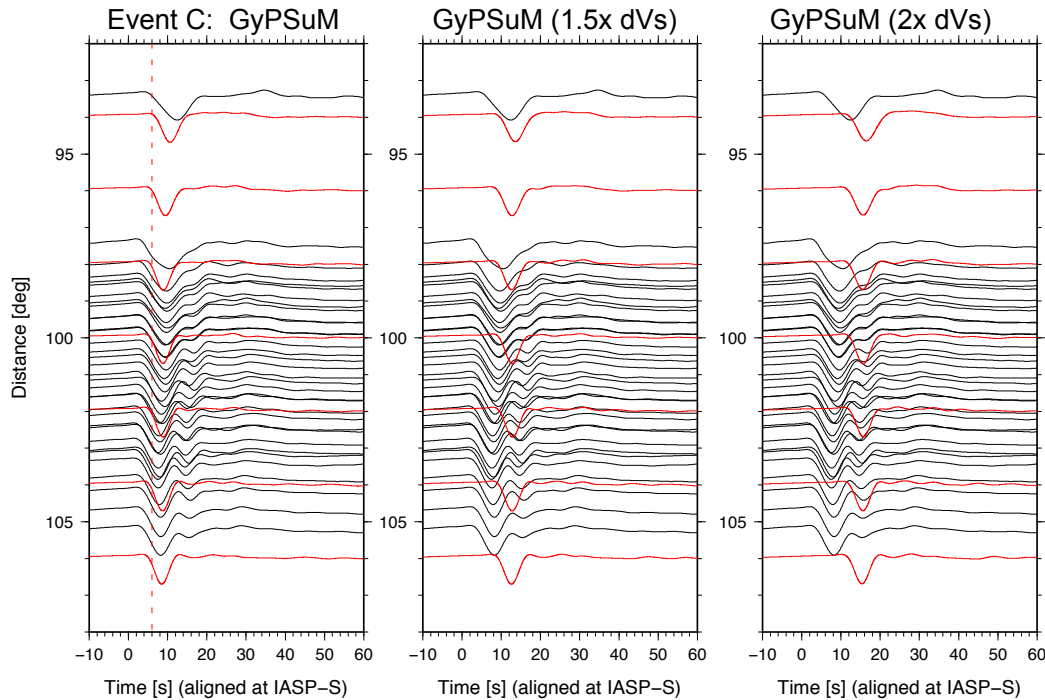


**Figure 6.12:** The record sections comparing stacked tangential displacement data from Event C (in black) and synthetics generated using GyPSuM model. Increasing the perturbation of the velocity in the tomography model by a factor of 1.5 and 2 do not reproduce the multipathing observed in data.

phase, and hence contribute to further reducing the differential travel time. In our model, the plume is modeled to be extending upward for at least 700 km with a velocity reduction of 5% and narrows towards the top.

Modeling purely the travel time of ScS and S for Event A and Event B severely limits our capability of resolving detailed structures, particularly the plume. However, as the ULVZ location is more constrained by the sensitivity of S\*, after allowing the combination of structures (ULVZ, slab, and plume) to move along the core mantle boundary, the model that best fits the observations requires the ULVZ to be located close to the edge of the LLSVP and the fast structure outside of the LLSVP. The plume is hypothesized to be at the edge of the LLSVP. The best fitting results are shown in Figure 6.18 (Event A and B) and Figure 6.19 (Event C). For Event C, the addition of the fast structure and plume does not alter the multipathing effect of Sdiff and brings slight improvement to waveform fitting at distances around 90 degree. As a whole, a combination of ULVZ, fast structure, and plume is needed to explain the observations of all three events along the same azimuth. The multipathing of Sdiff and the delay of ScS at shorter distances is caused by the ULVZ structure,

followed by the rapid decrease of differential time at larger distances by speeding up ScS due to the fast structure outside of the LLSVP and slowing down S by a potential plume.

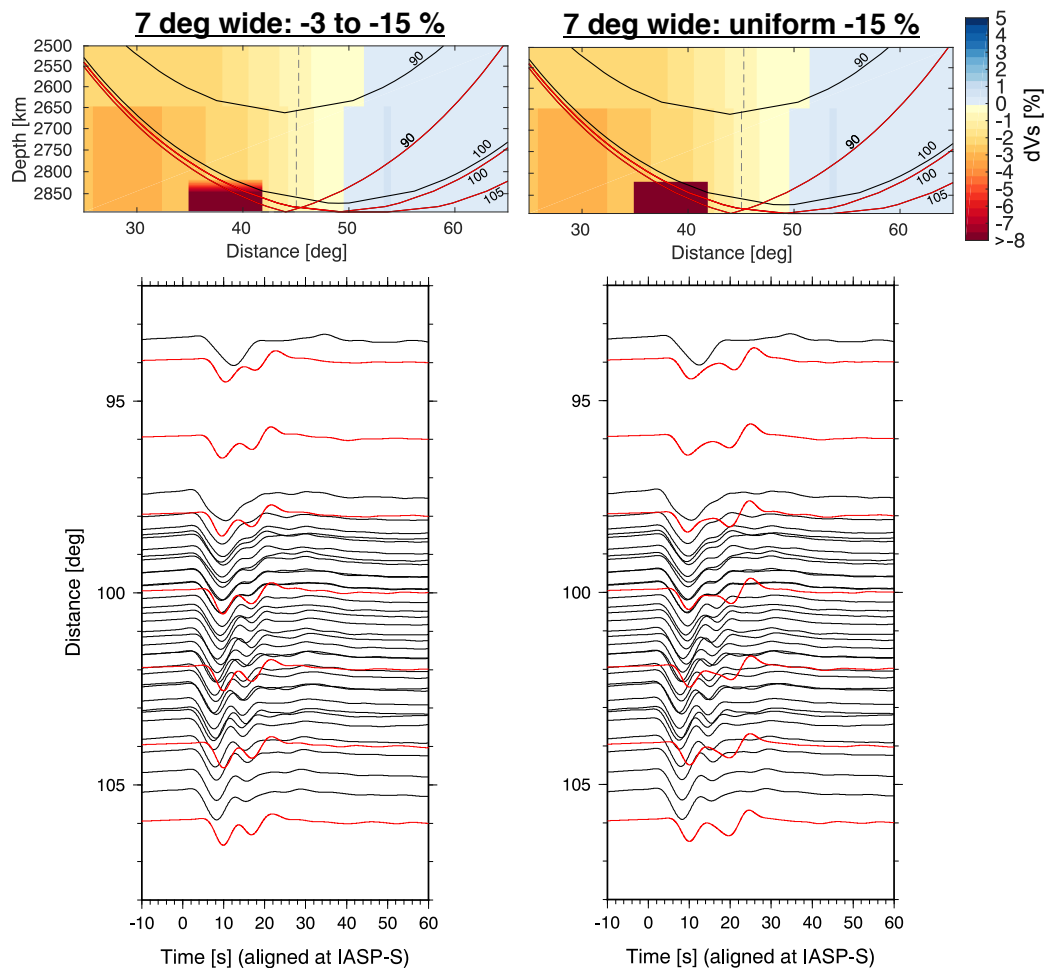


**Figure 6.13:** We test two models of ULVZ (left:  $dVs = -3$  to  $15\%$ , 80 km tall, 7 deg wide; middle: uniform  $dVs = -15\%$ , 80 km tall, 7 deg wide; right:  $dVs = -15\%$ , 70 km tall, 3 deg wide, same as Sun et al. [7]) to see if the velocity gradient of the ULVZ can be constrained by the  $S^*$  observation, which has implications on the composition of the ULVZ. All models show some degrees of multipathing. However, based on the characteristics of multipathing observed in this study, we prefer a model that has a gradient velocity structure, rather than a uniform velocity which  $S^*$  arrival is more delayed than observed.

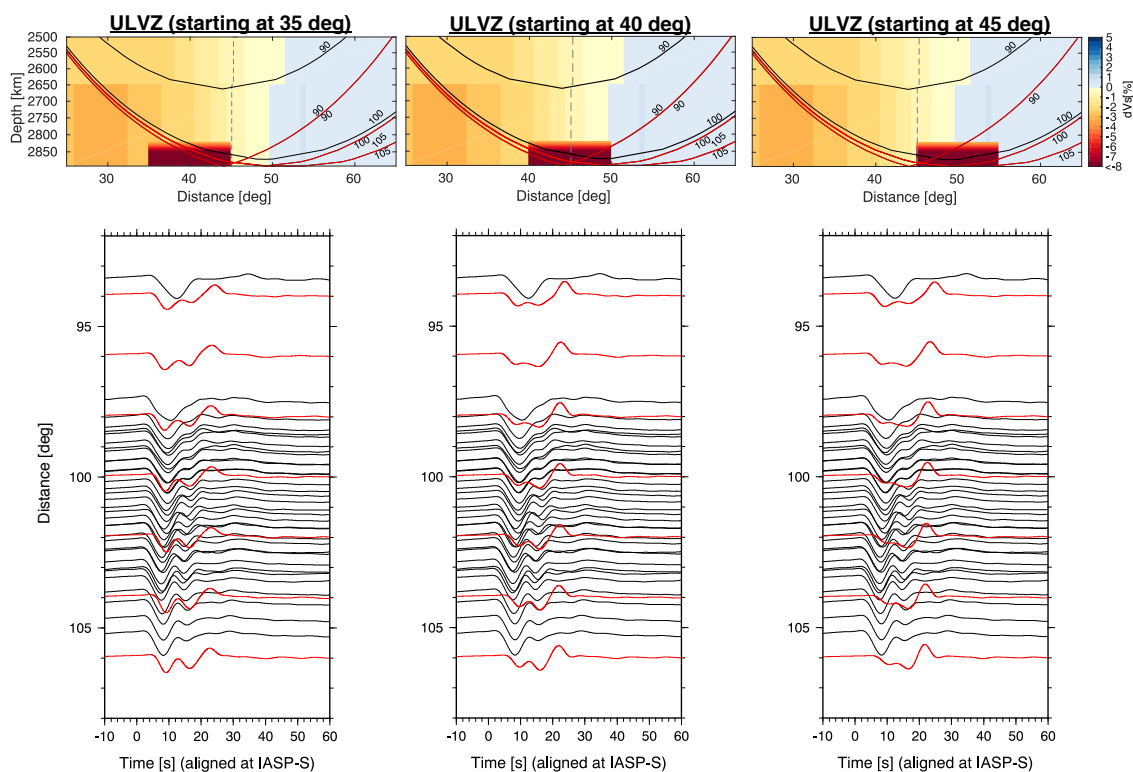


**Figure 6.14:** Event C shows a strong case of multipathing where there are late arrivals following SH diffracted phase, namely  $S^*$  that has a lower amplitude compared to the main SH diffracted phase. Here we run several 2D simulations, using models of ULVZ (10 deg wide) at different starting locations, and show that  $S^*$  is generated when the ray path of ScS crosses the top of the ULVZ structure, multipaths and travels as a delayed pulse. ULVZs at other location will also produce multipathing, but with a different shape and strength, and hence we can use the observed  $S^*$  to constrain the location of the ULVZ.

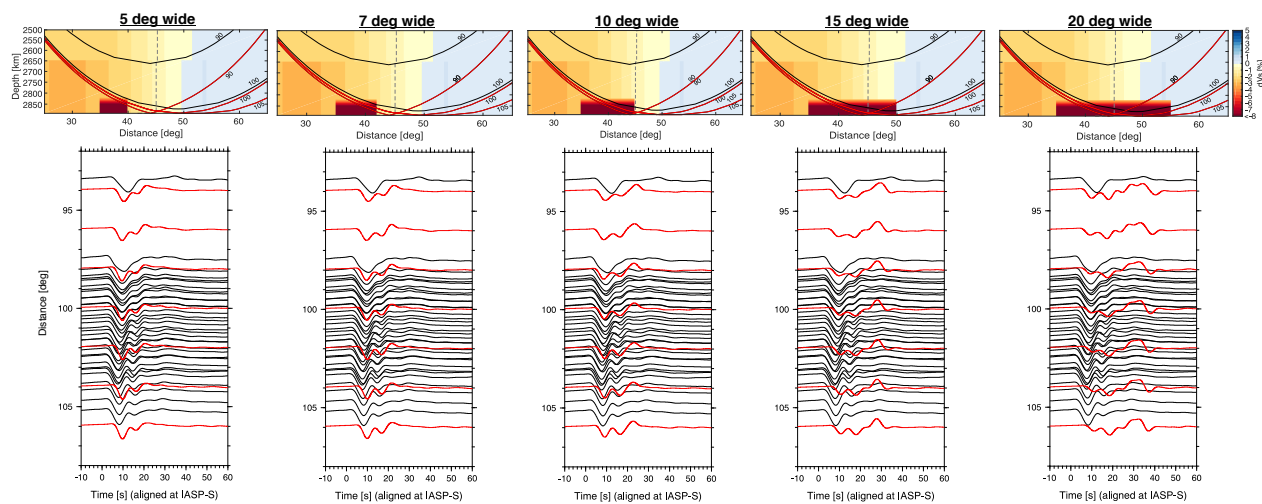


**Figure 6.15:** As shown in Figure 6.14, the amplitude ratio of SH diffracted and S\* are sensitive to the location of the ULVZ. We fix the starting location of ULVZ, and test several models of ULVZ with different widths. The 2D synthetics show that ULVZ with width between 5 to 10 degree produces similar pulse shapes, while ULVZ greater than 15 degree introduces severe multipathing and is unable to preserve the relatively simple two-pulse shape. The observation limits the size of ULVZ to be between 5 and 10 degree.

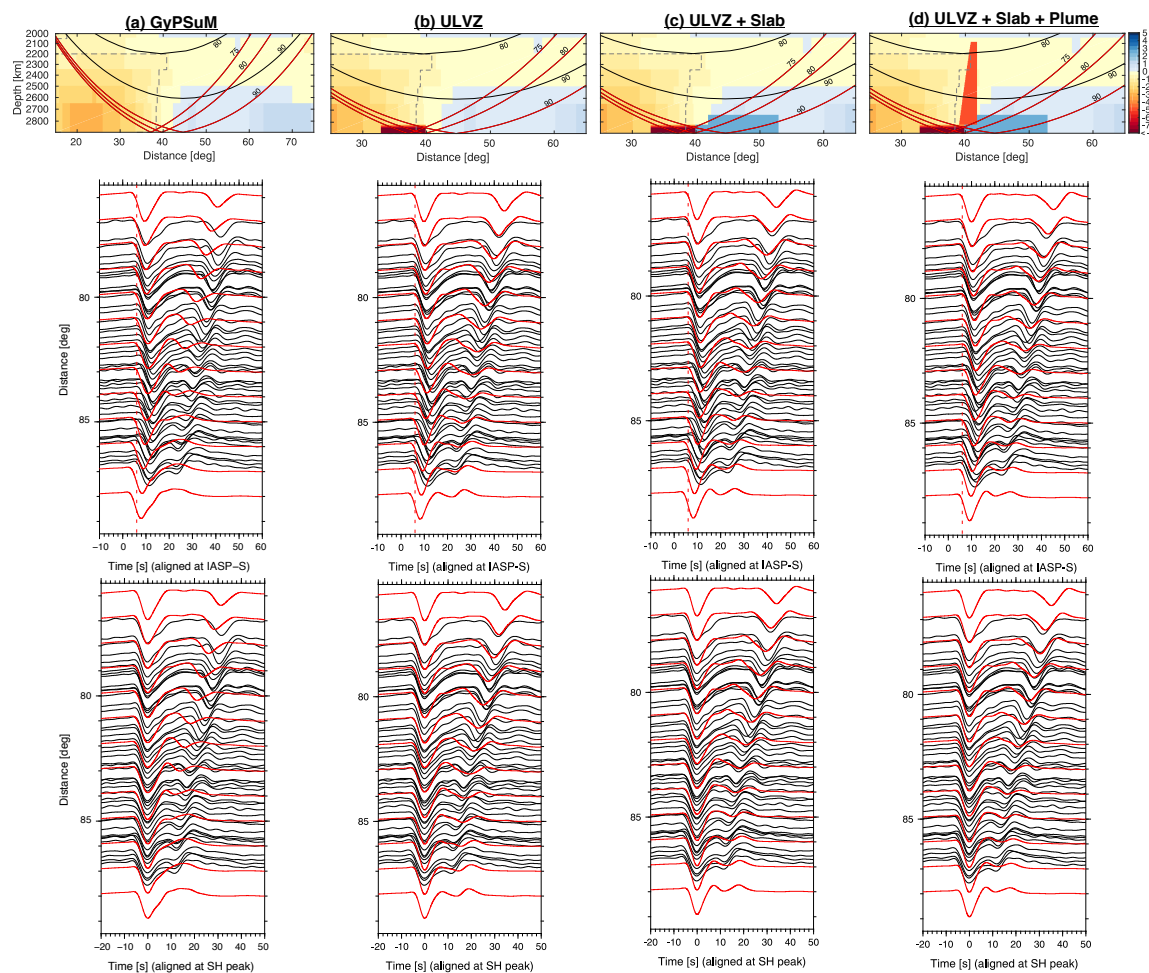


**Figure 6.16:** We show the effect of each structure in our preferred model for Event B at depth 235 km (ULVZ:  $dV_s = -3$  to  $15\%$ , 80 km tall, 7 deg wide; plume:  $dV_s = -5\%$ , 700 km tall, 3 deg wide at the bottom, 1 deg wide at top; slab:  $dV_s = +2.5\%$ , 150 km tall, 17 deg wide). Record sections show data in black, and synthetics from the 2D modeling in red with two types of alignments (top: aligned at expected IASP-S arrival; bottom: aligned at the peak of SH arrival). The presence of ULVZ is necessary due to the observations of  $S^*$  in Event C, which in turn delays the ScS arrivals, particularly for distance less than  $80^\circ$ . In order to fit the differential ScS-S time, a fast slab outside of the LLSVP is necessary to speed up ScS at greater distances. The plume, suggested by the observed slowdown of S independent of ScS, can further contribute to the fitting of differential ScS-S time by delaying the S arrival by 1 to 2 seconds for distance between  $83^\circ$  and  $86^\circ$ . However, the geometry and velocity reduction of the plume cannot be well-constrained.

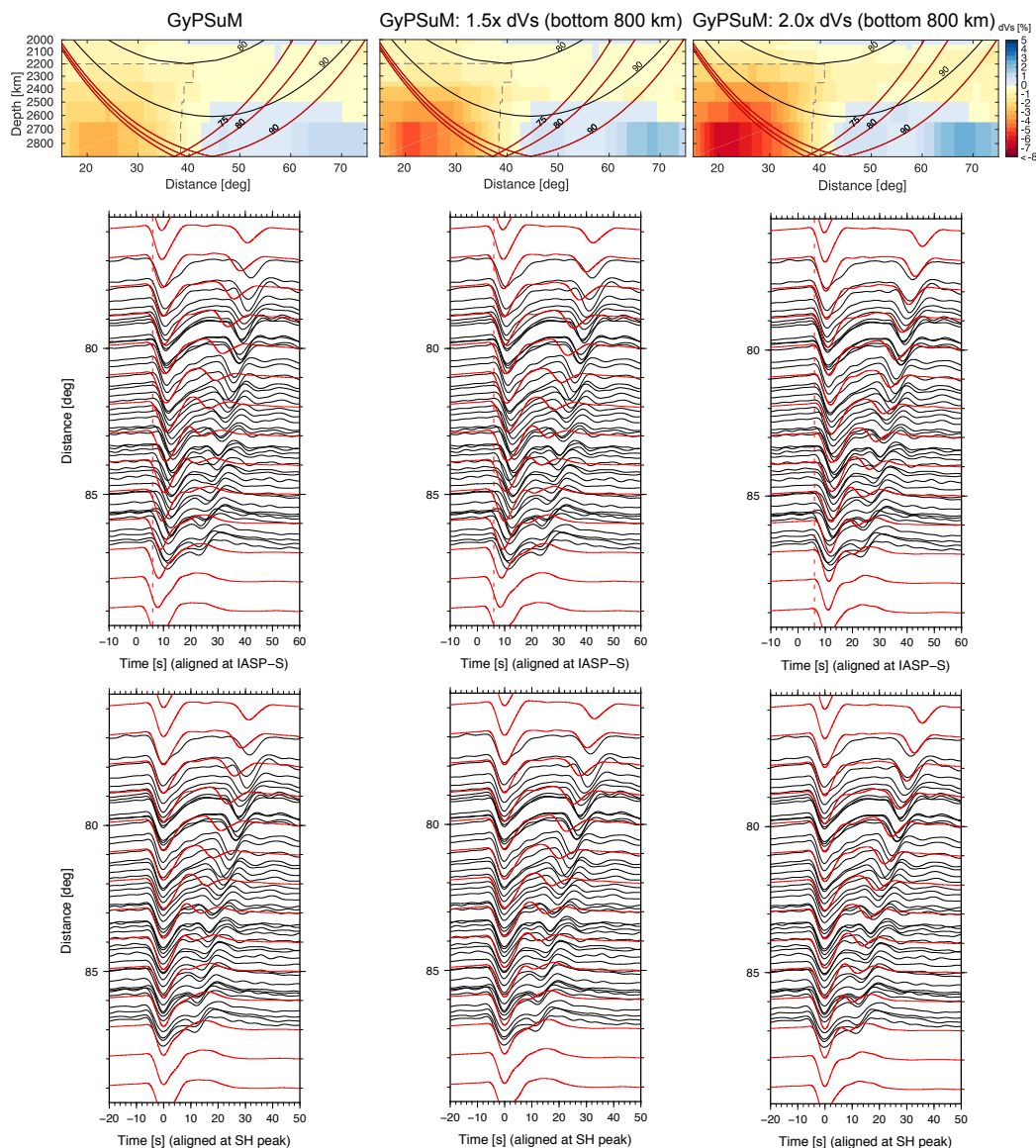


**Figure 6.17:** The record sections comparing stacked tangential displacement data from Event B (in black) and synthetics generated using GyPSuM model (in red). Increasing the perturbation of the velocity in the tomography model by a factor of 2 may fit the differential ScS-S time. However, it is still not sufficient in explaining the rapid lateral variation in the differential travel time behavior across azimuths.

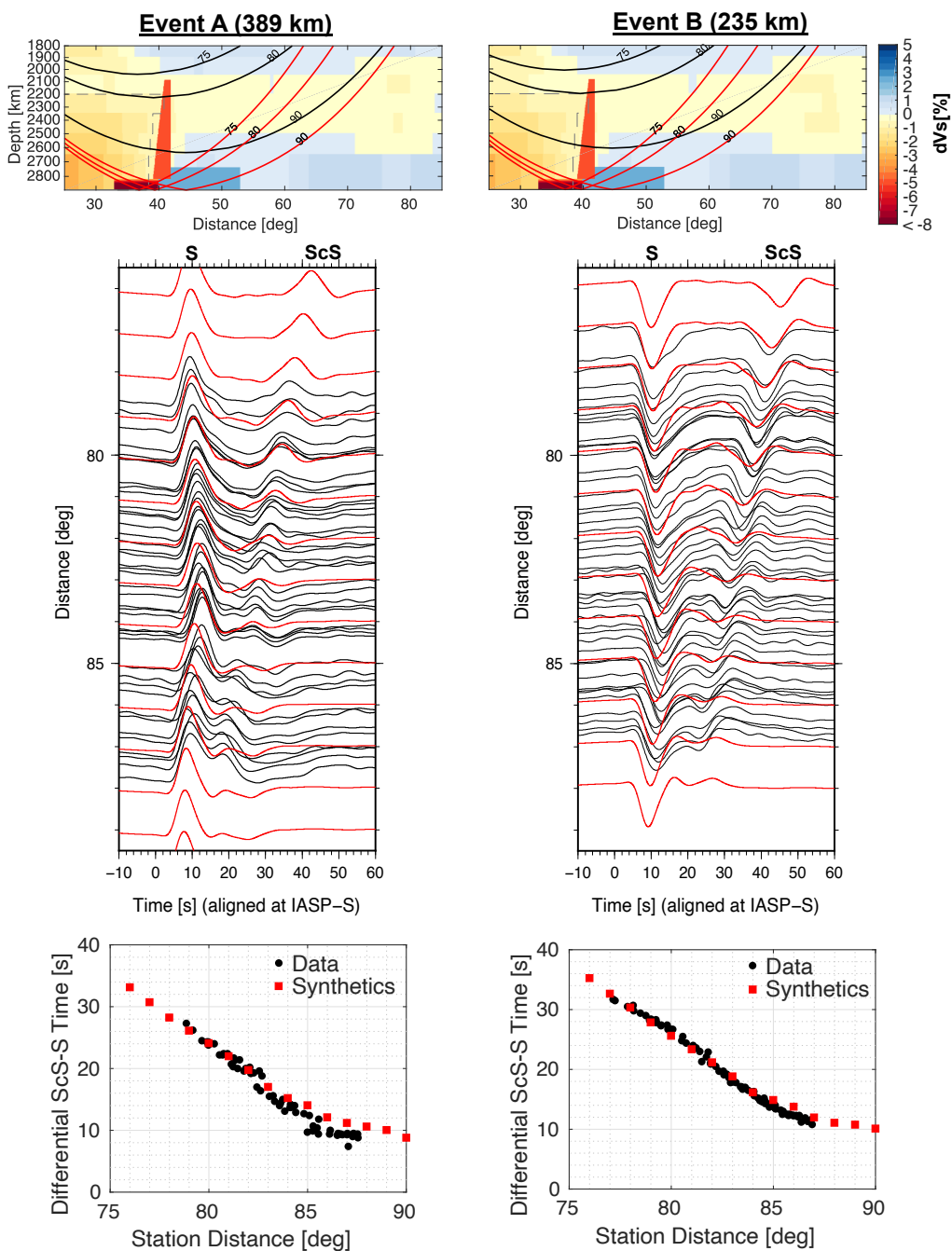


**Figure 6.18:** Left panel shows the record section of SH diffracted data from Event A, at azimuth 50-52° in black, against 2D synthetics (in red) using a model consisting of a ULVZ (-3 to -15%, 7 deg wide, 80 km tall), a plume (-5%; up to 800 km tall; 3 deg wide at bottom and 1 deg wide at top) and a fast slab (+2.5%; 150 km tall). The synthetics matches the observed differential ScS-S time well. Right panel shows a similar record section of data (azimuth 49 – 51°; black) and synthetics (red) for Event B.

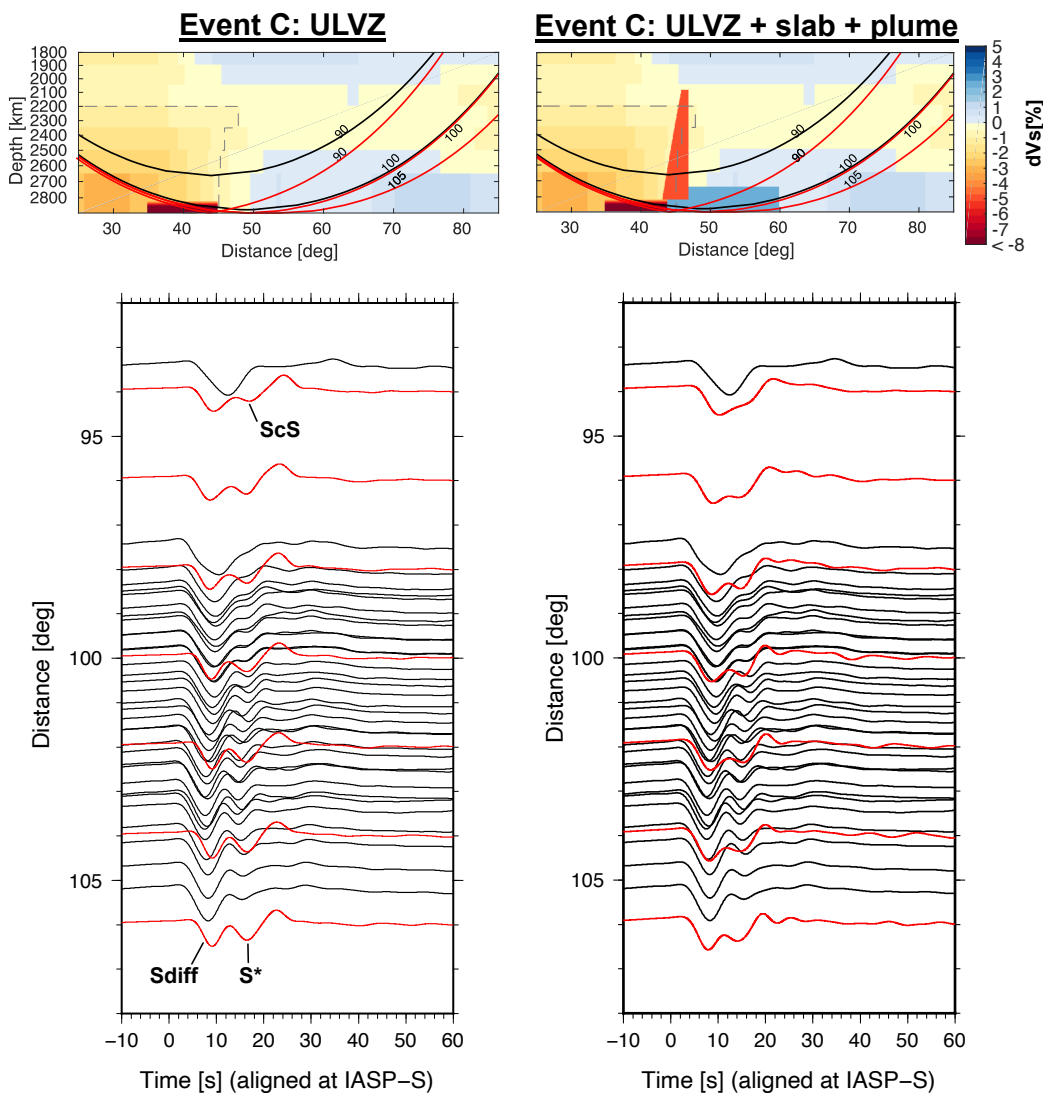


**Figure 6.19:** Left panel shows the record section of SH diffracted data from Event C, at azimuth  $50\text{--}52^\circ$  in black, against 2D synthetics (in red) using model with the presence of ULVZ ( $-3$  to  $-15\%$ ,  $9$  deg wide,  $80$  km tall). The ray paths of ScS crossing the top of ULVZ is the source of the multipathing and generation of the late arriving  $S^*$ . Right panel shows the record section of data against synthetics from the preferred model, with the ULVZ, plume and fast slab ( $2.5\%$ ). The geometry of the plume and slab is the same shown in Figure 6.18. The presence of slab speeds up ScS slightly for distances less than  $100^\circ$  and speeds up SH diffracted arrivals, noticeably for distances greater than  $102^\circ$ , while the plume has minimal impact on the overall waveform.

## 6.5 Discussion

Hotspots are thought to be formed by convection plumes from the deep mantle [2], where the hotspot chains are associated with the magmatism from the remaining plume tail after the plume head has risen and erupted as large igneous provinces [38]. From the finite-frequency tomographic study by Montelli et al. [39], the Hawaiian plume is thought to be well-connected into the lower mantle but the seismic resolution in the lower mantle remains lacking due to poor sampling of seismic rays. This study focuses on constraining the velocity structure at the lowermost mantle near the edge of the Pacific LLSVP near Hawai'i as plumes are hypothesized to originate from the edges of the LLSVP at the core mantle boundary. Several plate reconstruction studies (e.g. [40, 41]) show strong spatial correlation of large igneous provinces, hotspots, and kimberlites to the edges of LLSVP. Yu and Garnero [12] have also found that the ULVZs are more commonly found in the edges of LLSVP and hotspots, although the correlation to the hotspots is not statistically robust. Nonetheless, strong lateral temperature gradients across the edges of LLSVP, further assisted by the heating of the basal part of subducted slab, can facilitate the initiation of plumes and ascend from the narrow edges of the LLSVP [42].

Based on rapid changes in differential ScS-S travel times and multipathing, we propose a strong ULVZ structure located near the edge of the Pacific LLSVP, potentially pushed laterally by a subducted slab, providing the necessary temperature gradient for plume generation. Studies from multiple ScS travel time ([21]; this study) also show that the velocity and Q structure directly beneath current Hawaiian hotspot is close to average mantle and therefore the Hawaiian plume is unlikely to be a broad, mantle plume directly beneath present day Hawaii. Therefore, we further hypothesize that the source of the Hawaiian plume is not directly below the present-day location but about  $10^\circ$  southeast of it, at around latitude  $10^\circ$ , longitude  $-145^\circ$  (Figure 6.1).

This edge of the Pacific LLSVP has shown to be complicated with rapid changes in core-mantle boundary. Previously, Lay et al. [9] show a strong lateral velocity heterogeneity from the interior of LLSVP towards the margin, where the fast post-perovskite lens thins towards the edge and the ULVZ layer increases in thickness. Recently, through deconvolution and stacking, Zhao et al. [8] model the ScS precursor and postcursor energies and hypothesize a non-uniform distribution of ULVZs of various thickness (4 - 20 km) and velocity reduction (15 to 30%) along the corridor, and the location of the heterogeneity corresponds to the same vicinity

where we observe strong multipathing in Sdiff (Figure 6.1, Box C). Sun et al. [7] also observe complex ScS arrival further north along the edge of the LLSVP due to a different ULVZ-type structure, further emphasizing the 3-D heterogeneity along this edge.

In our forward modeling, we do not have the sensitivity to reproduce the heterogeneity, but we use simple block models to show that this edge is further complicated with the presence of slab pushing against the LLSVP and the strong localized ULVZ structure. Based on SKS-SKKS splitting measurements, similar complexity at the edge is also proposed LLSVP by Reiss et al. [17], where the lowermost mantle flow near the eastern edge of the African changes geometry from a slab-driven horizontal flow to vertical upwelling at the edge of the LLSVP. The proximity of our ULVZ structure to the edge of the LLSVP and slab structure outside of the LLSVP can be a consequence of either or both (1) accumulation of dense material towards upwelling regions due to deep mantle flow along the margins of LLSVP [43] and (2) iron enrichment from the partial melting of subducted slab sitting on the core-mantle boundary, which is dense and gravitationally stable [44, 45, 46]. The ULVZ could also be a distinct structure composed of a low-velocity and low-viscosity solid phase like iron-rich (Mg,Fe)O magnesiowüstite [16, 47].

The strong thermochemical convection within LLSVP and from the slab descent are conducive to generating a long-lasting plume rising along the edge of the LLSVP [42, 48]. The plume structure is not well-resolved in our modeling; however, the observed rapid variation of differential ScS-S travel time, plus the presence of both ULVZ and slab, suggests the possibility of a plume structure and should warrant more detailed study with other independent observations in future.

In addition, the interaction of a subducted slab with the LLSVP provides a viable mechanism to explain another important feature of the Hawaiian volcanic chains, i.e. the major difference in geochemical characteristics between the two trends of the Hawaiian volcanic chains, namely the Kea and Loa trends. This chemical contrast is developed when the ascending plume preferentially draws materials from two distinct sources within the deep mantle, for example regions inside and outside of the LLSVP boundary [49]. From high-resolution 3D geodynamic models, Dannberg and Gassmöler [50] emphasize the importance of slab in inducing strong lower mantle flow towards the edge of the LLSVP, which can trigger upwelling of materials originating from both the thermal boundary layer and chemical pile, creating the asymmetry within the plume and preserving the chemical gradient

across the edge of the LLSVP. They also show that the direction of current Pacific plate motion, which is perpendicular to the proposed chemical gradient, is favorable in the development of such bilateral chemical zoning for the Hawaiian plume. The subducted slab can also interact and deform the LLSVP, and push the source of hotspot to its current vicinity, which is demonstrated by Hassan et al. [5] and close to our observations in this study.

## 6.6 Conclusion

In this paper, we model the observed rapid variation of differential ScS-S travel time and multipathing of Sdiff and propose a ULVZ-plume-slab interaction at the northeastern edge of the Pacific LLSVP, 10 degree southeast of present-day Hawaii. The configuration and location of this ULVZ-plume-slab interaction can explain many defining features of Hawaii-Emperor Seamount chain, which are the Hawaiian-Emperor bend and migration rate of the seamounts modeled in mantle flow models, and the geochemical characteristics of the Hawaiian volcano trends by initiating and preserving a bilaterally-zoned asymmetric plume.

## 6.7 Acknowledgements

This work is primarily advised by Professor Emeritus Don Helmberger. The project is supported by grant NSF-CSEDI-EAR-1161046. Data from the TA network were made freely available as part of the EarthScope USArray facility, operated by Incorporated Research Institutions for Seismology (IRIS) and supported by the National Science Foundation, under Cooperative Agreements EAR-1261681. Several plots were made using the Generic Mapping Tools version 4.2.1 ([www.soest.hawaii.edu/gmt](http://www.soest.hawaii.edu/gmt); Wessel and Smith, 1998).

## References

- [1] J. T. Wilson. A possible origin of the Hawaiian islands. *Canadian Journal of Physics*, 41(6):863–870, 1963.
- [2] W. J. Morgan. Convection plumes in the lower mantle. *Nature*, 230(5288):42, 1971.
- [3] J. Tarduno, H.-P. Bunge, N. Sleep, and U. Hansen. The bent Hawaiian-Emperor hotspot track: Inheriting the mantle wind. *Science*, 324(5923):50–53, 2009.
- [4] B. Steinberger, R. Sutherland, and R. J. O’connell. Prediction of Emperor-Hawaii seamount locations from a revised model of global plate motion and mantle flow. *Nature*, 430(6996):167, 2004.

- [5] R. Hassan, R. D. Müller, M. Gurnis, S. E. Williams, and N. Flament. A rapid burst in hotspot motion through the interaction of tectonics and deep mantle flow. *Nature*, 533(7602):239, 2016.
- [6] N. A. Simmons, A. M. Forte, L. Boschi, and S. P. Grand. GyPSuM: A joint tomographic model of mantle density and seismic wave speeds. *Journal of Geophysical Research: Solid Earth*, 115(B12), 2010.
- [7] D. Sun, D. Helmberger, V. H. Lai, M. Gurnis, J. M. Jackson, and H-Y Yang. Slab control on the northeastern edge of the mid-Pacific LLSVP near Hawaii. *Geophysical Research Letters*, 46(6):3142–3152, 2019.
- [8] C. Zhao, E. J. Garnero, M. Li, A. McNamara, and S. Yu. Intermittent and lateral varying ULVZ structure at the northeastern margin of the Pacific LLSVP. *Journal of Geophysical Research: Solid Earth*, 122(2):1198–1220, 2017.
- [9] T. Lay, J. Hernlund, E. J. Garnero, and M. S. Thorne. A post-perovskite lens and D'' heat flux beneath the central Pacific. *Science*, 314(5803):1272–1276, 2006.
- [10] A. To, Y. Fukao, and S. Tsuboi. Evidence for a thick and localized ultra low shear velocity zone at the base of the mantle beneath the central Pacific. *Physics of the Earth and Planetary Interiors*, 184(3-4):119–133, 2011.
- [11] Y. He and L. Wen. Geographic boundary of the “Pacific Anomaly” and its geometry and transitional structure in the north. *Journal of Geophysical Research: Solid Earth*, 117(B9), 2012.
- [12] S. Yu and E. J. Garnero. Ultralow velocity zone locations: A global assessment. *Geochemistry, Geophysics, Geosystems*, 19(2):396–414, 2018.
- [13] N. Sun, W. Wei, S. Han, J. Song, X. Li, Y. Duan, V. B. Prakapenka, and Z. Mao. Phase transition and thermal equations of state of (Fe, Al)-bridgmanite and post-perovskite: Implication for the chemical heterogeneity at the lowermost mantle. *Earth and Planetary Science Letters*, 490:161–169, 2018.
- [14] M. J. Fouch, K. M. Fischer, and M. E. Wysession. Lowermost mantle anisotropy beneath the Pacific: Imaging the source of the Hawaiian plume. *Earth and Planetary Science Letters*, 190(3-4):167–180, 2001.
- [15] L. Parisi, A. M. G. Ferreira, and J. Ritsema. Apparent splitting of S waves propagating through an isotropic lowermost mantle. *Journal of Geophysical Research: Solid Earth*, 123(5):3909–3922, 2018.
- [16] G. J. Finkelstein, J. M. Jackson, A. Said, A. Alatas, B. M. Leu, W. Sturhahn, and T. S. Toellner. Strongly anisotropic magnesiowüstite in Earth’s lower mantle. *Journal of Geophysical Research: Solid Earth*, 123(6):4740–4750, 2018.

- [17] M. C. Reiss, M. D. Long, and N. Creasy. Lowermost mantle anisotropy beneath Africa from differential SKS-SKKS shear-wave splitting. *Journal of Geophysical Research: Solid Earth*, 124(8):8540–8564, 2019.
- [18] D. Zhao. Global tomographic images of mantle plumes and subducting slabs: insight into deep Earth dynamics. *Physics of the Earth and Planetary Interiors*, 146(1-2):3–34, 2004.
- [19] S. W. French and B. Romanowicz. Broad plumes rooted at the base of the Earth’s mantle beneath major hotspots. *Nature*, 525(7567):95, 2015.
- [20] B. R. Julian, G. R. Foulger, J. H. Natland, D. C. Presnall, and D. L. Anderson. What can seismology say about hotspots? *Special Papers - Geological Society of America*, 388:155, 2005.
- [21] H. Kanamori and L. Rivera. Near-vertical multiple ScS phases and vertically averaged mantle properties. *The Interdisciplinary Earth: A Volume in Honor of Don L. Anderson*, 71:9–31, 2015.
- [22] W. J. Best, L. R. Johnson, and T. V. McEvelly. ScS and mantle beneath Hawaii. In *Transactions-American Geophysical Union*, volume 55, pages 1147–1147. American Geophysical Union, 1974.
- [23] J. Ritsema, A. Deuss, H. J. Van Heijst, and J. H. Woodhouse. S40RTS: a degree-40 shear-velocity model for the mantle from new Rayleigh wave dispersion, teleseismic traveltimes and normal-mode splitting function measurements. *Geophysical Journal International*, 184(3):1223–1236, 2011.
- [24] P. Moulík and G. Ekström. An anisotropic shear velocity model of the Earth’s mantle using normal modes, body waves, surface waves and long-period waveforms. *Geophysical Journal International*, 199(3):1713–1738, 2014.
- [25] D. Komatitsch and J. Tromp. Spectral-element simulations of global seismic wave propagation—i. validation. *Geophysical Journal International*, 149(2):390–412, 2002.
- [26] S. W. French and B. A. Romanowicz. Whole-mantle radially anisotropic shear velocity structure from spectral-element waveform tomography. *Geophysical Journal International*, 199(3):1303–1327, 2014.
- [27] K. Hosseini, K. J. Matthews, K. Sigloch, G. E. Shephard, M. Domeier, and M. Tsekhmistrenko. Submachine: Web-based tools for exploring seismic tomography and other models of Earth’s deep interior. *Geochemistry, Geophysics, Geosystems*, 19(5):1464–1483, 2018.
- [28] D. A. Frost and S. Rost. The P-wave boundary of the large-low shear velocity province beneath the Pacific. *Earth and Planetary Science Letters*, 403:380–392, 2014.

- [29] D. Sun, D. Helmberger, S. Ni, and D. Bower. Direct measures of lateral velocity variation in the deep Earth. *Journal of Geophysical Research: Solid Earth*, 114(B5), 2009.
- [30] K. Hosseini, K. Sigloch, M. Tsekhmistrenko, A. Zaheri, T. Nissen-Meyer, and H. Igel. Global mantle structure from multifrequency tomography using P, PP and P-diffracted waves. *Geophysical Journal International*, 220(1):96–141, 2019.
- [31] C. Lu and S. P. Grand. The effect of subducting slabs in global shear wave tomography. *Geophysical Journal International*, 205(2):1074–1085, 2016.
- [32] L. Liu, Y. Tan, D. Sun, M. Chen, and D. Helmberger. Trans-Pacific whole mantle structure. *Journal of Geophysical Research: Solid Earth*, 116(B4), 2011.
- [33] Y. Tan and D. V. Helmberger. Trans-Pacific upper mantle shear velocity structure. *Journal of Geophysical Research: Solid Earth*, 112(B8), 2007.
- [34] J. B. Gaherty, T. H. Jordan, and L. S. Gee. Seismic structure of the upper mantle in a central Pacific corridor. *Journal of Geophysical Research: Solid Earth*, 101(B10):22291–22309, 1996.
- [35] D. Li, D. Helmberger, R. W. Clayton, and D. Sun. Global synthetic seismograms using a 2-D finite-difference method. *Geophysical Journal International*, 197(2):1166–1183, 2014.
- [36] D. Li, D. Sun, and D. Helmberger. Notes on the variability of reflected inner core phases. *Earthquake Science*, 27(4):441–468, 2014.
- [37] M. S. Thorne and E. J. Garnero. Inferences on ultralow-velocity zone structure from a global analysis of SPdKS waves. *Journal of Geophysical Research: Solid Earth*, 109(B8), 2004.
- [38] M. A. Richards, R. A. Duncan, and V. E. Courtillot. Flood basalts and hot-spot tracks: plume heads and tails. *Science*, 246(4926):103–107, 1989.
- [39] R. Montelli, G. Nolet, F. A. Dahlen, and G. Masters. A catalogue of deep mantle plumes: New results from finite-frequency tomography. *Geochemistry, Geophysics, Geosystems*, 7(11), 2006.
- [40] K. Burke and T. H. Torsvik. Derivation of large igneous provinces of the past 200 million years from long-term heterogeneities in the deep mantle. *Earth and Planetary Science Letters*, 227(3-4):531–538, 2004.
- [41] T. H. Torsvik, K. Burke, B. Steinberger, S. J. Webb, and L. D. Ashwal. Diamonds sampled by plumes from the core–mantle boundary. *Nature*, 466(7304):352, 2010.

- [42] K. Burke, B. Steinberger, T. H. Torsvik, and M. A. Smethurst. Plume generation zones at the margins of large low shear velocity provinces on the core-mantle boundary. *Earth and Planetary Science Letters*, 265(1-2):49–60, 2008.
- [43] M. Li, A. K. McNamara, E. J. Garnero, and S. Yu. Compositionally-distinct ultra-low velocity zones on Earth’s core-mantle boundary. *Nature Communications*, 8(1):177, 2017.
- [44] G. K. Pradhan, G. Fiquet, J. Siebert, A.-L. Auzende, G. Morard, D. Antonangeli, and G. Garbarino. Melting of MORB at core-mantle boundary. *Earth and Planetary Science Letters*, 431:247–255, 2015.
- [45] J. K. Wicks, J. M. Jackson, W. Sturhahn, and D. Zhang. Sound velocity and density of magnesiowüstites: Implications for ultralow-velocity zone topography. *Geophysical Research Letters*, 44(5):2148–2158, 2017.
- [46] M. S. Thorne, N. Takeuchi, and K. Shiomi. Melting at the edge of a slab in the deepest mantle. *Geophysical Research Letters*, 46(14):8000–8008, 2019.
- [47] R. Reali, J. M. Jackson, J. Van Orman, D. J. Bower, P. Carrez, and P. Cordier. Modeling viscosity of (Mg, Fe) O at lowermost mantle conditions. *Physics of the Earth and Planetary Interiors*, 287:65–75, 2019.
- [48] A. M. Jellinek and M. Manga. Links between long-lived hot spots, mantle plumes,  $D''$ , and plate tectonics. *Reviews of Geophysics*, 42(3), 2004.
- [49] D. Weis, M. O. Garcia, J. M. Rhodes, M. Jellinek, and J. S. Scoates. Role of the deep mantle in generating the compositional asymmetry of the Hawaiian mantle plume. *Nature Geoscience*, 4(12):831, 2011.
- [50] J. Dannberg and R. Gassmüller. Chemical trends in ocean islands explained by plume-slab interaction. *Proceedings of the National Academy of Sciences*, 115(17):4351–4356, 2018.

*Chapter 7*

## CONCLUSION

In this thesis, we aim to improve our description of the observed seismic waveforms with the goal of understanding the dynamics during various natural hazards and the long-term dynamics of Earth's evolution. Many methods within seismic waveform modeling are employed, including characterizing the seismic sources through moment tensor inversion, deriving mechanistic model for new seismic sources, and performing numerical simulations to resolve fine-scale structures in Earth's interior. The key results and insights from each study are summarized in the following:

In Chapter 2, we study the evolution of the Kilauea volcano during the 2018 eruption by characterizing the seismic events at the summit. Although moment tensor inversions using data close to the summit reveal a remarkable evolution, from explosive eruptions to the caldera collapse, there are several challenges in determining the solutions such as inherent tradeoff between parameters for shallow non-double couple events. We show that the infrasound measurement is particularly useful in providing additional constraints to the moment tensor solution when inversion from seismic data alone cannot distinguish the solutions. The characterization of these large seismic events allows us to infer the underlying mechanisms for the explosions and collapse at the Kilauea caldera.

In Chapter 3, we close an important gap in debris flow studies by replacing an empirical approach in describing debris flow with a physics-based mechanistic model that accounts for the size of the debris flow and the propagation of seismic waves from the flow to the sensor. The power of this model is showcased in the 2018 Montecito debris flows where key parameters of the debris flows such as boulder size and flow rate, and their evolution during the event, can be determined using just a single seismic station and are corroborated by field observations. Similar to earthquake early warning where we exploit the physics behind predicting the travel times of P, S, and surface waves, a physics-based model for the debris flows will allow us to design a robust early warning system for the most devastating debris flows.

In Chapter 4, we identify the need to understand the direct effect of sedimentary basins on ground motion, which is important particularly for the Los Angeles area

where shallow rupture of large earthquakes is expected. Many previous modeling studies have focused on large regional earthquakes which can mask the direct basin response. Therefore, we isolate the basin effect by only analyzing small earthquakes which occurred close to the basin but at different depths. From seismic waveform analyses, numerical simulations and dense array techniques, we show that a better description of the attenuation model, shallow basin structures and sharp boundaries in 3-D velocity models is crucial in accurately predicting the ground motion hazards.

In Chapter 5 and 6, we focus on understanding the long-term dynamics by modeling the sharp variation in velocity across important structural boundaries. These fine-scale structures are often hard to be resolved in seismic tomographic approaches due to the usage of non-ideal seismic waves (e.g. long period hence long wavelength) and the inherent smoothing in the inversion. The dense broadband station distribution, which record earthquakes that preferentially sample these boundaries, clearly show the anomalies within the waveforms caused by these sharp structures which can be modeled. In Chapter 5, we observed strong travel time variation across the San Andreas plate boundary which can be modeled by a strong velocity contrast at the lower crust – upper mantle across the boundary, which is not inferred in existing 3-D tomographic models. As velocity is a proxy to lithospheric strength, this improved knowledge of the lower crust-upper mantle can help infer the appropriate rheology for modeling long term plate deformation. In Chapter 6, to fit the observations of strong waveform complexity from Fiji-Tonga earthquakes recorded by USArray stations, we propose a combination of several structures which are ultra-low velocity zone (ULVZ), plume and slab at the northeastern edge of the Pacific Large Low Shear Velocity Province (LLSVP), southeast of present-day Hawaii. The particular configuration and location of this ULVZ-plume-slab interaction is important in deep mantle dynamics as it can explain many defining features of Hawaii-Emperor Seamount chain formed by the Hawaiian plume. The plume structure in our study is not highly resolved as it is only constrained by travel time but our results and its significant implication should spur interest for more targeted future studies in this region.

Seismic waveform modeling has been instrumental in bringing insights to many important dynamics-related problems. In many ways, the modeling process is only made possible by the abundant observations collected from a dense distribution of the seismic sensors. We also recognize that one of the major uncertainties in modeling either source or structure, particularly exemplified in Chapter 3 and 4, is the

attenuation model. As we move towards modeling shorter wavelength features with higher frequency waveforms, accurate models of attenuation structure will become increasingly important which warrant further investigation. On the other hand, we see the limitations of seismology, and have sought to complement seismology with observations from other types of data such as infrasound. This approach is not new and has been used extensively in studying large earthquakes through finite fault inversions, which combines both seismic and geodetic data. We see similar potential in volcano seismology where we can formally combine a diverse set of data such as infrasound and seismic data in inversion processes to better distinguish the non-double couple seismic sources and understand the dynamics from multiple perspectives.

Last but not least, the importance of incorporating a variety of data in our own research should perhaps serves as an inspiration to us all, as scientists, that at our scientific workplace, there is indeed value in promoting and investing in diversity, and that we may be enriched with new scientific perspectives as we learn from each other.